3-29-2006

Soot Measurements in Steady and Pulsed Ethylene/Air Diffusion Flames Using Laser-Induced Incandescence

Hayri Serhat Sapmaz
Florida International University, hayrisapmaz@gmail.com

DOI: 10.25148/etd.FI08081545

FLORIDA INTERNATIONAL UNIVERSITY

Miami, Florida

SOOT MEASUREMENTS IN STEADY AND PULSED ETHYLENE/AIR DIFFUSION FLAMES USING LASER-INDUCED INCANDESCENCE

A dissertation submitted in partial fulfillment of the

requirements for the degree of

DOCTOR OF PHILOSOPHY

in

MECHANICAL ENGINEERING

by

Hayri Serhat Sapmaz

2006

To: Dean Vish Prasad
College of Engineering and Computing

This dissertation, written by Hayri Serhat Sapmaz, and entitled Soot Measurements in Steady and Pulsed Ethylene/Air Diffusion Flames using Laser-Induced Incandescence, having been approved in respect to style and intellectual content, is referred to you for judgment.

We have read this dissertation and recommend that it be approved.

_____
Chaouki Ghenai

_____
Cheng-Xian Lin

_____
Yiding Cao

_____
Arvind Agarwal

_____
Norman D. H. Munroe, Major Professor

Date of Defense: March 29, 2006

The dissertation of Hayri Serhat Sapmaz is approved.

_____
Dean Vish Prasad
College of Engineering and Computing

_____
Interim Dean Stephan L. Mintz
University Graduate School

Florida International University, 2006

DEDICATION

I dedicate this thesis to my father, M. Ergun Sapmaz. Without his guidance, love, support, understanding, and belief in me, the completion of this work would not have been possible.

ACKNOWLEDGMENTS

I would like to thank Dr. Norman Munroe for his guidance throughout the completion of my dissertation. I wish to thank my supervisor, Dr. Chaouki Ghenai, for his support, patience and encouragement. He was not only my supervisor but also a great mentor to me. Aside from my dissertation work, he supervised me under several projects for the past five years. He has always been supportive, positive, encouraging and patient with me since I started my Ph.D. program. I also would like to thank the other committee members for their advice and encouragement. I would like to mention that without the financial support from Applied Research Center (ARC), the completion of this work would not have been possible. Dr. Cheng-Xian Lin, Dr. George Philippidis, Dr. Peter Skudarnov, Bill Youngblut, Maria Benincasa, Lee Schneider, Dr. John Laffitte and Dr. Rajiv Srivastava are among many people that I appreciate their invaluable support.

I am also grateful to Dr. Umit Koylu for giving me the necessary background in laser diagnostics and combustion as well as being my major professor during my Master's degree.

I would like to mention Dr. Ali Ebadian for pushing me to start the Ph.D. program and for his support.

I would like to take this opportunity to thank Dan Gregoria, National Weather Service meteorologist, for being a true friend and a great roommate, and updating me with severe weather conditions in Miami during the hurricane season.

I couldn't be here without love and support given by my parents (Ergun Sapmaz and Melehat Sapmaz), sister (Sinem Sapmaz), and brother (Serkan Sapmaz) who are all residing in Ankara, Turkey.

ABSTRACT OF THE DISSERTATION

SOOT MEASUREMENTS

IN STEADY AND PULSED ETHYLENE/AIR DIFFUSION FLAMES

USING LASER-INDUCED INCANDESCENCE

by

Hayri Serhat Sapmaz

Florida International University, 2006

Miami, Florida

Professor Norman D. H. Munroe, Major Professor

Combustion-generated carbon black nano particles, or soot, have both positive and negative effects depending on the application. From a positive point of view, it is used as a reinforcing agent in tires, black pigment in inks, and surface coatings. From a negative point of view, it affects performance and durability of many combustion systems, it is a major contributor of global warming, and it is linked to respiratory illness and cancer.

Laser-Induced Incandescence (LII) was used in this study to measure soot volume fractions in four steady and twenty-eight pulsed ethylene diffusion flames burning at atmospheric pressure. A laminar coflow diffusion burner combined with a very-high-speed solenoid valve and control circuit provided unsteady flows by forcing the fuel flow with frequencies between 10 Hz and 200 Hz. Periodic flame oscillations were captured by two-dimensional phase-locked LII images and broadband luminosity images for eight phases (0° – 360°) covering each period. A comparison between the steady and pulsed flames and the effect of the pulsation frequency on soot volume fraction in the flame

region and the post flame region are presented. The most significant effect of pulsing frequency was observed at 10 Hz. At this frequency, the flame with the lowest mean flow rate had 1.77 times enhancement in peak soot volume fraction and 1.2 times enhancement in total soot volume fraction; whereas the flame with the highest mean flow rate had no significant change in the peak soot volume fraction and 1.4 times reduction in the total soot volume fraction. A correlation ($f_v \mathrm{Re}^{-1} = a + b \cdot Str$) for the total soot volume fraction in the flame region for the unsteady laminar ethylene flames was obtained for the pulsation frequency between 10 Hz and 200 Hz, and the Reynolds number between 37 and 55. The soot primary particle size in steady and unsteady flames was measured using the Time-Resolved Laser-Induced Incandescence (TIRE-LII) and the double-exponential fit method. At maximum frequency (200 Hz), the soot particles were smaller in size by 15% compared to the steady case in the flame with the highest mean flow rate.

TABLE OF CONTENTS

LIST OF TABLES

LIST OF FIGURES

FIGURE PAGE

LIST OF SYMBOLS

Symbol	Description	Value	SI Unit
B	Boltzmann constant	1.38065×10^{-23}	J/K
c	Speed of light	3×10^{8}	m/s
c_s	Specific heat of soot	0.0021	J/kg/K
C	Calibration factor	4.94185×10^{-4}	ppm/a.u.
D	Optical density of filters	Variable	-
D_{1/e^2}	Gaussian diameter of laser beam		m
d_p	Primary particle diameter	Variable	m
e_b	Blackbody spectral exitance	Variable	$W/m^2/nm$
E(m)	Refractive index function	$Im((m^2-1)/(m^2+2))$	-
f	Focal length of lens	Variable	m
f_v	Soot volume fraction	Variable	ppm
G	Geometry-dependent heat transfer function	22.064	-
h	Planck's constant	6.626×10^{-34}	J.s
i		$\sqrt{-1}$	-
I_0	Incident laser beam	Variable	
I_T	Transmitted laser beam	Variable	
k	Wave number	$2\pi/\lambda$	m^{-1}
k_a	Heat conduction coefficient for air	0.12	W/m/K
K	Optical coefficient	Variable	m^{-1}
m	refractive index of soot, $n + i\kappa$		-

n	Real part of the refractive index of soot		-
q(t)	Laser intensity	Variable	W/m^2
P	Pulse parameter	Variable	-
P_v	Vapor pressure of soot	Variable	Pa
R	Universal gas constant	8.314	J/kg/K
$R(\lambda)$	Spectral response function	Variable	-
Re	Reynolds number	Variable	-
Str	Strouhal Number	Variable	-
T	Temperature	Variable	K
T_0	Temperature of surrounding gas	1800	K
w	Laser sheet half width	0.3×10^{-3}	m
x_p	Primary particle size parameter	$\pi d_p/\lambda$	-
σ	Stefan's constant	5.67×10^{-8}	$W/m^2/K^4$
ε	Soot particle emissitivity		-
β	Evaporation coefficient	0.8	-
ρ_s	Density of soot	2200	kg/m^3
λ	Laser wavelength	532×10^{-9}	m
η	Nondimensional axial coordinate	Variable	-
λ_{MFP}	Mean free path of the medium	0.5665×10^{-6}	m
ϕ	Phase of phase-locked images	Variable	degrees
κ	Imaginary part of the refractive index of soot		-
ΔH_v	Heat of vaporization of graphite	Variable	J/mole

CHAPTER I

INTRODUCTION

1.1 Motivation

Combustion is the oldest technology of mankind, having been used for more than one million years. Combustion provided about 90% of the worldwide energy support in 2000 (Warnatz et al. 2001). In the United States, combustion provided 85% of the energy (Urban 2005). Although combustion has a long history, its scientific investigation was not until the beginning of the twentieth century. Combustion is a complex process since it involves thermodynamics, fluid mechanics, chemical kinetics, and transport processes. In recent years, great improvements in understanding this complex process has been achieved as a result of advances in computer capabilities and experimental techniques, such as optical diagnostics. However, detailed investigation of combustion processes, such as, soot formation in combustion devices, is either practically impossible or very complicated (Wagner 1981). Some of the areas of application of combustion science are furnaces and boilers, piston engines, gas turbines, jet engines, rocket engines, guns and explosives, forming of materials, chemical processing, fire hazards and safety, and chemical lasers (Linan and Williams 1993).

Most of the particulate matter from practical combustion systems is solid carbon matter formed during the process of combustion. These solid carbon particles are known as *soot*. The formation of soot accompanies many practical combustion processes, often with undesirable consequences. The most familiar are the visible soot emissions from diesel engines and industrial smokestacks. Less obvious are the adverse health effects

associated with soot. Specifically, soot emitted from automobile engines, power plants, and other sources are blamed for increasing the risk of death by as much as 15% in cities with heavy air pollution product. Soot formation limits the operation of most practical combustion systems. For example, excessive quantities of soot in gas turbines can cause erosion of the turbine blades. In addition, the emission of soot usually represents some loss of efficiency in the operation of a combustion device since some of the fuel escapes in non-oxidized form. On the positive side, soot is responsible for the yellow luminosity from flames due to its black body emission. The enhanced radiation heat transfer makes soot a useful product in industrial furnaces, provided that, of course, burnout of the soot is done in a region where sufficient oxygen is supplied before it exits the stack.

1.2 Definition of soot

Soot is a carbonaceous solid material formed in flames due to incomplete combustion. Soot produced under widely different combustion conditions shows great chemical and structural similarity, indicating a strong likelihood that similar mechanisms are operative. It normally looks like luster-less black and is different from graphite. The main constituents are carbon atoms (Wagner 1981). Soot usually forms at temperatures from 1000 °C to 2500 °C. Solid phase of soot particles is formed from fuel molecules in the order of milliseconds. Soot contains up to 10 mole percent hydrogen. The hydrogen-carbon ratio of soot decreases as the soot ages in the flame. Physically, soot appears as grape-like clusters of small spheres (primary particles or spherules). The spherules typically reach to mean diameters around 20 to 30 nm in diameter, but the clusters can grow to macroscopic sizes, depending on the combustion conditions. The density of these

particles seems to be less than 2 g/cm^3 due to large interplanar spacing. Polycyclic aromatic hydrocarbons (PAH) are produced with the soot produced. PAHs are often identified as important intermediates to soot formation.

1.3 Environmental and Health Aspects of Soot

Since man discovered the use of fire for heating, cooking, and industrial use, pollution has been associated with burning (combustion), which is now found in almost all aspects of society, both industrial and domestic. Aerosols, whose large positive component of the radiative forcing due to black carbon soot released from the burning of fossil fuel and biomass, and to a lesser extent, natural fires, affect the Earth's temperature and climate by altering the radiative properties of the atmosphere (Chigier 1975; Wilson and Spengler 1996). From studies of aerosol radiative forcing, it is known that black carbon can exist in one of several possible mixing states; distinct from other aerosol particles (externally mixed) or incorporated within them (internally mixed), or a black-carbon core surrounded by a well mixed shell (Jacobson 2001). He also suggested that black carbon might be the second most important component of global warming after CO_2. New research from NASA scientists in 2003 also suggested that emissions of black soot alter the way sunlight reflects off snow, and according to a computer simulation, black soot may be responsible for 25 percent of observed global warming over the past century. The loss of ozone on carbon soot aerosol has also been investigated since annually about 13 Tg (a teragram, Tg is 10^{12} g) of black carbon are emitted into the atmosphere. Ozone is decomposed on carbon aerosol in a fast surface reaction, which results in the loss of one monolayer equivalent of ozone. Due to its irregular agglomerate

structure soot aerosol offers a large specific surface area for interactions with reactive trace gases like ozone (Kamm et al. 1999). Soot, as an airborne particle, has been a part of model studies (Kleeman and Cass 1998) to incorporate all of the major processes relevant to regional air pollution studies, including emissions, transport, deposition, gas-to-particle conversion and fog chemistry. Soot aerosol contribution in the atmosphere by aircraft was also studied considering that the soot emission index (EI) of a Concorde supersonic jet aircraft has EI as 5E-5 (0.05 grams per kg fuel burnt). Black carbon aerosol (BCA) has the highest absorption cross section of any compound known. Thus, it can absorb solar radiation to cause atmospheric warming (Pueschel et al. 1995). A new NASA climate study has found that large amounts of black carbon (soot) particles and other pollutants are causing changes in precipitation and temperatures over China and may be at least partially responsible for the tendency toward increased floods and droughts in those regions over the last several decades (Menon et al. 2002). Soot is the aerosol most responsible for reducing atmospheric transparency and visibility, by so much in India and China that agricultural productivity is reduced an estimated 10-20% with additional loss from soot deposited on plant leaves (Hansen and Nazarenko 2003).

Size of the particles is the key factor for evaluating the impact of soot particles on human health because the particles with a diameter of 1 μm or less are deposited in the human respiratory system. Soot particles suspended in large quantities in the air that we live in are of respiratory size, that is they are deposited in the human respiratory tract where they may cause life-threatening diseases. It is estimated that 460,000 people die worldwide every year from respiratory particles produced by automotive traffic. Considering that cigarette smoking is estimated to kill more than 3 million people every

year, one can say that smoke from traffic approaches the danger of cigarettes. The danger from inhaling combustion aerosols was expressed in units of standard cigarettes. For example, the amount of exposure for a person living in San Francisco, and traveling by car on 280 to work at Stanford University was expressed as DACEE (the Daily Cigarette Exposure Equivalent) being equal to 3.6 while DACEE being 1.0 represents a standard cigarette smoker (Siegmann and Siegmann 1997). In October 1995, International Agency for Research on Cancer assessed the results on a scientific basis with regard to a possible carcinogenic effect using carbon black (Brockmann et al. 1998).

1.4 Soot in Industry

Soot produced with special properties is an important chemical known as carbon black. In 1904, S. C. Mote discovered that carbon black has a reinforcing effect on rubber. In 1912, B. F. Goodrich first started using large quantities of carbon black to increase the durability of automobile tire rubber. Now, automobile tires contain near 4 kg of carbon black, or about 35% of their weight. Ninety-five percent of the carbon black produced goes into rubber products and most of this into tires. The remaining fraction is used in inks, conductive plastics, copy machine toners and many other applications. In 1988, production of carbon black in the United States was 1.3 billion kg, making it the thirty-eighth largest chemical commodity. The industry experienced immediate and constant growth from the approximate 11 million kg manufactured from 1912 to 1998 when about 90% of the 1.6 billion kg production was shipped to the rubber industry in the United States (Melsom 1998). During this same time, approximately 6 billion kg was produced worldwide.

Carbon black is extremely useful in the production of a broad range of products, mainly in rubber (reinforcing filler in tires and technical rubber products), printing inks (pigmentation and rheology), lacquers (pigmentation, tinting), plastics (pigmentation, tinting, smoothing of conductors), fibers (pigmentation), paper (black and gray coloring, backing papers), building sector (coloring of cement), electrical industry (electrodes, batteries) (Brockman et al. 1998). Carbon black is used in automobile tires for its strength and resistance to abrasion. Other properties make carbon black a valuable ingredient in a host of non-rubber products. These characteristics include the intensity of its pigmentation, its ability to absorb ultraviolet light, and its lack of electrical conductivity. Different grades are used in printing inks, coatings, electrical cables, plastic films, pipes, and sealants. As little as two percent of carbon black in plastic products greatly minimizes the amount of sunlight degradation. Due to its lack of conductivity, it is also added to tires on large vehicles to prevent the buildup of electrostatic charge. In industry, the main methods of manufacturing carbon black are namely, lamp black, channel black, furnace black, thermal black and acetylene black. Lamp black is the oldest form since it is easily made by burning petroleum residues or tar oils in open pans and ducting off the smoke, allowing it to settle under gravity (Gaydon and Wolfhard 1979).

1.5 Soot Formation Process

The process of soot formation may be separated into six sequential steps.

- Gas phase molecular weight growth
- Nucleation or particle inception
- Surface growth

- Coagulation
- Agglomeration
- Oxidation

Molecular weight growth is the process under which the fuel molecules undergo homogeneous free radical chemical polymerization reactions. When the molecules grow larger than approximately 2000 amu, they are considered to be soot nuclei and reactions are considered heterogeneous. The somewhat arbitrary designation of the nucleation point at 2000 amu is due to the visibility limit of soot particles using a transmission electron microscope (TEM). Surface growth is a continuation of molecular weight growth and is believed to occur through a free radical mechanism. Concurrently with surface growth, the particles collide and coagulate to form new and roughly spherical particles. As residence time in flame increases, surface growth virtually ceases, possibly due to the soot becoming less reactive, the depletion of gas phase reactants, or both. The physical collision process changes as well; the particles continue to collide and stick together, but they retain their original shape. That is, clusters or chains of particles form rather than larger spheres. The individual members of the chains are called spherules. If sufficient oxidant is present, the particles will then be destroyed in the burnout process before being emitted.

Many different combustion configurations are used in practical systems. We may classify them by the fluid mechanics and by the fuel/oxidant geometry. The fluid mechanics may be either laminar or turbulent and the geometry may be premixed or diffusive. In premixed combustion, the fuel and oxidant are well mixed before entering the combustion zone. In diffusion (nonpremixed) flames, the mixing occurs

simultaneously with the reactions. Most practical combustion systems, such as gas turbines or diesel engines, are turbulent diffusion flames. They are the most complex to study because of their temporal and spatial inhomogeneities.

In order to modify and control the formation of soot, we need to understand its dynamics. Two approaches are possible here. The first is to work with real, complex combustion systems (e.g. a diesel engine on a test stand). This approach may be valuable in finding solutions to some specific operational problems. However, the results are not easy to find and are not generally applicable. In contrast, the other approach is to examine a simpler system, i.e., a laminar diffusion flame in our case. This combustion system is neither extremely simple nor very complex. It is not that simple because soot properties are changing radially and axially in the flame. Also, it is not too complex in that it is not turbulent. We cannot take any result directly from this flame and apply it to a practical combustor. Instead we can derive fundamental kinetic information from the data. This kinetic knowledge is then widely applicable to more complex combustion systems using advanced computational models.

Although many studies have been published on soot, we still do not have a clear picture of the chemical and physical processes involved. One problem is the tremendous number of experimental systems which researchers use for soot studies. Data are published on premixed and diffusion flames, laminar and turbulent flows, with the degrees of freedom in buoyancy, pressure, temperature, diluent content, and additives. Hundreds of different fuels are examined from methane to heavy aromatic hydrocarbons. Papers are also published correlating soot production to operating parameters of practical systems such as diesels. Over the years, the theories and the models on combustion and

soot formation have become more sophisticated mainly because of advances in technology. Two major advances are as follows. First, lasers have become the most common source of light in the laboratory since they become more and more compact in size with better shot to shot repeatability with better spatial profile and higher temporal resolution. Second, there are now large kinetic models that be integrated numerically in short periods of time with the advance in computers.

CHAPTER II

LITERATURE REVIEW

2.1 Introduction

This chapter contains a review of the published literature in the area of soot formation, soot structure, soot optical properties, laser diagnostics for soot, and mainly Laser Induced Incandescence (LII). Soot has generated a great deal of interest in the literature. There has been a steady and rapid increase in the number of papers from the early sixties until now. Over the years, there have been many new theories and models of combustion as a sign of advances in technology.

2.2 Previous Research

Past studies of soot processes in flames have been reviewed by Glassman (1977) and Wagner (1981). The difficulty of measuring soot properties in turbulent flames due to their fluctuating flow fields have motivated studies of laminar flames, which are experimentally and computationally more tractable. Since 1983, there have been papers published on two popular configurations for experimental studies of soot properties, which are the coflow and counterflow laminar flames (Kent et al. 1981; Santoro et al. 1983; Santoro et al. 1987; Glassman 1989; Dobbins et al. 1990, 1998; Sunderland and Faeth 1996; Kennedy et al. 1996; Kang et al. 1997; Zhang and Megaridis 1998; Mohammed et al. 1998; Hepp and Siegmann 1998; Smooke et al. 1999; Xu and Faeth 2002; El-Leathy et al. 2003; D'Anna et al. 2005; McCrain and Roberts 2005). The center of attention in most of these studies has been the measurement of the soot volume

fraction, which is needed for estimating particle formation/growth rates. These results suggested that the primary soot particles in the initial formation regions of flames are small and unaggregated. With the surface growth mechanism, primary particles increase in size, reaching typical diameters of 25-50 nm. The higher values are associated with heavily sooting fuels. In the meantime, these spherical particles form aggregates that also increase in size with residence time due to the Brownian (random) motion of particles. Aggregate sizes vary considerably at a particulate flame location in contrast to the primary particles, which have nearly uniform diameters. If the residence time is long enough, soot can survive through the oxidation zone before being emitted from the flame. On the other hand, at shorter residence times (laminar smoke point), primary soot particles become smaller while aggregates break up due to the oxidation process. Koylu (1997) used a technique that can separately determine volume fractions of translucent and mature soot particles. This experimental method, referred as the Thermophoretic Sampling Particle Diagnostic (TSPD), makes it possible to use the TS/TEM experiments to obtain not only particle/aggregate size but also the local soot volume fraction without the prior knowledge of particle characteristics, such as, refractive index. For a comprehensive treatment of soot-containing flames, the proper analysis of in situ optical experiments has been established by various investigators, as mentioned early in this chapter based on the Rayleigh-Debye-Gans scattering theory. This analysis method can yield all the soot parameters of interest. However, this elaborate inverse technique is generally applicable when multi-angle scattering data are available, e.g., at every 10° between 20° and 160°. Such experiments are both time-consuming and complicated. Moreover, they may not be feasible in some combustion environments, such as turbulent

flames. This fact revealed the method of two-angle light scattering to investigate the soot distribution and the soot parameters in an ethylene diffusion flame in conjunction with the extinction measurements (Sapmaz 2000). Qi (2000) studied the same flame with TSPD technique and made the comparisons with two-angle light scattering/extinction technique. Even though his primary particle diameter results were comparable with the previous technique, he overly underestimated the soot volume fraction values in the entire flame. TSPD lacks in that it is an intrusive technique and the probe sampling time affects the results. It is time consuming, and has many other factors that might change the final results. Scattering/Extinction techniques needs pointwise measurements, are best utilized in laminar conditions, and are very difficult to use in turbulent flames where you need high temporal resolution. Extinction measurements will have uncertainties in tomographic inversion, more towards in the centerline of the flame. Reflections from burner tips and optics might be a possible problem when looking at forward scattered light due to the change in scattering volume by $1/\sin(\theta)$, θ being the scattering angle. Considering the drawbacks of the other methods, Laser-Induced Incandescence (LII) is a powerful tool for measuring soot particles. It has emerged as a non-intrusive diagnostic technique used to determine two dimensional soot concentration or soot volume fraction that is defined as ratio of the soot volume and the total volume. The first attempt to optimize this technique for the measurements of soot concentration was made by Melton (1984). Analyses by Melton showed that the thermal radiation is nearly proportional to the soot volume fraction. Long wavelengths should be preferred to minimize the size effect. Simultaneously, Dasch (1984) investigated the particle vaporization induced by high laser energy pulses experimentally and numerically. His study suggested that when

vaporization is present, it occurs at the surface and causes particle shrinkage. Cignoli et al. (1994) used LII for qualitative images of soot concentration in a diffusion flame. Quantitative measurements of soot concentration in steady laminar nonpremixed ethylene flames were performed in 1994-95 (Quay et al. 1994; Ni et al. 1995). They reached the soot concentrations from LII signal using the measurements from laser extinction in coflow jet diffusion flames (Santoro et al. 1983). These and earlier studies also established this particular diffusion flame as a standard ground for other researchers as well as this study (Koylu 1997; Sapmaz 2000; Qi 2000; Sapmaz et al. 2003). For the particle size measurements, Santoro observed different temporal decay rates for the LII signal, suggesting this was due to the variations in soot particle size in late 1995 (Ni et al. 1995). At the same time, Will et al. studied the sizing of soot particles by variations with LII decay rates. Following that, Mewes and Seitzman (1997) proposed alternative means of particle sizing based on different sized particles. Performance characteristics of TIRE-LII were given by Will et al. (1998). In the following year, Vander Wal et al. (1999) investigated TIRE-LII signals with TEM images of soot particles before and after laser pulses, and questioned the particle shrinkage mechanism during vaporization. Recently, several groups have been doing LII studies on verifying and modeling the particle size effects on particle size measurements, and the effects of high laser fluence on the structure and other properties (Jenkins et al. 2002; Allouis et al. 2003, Lehre et al. 2003; Snelling et al. 2004). Most of our current understanding of laminar diffusion flame behavior is based on experimental characterization of steady flames. Detailed characterization of flickering flames is considerably more limited. Vortex interactions with flames play a crucial role in many practical combustion applications. Such

interactions form the basis of understanding in naturally flickering buoyancy–induced flow instabilities. These instabilities lead to the formation of vortical motion that interacts with the flame front. A better understanding of flickering flame behavior will also improve the current understanding of turbulent combustion systems. Understanding of the interaction of diffusion flames with unsteady flow field has gained prominence in the investigation of unsteady turbulent combustion process (Yu et al. 1983; Poinsot et al. 1987). In the flamelet concept, the local structure of the turbulent reaction zone is described as an ensemble of strained laminar flame elements. These flamelets are stretched and convected by the turbulent flow field. The effect of time-varying flow field on the flame fronts are of considerable importance (Peters 1984). Little is known about the effect of periodic oscillations and the accompanying vortex structures on the chemical and thermal fields within the flame or emissions from the flame. Park and Shin (1997) presented experimental results on the development of transient jet diffusion flames using high-speed Schlieren visualization. They focused their study on the influence of the flow field on the diffusion flame. Papadopolous et al. (2002) used the PIV technique for phase resolved measurements of the velocity field in acoustically forced flickering laminar co-flowing methane/air diffusion flame. Phase locked measurements of the instantaneous two-dimensional velocity field at ten phases within a full excitation cycle were made using the PIV technique. Smyth et al. (1993) used elastic light scattering with OH laser induced fluorescence in methane/air diffusion flames to reveal that the soot scattering signal increased dramatically when flickered by using acoustic excitation of the fuel flow velocity compared with steady-state laminar conditions. Shaddix and Smyth (1994, 1996) used LII to measure the soot concentrations of methane, propane and ethylene flames in

steady and time varying flow fields. They used acoustic forcing of the fuel flow rate to phase lock the periodic flame flicker close to the natural flame flicker frequency caused by buoyancy induced instabilities. A loudspeaker attached to the plenum below the fuel tube was used for acoustical excitation of the flame. They focused their study on developing LII for quantitative applications, proper calibration measurements, signal detection which minimizes interferences from C_2 swan-band emission and broadband molecular fluorescence, correction for the laser beam focus/spatial averaging effect in the image measurements and correction for LII signal extinction within the flame. Pinder and Atreya (2003) utilized a speaker mounted underneath the mixing chamber for flow fluctuations experiments in nonpremixed ethylene jet flames. They observed frequency dependant changes in the flame structure, flame height, temperature and radiation in that flame height and temperature tended to decrease with Reynolds number and the frequency of oscillation.

Qian and Law (1997) theoretically analyzed the unsteady spreading motion of a diffusion flame from a cylindrical burner. They found that flame movement is mainly controlled by the ambient oxidizer concentration relative to the fuel concentration and transport diffusivity. McManus et al. (1997) applied a combination of laser-induced incandescence (LII) and line-of-sight laser extinction to detect and quantify soot particles in and above ethylene-air flames produced by a laboratory flat-flame burner. They also examined the onset of vaporization of the soot particles by the pulsed laser beam, and determined particle temperatures and cooling rates from spectral analysis of the incandescence as a function of time after the laser pulse. Zhang and Megaridis (1996) were successful at suppressing the soot by seeding fuel flow with ferrocene vapor in

ethylene/air nonpremixed flames by accelerating the particulate inception mechanisms and enhancing soot oxidation rates. Measurements of the morphology and optical properties of soot produced by the combustion, in the laboratory, of petrol, diesel, fuel oil, paraffin, butane and wood in still air were carried out by Colbeck et al. (1997). The results indicated that the soot particles, except that from wood, were fractal-like. Filippov et al. (1997, 1999) used LII on graphite particles in argon from the spark generator with known size and distribution with low laser energy fluences as well as high energy fluences, heating the particles from some hundred degrees above room temperature up to over 3000 K. They concluded that weakly bound primary particle clusters can be destructed by laser heat-up and the LII technique can be applied for structural analysis of highly aggregated aerosols. Fletcher et al. (1997) reviewed experiments that examine the formation, agglomeration and properties of coal derived soot, which has primary soot particle diameters in size range of 25-60 nm. Menguc and Mcdonough (1996) suggested using the tools of the "chaos" theory to reveal the true time-dependent nature of sooting turbulent flames. The hypothesis of using different chaotic maps to explain the complex systems, such as, turbulent flames might be very helpful if supported by experimental work. Vander Wal (1997) used LII-LIF (Laser-Induced Fluorescence) techniques in a turbulent, ethylene gas-jet diffusion flame. He stated that a LII-LIF image is obtained with a single laser shot, and this technique can be widely applied to transient asymmetric combustion processes.

Schraml et al. (2000) suggested Time-Resolved Laser Induced Incandescence (TIRE-LII) as a two-dimensionally resolved measurement of soot primary particle sizes in a combustion process from the ratio of emission signals obtained at two delay times

after a laser pulse since the cooling behavior is characteristic of particle size. Manta et al. (2000) used the two-color emission technique for the 2-D visualization of soot load and temperature. The theoretical approach of the technique and the experimental procedure of validation were described. Snelling et al. (1997, 2000) reviewed the state-of-the-art in LII methodology with details on the effects of laser fluence spatial profile and the effects of the temporal laser fluence distribution, demonstrating the significance of the spatial profile on the excitation curve, and the temporal distribution on the particle temperature and size.

Siegmann (2000) proposed a soot formation mechanism in diffusion flames. Vander Wal (1996, 1997, 2000) provided an extensive study of LII and issues related with it, such as, excitation wavelength, excitation laser fluence, calibration, detection wavelength, detection time, primary particle size effects. Vander Wal and Choi (1999) used high-resolution transmission electron microscopy to examine the laser-heated soot to resolve detailed morphological changes induced in the soot by pulsed high intensity laser light. They found partial graphitization, formation of hollow particles and the average number of graphitic planes formed within soot primary particles upon high intensity pulsed laser heating. However, they stated that this wouldn't cause any significant carbon mass loss. Yang et al. (2000) introduced the Particle Vaporization Velocimetry (PVV) technique, which is a form of flow tagging based on laser vaporization of soot particles at defined locations in the flow. This technique is actually very similar to LII in that particles are heated above their vaporization temperature for proper flow tagging. Choi and Jensen (1998) found a new calibration method for LII studies by using one single line-of-sight extinction measurement instead of calibration

using independent soot volume fraction measurements. Laser-induced incandescence signals are acquired in diffusion flames, a simulated exhaust flow, and a diesel engine exhaust and compared with measurements performed using a scanning mobility particle sizer (Wainner and Seitzman 1999; Green and Witze 2000). The use of LII for time-resolved measurements of soot volume fraction during engine transients was demonstrated at the exhaust-port exit of a production, four-valve, PFI spark-ignition engine (Witze 2001). Saito et al. (1998) showed that soot suppression in an acetylene diffusion flame by means of acoustic oscillation exceeded 90%. They related the enhanced mixing of fuel gas and surrounding gas due to acoustic oscillation to high flame temperature, which caused re-oxidation of soot particles.

Axelsson et al. (2001) applied the LII technique to a well-characterized premixed flat flame, for concentration and particle size measurements. The gate ratio method was used by taking the ratio of the LII signals from a prompt gate (0 ns) and a delayed gate (300 ns) for measurements of the primary particle size with a minimum detectable particle size of 10nm utilizing the conversion from experimental data to particle size which was relying on a model of the particle cooling. A similar study in a laminar methane/oxygen/nitrogen diffusion flame stabilized on a Wolfhard-Parker burner was performed by Moreau et al. (2003). Hult et al. (2002) used LII in laminar and turbulent ethylene diffusion flames by applying 2-D imaging techniques to obtain 3-D information by rapidly recording eight closely spaced planar images with eight CCD's in series by sweeping the laser beam through the measurement volume using a rapidly rotating mirror in less than 87 μs. This work showed the versatility of LII in that it could be applied in most of the flames of interest. Starke et al. (2003) showed that LII can be used not only in

reactive stationary flows but also in shock-induced reactive flows which was demonstrated in three examples: soot particle formation during high temperature pyrolysis of benzene, iron particle formation from iron pentacarbonyl, and formation of carbon-coated iron particles. Michelsen (2003) carried out an extensive study by developing a model for analyzing and predicting the temporal behavior of LII from soot, carbon black, and other carbonaceous, accounting for particle heating by absorption of light from a pulsed laser and cooling by sublimation, conduction, and radiation. The model also included mechanisms for oxidation, melting, and annealing of the particles. According to the model, at fluences above 0.1 J/cm^2, particle temperatures during the laser pulse were determined by absorption and sublimation, whereas at lower fluences particle temperatures did not reach the sublimation temperature, and temperatures were predominantly controlled by absorption and conduction. At fluences between 0.15 and 0.3 J/cm^2, the model overpredicted the initial decay rate during and immediately following the laser pulse. Whereas, at fluences between 0.3 and 0.7 J/cm^2, the model underpredicted the initial decay rate. Yang and Seitzmann (2003) used the previously mentioned PVV technique along with the LII technique to study soot formation and velocity in an acoustic burner with two acetylene nonpremixed flames. They found that the overall soot production was suppressed when acoustic forcing was present while soot temperature increased meaning more radiation from the flame to the surroundings.

Experiments in space have a new laboratory called U.S. Destiny Laboratory in International Space Station (ISS) with five racks to house various experiments in microgravity conditions. The combustion-integrated rack (CIR) will be hosting various combustion experiments under microgravity conditions (Jordan and Zell 2001).

Considering the fact that development of dedicated experiment equipment from a safety, reliability, and an automation point of view takes a considerable amount of time and will remain in orbit for several years, LII has a great shot to be used as an optical technique for nanoparticle concentration and sizing due to its versatility, high spatial and temporal resolution, and compactness.

2.3 Concurrent Research

Lifted nonpremixed jet flames were controlled by acoustic forcing at high amplitudes and middle frequencies (around 200 Hz), which changed the combustion regime and prevented reattachement. This was explained using the results obtained by analyzing the flow dynamics with high speed laser tomography, laser Doppler anemometry, particle image velocimetry, and Mie scattering techniques (Demare and Baillot 2004). Measurements showed that the excitation periodically generated axial velocities higher than the maximum velocity, leading to flame liftoff, then leading to quasi-homogeneous turbulence. This provided efficient mixing and improved the combustion regime. Stipe et al. (2004) suggested that UV photo fragmentation can be effective in controlling particle size and morphology, and can be a useful diagnostic for studying elements of the laser ablation process. They irradiated soot with 193 nm light from an ArF excimer laser at fluences ranging from 0.07 to 0.26 J/cm^2 with repetition rates of 20 and 100 Hz to produce a large number of small, unagglomerated particles, and a smaller number of spherical agglomerated particles with mean particle diameters from 20 nm to 50 nm. Walker et al. (2004) investigated strategies currently available to control the particulate matter (PM) emissions from Diesel engines by means of diesel particulate

filter and diesel oxidation catalyst. Tian et al. (2004) studied an atmospheric pressure, axisymmetric, coflow laminar ethylene/air diffusion flame for primary particle diameter size with sampling location 42 mm over the exit of the fuel tube and at the centerline of the flame. Primary particle diameters were measured manually with high-magnification TEM images by detecting the apparent circular outlines of the particles near the edges of the aggregates. After measuring 385 primary particles, he found that the diameters of the particles cover a range of 13–50 nm, with an arithmetic mean diameter 29.2 nm and a standard deviation of 7.1 nm with a normal distribution trend. Kim et al. (2004) studied soot surface growth and oxidation properties of round laminar jet diffusion flames at pressures of 0.1–1.0 atm for a variety of fuels (methane, acetylene, ethylene, propylene, propane, and benzene). These measurements yielded local soot surface growth and oxidation rates, as well as local flame properties that are thought to affect these rates. They concluded that soot surface oxidation rates in laminar diffusion flames for various hydrocarbon fuels could be correlated by assuming constant collision efficiency for OH.

A three-color emission method for the simultaneous estimation of temperature and soot volume fraction distributions in axisymmetric sooting flames was studied by Ai and Zhou (2005). The spectral radiation intensities at wavelengths of red, green, and blue were simulated for the inverse analysis followed by the simultaneous estimation by using a Newton-type iteration algorithm and the least-squares method. Unfortunately, the three-color method was found to be suitable for the reconstruction of flame structures with a single peak. Stipe et al. (2005) used an inverted, co-flow, methane/air/nitrogen burner to generate a wide range of soot particle sizes and concentrations. By adjusting the flow rates of air, methane, and nitrogen in the fuel, the mean electric mobility diameter and

number concentration were varied. They were able to achieve the concentrations spanning those produced by spark-ignited and diesel engines with mean particle diameters between 50 and 250 nm and number concentrations from $4.7 \cdot 10^4$ to 10^7 cm^{-3}. Liu et al. (2005) presented a numerical study on temperature histories of nanosecond-pulsed laser-heated soot particles of different primary particle diameters and different aggregate sizes using an aggregate-based heat transfer model. Results stated that after the laser pulse, the temperature of soot particles in larger aggregates decreases more slowly than that of particles in smaller aggregate. It was found that for a given aggregate size, the temperature of particles of smaller diameter decays faster as a result of a larger surface area-to-volume ratio. Results also indicated that when the gas temperature is low (such as room temperature, 300 K), the experimental effective particle temperature decay curve alone cannot differentiate non-aggregated large particles from large aggregates formed by small primary particles.

Shaddix et al. (2005) studied steady and pulsed, normal and inverse jet diffusion flames of methane/air and ethylene/air on a slot burner. OH and PAH laser-induced fluorescence (LIF), soot laser-induced incandescence (LII), and soot thermal emission have been measured in the lower flame region of steady and pulsed flames. They found enhancements in peak signals from soot are apparent in pulsed inverse diffusion flames. Murr et al. (2005) had TEM examination of representative nano particulate matter from the exhaust streams of numerous and common fuel-gas–air combustion sources including natural gas–air and propane–air kitchen stove top burners, roof-exhausting natural gas–air water heaters as well as laboratory methane–air flame exhausts. They stated that all of the combustion-generated particulates in the exhaust streams were observed to be aggregates,

ranging from carbon spherule aggregates to aggregates composed of mixtures of multi-wall carbon nanotubes (MWCNTs) and other fullerene nanoforms. This study is important in that it illustrated the occurrence of MWCNTs and other fullerenes in the exhaust streams of combustion sources. Ezekoye et al. (2005) investigated the effect of acoustic excitation in an axisymmetric, co-flow, acetylene–air diffusion flame at frequencies ranging from 230 to 1000 Hz. He reached the conclusion that at sufficiently high levels of the acoustic velocity at the fuel exit plane, the soot production of a normally heavily sooting flame can be almost completely suppressed. One other important key finding from this paper is that their comparisons of the acoustically forced flames to partially premixed flames supported the hypothesis that the acoustic field aids in partially premixing the flame. Kim et al. (2005) showed that soot formed in laminar diffusion flames of heavily sooting fuels (naphthalene, acetylene, toluene) evolves through four distinct growth stages which give rise to four distinct aggregate fractal morphologies. Each successive stage grows upon the previous stage; hence aggregates of one morphology, parameterized by a fractal dimension, form larger superaggregates of a different morphology with a different fractal dimension. For ethylene and methane flames, they found that fractal dimension is 1.8 and stages 2, 3, and 4 do not exist. Qamar et al. (2005) did measurements of soot volume fraction in three different turbulent diffusion flames using laser-induced incandescence (LII) to provide insight into the effect of global mixing rate on the instantaneous local and the average soot volume fraction. The three flames, produced by simple jet, precessing jet, and bluff-body jet burners with the same fuel, nozzle diameter, and flow rate were investigated to reveal an inverse relationship between global mixing rate and both the total amount of soot in the flame

and local instantaneous soot volume fractions, broadly consistent with trends in laminar flames.

A two-color LII technique for in situ measurements of particle size distributions was used by Lehre et al. (2005) based on the simultaneous detection of time-resolved LII signals at two different. The ratio of both LII signals yielded particle temperatures as a function of time and location along with numerical simulation based on a detailed cooling model for particle ensembles followed by multi-dimensional non-linear regression fit to obtain particle size distributions without requiring information on optical particle properties. Kruger et al. (2005) compared particle size measurements obtained with laser-induced incandescence (LII) and a scanning mobility particle sizer (SMPS) in a premixed laminar sooting flame. They observed that the LII and SMPS measurements gave similar results in terms of mean particle size but there was a discrepancy of a factor of two in the particle size distribution width. Delhay et al. (2005) showed that the effective probe volume, in which the LII signal is observed, is highly dependent on the laser irradiance profile by capturing LII images using two directions of observation: one counter to the propagation direction of the incident laser (backward LII) and one at right angles.

Burtscher et al. (2005) reviewed optical techniques used in industry for sampling and measuring the particles emitted from diesel engines based on light absorption. Another extensive study on this subject was done by Zhao (1998). Time resolved LII was mentioned with its advantages in that it is a very fast, sensitive, and relatively compact method, having no problems with transient tests and modern low-emission engines. It can be applied in undiluted gas, for example, directly at the end of the exhaust pipe. Xin et al. (2005) used LII technique to reach two dimensional soot distributions in methane and

ethylene buoyant turbulent fires. Following an extensive statistical analysis, he concluded that instantaneous distributions of soot volume fractions exhibit significant differences compared to the ensemble averages, strong fluctuation around the mean, and a relatively homogeneous probability density function.

Despite the effort made in the past, more studies are needed for understanding the effect of the unsteady flow field on diffusion flame and emissions from the flame, such as soot.

2.4 Research Questions and Hypothesis

Our work has been the experimental study on steady and flickering, coflowing, axisymmetric, laminar diffusion flames for the last four years. The main research questions and hypothesis of this study were:

Question#1: How to measure soot concentration in combustion systems in a reliable, cost effective, and time saving manner?

Hypothesis#1: LII is an attractive technique to measure the soot concentration with high temporal and spatial resolution. Therefore, this technique was utilized in this study in four different ethylene diffusion flames with steady and unsteady conditions.

Question#2: Can soot emission be suppressed by pulsing the flame?

Hypothesis#2: We experimentally found the total time-averaged and volume-integrated soot volume fraction values for steady and flickering flames to determine the possibility of suppressing the soot emission in non-premixed ethylene flames for the investigated fuel flow rates.

Question#3: Can soot particle size be determined using laser-induced incandescence technique?

Hypothesis#3: There are different methods recently applied for particle size determination for soot. We observed the applicability of time-resolved laser-induced incandescence (TIRE-LII) for different parts of the flame from a particle diameter determination point of view.

Question#4: What is the role of flow rate in the total soot production tendency of flames in steady and flickering cases?

Hypothesis#4: Four different fuel flow rates were studied with the corresponding visible flame heights of 35, 55, 75, 88 mm for their total and local peak soot volume fraction values with steady and seven pulsation frequencies between 10 Hz and 200 Hz.

Question#5: Can the total soot production in flames be expressed in the form of a correlation for different flow rates?

Hypothesis#5: Volume-integrated time-averaged soot volume fraction values will try to be expressed in the form of a correlation using Strouhal number for different flow rates.

2.5 Research Objectives

The problem to be investigated is soot volume fraction measurements in laminar, steady and flickered diffusion ethylene flames by using Laser Induced Incandescence (LII). The main objective of this study is to investigate the effect of flame pulsing frequency on soot formation in the flame. Phase lock soot images were obtained for flame pulsing frequency between 10 and 200 Hz. The post flame region was also investigated by taking measurements by a soot aerosol monitor for steady and flickering

conditions. The effect of Reynolds number by changing the fuel flow rate for the studied flames is another goal of this research. The final goal of this study is to investigate the possible methods, namely, spectral ratio method, gate ratio method, exponential fit method and double exponential fit method, in determining primary soot particle sizes by using the time history of LII signal. The benefit of this study is to have better understanding of soot formation and therefore, develop effective control strategies in producing changes in the flame structure, flame height, flame temperature and flame radiation by means of introducing frequency dependant changes by oscillating the fuel concentrations while holding same mean fuel flow rate and Reynolds number dependant changes by altering the exit fuel flow rate for limiting the emission of soot.

CHAPTER III

EXPERIMENTAL METHODS

3.1 Introduction

Experimental methods are discussed in this chapter. The combustion apparatus for laminar flames is considered first. Next, optical apparatus, light source, soot aerosol monitoring apparatus, other instruments and data acquisition and post processing softwares will be discussed. However, only the technical description will be given in each section. The details about operating conditions and setup construction will be given in the next chapter.

3.2 Combustion Apparatus

3.2.1 Burner System

The burner system consisted of a coflow burner and X-Y-Z manual positioners. The laminar burner was manufactured to duplicate the one developed by Santoro (1983). He provided us with the detailed drawings of his burner, which has been used by many researchers with slight modifications. The burner was manufactured in Miami by ALM Machine and its cross sectional drawing is given in Fig. 3.1. It consisted of two concentric tubes of 11.1 mm and 101.6 mm I.D., which were 101.6 mm long, with the fuel flowing through central brass tube and with air flowing between the outer and central tube. Air passage utilized a series of screens with a section filled with 3 mm diameter glass beads to provide a uniform air flow, and therefore, a uniform exit flow profile. A ceramic honeycomb section was the final section of the air flow passage. 1.5 mm square

cell size, cylindrical honeycomb, which was 25.4 mm long, was flush with the exit plane of the air tube. The fuel tube extended about 4 mm beyond the exit plane of the honeycomb. Honeycomb usage assured that air flow was parallel to fuel flow. The fuel tube was long enough that a fully developed laminar flow existed.

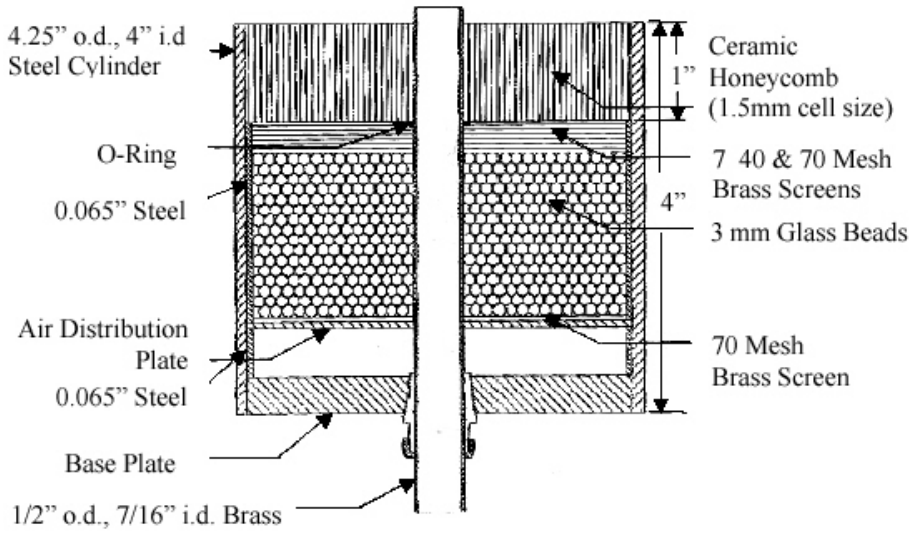

Figure 3.1 Schematic of the diffusion flame burner employed in this research

The burner was mounted on a unislide elevating table (Velmex, Model SPB2909P10) using a platform (Velmex, Model B4003XZ). They were mounted on an XY manual positioner (Velmex, Model A4012P10-S4). The company custom-coated these parts in black color in order to prevent the scattering from the surfaces. The whole system was mounted on the optical table platform by using an X-Y adaptor in a way that a positive angle of 45° was assured between laser sheet propagation direction and center axis of XY positioner in the longer direction. The reason for the angled mounting of the positioner was that the manual knob that allowed the movement of the burner in z

direction would not be blocking the plane ending in laser dumb. Positioners had the sensitivity of a thousandth of an inch, which is 0.02540 mm. Because of the angled position of the XY positioner, the sensitivity in the x and y direction was 0.01796 mm. The Z positioner had an 8 in. scale on it while the XY positioner had a 5 in. scale on it. The burner and positioners can be seen in Fig 3.3, which shows the top view of the optical apparatus and the burner system.

3.2.2 Fuel Delivery System

A sketch of the fuel delivery system is given in Fig. 3.2. The measurements were done using ethylene as fuel. Nitrogen gas was passed through the fuel tubing line for purging purposes. The detailed description of these gases is given in Table 3.1. Molecular weights (MW) and specific volume (υ) are given at 1 atm and 21 °C. These conditions are very similar to the conditions of the measurements done in the laboratory. Air Products E12215 Series two-stage pressure regulators were used at the exit of cylinders to lower the cylinder pressure in two steps. Nalgane 489 polyethylene tubing with 1/4" O.D. and 1/8” I.D. by Fisher Scientific was utilized to carry the fuel to the burner. Necessary rotary plug valves, fittings, reducers, union tees, ferules, male and female connectors were purchased from Accutech Instrumentation to be used in the fuel and air delivery system.

The fuel flowmeter (Matheson Model FM 1050-E406) and the process gage (Grainger Model 1X595) were placed on a panel, which were attached to the optical table. The flow meter had a very sensitive knob and large scale so as to reach the desired flame height easily, and to keep the flow rate variations at a minimum level, since having the same flame height during the experiments was crucial. A process gage was placed to

check the pressure of the fuel gas just before it entered the fuel tube. It was mainly used to check the fuel flow line for possible leak detection. This will be discussed in the next chapter.

Table 3.1 Chemical and physical properties of gases used in the experiments (P = 1 atm, T = 21 °C)

Gas	Ethylene	Air	Nitrogen
Formula	C_2H_4	-	N_2
Company	Air Products	Lab Supply	Air Products
Model	A02-D-16504	-	A01-T-39014
Cylinder Size	B	-	A
Grade	Chemically Pure	Filtered (5 μm)	Ultrapure Carrier
Purity Level (%)	99.8	-	99.9993
MW (g/mole)	28.05	28.96	28.01
υ (m^3/kg)	0.856	0.83	0.861

3.2.3 Air Delivery System

Pressure of air coming from the lab compressor was regulated and filtered up to 5 micrometers by using airline filter/regulator (Speedaire Model 5Z415). The flowmeter (Matheson Model FM 1050-E804), and process gage (Grainger Model 1X595) were placed on the same panel with the others. The air flow line was divided into two just before the burner entrance to have enough mixing for a uniform exit flow. The sketch of the air delivery system can also be seen in Fig. 3.2.

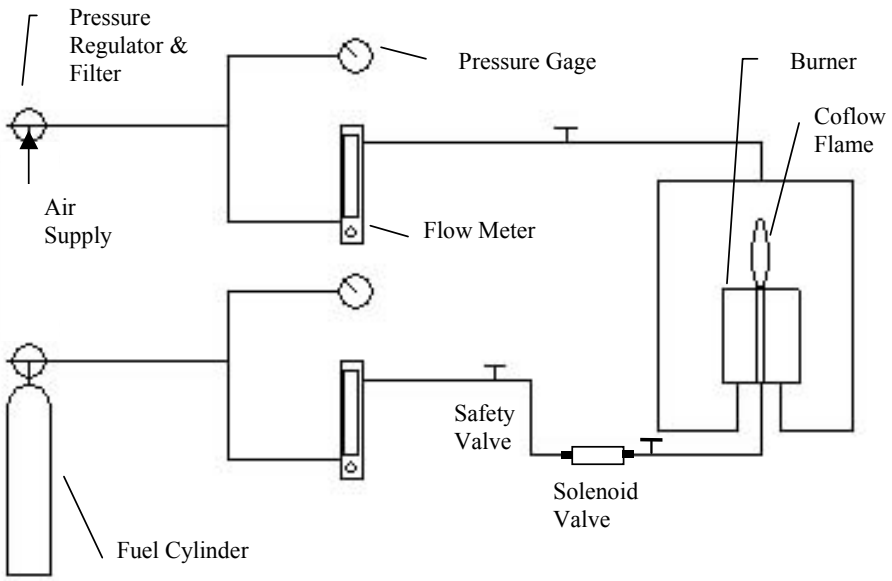

Figure 3.2 Sketch of fuel and air delivery system

3.2.4 Fuel Pulsation System

A Lee micro-dispensing VHS (Very High Speed) system was utilized in the fuel delivery line for pulsing the fuel gas with different frequencies. A high-speed solenoid valve, 5 mm in diameter and 21 mm in length (The Lee Company Model INKX0514300A) with response time less than 0.5 ms was selected according to the pressure and the flow rate of fuel. The valve was placed in the fuel line right before the entrance of the fuel tube of the axisymmetric burner. The valve's wedded materials were compatible with ethylene gas. The valve had an operating pressure range of 0-120 psig at the inlet and a maximum ideal operating frequency of 1000 Hz. A Minstac nozzle, a lee-tubing assembly, a minstac soft tube adapter, a minstac torque wrench, a lead wire assembly, and a mounting clip were used to complete the necessary tubing connections with the fuel delivery line and the electrical connections with the spike and hold driver.

The spike and hold driver (The Lee Company Model IECX0501350A) used a 24 V power supply for spike voltage (to open the valve) and a 3.5 V power supply for hold voltage (to keep the valve open). The wave generator (Pragmatic Instruments Model 2711A) was providing the spike and hold driver with square waves at selected frequencies.

3.3 Optical Apparatus

The optical apparatus is shown in Fig 3.3. Most of the parts are scaled in the drawing for their size and location so that the real dimensions can be imagined. Additionally, the major components of the experiments were tabulated along with the manufacturers and model numbers in Table 3.2. All optical apparatus and other instruments were placed on an optical table with 4 ft. width, 10 ft. length, and 8 in. thickness (Newport Model RS1000-410-8), which had excellent static rigidity and flatness. The only exception to that was the ICCD camera, which was mounted on a tripod, also shown in Fig. 3.3. The laser induced incandescence apparatus will be explained in the order that the laser light passes through optical apparatus. First, the laser beam direction was changed by 90° using 25.4 mm valumax dialectric mirrors (Newport Model 10D510BD.1). These mirrors had 99% efficiency for reflecting any polarization of light. A beam steering device (Newport Model BSD-1), which had two 25.4 mm., aluminum coated, highly reflecting mirrors, was placed on the optical table to set the laser beam's elevation and to precisely control the azimuth and elevation angles of the beam leaving the instrument. A light sheet adjuster module with a 25.4 mm outside diameter (Dantec Dynamics Model 80X63) consisting of a focusing lens and a cylindrical

lens was selected so as to form a laser light sheet from a laser beam with the desired height and thickness. The module had an optical coating of the same laser wavelength of the laser (532 nm) and had a transmission better than 90%. The damage threshold was 100 mJ for the 5 ns pulsed laser and 4 mm beam diameter. It was placed 200 mm from the burner tip center. The laser sheet formed had a thickness of 0.6 mm and a height of 150 mm. Since the biggest reflection of the laser beam was from the focusing lens surface, this surface was given a small angle and the reflected beam was captured by a beamstop box manufactured in the ARC machine shop from a metallic sheet coated in black. The beamstop box had two window openings in the direction of laser propagation, the first one having a 5 mm hole, the second having a slit of 2 mm by 150 mm.

Table 3.2 Major components of the experimental setup

#	Instrument / Part Name	Company	Model #
1	Nd:YAG Pump Laser	Quantel	Brilliant-B
2	Beam Attenuator Module	Big Sky Laser	OP/BAM
3	ICCD Camera	Princeton Instruments	PI-MAX 1024RB
4	High-Speed Camera	Vision Research	Phantom V.5.0
5	Aerosol Monitor	TSI	DustTrak 8520
6	Controller with PTG	Acton Research	ST-133 16/1M PTG
7	Spectrometer	Acton Research	SpectrPro 300i
8	CCD Detector	Acton Research	SpectruMM GS
9	Controller Unit	Acton Research	ST-133
10	Function Generator	Pragmatic Instruments	2711A
11	Solenoid [VHS] valve kit	The Lee Company	IKTX0322000AB
12	Mercury Lamp	Roper Scientific	MS-416
13	Laser Energy Meter w/ Thermopile Probe	Oriel Instruments	70260 & 70264
14	Interference Filter	Melles Griot	03 FIV 046
15	ICCD Camera Lens	Roper Scientific	Nikkor 1902
16	Neutral Density Filters	Oriel (Spectra-Physics)	50271-50281
17	Light Sheet Adjuster Module	Dantec Dynamics	80X63
18	Digital Oscilloscope	Tektronix	TDS 210
19	Optical Table	Newport	RS1000-410-8

The last component in the direction of the laser light was beam dumb manufactured according to our needs in the ARC machine shop in black color. The beam steering device, light sheet adjuster module, and dialectric mirrors had their connection to the optical table with steel rods (Oriel Model 12300), rail carriers (Oriel Model 11670), and standard optical rail (Oriel Model 11542). A multiple filter holder (Oriel Model 12800) was used when linearity checks were performed at the exit of Nd:YAG laser. It had the capacity of holding up to five filters in series. A neutral density filter set was used to reduce the laser light signal down to the desired levels with confidence, especially to very low levels that cannot be achieved with sensitivity using laser beam attenuator and that cannot be read precisely with a laser energy meter. It consisted of six, 25.4 mm diameter, glass metallic neutral density filters with 0.1, 0.2, 0.3, 0.4, 0.6, 1.0 density values (Spectra-Physics Model 50271-50281). The receiving optical apparatus, which consisted of an ICCD camera, an imaging lens and an interference filter was in 90° with the direction of the laser propagation. The ICCD camera (Princeton Instruments Model PI-MAX 1024RB) was mounted on a tripod shown in Fig. 3.3. The ICCD camera was the crucial equipment for the experiments because of the fact that gate width in the order of nanoseconds was necessary for capturing the prompt LII signal synchronized with the laser fire. At the same time, gate gain was needed to be able to detect the time history of LII signal. The ICCD camera system was with a thermoelectrically cooled camera head, 1024 X 256 pixel format, front-illuminated, 26 μm x 26 μm pixel definition, 40 ns of gating capability, 1:1 fiber-optic bonded 18 mm Grade 1 Plus Gen II image intensifier, a built-in Programmable Timing Generator (PTG) for controlled gate timings in linear and experimental increments, wide spectral range (200 nm-900 nm).

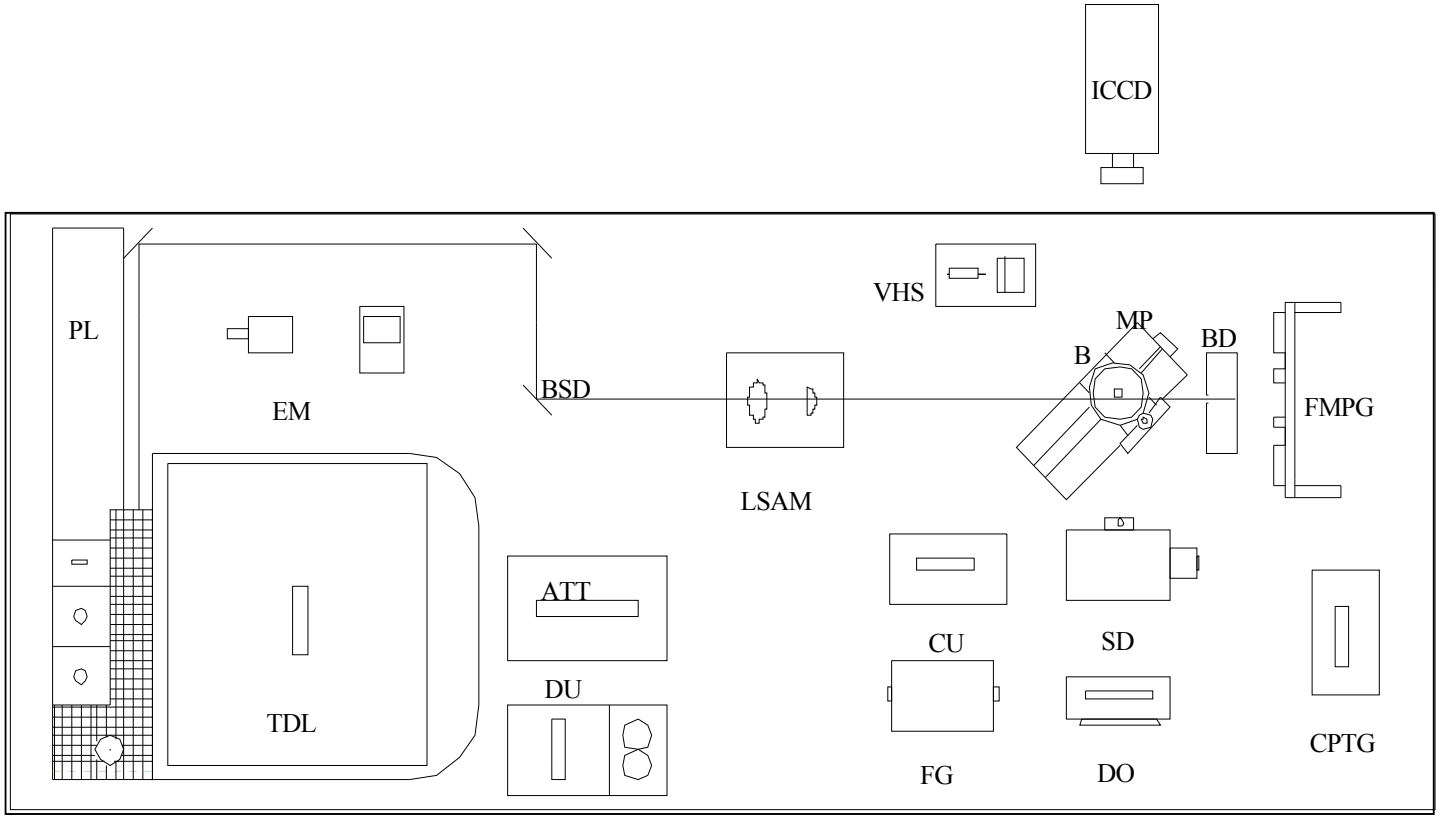

ATT: Automatic Tuning Terminal
B: Axisymmetric Burner
BD: Beam Dumb
BSD: Beam Steering Device
CPTG: Controller with Programmable Timing Generator

CU: Controller Unit

DO: Digital Oscilloscope
DU: Dye Unit
EM: Energy Meter
FG: Function Generator
FMPG: Flow Meters and Pressure Gages
ICCD: Intensified CCD camera with imaging lens and interference filter

LSAM: Laser Sheet Adjuster Module
MP: Manual Positioners
PL: Nd:YAG Pump Laser
SD: Spectrograph with Detector

TDL: Tunable Dye Laser

VHS: Very High Speed Valve with control circuit

Figure 3.3 Top view of experimental setup for LII measurements

The C-Mount was used to secure the 50 mm F1.4 imaging lens (Roper Scientific Model Nikkor 1902) in front of the camera. A 50 mm diameter interference filter (Melles Griot Model 03 FIV 046) with center wavelength of 607 nm, FWHM of 36 nm, and peak transmittance of 62% was oriented with the shiniest (metallic) side toward the burner (source of radiant flux) and placed in front of the imaging lens.

3.4 Light Source

A Quantel Brilliant B pulsed Nd:YAG pump laser combined with a Quantel TDL 90 Tunable Dye Laser (shown in Fig. 3.3) were available in the Combustion Lab in the Applied Research Center (ARC). However, the system was installed in a way that it required the laser user to use the lasers simultaneously having the laser output beam through the dye laser port. First, this synchronization issue was resolved by disconnecting the necessary wires going to the tunable laser control unit so that the user was able to operate the pump laser independently. In other words, a necessary change was done in the interlock loop so that the circuit was a closed loop for an independent pump laser usage. Secondly, the position of special laser mirrors were changed and aligned so that the pump laser beam was redirected into valumax dialectric mirrors for the experiments. Other modifications were necessary to have a 532 nm (second harmonic) wavelength laser output from a 1064 nm (first harmonic) wavelength. The second harmonic generation module (532 nm) was mounted in front of the pump laser. The third harmonic generation module (355 nm) was mounted right after the second harmonic generation module. The laser output was redirected from the second harmonic module output so that it would not pass through the third harmonic module. After careful investigation of laser performance,

it was decided that a beam attenuator module (Big Sky Laser Model OP/BAM), which was specially designed for this laser, was required so as to operate the laser with variable laser fluences by changing the laser intensity to the desired levels at the optimum performance (burning pattern, pulse width, and stability). To do this last modification, the third harmonic module was removed, and the second harmonic module was moved to the third harmonic module's position. Also, the beam attenuator module was mounted in the second harmonic module's original position. All the laser mirrors were realigned for the final configuration. All these modifications were performed by me under the guidance of the Big Sky Laser technical team. The Nd:YAG laser system consisted of an optical laser head, a power supply and a cooling group cabinet, a harmonic generation modules, a beam attenuator module, and a remote control. The remote control provided the user with full control of the laser and of its internal parameters. According to the manufacturer's specifications, Nd:YAG laser had +/- 4% shot to shot energy stability, 400 mJ maximum energy per pulse, 70% fit to Gaussian in the near field, 90% fit to Gaussian in the far field, 0.5 mrad divergence, and better than 80% polarization ratio (horizantal polarization) with a 10 Hz maximum repetition rate at 532 nm with a 5 ns pulse width. The shot to shot stability, beam burn spots, maximum energy, output energy versus Flash Lamp/Q-Switch delay, and temporal profile tests were done in the laboratory. The details of these test conditions and results will be given in the next chapter.

3.5 Soot Aerosol Monitoring Apparatus

The sketch of the soot aerosol monitoring setup is shown in Fig. 3.4. A collecting nozzle was centered at the burner tip and attached to steel rods and secured on the optical

table. A 4 ft. long Tygon plastic tubing (product of Norton company) with ¼ in. I.D. was positioned at the top of the collecting nozzle exit and was connected to the aerosol monitor inlet. Sampling was done 20 in. above the burner tip. Using a sampling tube longer than 4 ft. was not recommended by the manufacturer since particle transport losses in the tube could adversely affect the measurement. Also, usage of Teflon or silicone tubing was avoided because they can cause significant transport losses.

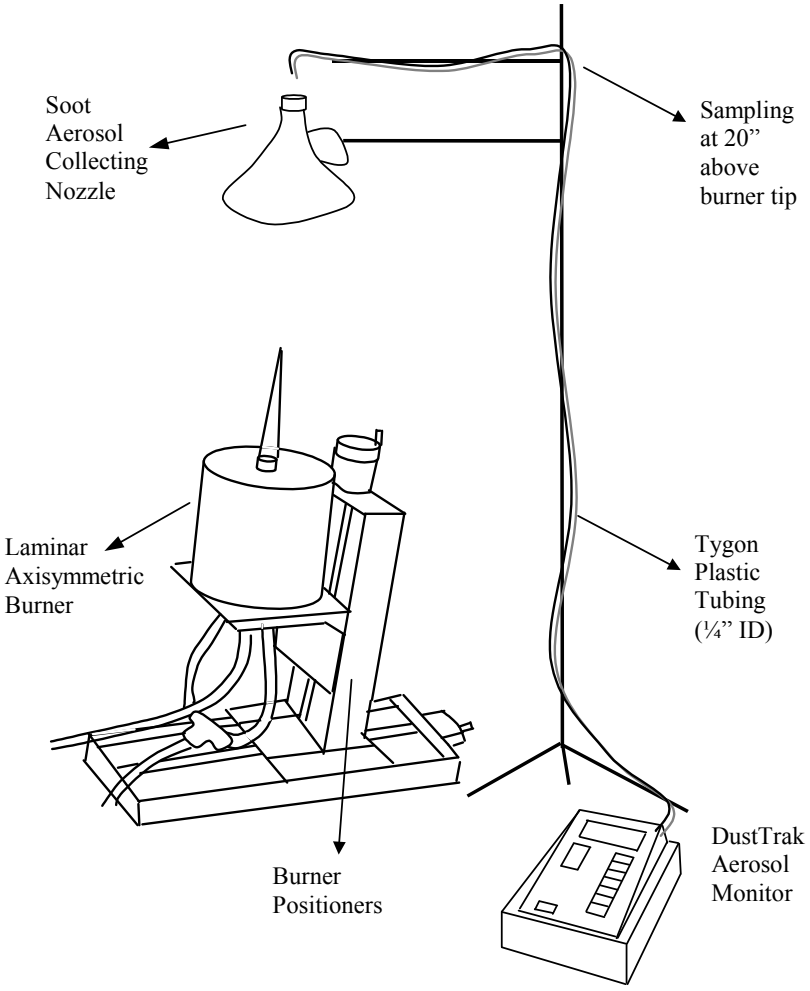

Figure 3.4 Sketch of the soot aerosol monitoring measurements

The aerosol monitor (TSI Model DustTrak 8520) was equipped with a 90° light scattering laser diode sensor, had 0.001–100 mg/m^3 range (calibrated to respirable fraction of standard ISO 12103-1, A1 test dust), ±0.001 mg/m^3 zero stability, and 0.1 to an approximate 10 μm particle size range.

3.6 Other Instruments

In this section, the spectrometer, CCD detector, mercury lamp, function generator, laser energy meter, Programmable Timing Generator (PTG), and the High Speed Camera will be discussed. A spectrometer (Acton Research Model SpectrPro 300i) with a CCD detector (Acton Research Model SpectruMM GS) was utilized for a spectral scan to observe the C_2 emission from the investigated flame. The spectrometer had a 300 mm focal length, 1 nm to 1400 nm mechanical range, 0.1 nm resolution, 14 mm height micrometer adjustable slit (from 10 μm to 3 mm wide), and 600 g/mm and 1200 g/mm gratings. The CCD detector (Acton Research SpectruMM GS) was a back illuminated 1024x128 pixel detector specifically designed to fit the CCD port of the spectrometer. The mercury lamp mounted in a flange (Roper Scientific Model MS-416) was used as a tool to calibrate the spectrometer with a CCD detector system. The function generator (Pragmatic Instruments Model 2711A) provided a square wave for the spike and hold driver of the solenoid valve. The square wave was labeled as a pulse wave in the list of standard waveforms of the function generator. It had the parameters of Delay, Rise, High, Fall, Polarity. The parameter “delay”(0.0-100.0 %) defined the phase of the function generated. The parameter “high”(0.0-100.0 %) defined the duty cycle of the function, and the parameter “polarity” was set to normal, with “rise” and “fall” parameters being zero

for a sudden rise and fall. The function generator had a sample rate range of 0.1 Hz to 2 MHz (10 s to 500 ns), a transition time less than 150 ns and an amplitude range of 1.00 to 10 V (10 mV resolution). It had the Sync Trigger Out and Trigger Input capabilities for gated, burst, toggled, and master-slave modes. The laser energy meter with Thermopile probe (Oriel Instruments Model 70260 & 70264) was used in laser energy per pulse measurements before, during and after the experiments. The laser type was set to "Nd:YAG", and the energy threshold was set to"low". It was calibrated by ThermoOriel for linearity (1%) and accuracy (2%) with a energy density threshold of 1 J/cm^2. The controller with Programmable Timing Generator (PTG) supplied power to the ICCD camera along with the transmission of the signal to and from the camera with the head cable and controlled the gating parameters with the timing cable. The controller with PTG also had a dual 16 bt 100 KHz and 16 bit 1 MHz A/D converter along with a high speed PCI interface package for data transfer between the computer and the controller with PTG through a 15 ft. high-speed serial cable. The details of the connections, set parameters and timing diagram will be given in the next chapter. The high-speed camera with 1024x1024 pixels (Vision Research Model Phantom V.5.0) was used to assure that the phase locked images (captured by ICCD camera) were consistent with images taken by the ICCD camera within one period, and from one period to another by capturing 1,000 images in one second.

3.7 Data Acquisition and Post Processing Softwares

The softwares used in this study are tabulated and given in Table 3.3. WinView/32 was used to capture the LII data with the necessary camera triggering,

temperature settings, and PTG preferences, post processing such as, Image Orientation, Cross Section, Binning and Skipping, Area Under Curve, Spectra Math, Clipping and Threshold, Histogram, and Statistics. The WinSpec/32 software was used for the time history analysis of LII data, a 3-D image spectra view, and to convert data with the extension "spe" and/or "tiff" to ASCII files by the ASCII Snap-in tool. Some crucial screenshots of setup parameters of WinView/32 software will be given in the next chapter. Spectrasense was the software for the spectrometer with a CCD detector system. The Phantom software was associated with Phantom high-speed camera experiments. The TrakPro software was used to transfer the soot aerosol experimental data from DustTrak monitor to the computer. Finally, Mathcad, Origin, and Excel were used for post processing purposes of the ASCII data.

Table 3.3 Utilized softwares for data analysis and post processing

#	Software Title	Company	Version #	Year Released
1	WinSpec/32	Roper Scientific	2.5.15	2005
2	WinView/32	Roper Scientific	2.5.8	2002
3	Spectrasense	Acton Research	4.1.0	2000
4	Origin	Microcal Software	5.0	1997
5	Mathcad	Mathsoft	7.0	1997
6	Trakpro	TSI	3.41	2003
7	Phantom	Vision Research	5.0	2004

CHAPTER IV

MEASUREMENT TECHNIQUES

4.1 Introduction

The extent of soot formation depends on the type of flame (diffusion or premixed), type of fuel, pressure and temperature, but the structural properties of the final soot particles have many striking similarities for different fuels and flame conditions. When examined under an electron microscope, the soot particles are usually chain-like aggregates of approximately monodisperse spherical units. The diameter of the spheres typically ranges from 10 to 60 nm. The smallest particles are found in luminous, but not sooting flames, while the largest ones are found in heavily sooting flames. The number of spheres per aggregate ranges from several to more than a thousand.

An important property of soot, the complex refractive index ($m = n - i\,\kappa$), is not well characterized. The variation of the refractive index with temperature, wavelength, and the chemical nature of the soot is still uncertain. It has been postulated that the room temperature values of m are valid at flame temperatures (Dalzell and Sarofim 1969). The value $m = 1.90 - 0.55i$ is used as an average value in the visible region in this study, given by Dalzell and Sarofim (1969).

4.2 Optical Technique for Soot Measurements

Optical techniques have made it possible to ascertain the presence of soot particles in flames with in-situ measurements, and further, to measure their size, concentration, and temperature. The use of these techniques, instead of probe sampling

and thermocouple measurements, has the advantage of not disturbing the aerodynamics and chemistry of the flame. In recent years, the LII and TIRE-LII techniques have emerged to be used in order to obtain information about soot formation in flames (as stated in the literature review).

The Laser-induced Incandescence originates from the heating of soot particles from the normal combustion temperature (typically 2000 K) to near or above the vaporization temperature (typically near 4000 K) by a highly energetic laser pulse and detects the enhanced thermal radiation, also called incandescence.

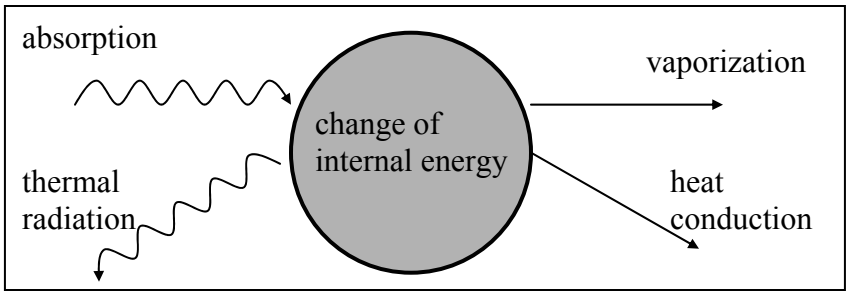

Figure 4.1 Schematic representation of the power balance of a laser-heated soot particle

The energy balance equation given by Melton (1984) for a single spherical soot particle heated by a laser radiation has the following form.

(4-1)

$$\frac{\pi^2 d_p^3 E(m)}{\lambda} \cdot q(t) - \frac{2k_a(T-T_0)\pi d_p^2}{d_p + G\lambda_{MFP}} + \frac{\Delta H_v}{M_v}\frac{dM}{dt} - \sigma\pi d_p^2(T^4 - T_0^4) - \tfrac{1}{6}\pi d_p^3 \rho_s c_s \frac{dT}{dt} = 0$$

where

$$\frac{dM}{dt} = \frac{1}{2}\rho_s \pi d_p^2 \frac{d(d_p)}{dt} = -\pi d_p^2 \beta P_v(T)\sqrt{\frac{M_v}{2\pi RT}} \qquad (4\text{-}2)$$

The terms, shown in Fig. 4.1, are in order, laser energy absorbed by the soot particle per second, the rate of heat transfer (conduction) to the medium, the energy expended in vaporization of carbon, the rate of energy loss by blackbody radiation, and the rate of internal energy rise. The description of the terms with typical values and corresponding units are given in Table 4.1.

Table 4.1 LII energy balance equation terms by Melton (1984)

Symbol	Description	SI Unit
d_p	Primary particle diameter	m
E(m)	Refractive index function for absorption	-
λ	Laser wavelength	m
q(t)	Laser intensity	W/m^2
k_a	Heat conduction coefficient for air	W/m/K
T_p	Temperature of soot primary particle	K
T_0	Temperature of surrounding gas	K
G	Geometry-dependent heat transfer function	-
λ_{MFP}	Mean free path of the medium	m
ΔH_v	Heat of vaporization of graphite	J/mole
M_v	Molecular weight of soot vapor	kg/mole
P_v	Vapor pressure of soot	Pa
ρ_s	Density of soot	kg/m^3
c_s	Specific heat of soot	J/kg/K
σ	Stefan's constant	$W/m^2/K^4$
β	Evaporation coefficient	-
R	Universal gas constant	J/kg/K
m	Refractive index of soot	-
$R(\lambda)$	Spectral Response function	-

When the soot particles absorb energy from the laser beam, their temperature increases. The temperature will rise to a level where significant incandescence will occur with sufficient laser fluence. When the temperature reaches around 4000 K (3915 K is the vaporization temperature for graphite), rapid vaporization begins presumably at the particle surface. As the temperature of the particle increases, the vaporization rate

increases until a balance is attained and the particle temperature levels out. As the laser pulse ends, the temperature drops and the vaporization rate falls with it (Wainner 1999). Vaporization is the dominant mechanism earlier (approximately for the first 100 ns after the laser pulse ends), and afterwards the conduction term determines the temperature decay. The contribution of the radiation heat transfer term is small at all times. S. Will et al. (1998) stated that the typical LII signal is typically observed, as shown in the following expression, with the assumption of a uniform particle temperature and a diameter within a volume element.

$$S_{LII} \alpha \quad d_p^2 \int R(\lambda)\varepsilon(d_p,\lambda)e_b(T,\lambda)d\lambda \tag{4-3}$$

$R(\lambda)$ is a combined spectral response function for the sensitivity of detector and the transmission of the optical system. The next two terms together are standing for Planck radiation. Since the temperature and the diameter of the soot particle are functions of time, LII signal (S_{LII}) will be a function of time as well. Analyses by Melton (1984) stated that under certain conditions (i.e. high laser fluencies and small particles diameters) that the thermal radiation (incandescence) is proportional to the soot volume fraction at the moment of maximum soot temperature. The small particles diameters are considered such that they are much smaller than the laser wavelength ($\pi d_p/\lambda << 1$). In this case, the particles should absorb and emit closely proportional to their volume (d_p^3). However, the primary energy loss mechanisms of conduction and evaporation are proportional to surface area (d_p^2). Two analysis methods based on the LII signal have been reported for extracting the primary particle size from the LII data. The first method

uses the ratio of signal intensity with the same time delay and duration at two detection wavelengths. The second method is called the gate ratio method, which uses the same temporal curve obtained at a single detection wavelength.

4.3 Experimental Preparation

The components of experimental setup were explained with their specifications in detail in Chapter 3. In this section, the preparation steps taken will be discussed briefly before the initial tests and the linearity checks.

After the flatness of the research grade optical table in the x and y direction was checked, the preparation of the experimental setup was started. First, the laser was positioned on the optical table (shown in Fig 3.3) and the laser mirrors were aligned by a Quantel technical person. The optical components of the setup were aligned using very low laser energy. The beam steering device made the alignment process faster by allowing changes in the azimuth and elevation angles. The burner system was placed after the optical rail on the right side somewhere near the center of the radius of the plate. The burner was lowered by using the Z positioner until the lowest possible point was achieved. Then, the burner was lifted 120 mm, followed by minor adjustments by using the following procedure. A circular aperture of 1 mm in diameter was placed on the optical rail. Its height was the same as the burner tip height from the optical rail. Then, it was slid completely along the rail observing that the laser was staying in touch with the 1mm hole in the aperture. After this procedure was satisfied, the light sheet adjuster module was positioned 280 mm before the center of the burner tip. The laser sheet obtained had a 150 mm height and 0.6 mm width. The burner was lowered 50 mm by the

Z positioner, allowing 100 mm (+/- 50 mm from the center) out of 150 mm laser sheet to be used for imaging. Then, the burner was moved with the XY positioner so that the laser beam touched the end surface of the burner tip, and with a further small adjustment, half of the beam was made to pass the burner tip while the other half was stopped by the surface. The XY location from the positioner was called point A. The same steps were taken for the other end of the surface of burner tip, and this location was called point B. The mean of these two points was, in fact, the location of the burner tip center.

The ICCD camera (1024 x 256 pixels) with an imaging lens was mounted on a tripod and placed perpendicular to the direction of the laser propagation. It was rotated so that 1024 pixels were counted in the direction of the flame propagation and 256 pixels were counted in the horizontal axis of the burner tip. The distance between the front of the camera (the intensifier photocathode) and the burner tip center was approximately 400 mm. A calibration target was placed on top of the burner tip to check that the laser sheet was vertical to the burner tip axis and that the ICCD camera was focused at the center of the burner tip.

4.4 Initial Tests, Timing and Calibration Procedures for Experimental Setup

4.4.1 Introduction

In the previous section, the preparation and alignment of the experimental setup was described. However, there were still some initial tests and calibration procedures that needed to be done prior to starting with the measurements. Furthermore, timing and triggering issues, LII signal trapping parameters needed to be found and optimized before we could collect the LII data. These basic tasks are explained in the following sections.

4.4.2 Tests on Coflow, Laminar Flame

Laminar nonpremixed flames fueled by ethylene were studied under atmospheric conditions. The burner system with the air and fuel delivery lines were described in detail in Chapter 3. The flames studied were laminar, steady and unsteady, coflow, non-premixed flames, whose flow conditions are given in Table 4.2.

Table 4.2 Flow Conditions

Fuel	Flame Name	Fuel Flow Rate (cm^3/s)	Fuel Velocity (cm/s)	Air Flow Rate (cm^3/s)	Air Velocity (cm/s)	Visible Flame Height (mm)
Ethylene	E1	4.06 ∓ 0.19	4.20 ∓ 0.19	1000 ∓ 50	12.48 ∓ 0.62	88 ∓ 0.5
Ethylene	E2	3.52 ∓ 0.17	3.64 ∓ 0.17	1000 ∓ 50	12.48 ∓ 0.62	75 ∓ 0.5
Ethylene	E3	2.69 ∓ 0.13	2.78 ∓ 0.14	1000 ∓ 50	12.48 ∓ 0.62	55 ∓ 0.5
Ethylene	E4	1.86 ∓ 0.09	1.92 ∓ 0.10	1000 ∓ 50	12.48 ∓ 0.62	35 ∓ 0.5

The very first check was to see whether there was a leak in the fuel delivery system. For that reason, the bubble leak detector was used to check for major gas leakage from the fuel line. To check for minor leaks in the line, the flame was started and the fuel flow was stopped by turning off the fuel flow meter knob. Then, the gas regulator knob was also turned off in order to have the fuel gas in the fuel line with no escape except for at any leak points, if there were any. The pressure gage reading was recorded and checked after 24 hours. The decrease in pressure was negligible, ensuring that the fuel line was safe to run flames. Before connecting the very high speed (VHS) in the fuel delivery system, fuel line was purged by using nitrogen gas (ultrapure carrier grade) for 15 minutes. The VHS valve was placed as close as possible to the fuel tube of the burner

to minimize the delays when pulsation was carried out. The distance between burner tip and valve exit was 430 mm.

It should be mentioned that we did not introduce any possible object above the flame that could potentially disturb the nature of the flame. Instead, a cylindrical Plexiglas hollow tube, with a 2.5 mm thickness, was extended above the top of the outer burner steel cylinder for 650 mm. Flame movements were negligible, especially low in the flame. The fluctuations observed high in the flame were tested by using high speed camera with 1000 picture frames per second and fluctuations at the tip of the flame were found to be under 1 mm. The third potential problem was how axisymmetric the flame was. It was realized that the good match between the honeycomb and the inner surface of the outer tube of the burner, and between the outer surface of the fuel tube and the honeycomb played an important role for the axisymmetric structure and the vertical surrounding air flow, which also affected the axisymmetry of the flame. Experimental results showed that the flame was quite axisymmetric from different views. That was also confirmed by observing equal height wings at the top of the ethylene flame from different angles by the naked eye.

4.4.3 Rotameter Calibration

Two flowmeters were used during the experiments, namely, a Matheson FM-1000 glass tube flowmeter with a 65 mm tube for air flow rate measurements, and a Matheson FM-1050 glass tube flowmeter with a 150 mm tube for fuel flow rate measurements. The air flow meter was calibrated for air and delivered with direct SLPM readings and needed no calibration. However, the second flowmeter, which was a high accuracy flowmeter with glass and steel floats for ethylene flow rate measurements, was factory calibrated for

only methane and carbon monoxide. Therefore, calibration for the FM-1050 flow meter was necessary for ethylene gas.

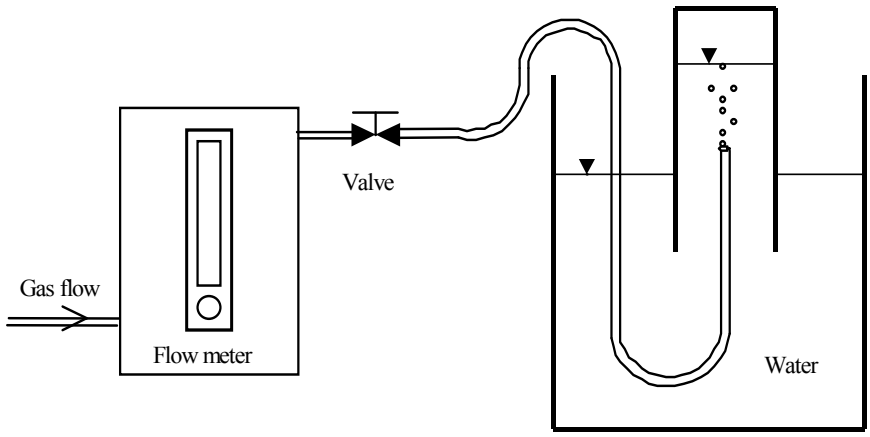

Figure 4.2 Fuel flow rate measuring apparatus

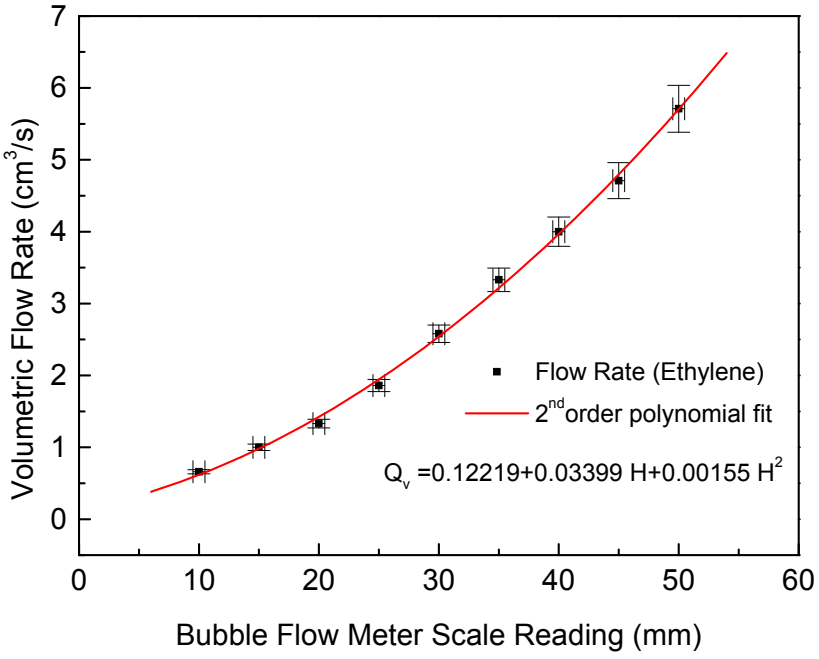

Figure 4.3 Rotameter calibration scale for fuel supply

The 100 mL scaled glass container was inverted in a big glass container serving as a water tank. The polyethylene tubing was inserted in the small container as depicted in Fig. 4.2. The water displacement was timed between 20 mL and 100 mL for a total volume of 80 mL for several scale readings on the flow meter. The second order polynomial fit for the calibration data is given in Fig. 4.3. The horizontal error bars are indicator of the errors by the flowmeter scale reading. The vertical error bars are indicators of the total error caused by uncertainty of volume and time readings. Since experiments were carried out depending on the visible flame heights, another set of experiments were necessary to show the dependence of the visible flame height on the flowmeter scale reading.

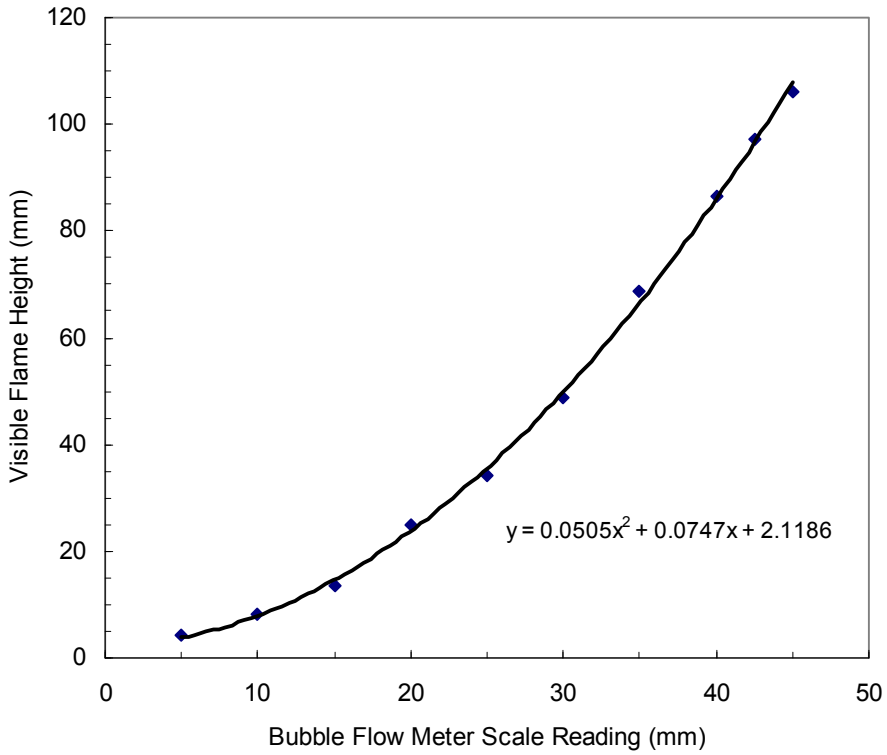

Figure 4.4 Visible flame height versus flow meter glass float reading

Since the flame height has a linear dependance on the flow rate, a similar second order polynomial fit was found for this experiment, and shown in Fig. 4.4. The flame heights were calculated from the emission images of the flames by the ICCD camera. Using the information we have from these two fits, the flow rate values for the studied flames with the uncertainties were calculated and given in Table 4.2.

4.4.4 Neutral Density Filters Check

Six different neutral density filters whose density values were between '0.1' and '1' were used individually or in series with others in the detector linearity check experiment and the LII fluence curve experiment. A linear extrapolation between 500 nm and 550 nm was used to reach NDF's transmittance values at the Nd:YAG laser wavelength of 532 nm and given in Table 4.3. The transmittance, T, is I_T/I_0 and is given by:

$$T = 10^{-OD} \tag{4-4}$$

where OD is the optical density, I_0 the incident beam intensity, and I_T the transmitted beam intensity.

Table 4.3 Neutral density filter transmittance values

Filter #	Optical Density (OD)	Transmittance(T)
50271	0.10585	0.78369
50272	0.18951	0.64638
50273	0.30624	0.49404
50274	0.38001	0.41686
50276	0.61971	0.24004
50281	0.93391	0.11644

The average error on the filter transmittance values was found to be 0.6% when the filters were well centered with respect to the laser beam. The centering was assured by the usage of a self-centering filter holder.

4.4.5 Laser Energy Stability Check

The argon-ion laser was checked for stability of output power. First, the laser was run for 30 minutes after the cooling group unit temperature reached 38 °C, releasing the interlock by the thermal sensor. The 200 different laser shots were recorded by the laser energy meter in four different days. The shot-to-shot repeatability was found to be +/- 4.5 % with 99% confidence. In other words, the standard deviation (SD) of energy per pulse for the laser beam of 20 mJ average output was about 0.45 mJ.

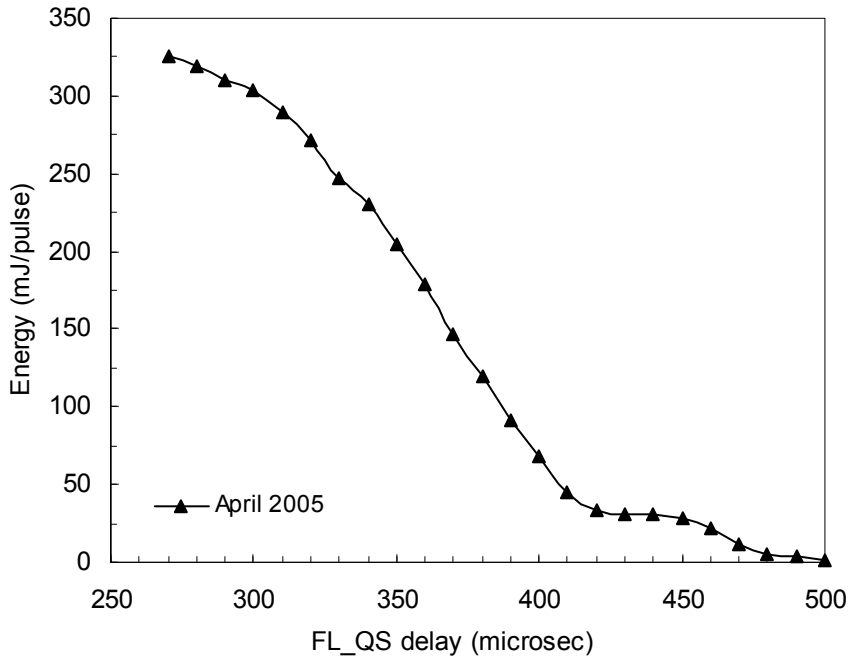

Figure 4.5 Laser Output Energy versus FL-QS delay for the Quantel Nd:YAG laser

The laser was operated at the lowest Flash Lamp Q-Switch (FL-QS) delay of 270 μs for the best shot-to-shot stability and the narrowest laser pulse width. The output energy versus the FL-QS delay behavior is given in Fig. 4.5. The curve show similar behavior compared to manufacturer suggested trend in regard to energy response of the laser by the Flash Lamp-Q Switch adjustment. The slightly observed energy loss can be attributed to the fact that the laser flashlamp had been used for 7-8 months for extensive hours and flashlamp efficiency decreases with the number of accumulated shots.

4.4.6 Laser Spatial and Temporal Profile

The laser sheet spatial profile in the radial and axial location had to be determined to investigate the Gaussian profile match in radial direction and laser energy distribution in axial direction and its affect on LII signal. The ICCD camera was gated with a low intensifier gain and interference filter with a low bandwidth (3 nm) and 532 nm center wavelength was placed in front of the camera to detect only scattered laser light. A piece of rectangular white paper was placed vertically on top of the burner tip with a 45° angle so that the laser light would hit the paper surface and be in the imaging view of camera. The resultant image was analyzed to reach the spatial profiles of the laser sheet in the radial and axial directions, and given in Fig. 4.6 and Fig. 4.7 respectively. The reason why the axial profile had noisy cross section is that the cross sectional profile was only obtained in the center of the laser sheet, unlike the radial profile where cross sectional averaging was done throughout the laser sheet height of 100 mm. The laser intensity was normalized to be able to see the percentage decrease in the laser intensity in both the radial and axial directions.

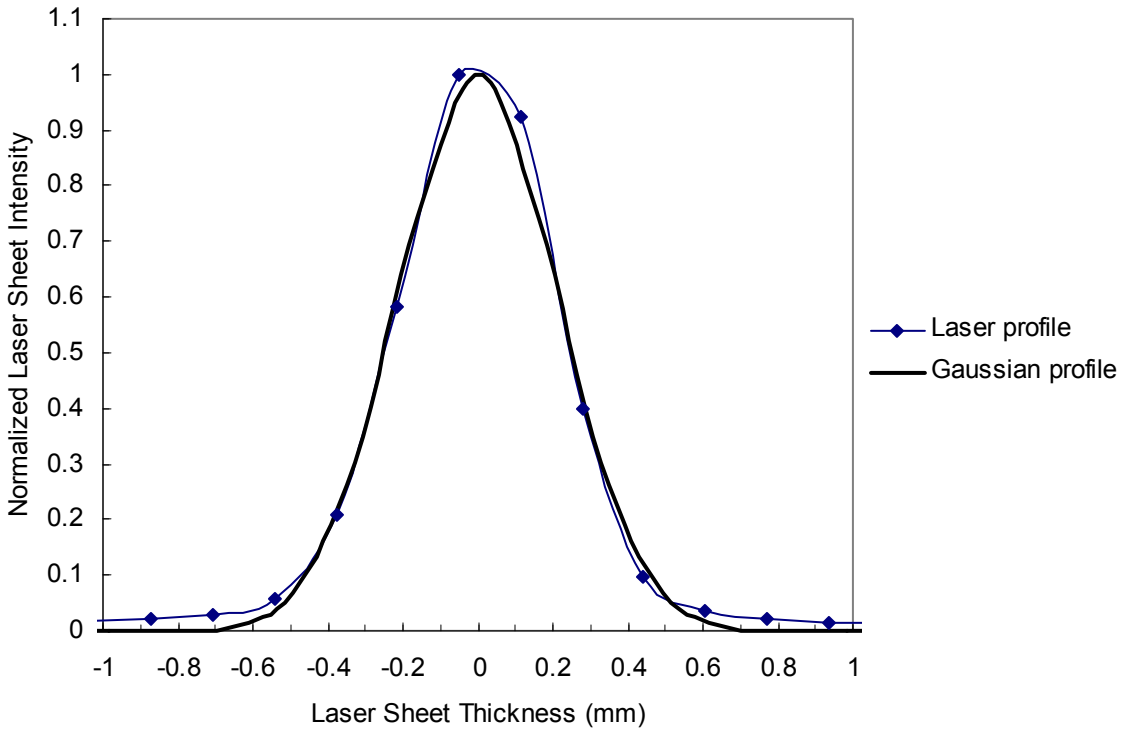

Figure 4.6 Laser sheet radial profile (burner center is 0 mm) and Gaussian fit

The Gaussian fit for the laser sheet (shown in Fig. 4.6) indicates that the laser sheet has a Gaussian profile in the radial direction and is expressed in the following form;

$$F(r) = F_0 \cdot e^{-r^2/w^2} \tag{4-5}$$

where *F(r)* is the laser fluence, F_0 is the laser fluence at the center of the laser sheet, and *w* is the laser sheet half width which was found to be 0.3 mm. Furthermore; the laser sheet stays within 80% of its intensity for the center half of its axial length of interest. The temporal profile, which is given in Fig. 4.8, was estimated by taking a series of time-delayed images of the laser with a minimum gate width before, during and after the laser pulse. The FWHM for laser was about 5 ns.

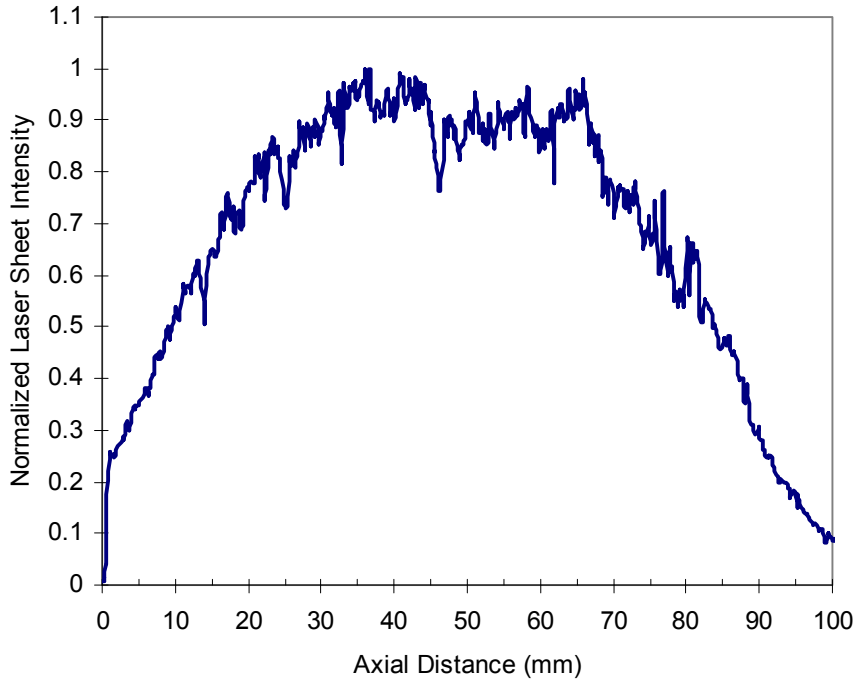

Figure 4.7 Laser sheet axial profile (burner tip is 0 mm)

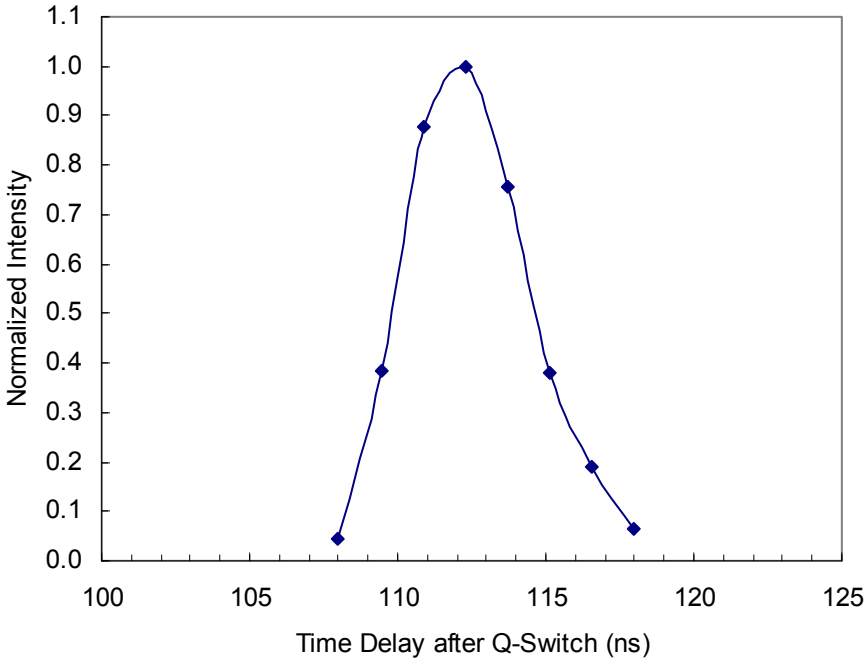

Figure 4.8 Temporal profile of the laser sheet (FWHM ≅ 5 ns)

4.4.7 ICCD Camera Linearity Check and Dark Charge Test

The linearity test was important and necessary in order to decide on the linear output range of the camera for the LII experiments. The dark charge test was also necessary so that it can be subtracted from the LII images in the data analysis. To perform these tests, two parameters were important, namely, detector temperature locked, and intensifier gain of the detector. The intensifier gain was kept high for more sensitivity and this caused a higher dark charge. For this reason, the detector temperature was kept at the minimum possible temperature (-20 °C) for the lower dark charge. Since the laboratory lights were not turned off during the LII experiments, all of the laboratory conditions were kept the same along with the timing parameters of the detector. The laser light scattered from the burner tip was captured by the ICCD camera with a 532 nm interference filter in front. The neutral density filters were used individually and in series with a multiple filter holder to decrease the laser intensity, providing a wide range of input signal to investigate the output signal. The linearity test result is shown in Fig. 4.9. The linear region is indicated on the figure. When the light intensity is higher than the upper value of the linear range, the camera starts to saturate. On the other hand, when the intensity is very low, the signal becomes comparable with the dark charge and it should be avoided.

The detector (ICCD camera) with a 600 nm center wavelength and 40 nm bandwidth interference filter in front under the same experimental conditions and LII operating parameters with laboratory lights on collected the dark charge pattern. It should be noted that the laser light was blocked from reaching the burner and the flame was not started. As mentioned earlier, a larger and less uniform background was expected for a

longer exposure time, higher intensifier gain and warmer detector. After the temperature lock was established, another 30 minutes of time was given before taking a few dark charge readings with the detector, operated with the MCP On/Off switch set to off. This was necessary for the detector to completely stabilize.

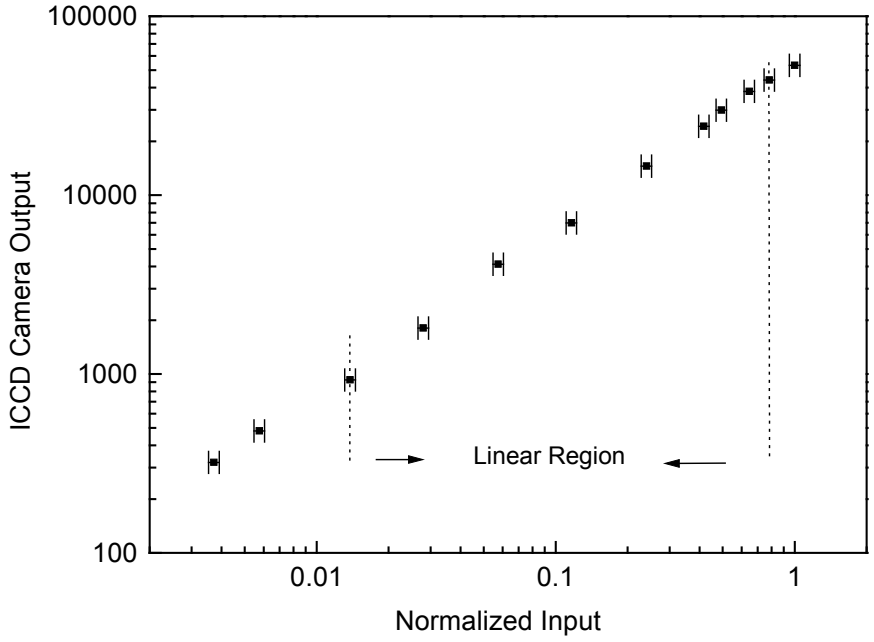

Figure 4.9 ICCD camera linearity check

The averaged image of the baseline signal responsible for the dark charge and laboratory lights had a mean intensity of 437 (a.u.) and a standard deviation (SD) of 32 (a.u.). This baseline average value was used for calibration purposes, explained in Chapter 5.

4.4.8 VHS Valve Operation Test

The control signal (5 VDC), the hold voltage power supply (3.5 VDC, 2000 mA), and the spike voltage power supply (24 VDC, 830 mA) were connected to the spike and

hold driver. Figure 4.10 shows the operation of the spike and hold circuit. The function generator produced a TTL signal (0-5 Volts pulse), which acted as the control voltage. The on time, duty cycle and the operating frequency of the valve were determined by this input signal. When the control signal was low (0 VDC), the circuit and valve were not energized. When the signal was high enough (5 VDC), the circuit energized the spike timer and the hold voltages to the valve. Spike time for the valve was 0.1 ms. After the spike period, the circuit turned off the spike voltage and left the hold voltage energized for as long as the control signal remained high. When the control signal became low all the power to the valve was turned off regardless of the spike timer status.

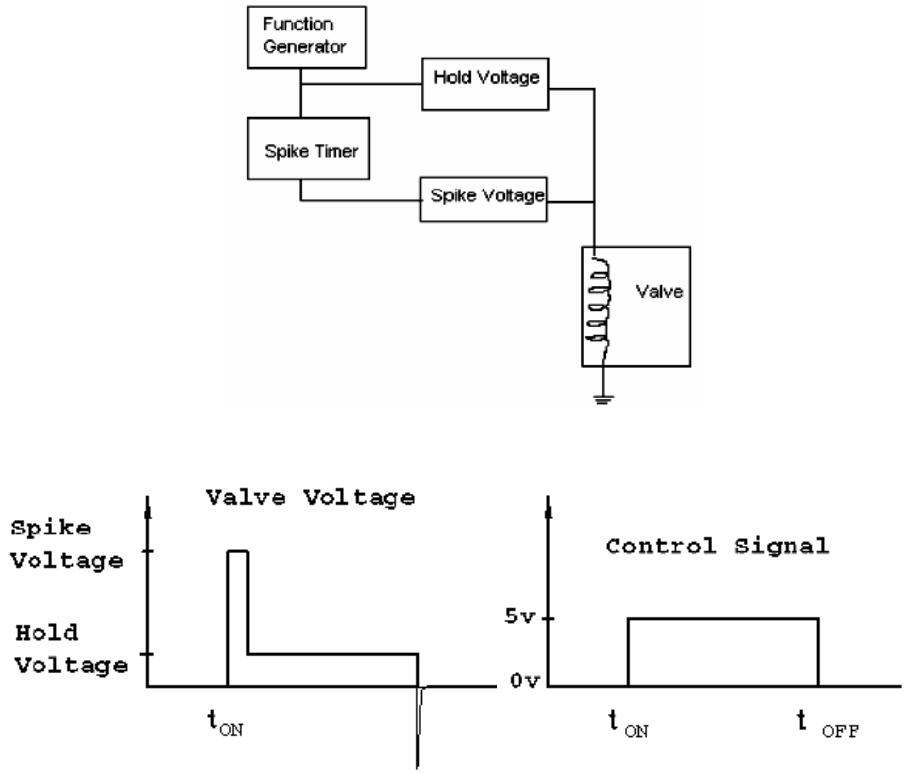

Figure 4.10 Block diagram of the VHS circuit operation (top), of the control signal provided to the spike and hold driver by the function generator (bottom right), and of the amplified signal provided to the VHS valve by the spike and hold driver (bottom left)

As an example, when the function generator supplied a control signal for 200 Hz and 20% DC, the ideal time that the valve was kept open was 1 ms and the ideal time that the valve was kept closed was 4 ms, giving a total period of 5 ms. To check the value of spike time and the expected amplified signal going to the valve (Fig. 4.10 bottom left), a digital oscilloscope was used with 10x probes connected to Terminal 6 and Terminal 5 of the spike and hold driver with the valve connected. The difference between the two terminals concluded that the valve was receiving the optimum voltages and not overheating at high operating frequencies. The final test on the valve was done by measuring the mean flow rate of nitrogen with the same duty cycle (50%) and different operating frequencies (10 Hz to 1000 Hz). It was found that the mean flow rate decreased by about 10% when the time that the valve was kept open was less than 1 ms, corresponding the case with 1000 Hz pulsing frequency and 50% duty cycle where the time the valve kept open was 0.5 ms. It should be mentioned that this test was necessary in that it enabled us to know the condition at which the VHS valve started to response slower to the flow field. In this study, the most extreme condition was with 200 Hz and 20% duty cycle. The valve responded well in this condition.

4.4.9 Field of View for the Imaging System

The ICCD camera imitated a standard 35 mm camera for two-dimensional imaging. The field of view at a given distance can be expressed by the following expression and depicted in Fig. 4.11.

$$M = \frac{FD}{(D-B)^2} \tag{4-6}$$

where D is the distance between the object and the intensifier photocathode (400 mm), B is 46.5 mm for F-mount, F is the focal length of the lens (50mm), S is the photocathode horizontal or vertical dimension, O is the field of view diameter covered at a distance D, and M is the magnification, given by, $M = \frac{S}{O}$. Magnification was found to be 0.160048 using the above expression.

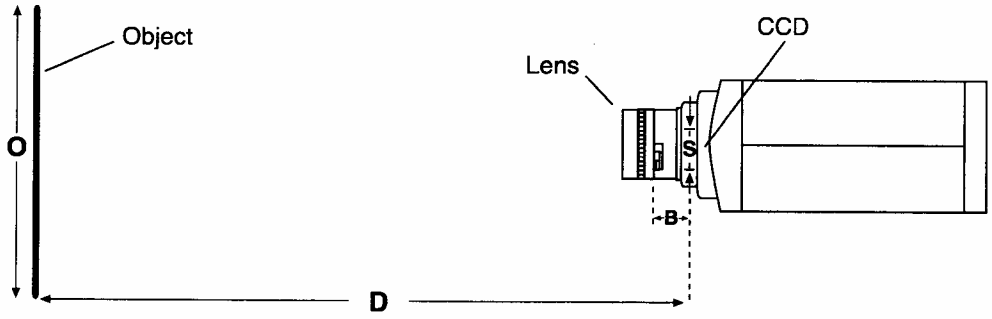

Figure 4.11 Imaging field of view for ICCD camera

Since the measurement of distances could produce human error, a more precise way of finding the magnification is by means of using a calibration target. The calibration target by Dantec Dynamics (190 mm x 270 mm with 5 mm diameter white dots on a black background with 20 mm dot spacing) was placed on top of the burner center with white dots facing the camera. The laser sheet passed through this front surface and illuminated it. The image was analyzed to give the histogram values shown in Fig. 4.12. The pixels are in the axial direction and its peak points are indicators of white dots' center locations. There are a total of 5 dots in the imaging view with the following pixel locations: 229, 351, 473, 595, and 717. Since the total distance between the first and the fifth dot was 80

mm, corresponding to 488 (=717-229) pixels, each pixel is equivalent of 164 μm at the object distance. Since the ICCD camera had a 26 μm x 26 μm array, each pixel at the photocathode surface was 26 μm. Therefore, magnification was found to be 0.158537 (=26 μm /164 μm) with higher precision compared to earlier estimation, which was 0.160048. Even though these two values are very close, it would make an error of 1586 μm in calculating 1024 pixel value.

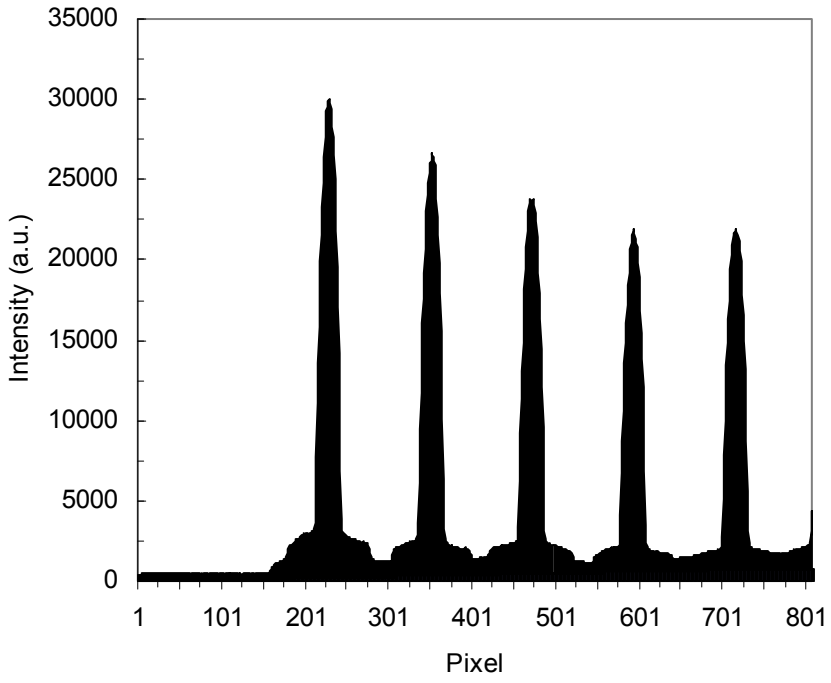

Figure 4.12 Calibration target histogram for precise magnification determination

One last note to be mentioned here is that even though the ICCD camera had 1024 pixels, the camera was able to see a circular window (only 680 pixels from pixel 180 to pixel 860) in a rectangular window (1024 x 256) due to the usage of the circular C-mount

and focusing lens. This also explains why there are no peaks (Fig. 4.12) between pixel 1 and pixel 229. Pixel 808 is the vertical position of the burner tip.

4.4.10 Timing and Triggering Mechanism for the LII Signal

In this section, two important questions were answered before the experimental setup was ready. To find the best solution to those questions was critical. A considerable amount of time was given to develop the most consistent and reliable synchronization system. The first question was " How is this gated experiment triggered?" Electrical signals were the lifeblood of the fast-gated experiment. Insertion and cable delays caused by the cables, the programmable timing generator (PTG), the detector (ICCD camera) were crucial to be identified. The value of a good oscilloscope (Tektronix Model TDS-210 with 100 MHz and 1 GS/s Sample Rate) should be addressed to be able to monitor these delays.

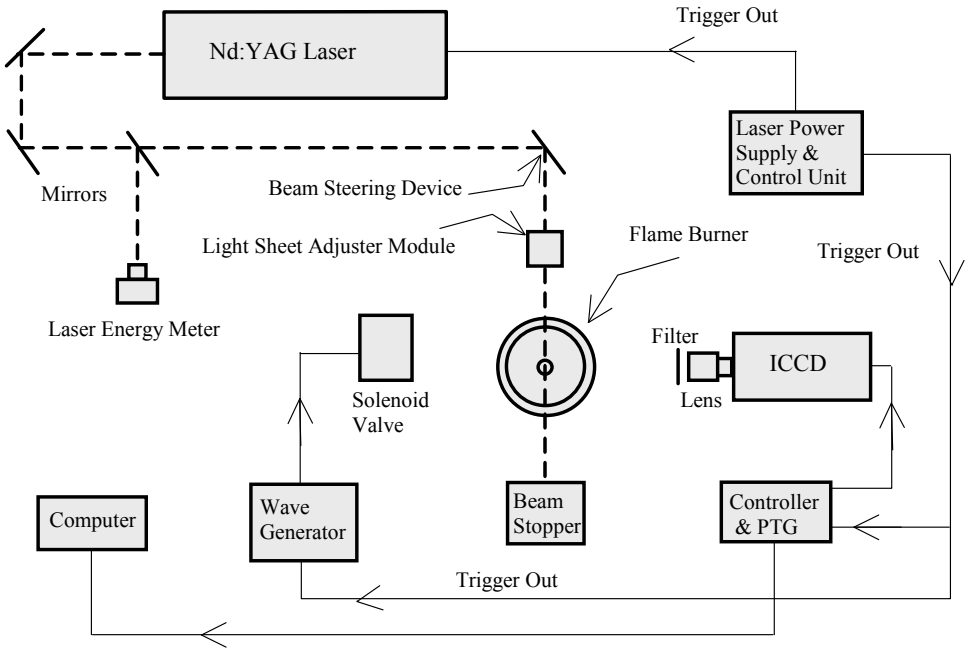

Figure 4.13 Triggering mechanism of the LII experiments

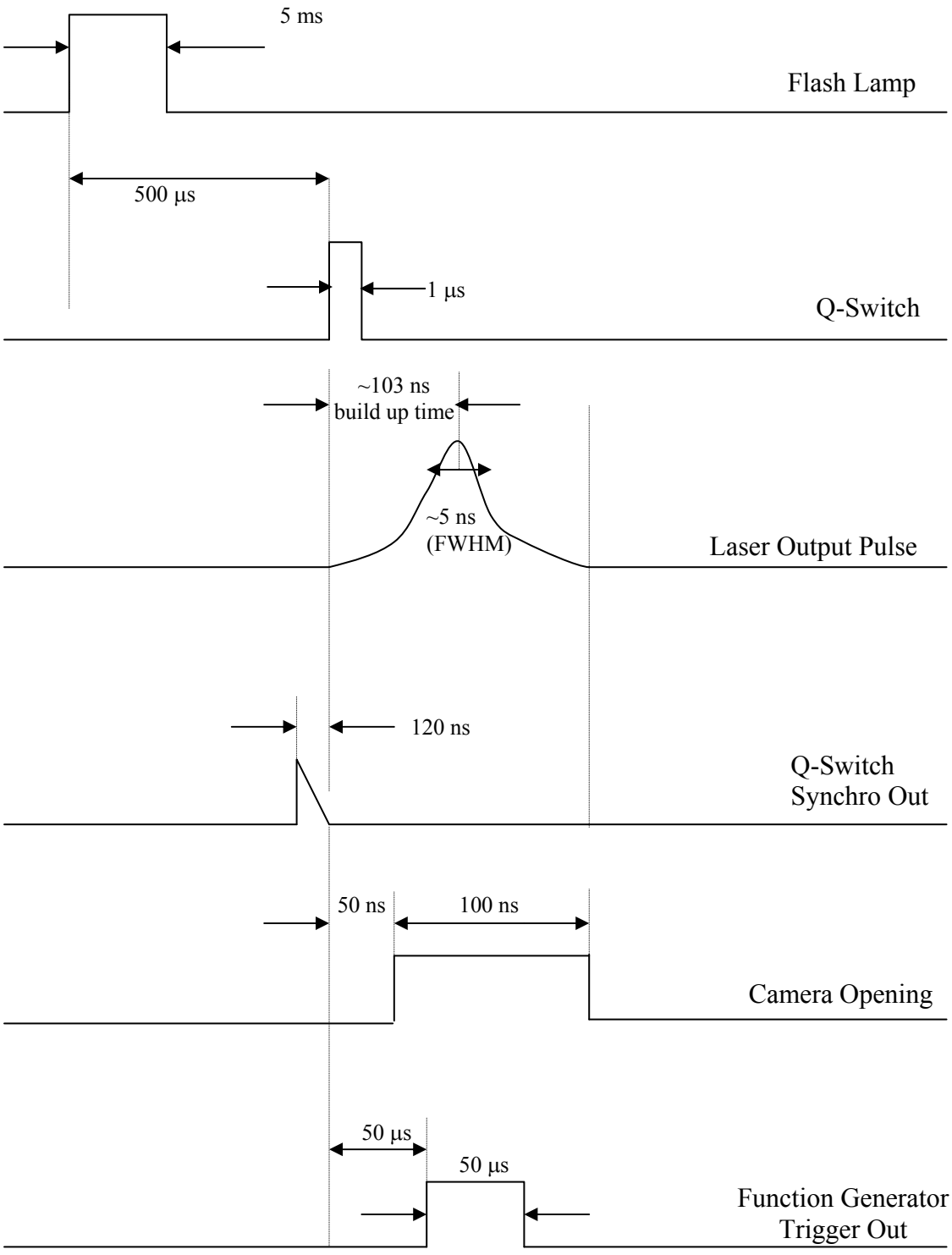

Figure 4.14 Timing diagram for components of the LII experiments

The second question was " What will be the master clock (the trigger master) in the experiment?" Because the LII experiments were gated and repetitive experiments, a Q-switch pulse from the laser was selected to be the trigger source. The optical set-up for the LII measurements was shown in the previous chapter (Fig. 3.3). Figure 4.13, however, not only shows the main components of the experimental setup (pulsed laser source, beam delivery and signal collection optics, and detector) but also the timing electronics synchronizing the laser, camera and the data acquisition system. Figure 4.13 and Figure 4.14 show the detailed representation of the trigger mechanism and the delays. In short, the Q-Switch Synchro Out signal from the laser control and cooling unit was the master clock. It triggered the laser fire, the ICCD camera control and the PTG unit, which controlled the ICCD camera, and the function generator, which provided the control signal to the VHS valve. The total delay time for the ICCD camera to open after it received the trigger signal was found to be 120 ns. For this reason, the Q-Switch Synchro Out signal was set to be released 120 ns before the Q-Switch signal. The laser fired approximately 113 ns after the Q-Switch signal, this is also called build up time of the laser pulse. The last step was signal trapping so that the laser pulse, therefore the LII signal must fall in ICCD camera gate window also shown in Fig. 4.15. The experiments were either Static Gate also referred as Repetitive-Continuous in that there was a repetitive trigger, and both gate width (GW) and gate delay (GD) were fixed (See Figure 4.14, GW=100 ns and GD=50 ns) or Swept Gate also referred as Repetitive-Sequential in that the trigger was again repetitive, gate width (GW) was fixed but gate delay (GD) was varied over the course of the measurement. The latter case was used to measure lifetime

decays. Therefore, the former case was for the LII experiments and the latter case for the TIRE-LII experiments.

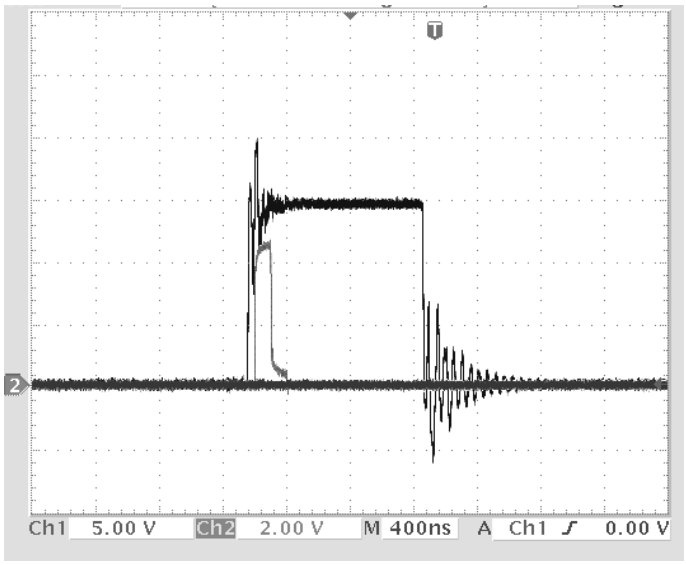

Figure 4.15 Digital oscilloscope screenshot (Ch1 is Q-Switch, Ch2 is camera opening)

4.4.11 Phase-locked Imaging

As described in the previous section, the function generator was also triggered by the Q-Switch Synchro Out signal. At the same time, the function generator provided the control signal (pulse wave) with the desired frequency and duty cycle to the VHS valve. Depending on the phase (ϕ) required, the pulse delay (%) was set on the function generator. The phase in degrees (ϕ) can be expressed as [100- Pulse Delay (%)] x 3.6°. The pulse delay couldn't be bigger than [100-Duty Cycle (%)] as a limitation of the function generator, which means the smallest phase that can be achieved after 0° would be the phase expressed as [Duty Cycle (%)] x 36°. The duty cycle for all the experimental cases was 20% (the valve opened for only 20% of the time period and closed for the

remaining 80% of the time period). Because the function generated was triggered, the specified phase was locked to the laser fire. Therefore, this image is called the phase-locked image. The delay caused by the function generator was found to be -50 μs, -35 μs, -25 μs, +25 μs, +100 μs for 200 Hz, 100 Hz, 50 Hz, 20 Hz and 10 Hz pulsing frequencies, respectively. These delays were negligible compared to the period of each corresponding pulsation (5 ms for maximum frequency and 100 ms for minimum frequency). The phase locked images for the pulsed flames revealed the entire motion process during one pulsation period with the phases ($\phi = 0^o$, 72^o, 90^o, 135^o, 180^o, 225^o, 270^o, 315^o and 360^o). Figure 4.16 shows the monitoring of the control signal with the Q-Switch signal for three different phase-locked cases, namely, 0° (top image), 72° (middle image), and 180° (bottom image). The phase-locked images obtained by the ICCD camera were compared to the ones captured by the high-speed camera images to assure that the images were phase-locked and repeatable, one after another. To do that, the high-speed camera was used to capture 1000 consecutive images 1 ms apart from each other for all the studied frequencies. From these images, it also was found that the period of all cases perfectly matched the control frequency of the function generator. In other words, every period repeated itself over and over again for every other 10 images for 100 Hz, 20 images for 50 Hz, and 100 images for 10 Hz, because every image followed the next one in 1 ms.

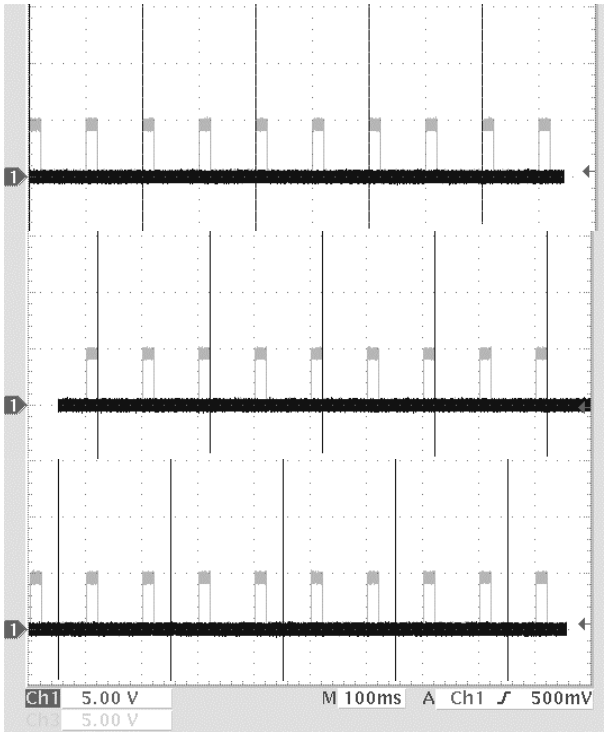

Figure 4.16 Digital oscilloscope screenshot (Ch1 is the Q-Switch, Ch2 is control signal for theVHS valve)

4.5 Experimental Steps

After performing the previous tests and calibrations, routine experiments were initiated. The basic experimental steps will be reviewed in this section.

- The laser safety panel arm was lifted activating the laser interlocks on the door and "Laser in Use" fixtures inside and outside the lab.
- Mirrors and lenses were cleaned with lens cleaning paper to swipe the dust from the surfaces before the laser is fired.
- The Nd:YAG pump laser was made ready to run by making sure that there was no system interlock. An additional 30 minutes of warmup time was given after the temperature lock was achieved before taking the data. Laser remote control was

used to set the following parameters: QS-out=120 ns (before QS), FL-QS delay= 270 μs, F/# =2 (for 5 Hz pulsing frequency). The laser sheet shape was checked by taking a burn spot on special laser burn paper along with its location and orientation. The eye level laser barrier with the laser window was placed in between the optical table and the computer, preventing any possible reflection to the user eye. The camera controller with PTG, energy meter, function generator, power supplies of spike and hold drive circuit, digital oscilloscope and the computer (WinView/32 software) were turned on.

- For steady flame, the function generator duty cycle was set to 100%. For unsteady flames, the duty cycle was set to 20% along with the desired pulsing frequency.
- The fuel and air lines were opened. The flame was ignited by using a propane gas torch. 30 minutes of time was given to the burner to reach steady state conditions. The visible flame height was adjusted by using the high-accuracy fuel flow meter and the observed real time on WinSpec/32 software window.
- The WinView/32 operating parameters were set as follows: (GG=255, GW=100 ns, GD=52 ns, Δt=200 ms (for 5 Hz), Gates for exposure=2). Before images were saved by WinView/32 software, an additional 30 minutes was given after temperature lock was achieved for complete stabilization of the ICCD camera.
- The Q-Switch signal, the camera opening signal, and the control signal for the VHS valve were always monitored with the oscilloscope during the experiments. The laser energy per pulse was checked before, during, and after the experiments.

CHAPTER V

DATA ANALYSIS AND RESULTS

5.1 Introduction

The results from measurements taken in steady and pulsed laminar ethylene diffusion flames are presented here. Measurements were acquired with pointwise detection using a spectrometer with CCD and with two-dimensional imaging using the ICCD camera. The ICCD images yield the laser-induced incandescence (LII) signals across the entire flame. Excitation of LII was achieved using the second harmonic (532 nm) output of the Nd:YAG laser. Post flame soot aerosol measurements acquired with the aerosol monitor at the post flame region in the case of observed emission of smoke from pulsed ethylene flames are also presented. In addition to the experimental methods and measurement techniques presented in Chapter 3 and Chapter 4, a number of issues regarding the LII of soot are included in this chapter.

5.2 Spectral Detection

5.2.1 Spectrometer Calibration

A mercury lamp (Roper Scientific Model MS-416) was used for wavelength calibration purposes. The mercury lamp was mounted on a flange that matched the slit body of the spectrometer. It was used in a normal laboratory environment in still air. There are many lines introduced by mercury, including 253.7 nm, 312.5 nm, 365.0 nm, 404.7 nm, 435.8 nm, 546.1 nm, and 579.0 nm wavelengths. The Spectrasense software was used to do the calibration observing peak intensities and matching them with known

peak wavelengths with very narrow bandwidths mentioned above. The results are given in Table 5.1 and shown in Appendix A.1.

Table 5.1 Mercury lamp peaks (nm) and calibrated spectrometer scan peaks (nm)

Peak #	P1	P2	P3	P4	P5	P6	P7
Mercury Lamp	253.7	312.5	365.0	404.7	435.8	546.1	579.0
Spectrometer	253.3	312.5	364.6	404.2	435.3	545.5	578.2

5.2.2 Filter Transmittance

With the gate gain of the camera being equal to 128 (nominal gain), the laser light scattered from the burner tip was recorded with and without the 600 nm interference filter with 80 nm nominal bandwidth. After corrected by dark charge of the camera, this filter was found to let about 3% of scattered light pass through it. In other words, the transmittance of the filter was 3% at 532 nm. Because scattering was contaminating the LII signal from the flame, elimination of this scattering light was crucial. This filter was changed with the filter of 607 nm center wavelength and 36 nm nominal bandwidth. The same test was repeated.The transmittance was negligible, less than 0.06 %. The combined transmissivity (detector cathode sensitivity multiplied by filter transmissivity) curve, which defined the center wavelength and spectral range of detection for the LII experiments, was obtained for the interference filter used (peak transmission at 600 nm with 588.8-624.8 FWHM coordinates) and is given in Fig. 5.1.

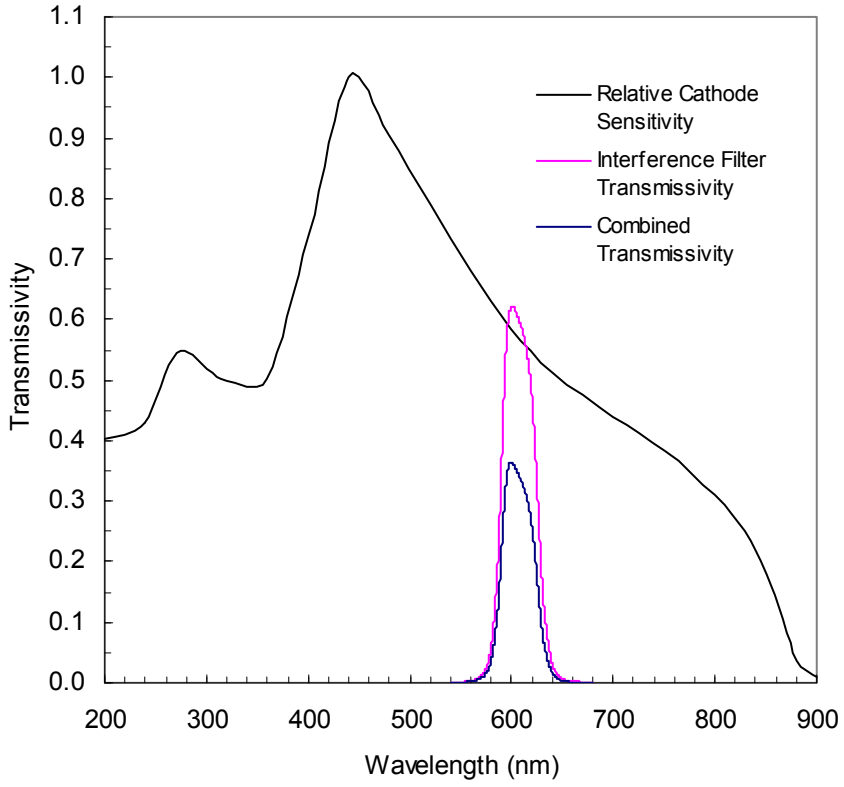

Figure 5.1 The combined transmissivity (detector cathode sensitivity multiplied by filter transmissivity) curve for ICCD camera

5.2.3 C_2 Interference

As a part of laser heating, some of the laser energy (located around the center of the Gaussian laser sheet) produces molecular carbon species (C_2) from the surface of soot particles near or above the vaporization temperature of soot. The laser-induced fluorescence in C_2 (C_2 LIF) from laser vaporized soot and/or laser-induced fluorescence of the C_2 radicals, which are already present in the flame, can be strong for high intensity excitation. On the other hand, emission from the Swan bands of C_2 is on the verge of detectability with low intensity cases and delayed detection cases. In comparing the

fundamental (1064 nm) and doubled (532 nm) Nd:YAG beams, there is a big reduction in C_2 interference for infrared excitation. C_2 interference changes linearly with laser fluence while the LII signal comes to a threshold value. It will affect the overall signal detected more than LII at detection near the emitting C_2 bands. In other words, the C_2 signal does not necessarily behave like the LII signal and it should be treated as a contamination of the LII signal. This suggests the IR excitation for LII purposes to avoid the C_2 interference. However, visible excitation (532 nm) is used for the LII experiments and the LII signal had to be carefully detected after the LII spectra investigation and filter transmittance combined with the detector cathode sensitivity curve. The peak laser fluence for the Gaussian sheet in the experiments was 0.07 mJ/cm^2, which was slightly under the onset of soot particle vaporization (0.1 to 0.2 mJ/cm^2 are reported in the literature). The six sequences in the Swan bands of C_2 between violet and red spectra are namely, 438.3 nm, 473.7 nm, 516.5 nm, 563.6 nm, 619.1 nm, and 667.7 nm (Herzberg 1950; Straughan and Walker 1976). There is an intensity distribution in these band systems and some of the Swan bands can differ considerably. A spectrometer scan was conducted for the ethylene flame and given in Appendix A.2. It showed three peaks at 470 nm, 514 nm, and 567 nm, revealing the presence of significant C_2 emission in the $\Delta v=+1$, $\Delta v=0$, and $\Delta v=-1$ Swan bands at 473.7 nm, 516.5 nm, and 563.6 nm, respectively. This was also suggested by Shaddix and Smyth (1996) and Wainner and Seitzman (1999). Very low C_2 emission (just on the verge of detectability) was observed at 438 nm and 619 nm corresponding to $\Delta v=+2$ (438.3 nm), and $\Delta v=-2$ (619.1 nm), respectively.

5.3 Fluence Dependence

Increasing laser fluence (energy per unit area) will increase the LII signal up to some point, also referred as the LII threshold. Beyond this value, the LII signal level decreases with further increase of the laser intensity. Even though this is the trend expected from the LII signal by the LII models using the tophat profile, because of the Gaussian nature of the lasers and the different shape of the laser formed for different experiments (near tophat profile, Gaussian beam, Gaussian sheet), different behaviors of LII signals were reported in the literature, such as, signal levels that are nearly constant after the threshold (laser sheet), increasing beyond the threshold value with a lower rate than below threshold (laser beam), or decreasing much more rapidly after the threshold (near tophat profile). The Gaussian sheet has nearly a Gaussian distribution, expressed by Eq.4-5. The Gaussian beam has nearly a Gaussian distribution as well, expressed in the following form;

$$F(r) = F_0 \cdot e^{-2r^2/w^2} \tag{5-1}$$

where $F(r)$ is the laser fluence, F_0 is the laser fluence at the center of laser beam (2 times the value of the average fluence value), w is the radius where intensity falls to $1/e^2$ (or 0.135) of its centerline (r =0) value. The laser beam radius, w, was approximately 0.164 mm. Nearly 86% of the total energy is contained within the radius w.

In the literature, different terms are used to describe laser fluence, such as, laser energy fluence, peak laser energy fluence, and the laser power fluence. The results from the laser intensity dependence of LII signal are given with the laser energy per pulse. The desired parameters can further be calculated using the temporal and spatial profile of the

laser given in Section 4.4.6. The LII signals, integrated over 100 ns, and normalized with the minimum detectable LII signal which was set by the detection system are plotted at HAB=40 mm and at the annular region of 88 mm steady laminar ethylene flame where the peak LII signal occurs. This position corresponds to the maximum soot volume fraction for the overall flame. Figure 5.2 shows the LII signal trend for the laser beam. Figure 5.3 represents the experimental result for the laser sheet from averaging ten data points.

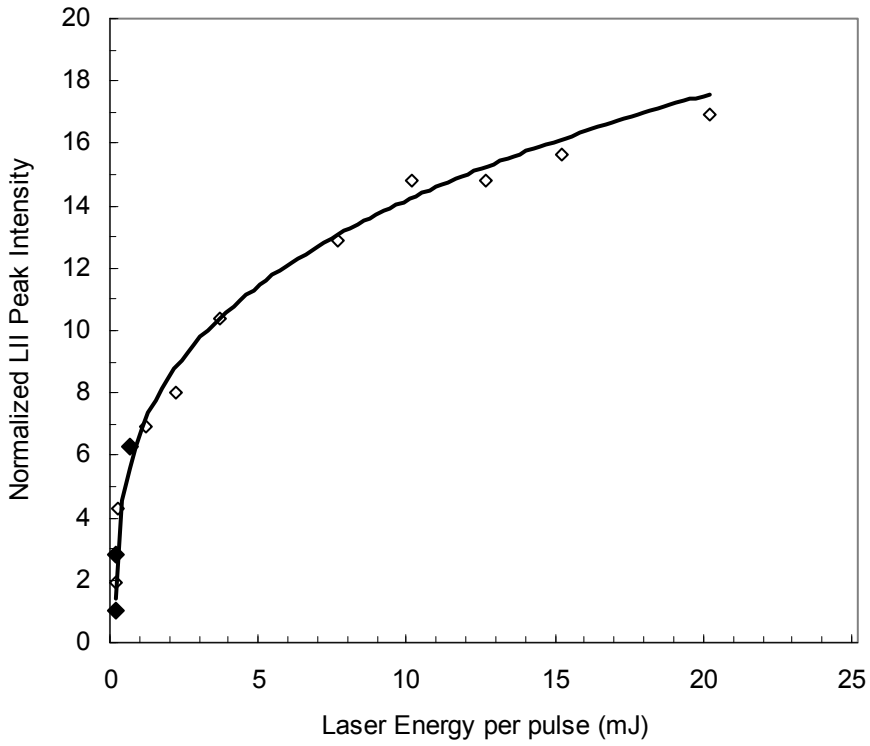

Figure 5.2 Fluence dependence of LII measured at 40 mm in ethylene/air flame with the laser beam

The first filled point on the plot corresponds to the laser energy (0.005 mJ) where the first detectable LII signal was achieved. The second filled point corresponds to the critical fluence (0.1 J/cm^2) for the onset of soot particle vaporization. The laser energy at this point is 0.02 mJ. The third filled point on the plot corresponds to fluence (≥2 J/cm^2) in order to have a small change in the LII signal for absolute changes in laser fluence. The laser energy at this point is 0.5 mJ. The solid line shown in Fig. 5.2 is a power fit of data for fluences from 0.024 J/cm^2 (0.005 mJ per pulse); the fit follows the expression: signal α fluence$^{0.30}$. This value was very close to 0.34, which was suggested by Shaddix and Smyth (1996).

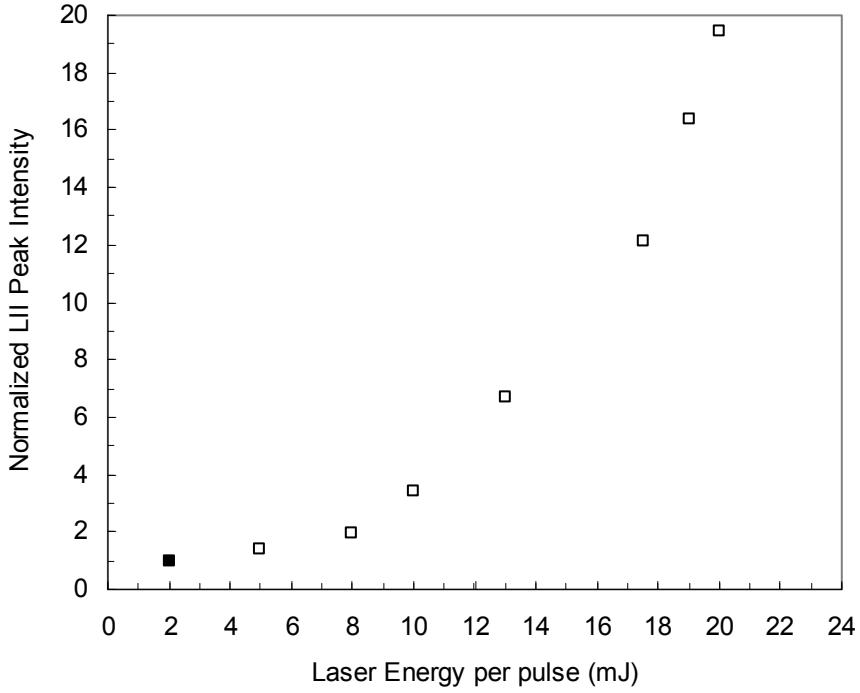

Figure 5.3 Fluence dependence of LII measured at 40 mm in ethylene/air flame with the laser sheet

Again, the first filled point in Fig. 5.3 corresponds to the laser energy (2 mJ) where first detectable LII signal was achieved. This value was 400 times the laser energy required from the laser beam as the laser fluences (energy per unit area) drastically dropped because of the change in the length of the laser (>300 times) for the laser sheet case. The last point in Fig. 5.3 corresponds to 0.07 J/cm^2, which is very close to the critical fluence (10^7 W/cm^2 for 10 ns pulse width Nd:YAG laser or equivalent to 0.1 J/cm^2) for the onset of soot particle vaporization (Bengtsson and Alden 1995). The laser sheet with 20 mJ output was the maximum allowable energy for the optical setup because of the laser energy threshold value of dialectric mirrors, beam steering device, and the optical coating of the laser sheet adjuster module. Because of the low laser fluence obtained with the laser sheet, the laser heated particles just near their vaporization temperature (≤4000 K) and the LII signals had a stronger (linear) dependence to laser energy. This dependence was analyzed and given as an experimental uncertainty in Chapter 6.

5.4 Detector Parameters

The fiber coupled ICCD camera (PI·MAX 1024RB) had the option of operating the intensifier at an extremely high net gain, greatly intensifying the light reaching the CCD. The advantage of a high sensitivity ICCD is not only that it provided a higher S/N ratio with a reasonably sized signal, but that it allowed the experiment to be optimized to the condition where there is enough signal to measure (low heights in the flame). Because of the damage threshold of mirrors and the optical coating on the sheet adjuster module, 20 mJ per pulse was the energy limit for the experiments. Peak fluence was slightly under

0.1 mJ/cm^2 bringing the soot primary particles near their vaporization temperature. The LII signal detected was low and the signal to noise ratio (S/N) was very poor. To optimize the experiment, the camera gate gain changed from medium value (128) to the highest value (255), while the detector became around 35 times more sensitive, which can be seen in Fig. 5.4. Due to the high camera gain, the CCD cooling temperature was locked down to the minimum degree (-20°C) to keep the dark charge the same. The highest LII signal (40mm HAB) was within the dynamic range of the ICCD because the available signal should just fill the detector's dynamic range for maximum S/N. This optimization procedure was achieved with the maximum allowable laser energy of 20 mJ per pulse of the beam (less than the dielectric mirrors threshold value) at the maximum soot volume fraction point of 88 mm ethylene flame (at z = 40 mm and annular region), and the maximum LII signal detected was 1300 (a.u.) with a gate gain of 128. This value was very comparable to the dark charge. Considering the fact that low in the flame, soot volume fraction was very low, the gate gain of the camera was increased from 128 to 160, and then to 200 and finally to 255 (maximum). The LII signal increased from 1300 (a.u.) to 2600 (a.u.), and then to 6900 (a.u.), and finally to 29000 (a.u.). A detector linearity check at this highest gain (GG=255) was performed and explained in Section 4.4.7. The linear response region of ICCD camera was determined to be from 900 to 45,000 counts (or a dynamic range of 50) for this gain setting. Between 300 and 900 counts, detector had a slight non-linear response due to phosphor nonlinearity. It should be noted that the dark charge was 437 (a.u.) with a standard deviation of 32 (a.u.) in the region of interest. The background in the presence of the laser sheet with no flame in the region of interest was 476 (a.u.) with a standard deviation of 137 (a.u.).

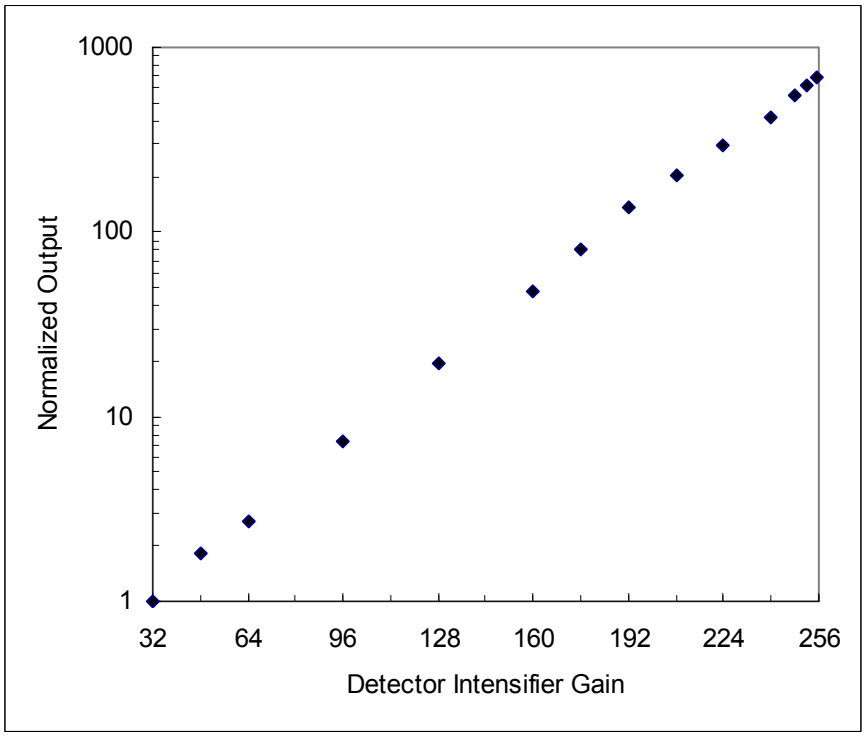

Figure 5.4 Intensifier gain effect on sensitivity of the ICCD camera

The other key parameters with the ICCD camera were the gate width and gate delay along with the other operating parameter that was controlled by the WinView/32 software. The gate delay was the determining factor for synchronization with the laser fire and the gate width was the controlling factor for how long the prompt LII signal would be integrated by the ICCD camera. The details of the decisions made on the set value of these parameters are given in Section 4.4.10. The key parameters are given in Table 5.2. Appendix B gives extensive information for all the parameters.

Table 5.2 Summary of key parameters set for LII experiments

Part Name / Condition	Controller	Parameter	Set Value
Excitation Wavelength	Nd:YAG Laser	Second Harmonic Module	532 nm
Detection Wavelength	Interference Filter	Nominal Bandwidth 36nm	607 mn
Laser Shape	L.S. Adjuster Module	Laser Sheet	0.6mmx100mm
Nd:YAG Laser	Beam Attenuator	Energy per pulse	20 mJ
Nd:YAG Laser	Remote Control	QS-Out Delay	-120 ns
Nd:YAG Laser	Remote Control	F/# (frequency)	2 (5 Hz)
Nd:YAG Laser	Remote Control	FL-QS Delay	270 μs
ICCD Camera	WinView/32	Gate Gain	255
ICCD Camera	WinView/32	Gate Width	100 ns
ICCD Camera	WinView/32	Gate Delay	52 ns
ICCD Camera	WinView/32	Temperature Lock	-20 °C
ICCD Camera	WinView/32	Exposure Time	200 ms
ICCD Camera	WinView/32	Gates per Exposure	2
Function Generator	Pulsing Frequency	Frequency (Hz)	10,15,20,30,50,100,200
Function Generator	Duty Cycle	High (%)	20
Function Generator	Phase	Delay (%)	0,12.5,25,37.5,50,62.5,75,80

5.5 Soot Volume Fraction Calibration

The LII signals were treated in the following order. First, the LII signals were binned in the radial direction to give an effective resolution of 0.381 mm. Radial cross sections at several axial locations (from HAB=10 mm to HAB=70 mm) were then obtained. This was followed by corrections to account for the effects of the laser beam extinction (extinction of the incident laser beam through the flame due to high soot concentrations) and for the LII signal extinction (also called LII signal trapping to account for the extinction of the LII signal itself). The 3pt.-Abel inversion technique, which was applied to the transmittance data for the 88 mm ethylene flame (Sapmaz 2000), was used to find the symmetrical extinction coefficients, K_{ext} (mm^{-1}). A further detailed analysis of this inversion is given in Appendix C.1. By assuming $K_{abs} \cong K_{ext}$

(assuming that soot particles are in the Rayleigh limit, wherein particle scattering is negligible compared to absorption), and knowing that $K_{ext}>>K_{scat}$, the soot volume fraction, f_v, can be obtained approximately from extinction measurements as:

$$f_v = \lambda K_{ext} / (6\pi E(m)) \tag{5.2}$$

Where λ is the wavelength of the laser, $E(m) = -Im\ (\ (m^2-1)/(m^2+2)\ )$ is a refractive index function ($m = n\text{-}i\kappa$) . It can also be expressed as:

$$E(m) = \frac{6n\kappa}{(n^2 - \kappa^2 + 2)^2 + 4n^2\kappa^2} \tag{5.3}$$

For the refractive index used in this study (m=1.90-0.55i), $E(m)$ was found to be 0.2. A computer program written in Pascal programming language (Sapmaz 2000) handled these two corrections by taking the local extinction coefficients and hteradial positions of the LII signal, and the step size (0.381 mm) associated with the extinction coefficients for the axisymmetric flame in order to calculate these correction values. It must be stated that this type of correction was only possible when there was the line-of-sight measurements of signal extinction measurements available only for the 88 mm ethylene flame. The correction factors are tabulated and presented in Appendix C.2. The maximum correction factor was 1.4 which was in the annular region at HAB=40 mm. Then, the LII signals were symmetrized (averaged about the centerline) and normalized with the overall peak signal. Finally, the LII signals were placed on a quantitative basis by calibration to extinction-derived soot volume fractions (Tomographical inversion from Argon Ion laser extinction measurements by the Three-point Abel technique and an index of refraction of

1.90-0.55i, Sapmaz 2000). The calibration point was the peak point at 40 mm height above the burner (HAB=40 mm) and the soot volume fraction value at that point (shown in Fig. 5.5) was 14 ppm.

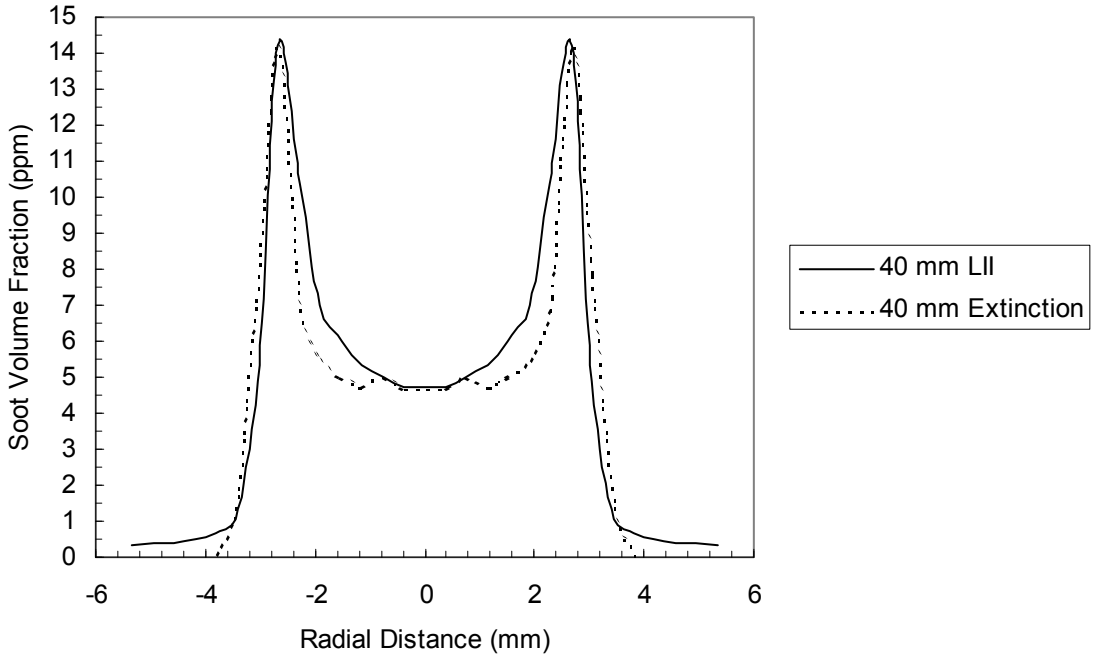

Figure 5.5 Comparison between the LII signal and the extinction-derived soot volume fraction at HAB=40 mm

There is a good agreement between the soot profiles from the LII and the extinction-derived soot volume fractions. A slightly wider profile given by extinction data is likely due to the signal averaging over the larger step size. Also, larger errors are expected from Abel inversion is towards the centerline (r =0). That is why the peak point was used to calibrate the LII data rather than using the area under curve match. The final values of the soot volume fractions are given in Fig. 5.6 for various heights.

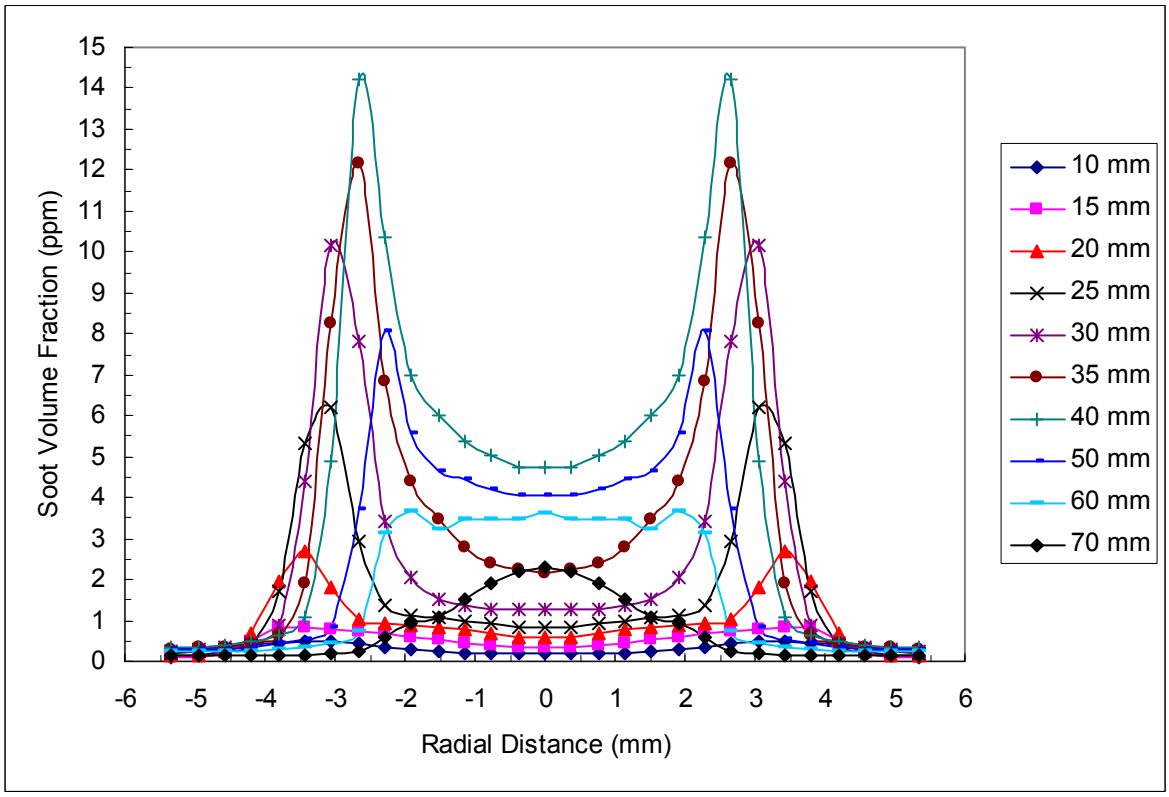

Figure 5.6 LII profiles for steady C_2H_4 flame at various axial heights

The comparisons between the LII signals with and without laser extinction and signal trapping are also given in Fig. 5.7 to show that this correction is necessary especially in the regions where there is heavy soot concentrations. There is also good agreement between the LII data presented by Shaddix and the present LII data. Figure 5.8 shows the sum of the radial LII profiles normalized with LII signal at HAB=40 mm over various heights (HAB=10, 15, 20, 30, 40, 50, 60, and 70 mm). The area under curve for both studies differ only by about 5% (our total soot volume fraction is 5% higher than Shaddix's results).

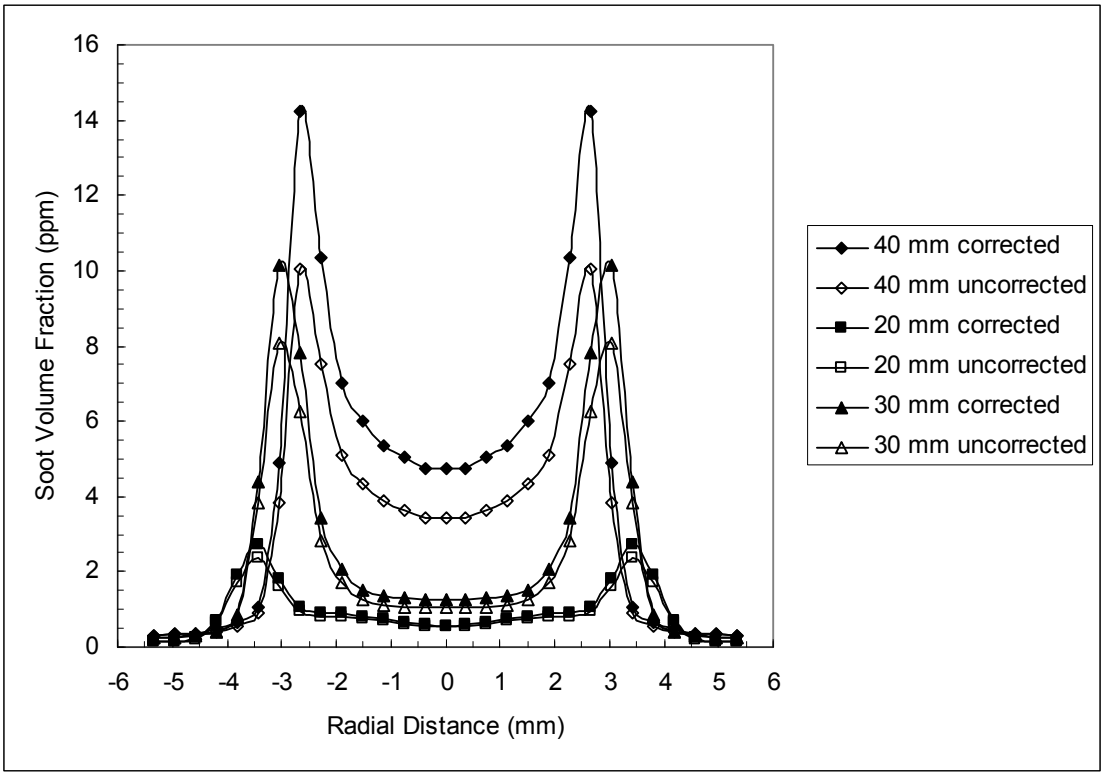

Figure 5.7 Corrected and uncorrected LII profiles for laser extinction and signal trapping at HAB=20, 30 and 40 mm

As mentioned earlier, self-correction for laser extinction and signal trapping was only possible for the 88 mm steady ethylene flame for which extinction values were available. To be able to compare the results from steady and pulsed flames with different fuel flow rates, this correction step was omitted and the results were calibrated with the calibration factor, C = 4.94185 x 10^{-4}. The LII calibration followed very similar trends with extinction-derived soot volume fraction (Equation 5.2) over soot volume fractions ranging from 0.05 ppm to 10 ppm over different effective soot particle sizes within the flames under the assumption that primary soot particle sizes remained less than 40 nm

with or without agglomerated structure in different regions of the flames (inception, growth, agglomeration, and oxidation).

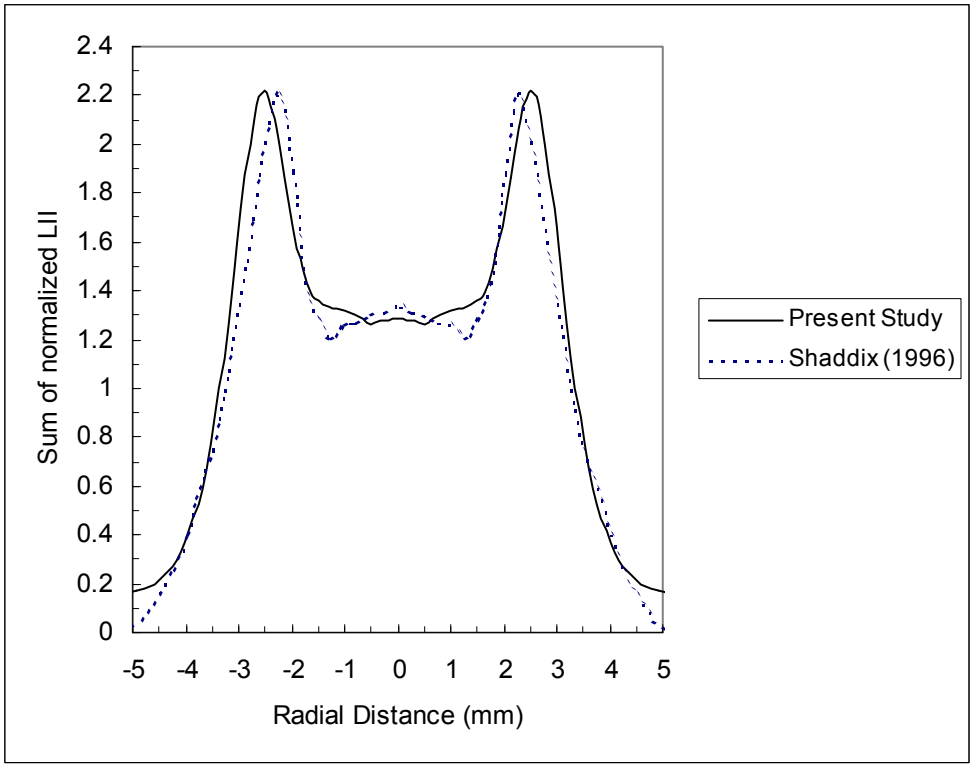

Figure 5.8 Sum of radial LII profiles normalized by HAB=40 mm over various heights (HAB=10, 15, 20, 30, 40, 50, 60, and 70 mm)

5.6 Soot Volume Fraction Measurements

Contour plots of the soot volume fraction for steady diffusion flames (E1, E2, E3, and E4) are given in Fig. 5.9, Fig. 5.10, Fig. 5.11, and Fig. 5.12. Indicated on each figure is the soot volume fraction value of each contour with axial locations from HAB=0 to HAB=100 mm and radial distances from r=-7 mm to 7 mm.

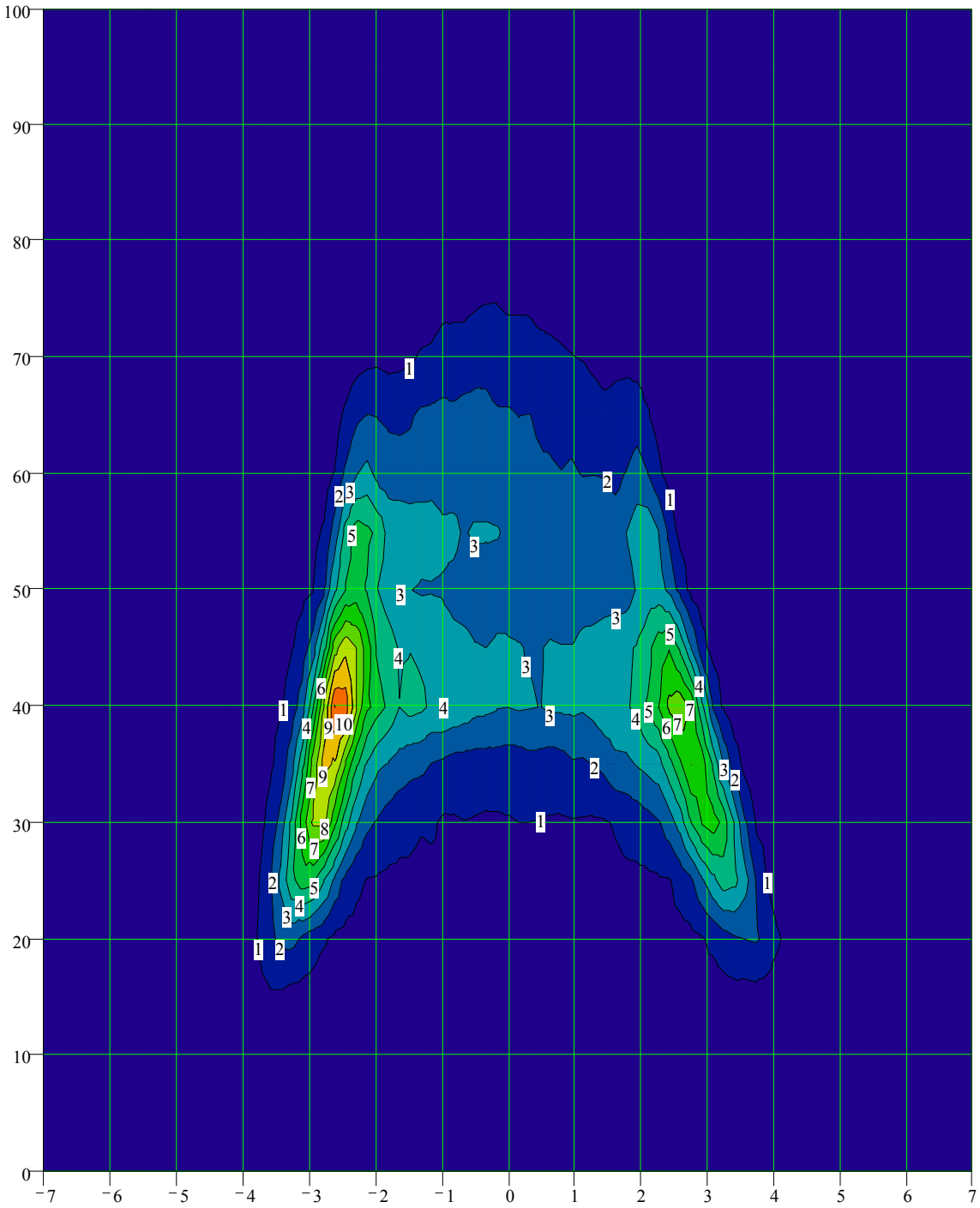

Figure 5.9 Contour plot of soot volume fraction (E1)

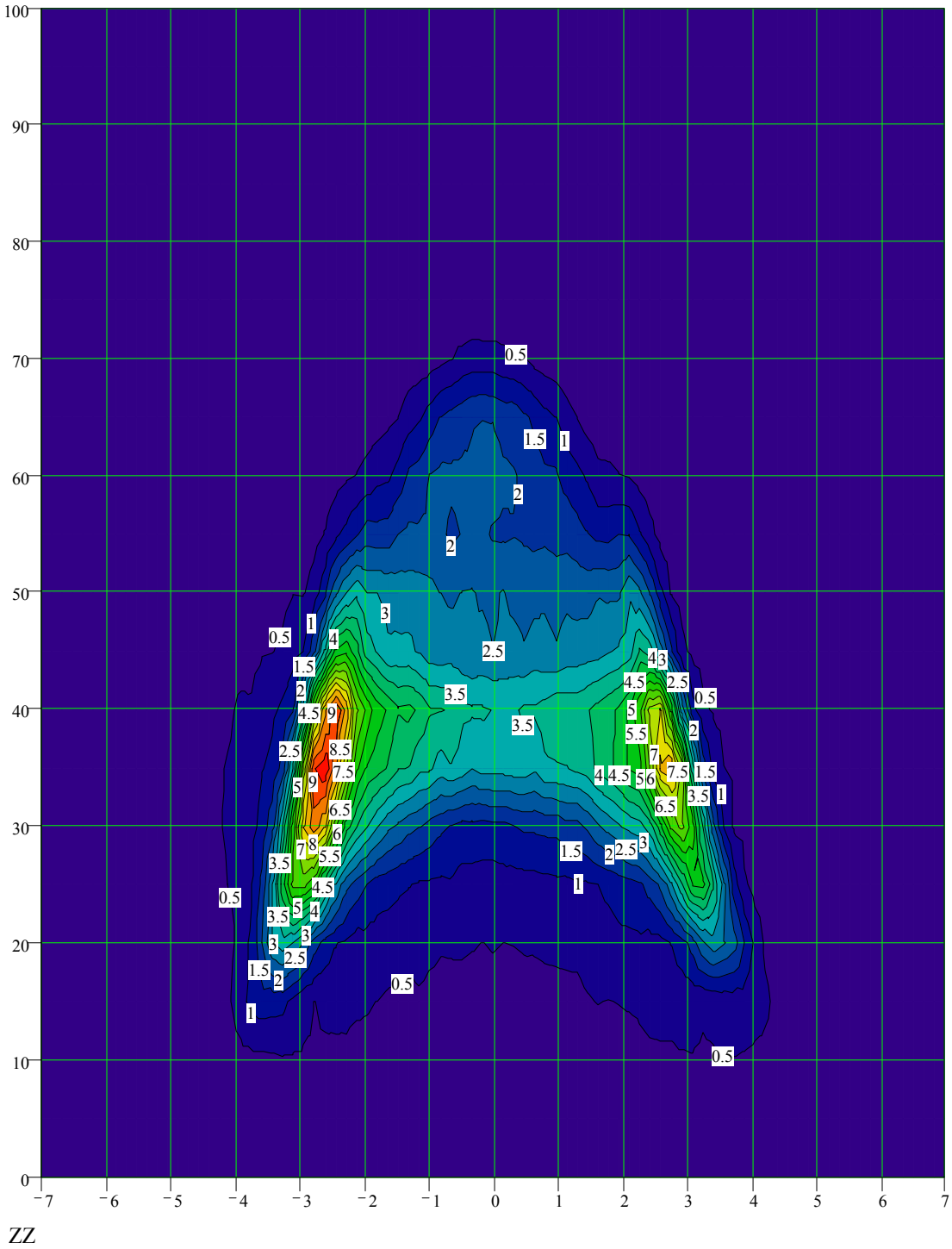

Figure 5.10 Contour plot of soot volume fraction (E2)

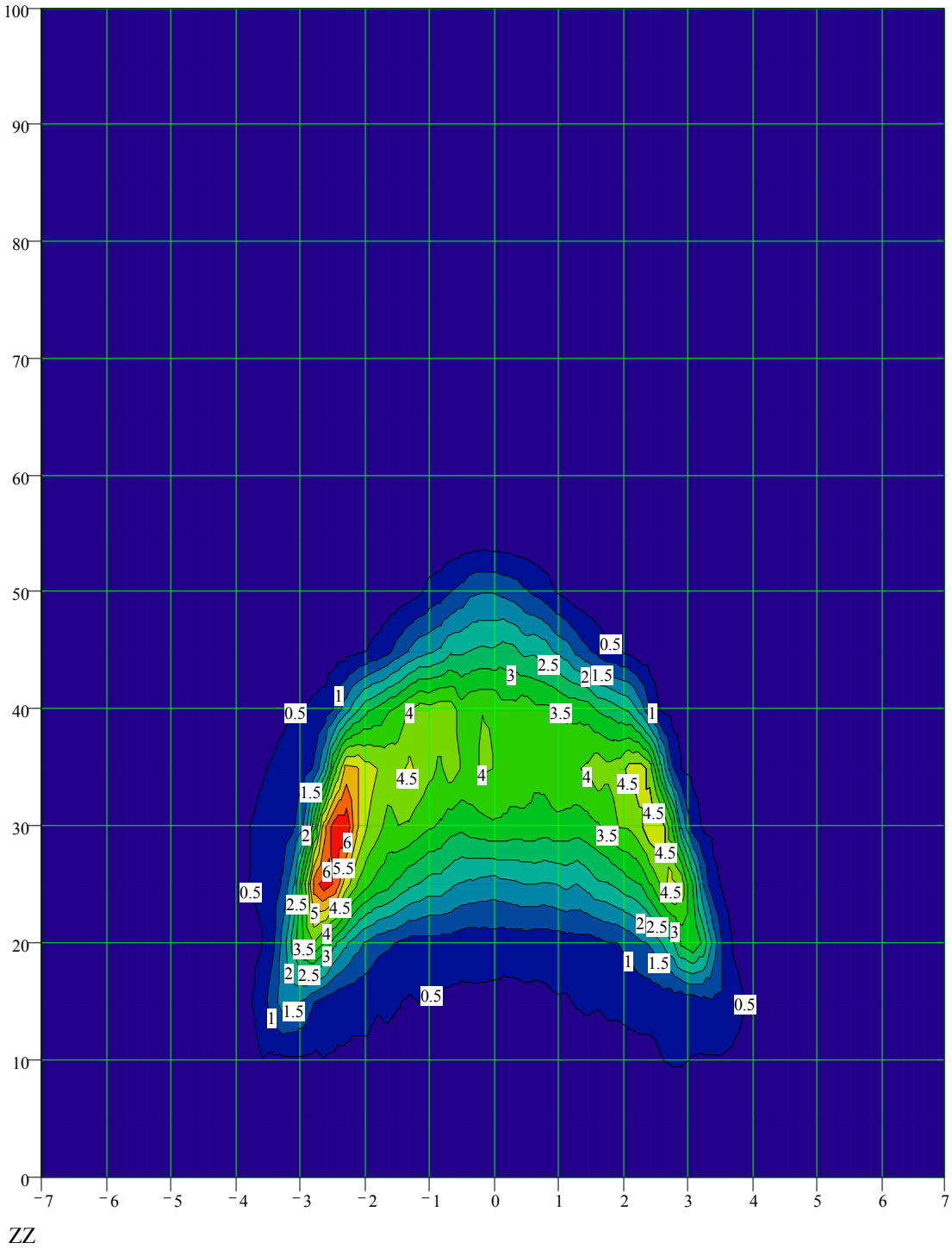

Figure 5.11 Contour plot of soot volume fraction (E3)

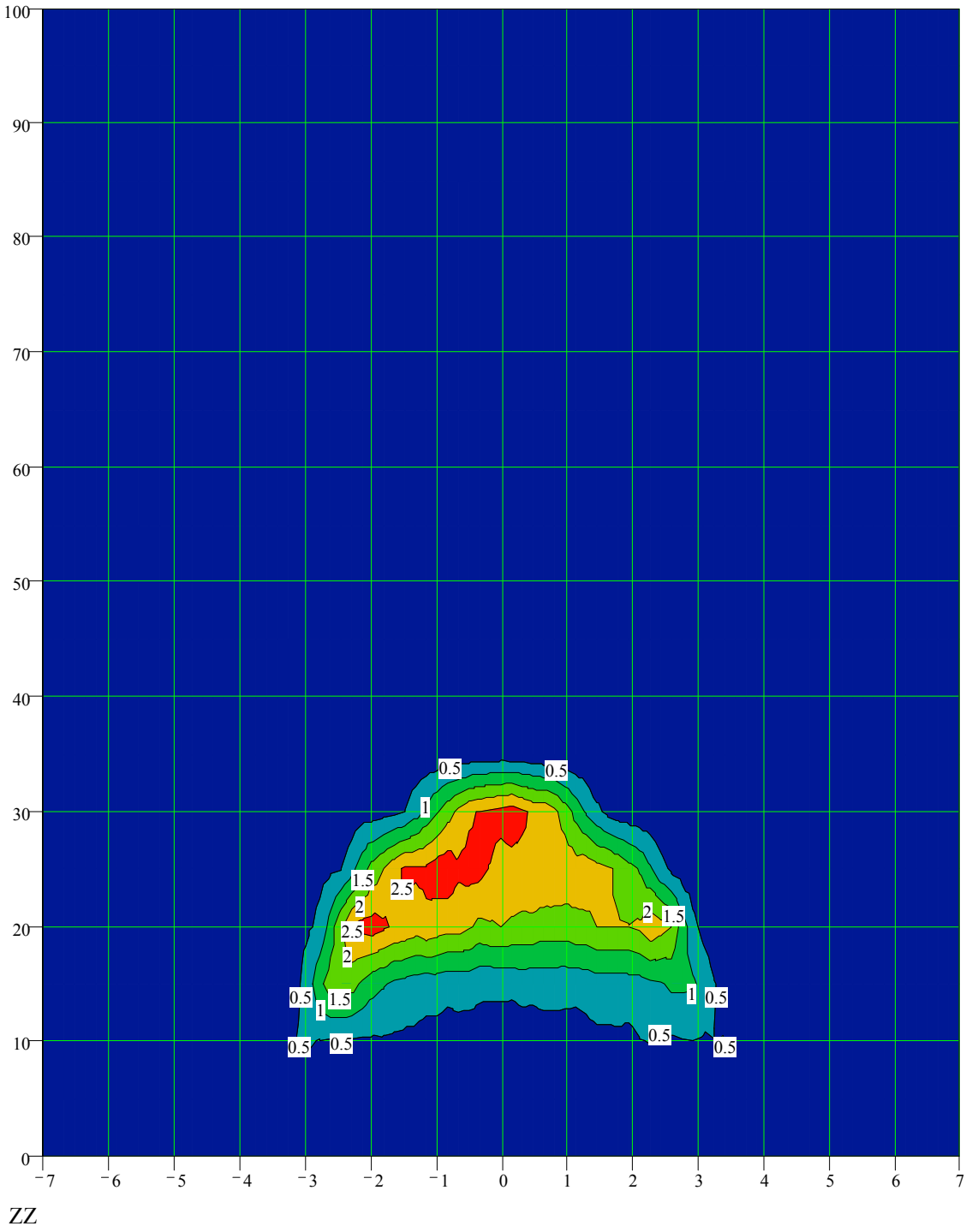

Figure 5.12 Contour plot of soot volume fraction (E4)

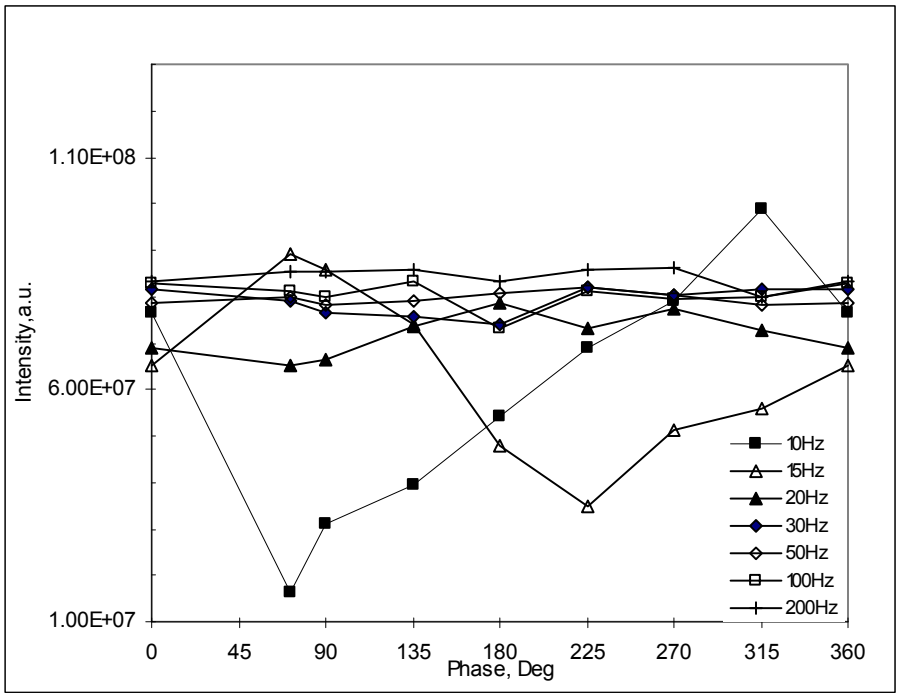

Figure 5.13 Space-integrated LII versus phases for different pulsation (E1)

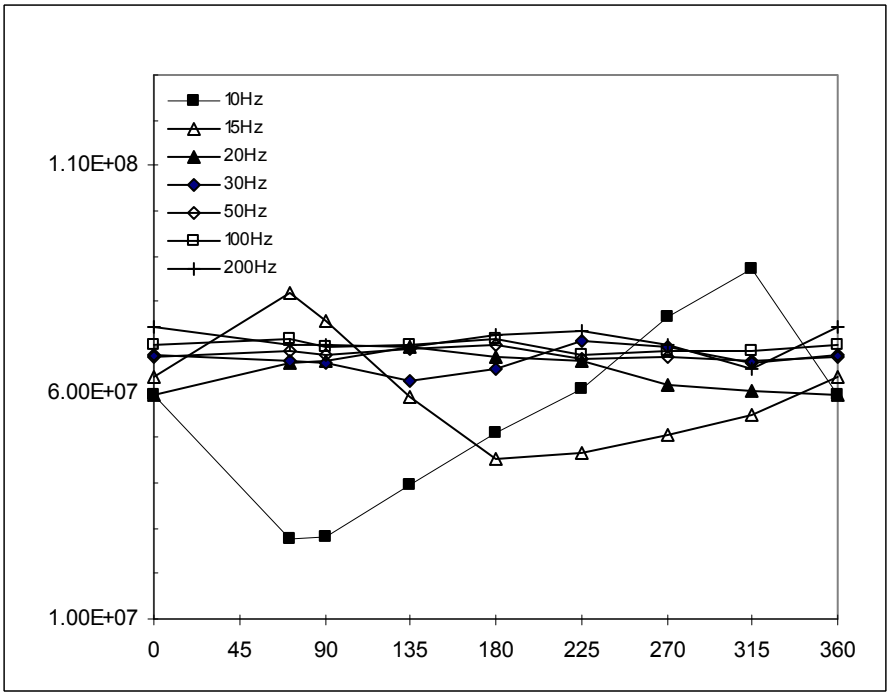

Figure 5.14 Space-integrated LII versus phases for different pulsation (E2)

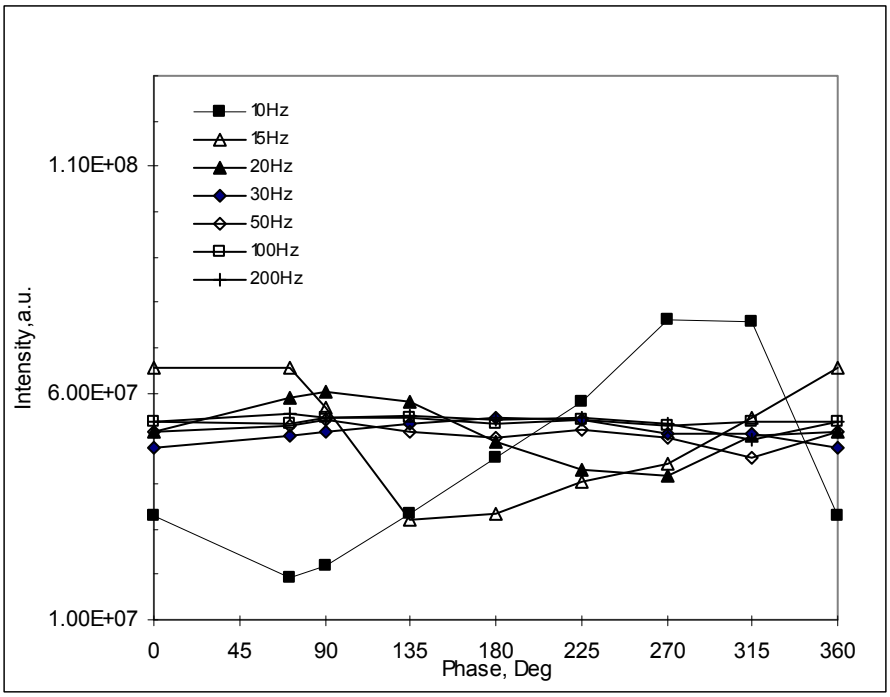

Figure 5.15 Space-integrated LII versus phases for different pulsation (E3)

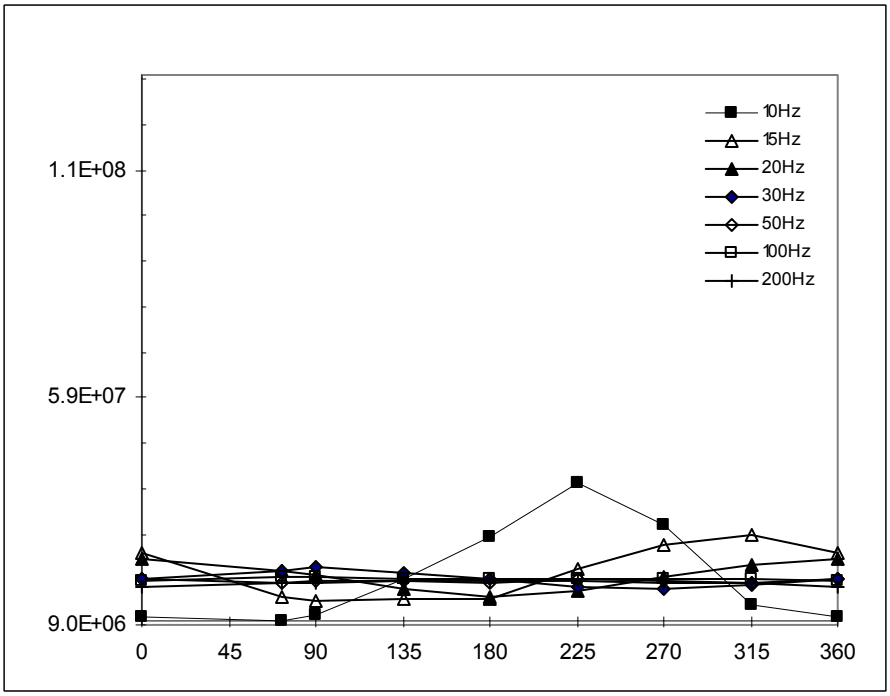

Figure 5.16 Space-integrated LII versus phases for different pulsation (E4)

Space-integrated LII versus phases for different pulsation for four fuel rates are given in Fig. 5.13, Fig. 5.14, Fig. 5.15, and Fig. 5.16. Using the information from these figures, the first maximum peak soot volume fraction of all of the peak soot volume fraction values are plotted and given in Fig. 5.17. Volume-integrated time-averaged soot volume fractions of pulsed flames is graphed and given in Fig. 5.18. The tabulated values are also given in Table 5.3 and 5.4 respectively.

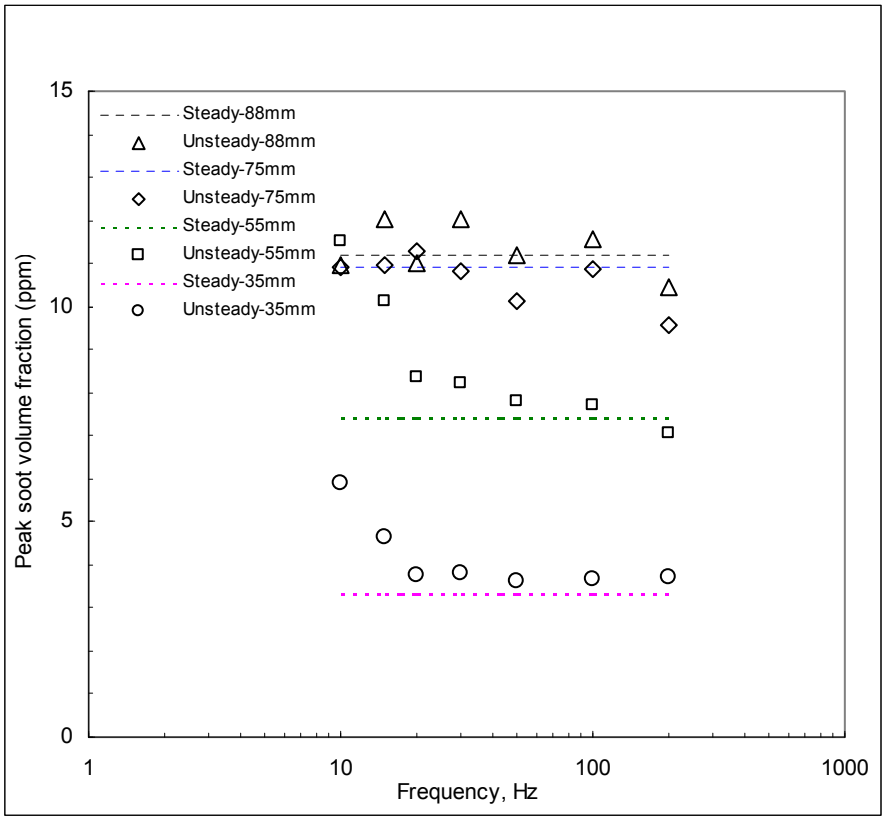

Figure 5.17 Peak soot volume fraction for studied flames for different pulsation

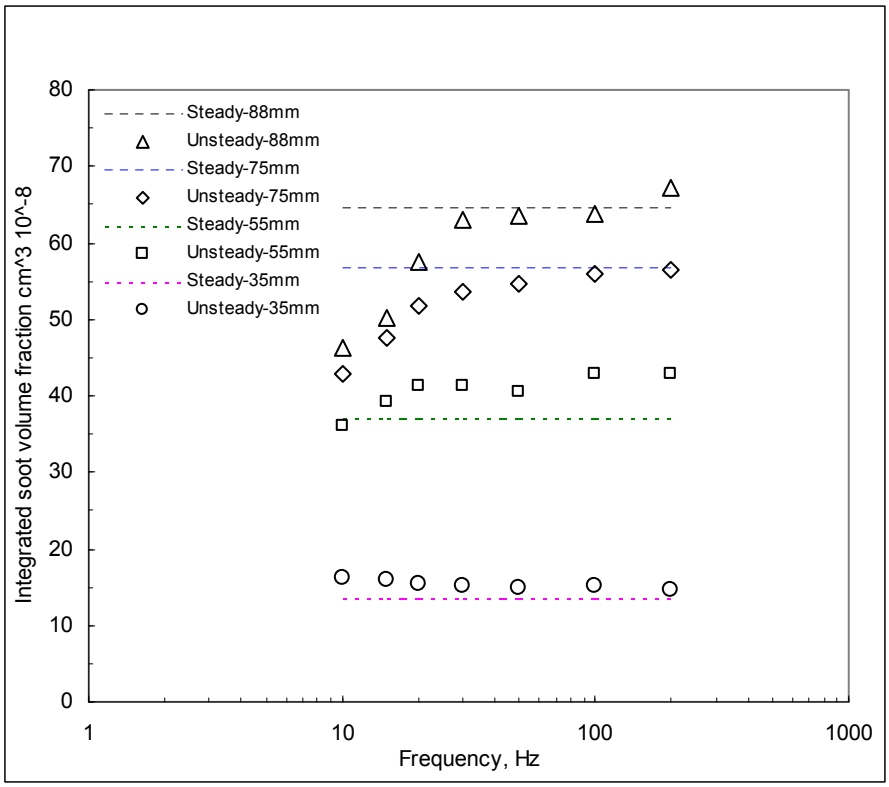

Figure 5.18 Volume-integrated time-averaged soot volume fraction for studied flames for different pulsation

Table 5.3 Peak Soot Volume Fraction in Steady and Flickering Flames f_v (10^{-6})

Flame Name	Steady flame	Unsteady flame (10Hz)	Unsteady flame (15Hz)	Unsteady flame (20Hz)	Unsteady flame (30Hz)	Unsteady flame (50Hz)	Unsteady flame (100Hz)	Unsteady flame (200Hz)
E1	11.19	10.94	12.01	10.99	12.02	11.19	11.56	10.46
E2	10.93	10.92	10.97	11.27	10.83	10.14	10.85	9.57
E3	7.45	11.54	10.12	8.38	8.20	7.80	7.72	7.05
E4	3.33	5.90	4.65	3.75	3.79	3.63	3.65	3.71

Table 5.4 Total Soot Volume Fraction in Steady and Flickering Flames (10^{-8} cm^3)

Flame Name	Steady flame	Unsteady flame (10Hz)	Unsteady flame (15Hz)	Unsteady flame (20Hz)	Unsteady flame (30Hz)	Unsteady flame (50Hz)	Unsteady flame (100Hz)	Unsteady flame (200Hz)
E1	64.55	46.22	50.19	57.40	62.92	63.51	63.86	67.21
E2	56.71	42.86	47.56	51.73	53.49	54.57	55.86	56.52
E3	37.08	36.18	39.17	41.21	41.25	40.65	42.82	42.85
E4	13.59	16.31	15.95	15.38	15.29	14.88	15.26	14.61

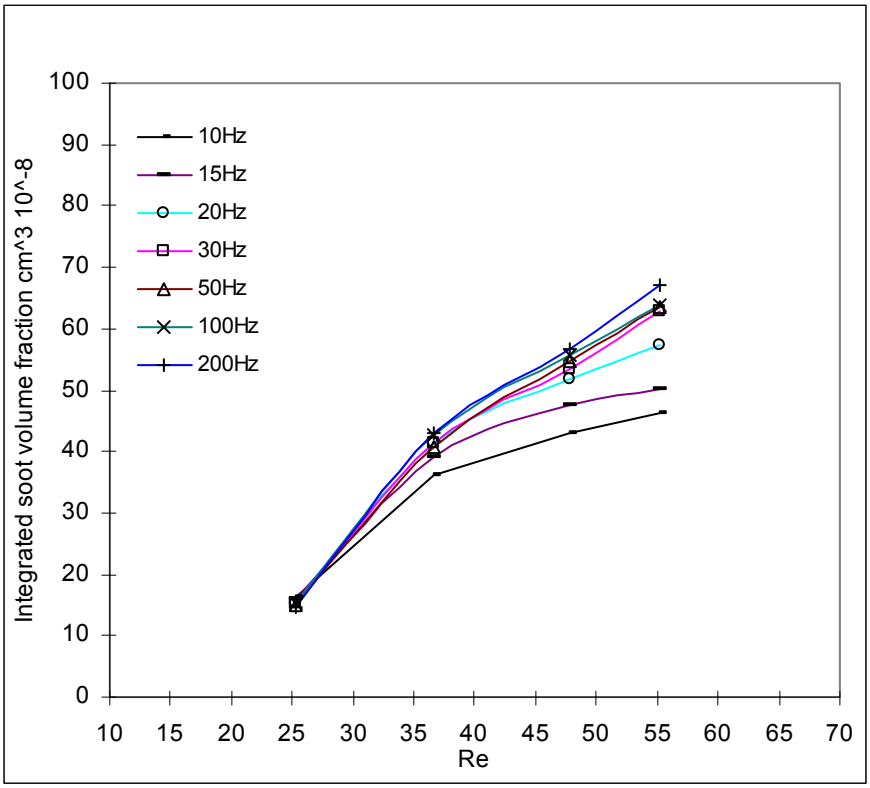

Figure 5.19 Volume-integrated time-averaged soot volume fraction versus Re for different pulsation

Figure 5.19 shows the trend of total soot volume fraction tendencies of diffusion flames with four different fuel flow rates under different pulsation frequencies in terms of Reynolds number.

5.7 Luminosity Measurements

Natural soot luminosity was measured using the same detection system and the same detector parameters in the absence of the laser fire and without any interference

filter, also called broadband luminosity over the complete sensitivity of the ICCD camera (200 nm-900 nm). The space-integrated luminosity versus phases for different pulsation for four fuel rates are given in Fig. 5.20, Fig. 5.21, Fig. 5.22, and Fig. 5.23. Using the information from these figures, the space-integrated time-averaged luminosity of pulsed flames is graphed and given in Fig. 5.24.

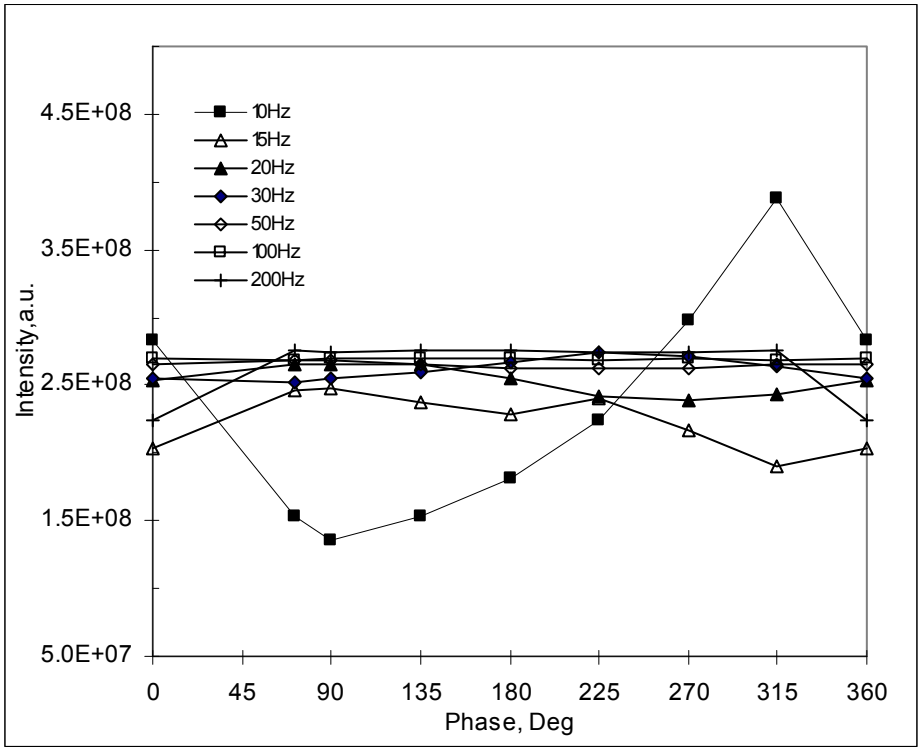

Figure 5.20 Space-integrated luminosity versus phases for different pulsation (E1)

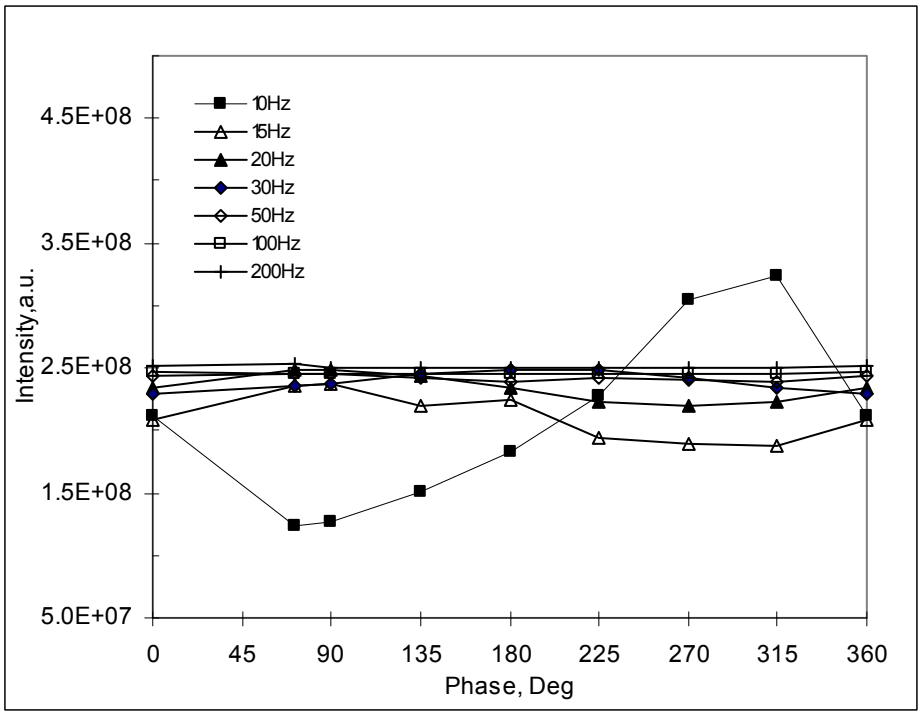

Figure 5.21 Space-integrated luminosity versus phases for different pulsation (E2)

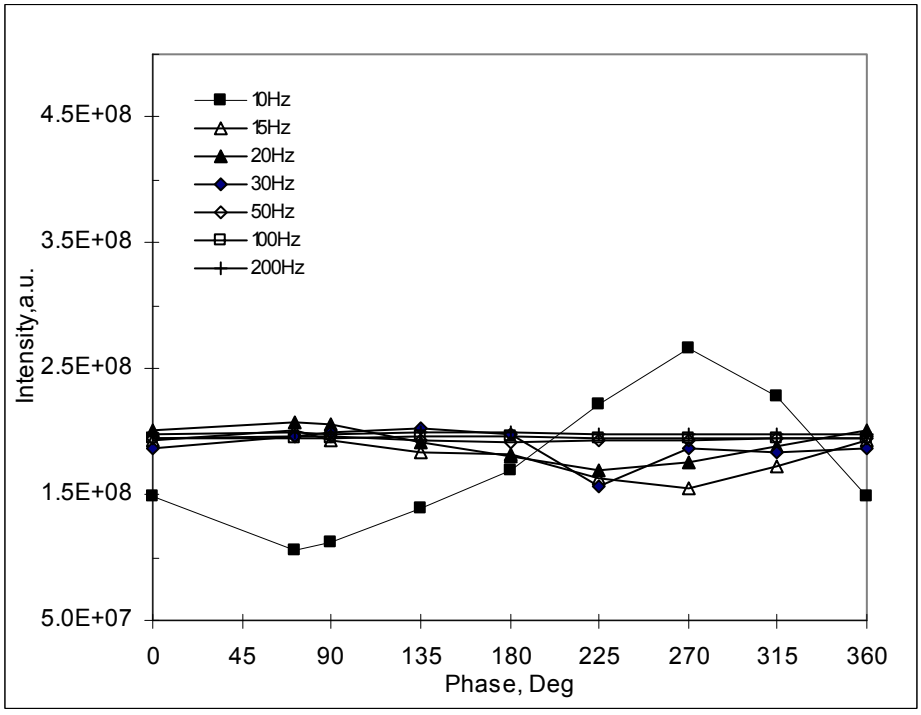

Figure 5.22 Space-integrated luminosity versus phases for different pulsation (E3)

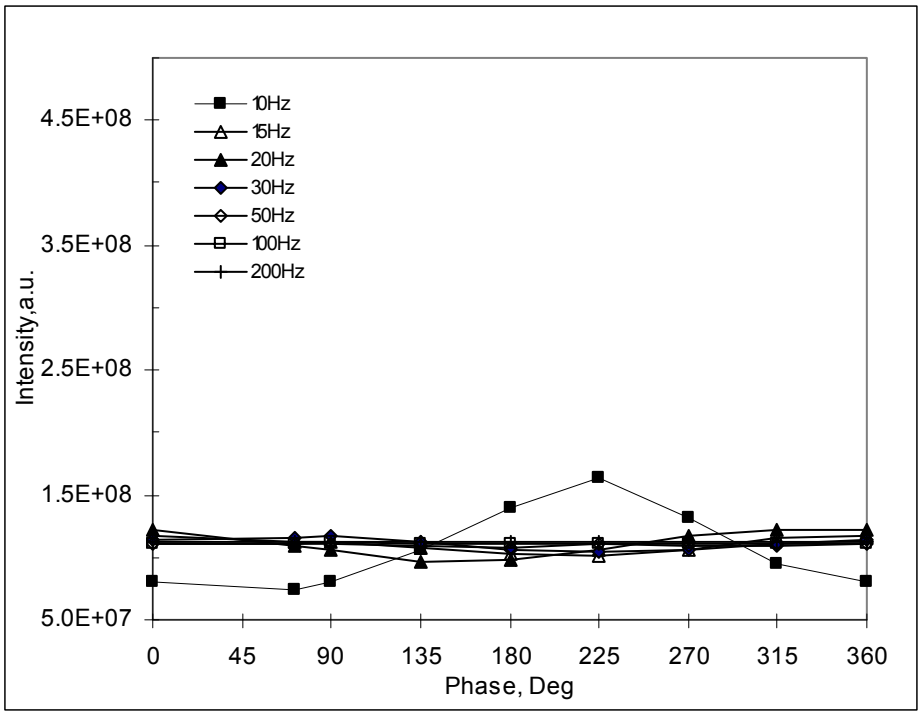

Figure 5.23 Space-integrated luminosity versus phases for different pulsation (E4)

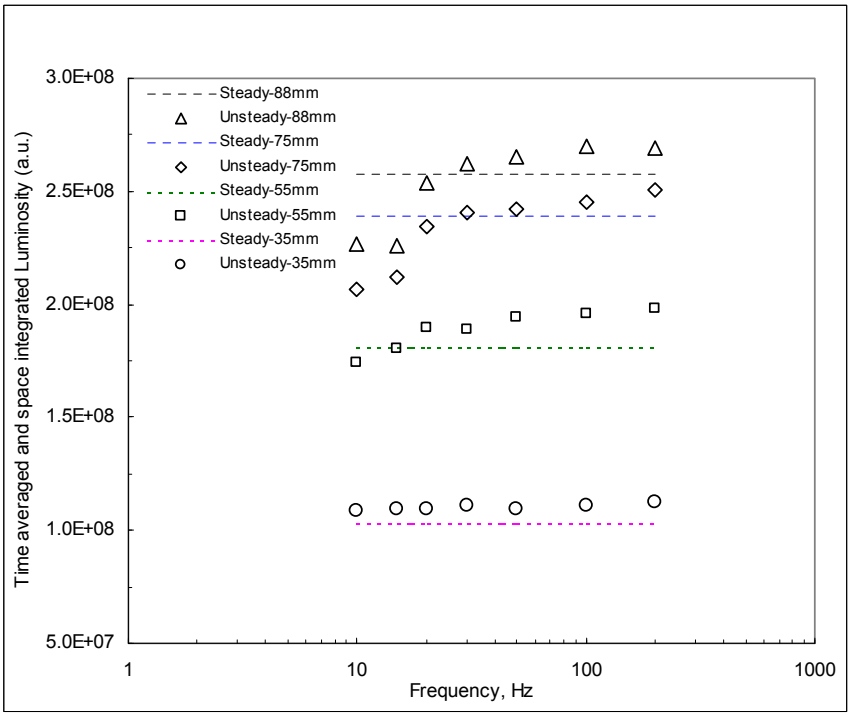

Figure 5.24 Space-integrated time-averaged luminosity for studied flames for different pulsation

5.8 Post Flame Aerosol Measurements

A considerable amount of emission of smoke from pulsed flames less than 30 Hz was observed for pulsed E1, E2 and E3 flames. The soot aerosol measurement results, which was obtained from averaging 50 single measurements done 20" above the burner tip, are given in Fig. 5.25. The background for the monitor was 0.015 mg/m^3. The sampling rate for the measurements was selected to be the minimum value of 1 sample/sec for all of the studied cases. The sampling time of 50 seconds was selected in our experiments to prevent possible particle depositions with time, which affected the results for sampling continuously more than 60 seconds.

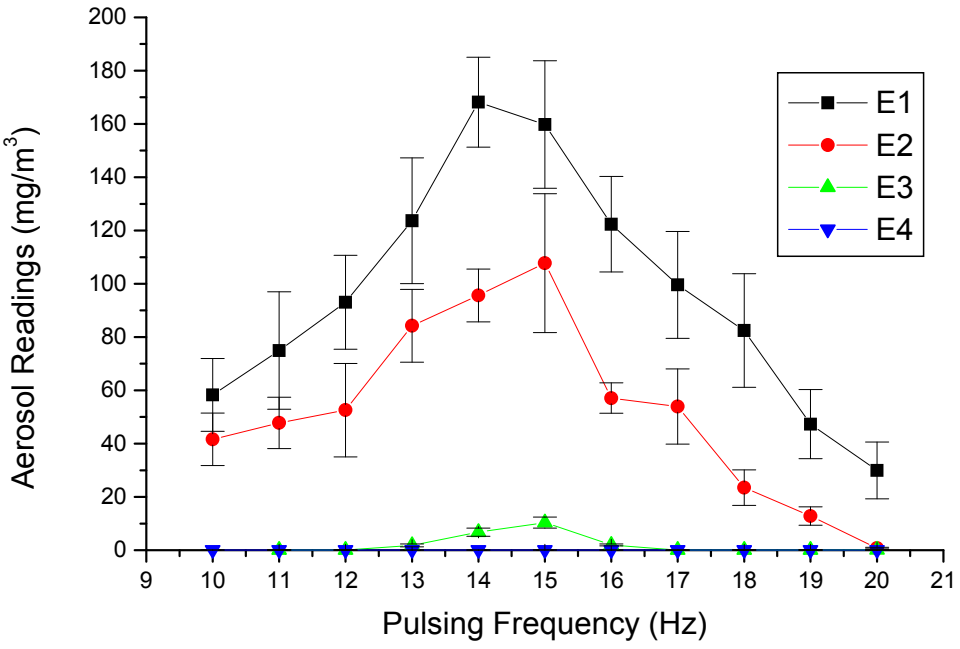

Figure 5.25 Post flame soot aerosol readings for studied flames

5.9 Particle Sizing Methods

A temporal profile of the normalized LII signal at HAB=40 mm in the maximum soot region (annular region) was obtained by increasing the gate delay between the camera opening and the laser fire by 50 ns increments (Fig. 5.26). The LII signals were integrated signals over the gate width (100 ns) of the intensified camera from 5 images. It should also be mentioned that each point is representing the LII signal from a different laser fire. In other words, we were limited by the sample rate of the camera. Because of the low laser fluence, the LII signal rises slowly and reaches its maximum just after the laser pulse, indicating that the temperature of soot particles is continuously increasing during the laser pulse. It is followed by a relatively long decay period (~1 μs), which was an expected characteristic of the LII signal.

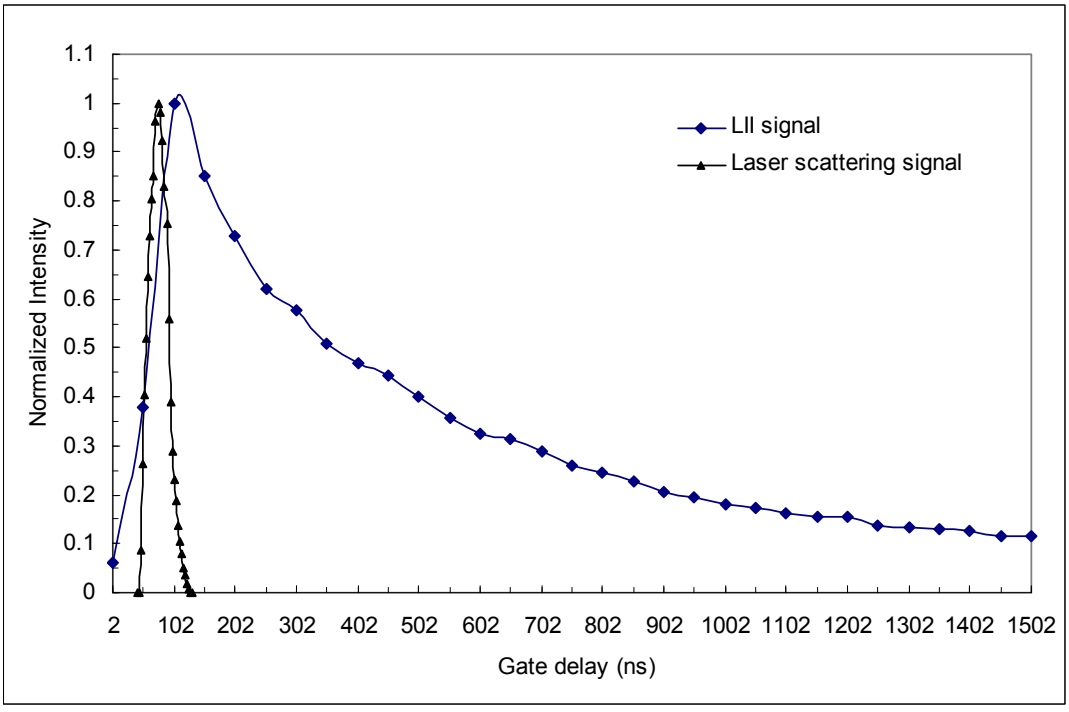

Figure 5.26 Time history of the peak LII signal (HAB=40 mm)

The first method of analysis to extract the primary size from the LII data, called the gate ratio method, used the same LII temporal curve by taking the ratio of the two signals taken at different gate delays after the excitation of the laser pulse. The second method called the exponential fit method utilized experimental data by fitting the signal decay to the single exponential fit for times 200 ns after the laser fire for 200-300 ns time period, [LII(t) = Aexp(-kt)]. The third method, called the double-exponential fit method, fit a double exponential fit, [$LII(t) = A+B_1\exp(-t/C_1)+B_2\exp(-t/C_2)$], for data points up to where the signal intensity decreased to 10% of its peak value. The results of these methods and a comparison among them are given in Fig. 5.27, Fig. 5.28, Fig. 5.29, Fig. 5.30, and Fig. 5.31.

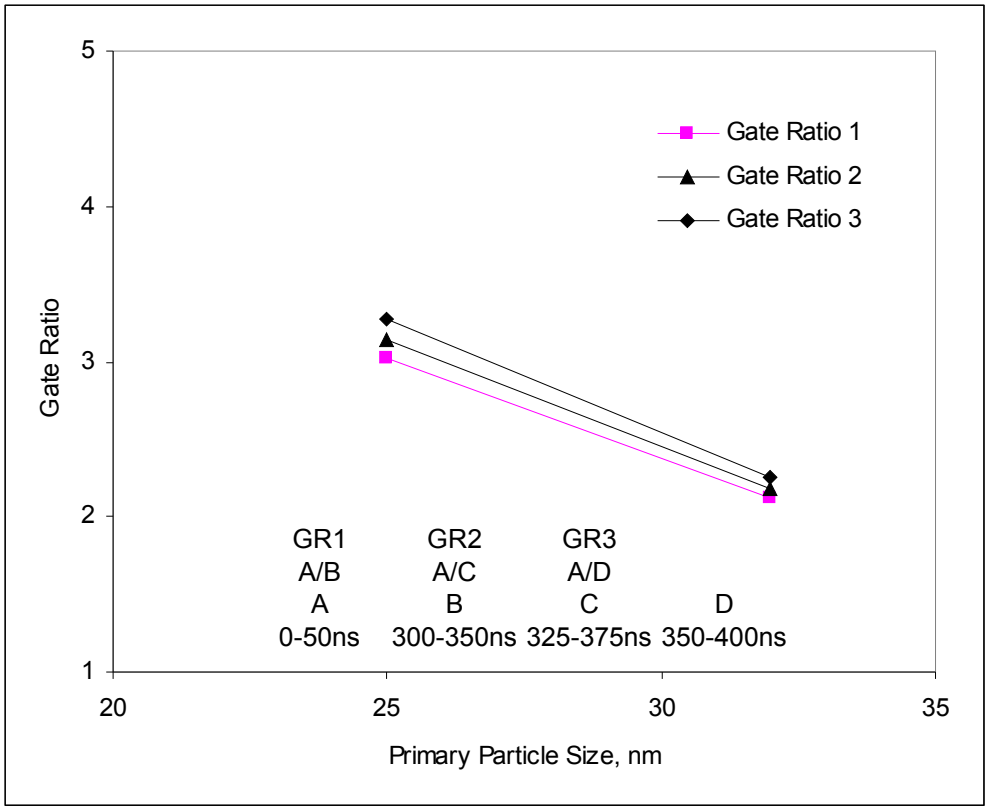

Figure 5.27 Gate ratio method applied at HAB=40 mm (E1)

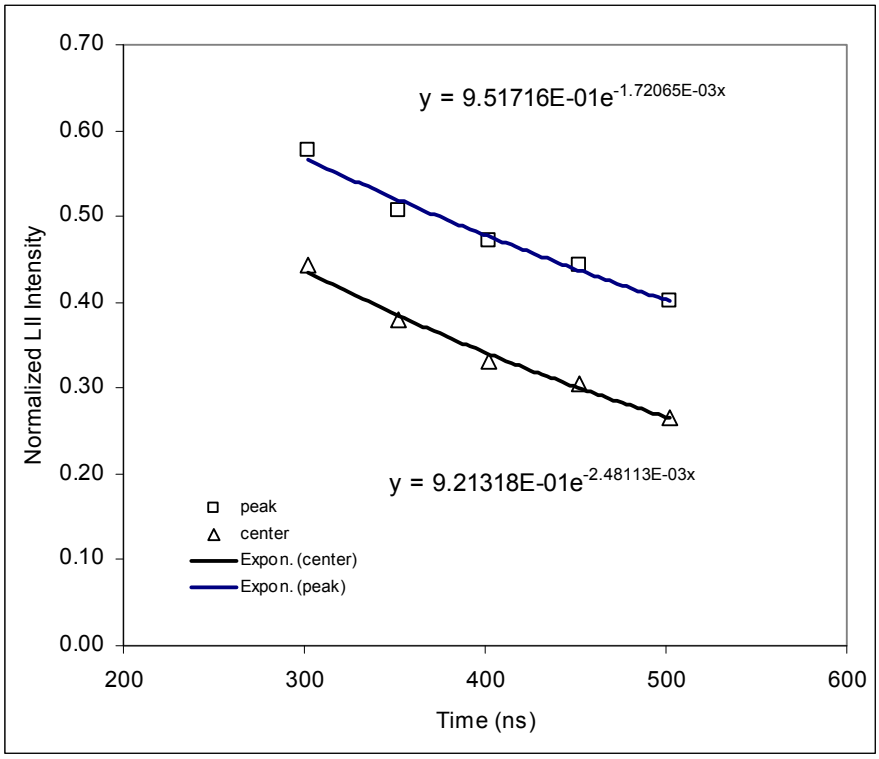

Figure 5.28 Exponential fit method applied at HAB=40 mm (E1)

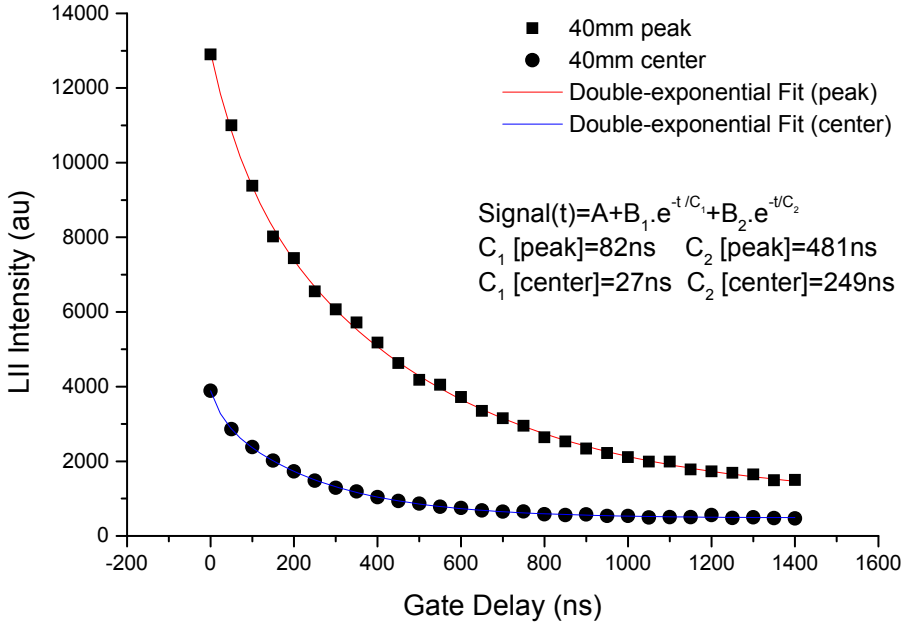

Figure 5.29 Double-exponential fit method applied at HAB=40 mm (E1)

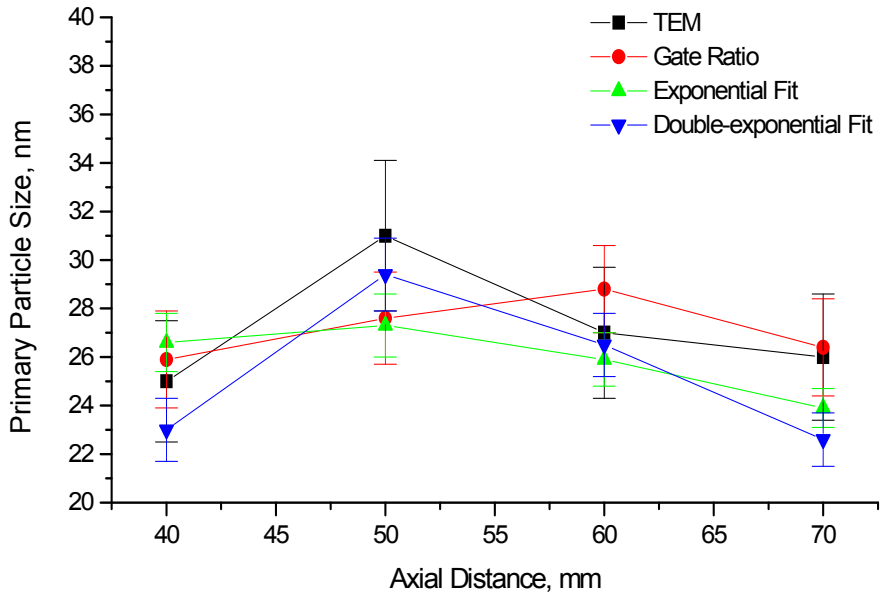

Figure 5.30 Comparison of methods applied at HAB=40 mm (E1)

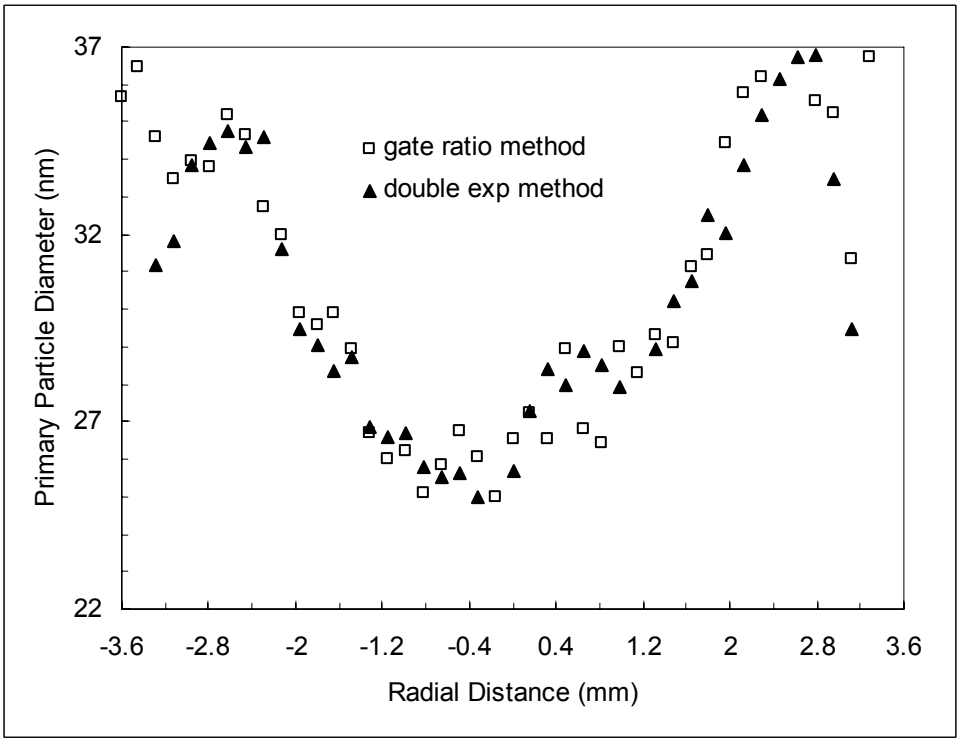

Figure 5.31 Radial variation of d_p predicted by two methods at HAB=40 mm (E1)

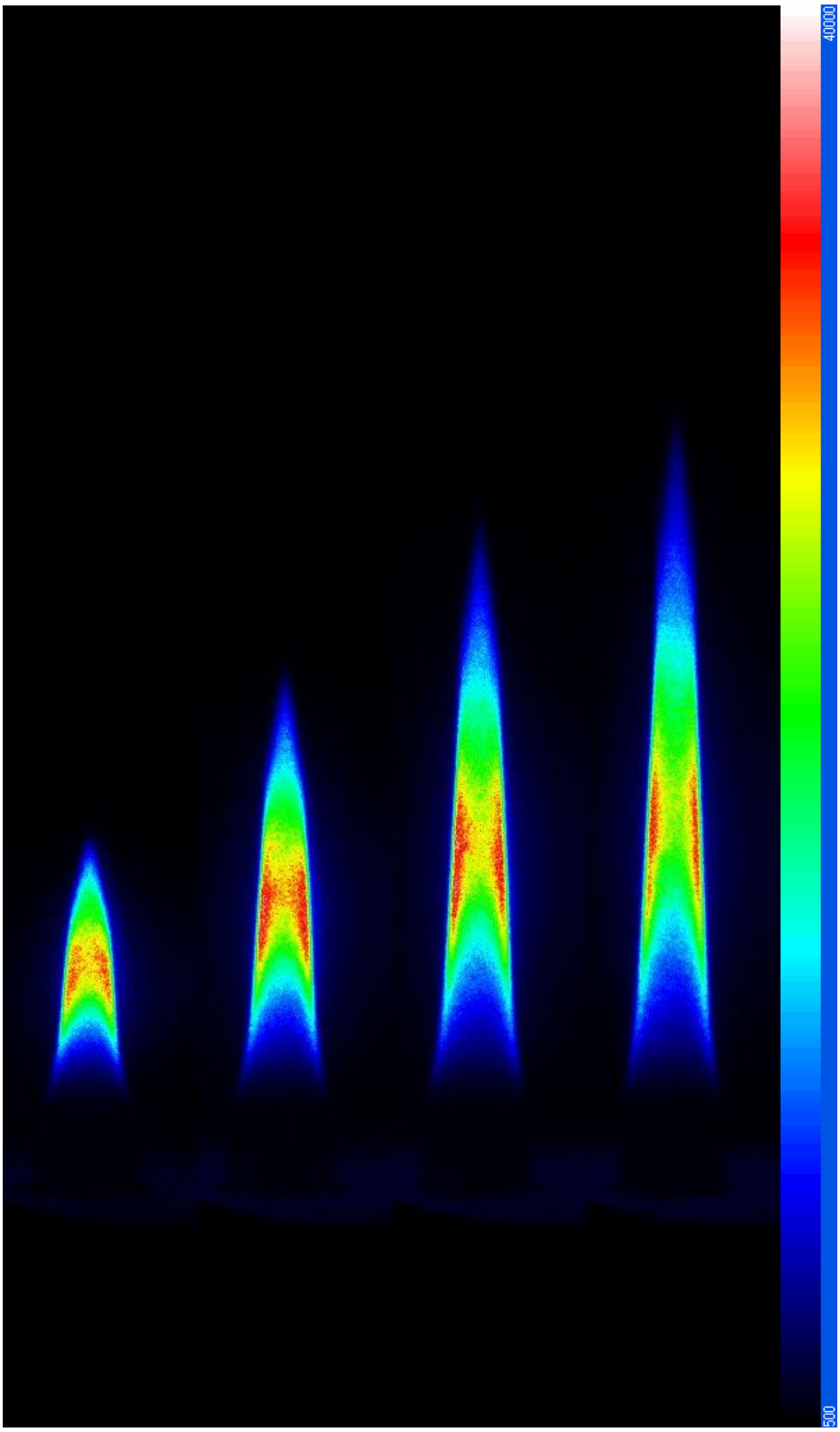

Figure 5.32 Emission images of steady flames (E1, E2, E3, and E4)

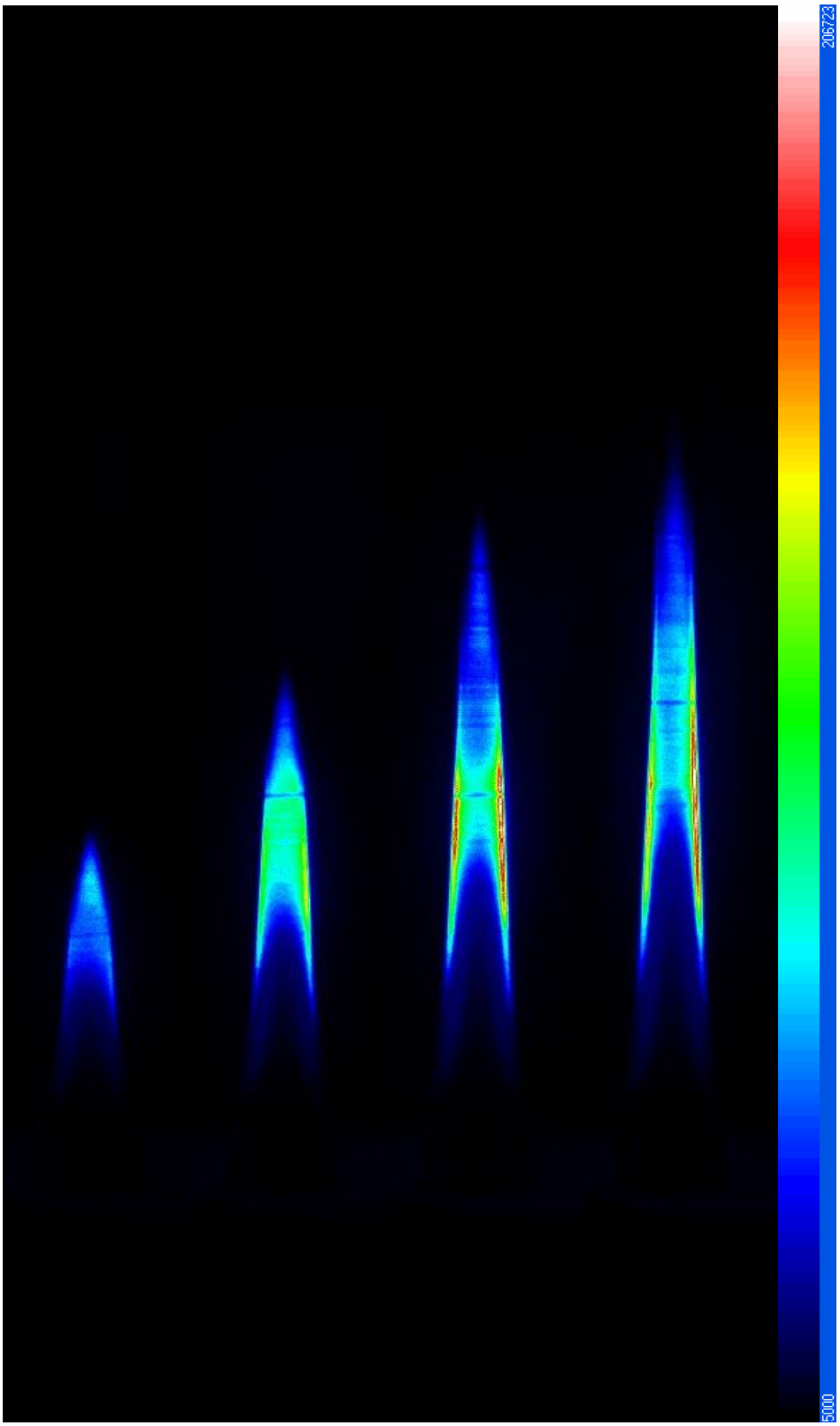

Figure 5.33 LII images of steady flames (E1, E2, E3, and E4)

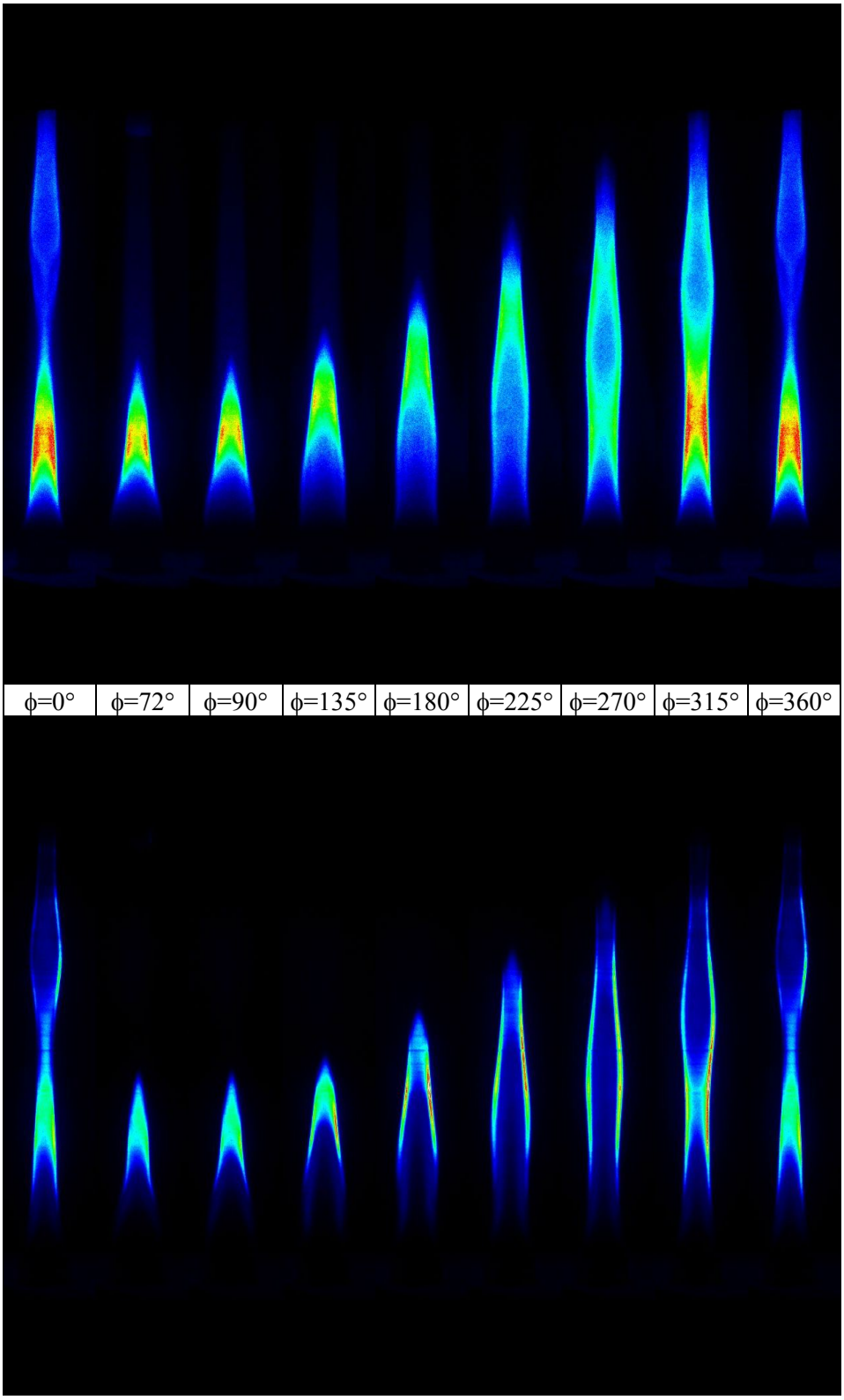

Figure 5.34 Phase-locked images of 88 mm pulsed flame (10 Hz)

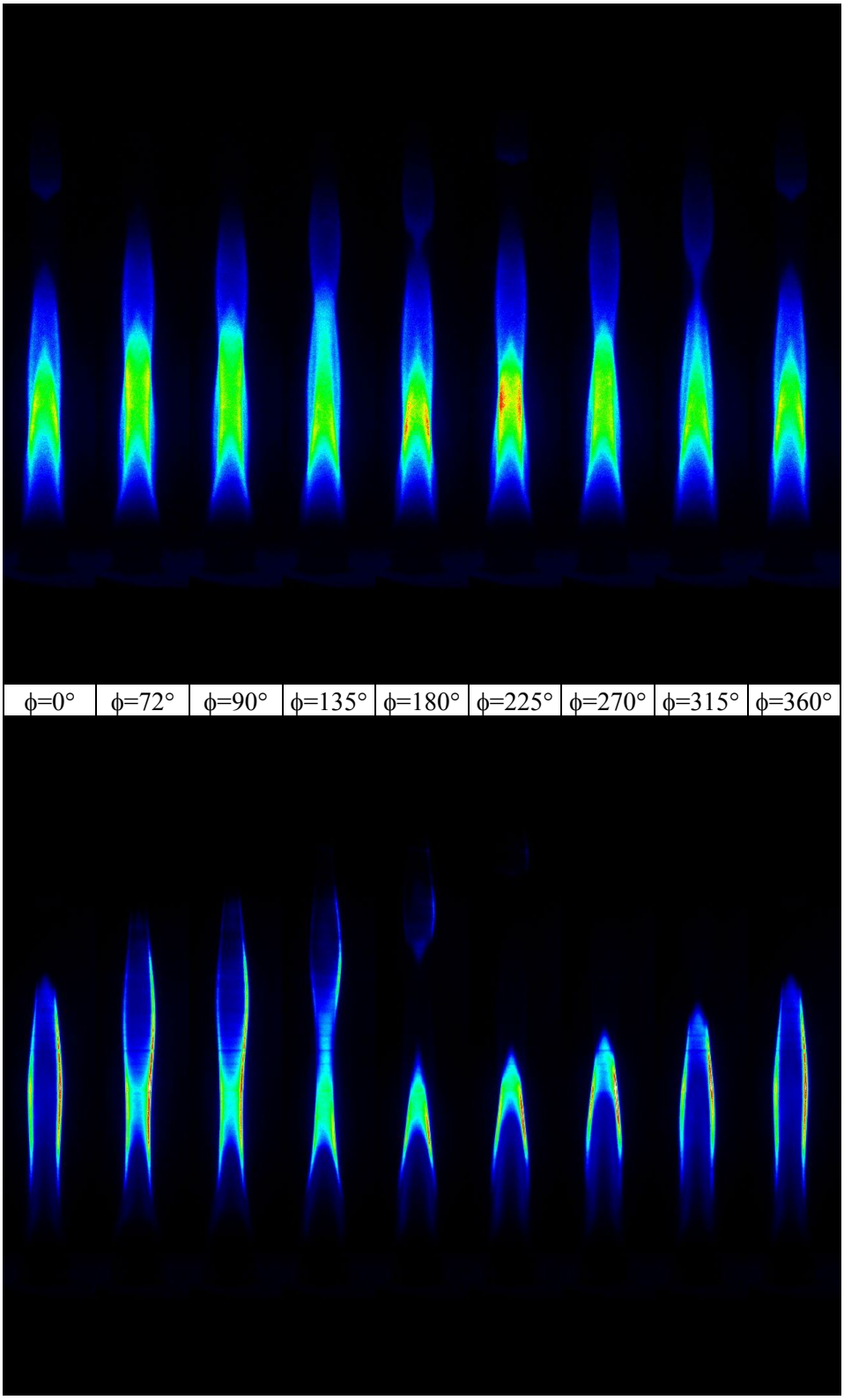

Figure 5.35 Phase-locked images of 88 mm pulsed flame (15 Hz)

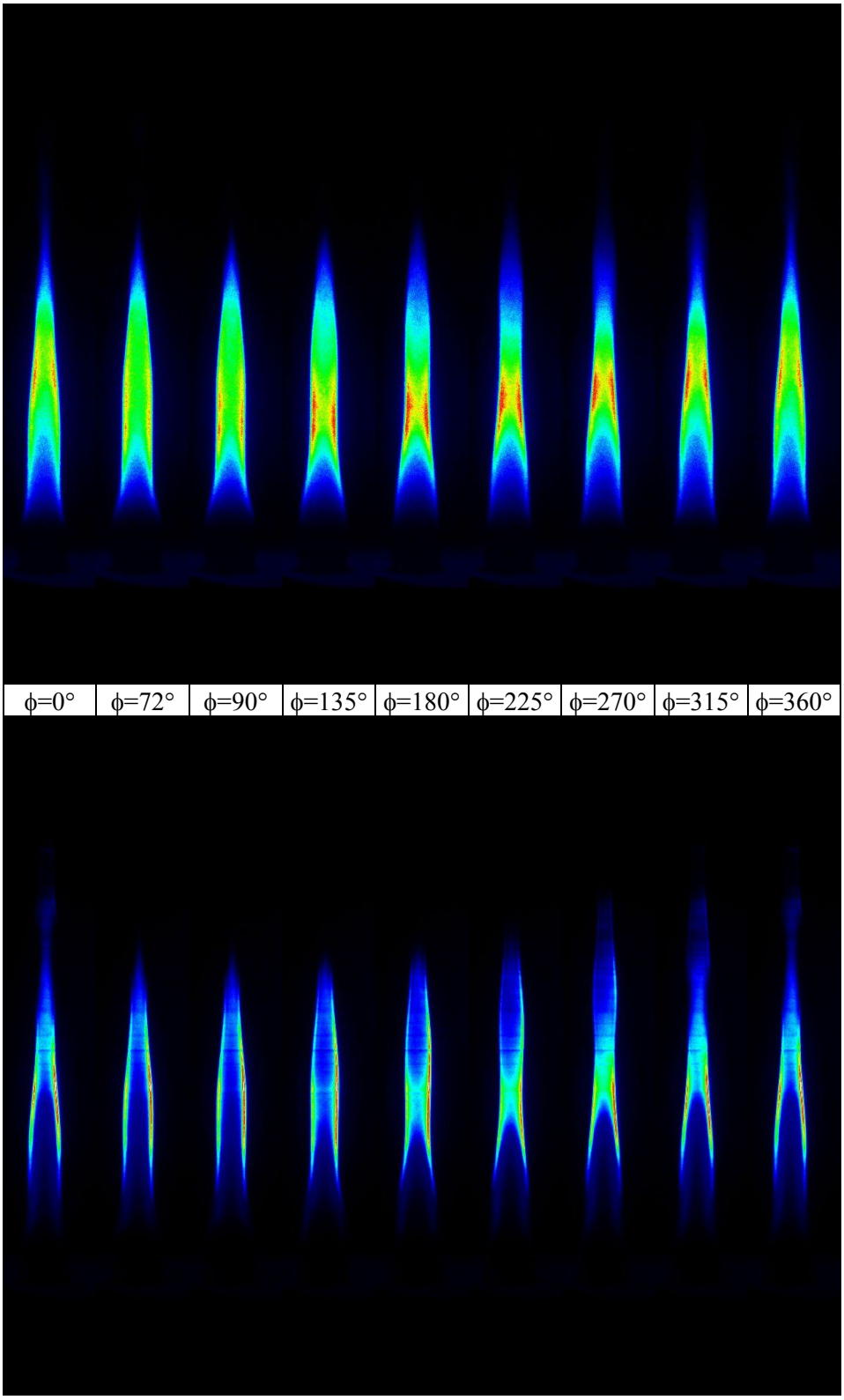

Figure 5.36 Phase-locked images of 88 mm pulsed flame (20 Hz)

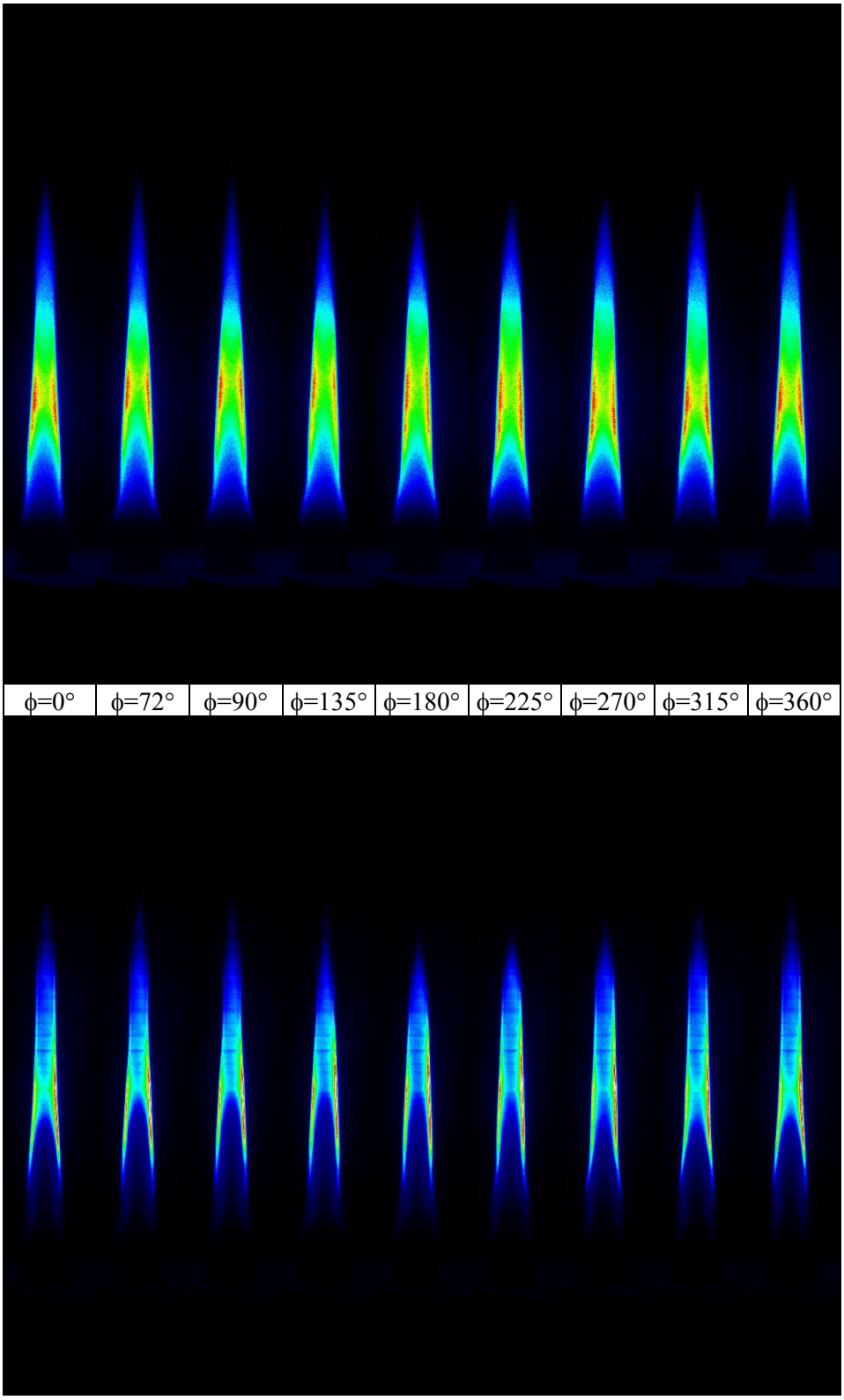

Figure 5.37 Phase-locked images of 88 mm pulsed flame (30 Hz)

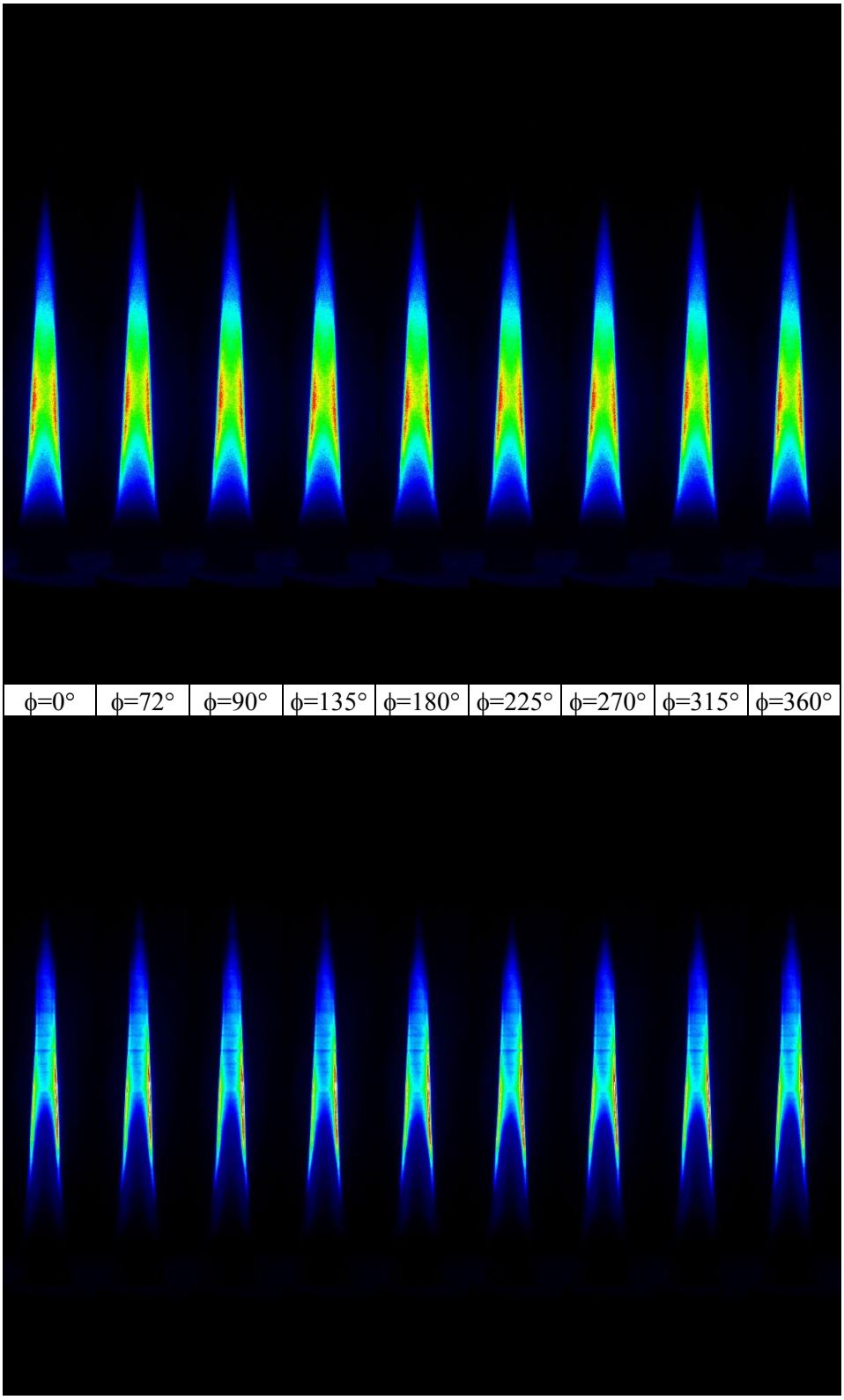

Figure 5.38 Phase-locked images of 88 mm pulsed flame (50 Hz)

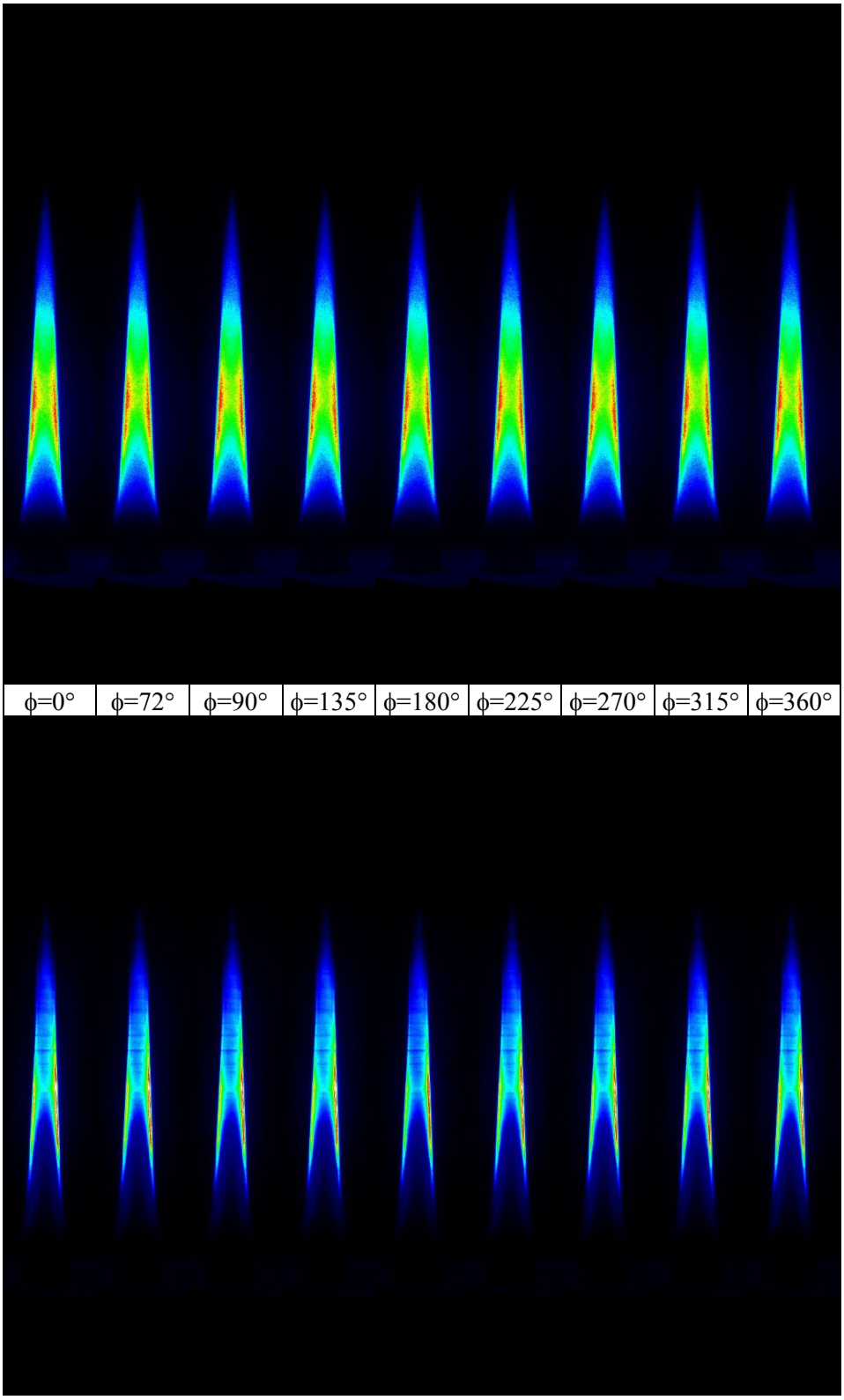

Figure 5.39 Phase-locked images of 88 mm pulsed flame (100 Hz)

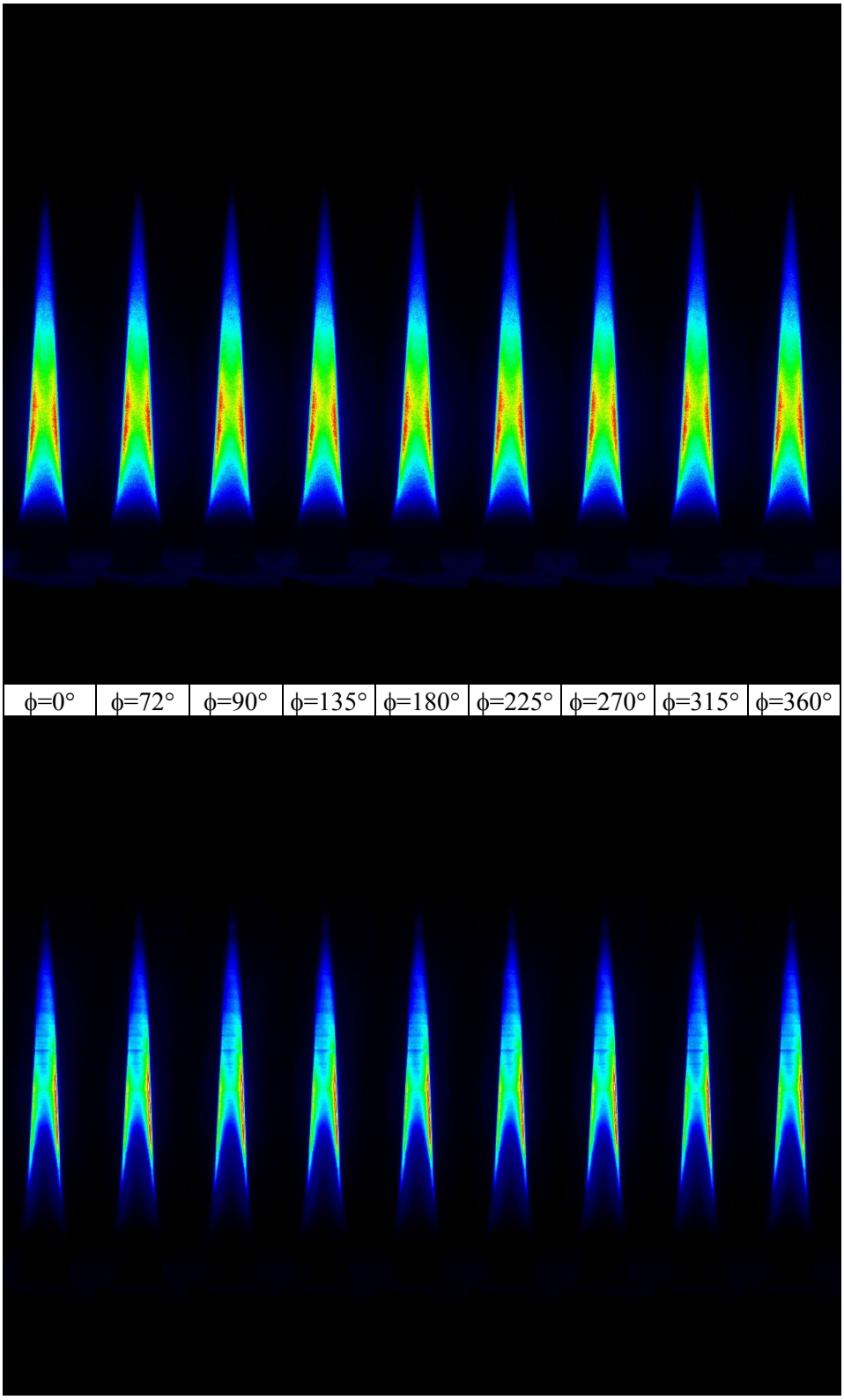

Figure 5.40 Phase-locked images of 88 mm pulsed flame (200 Hz)

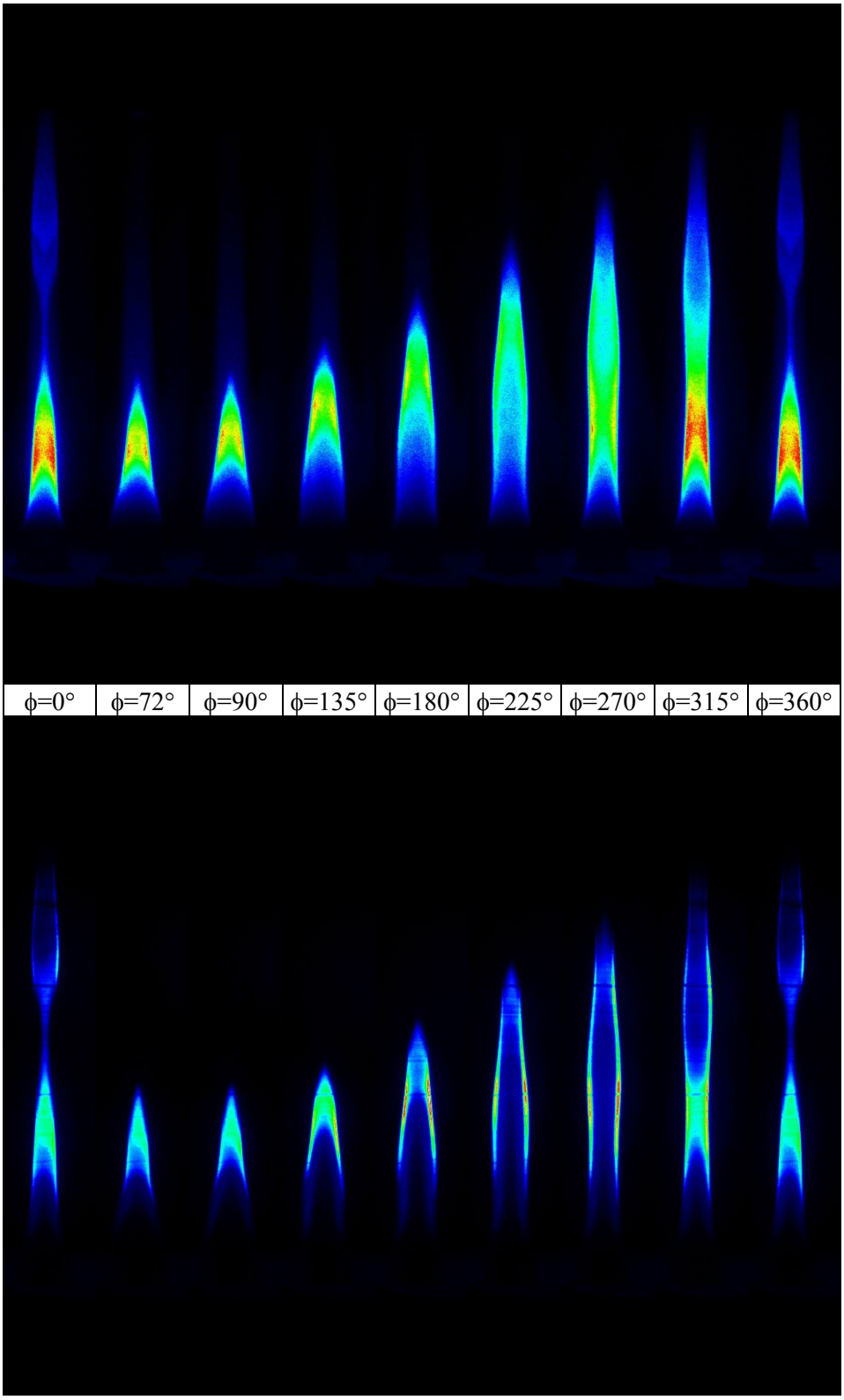

Figure 5.41 Phase-locked images of 75 mm pulsed flame (10 Hz)

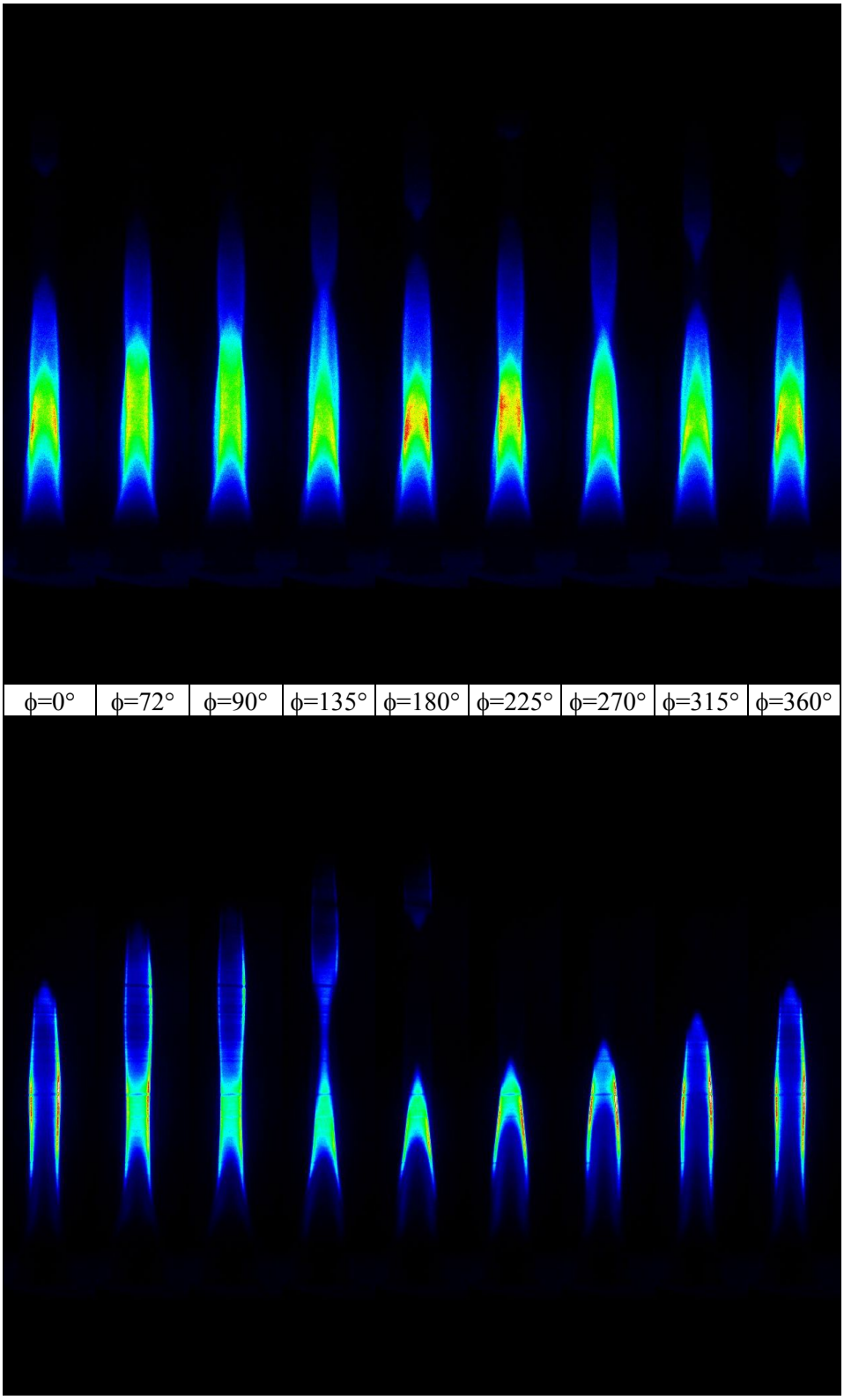

Figure 5.42 Phase-locked images of 75 mm pulsed flame (15 Hz)

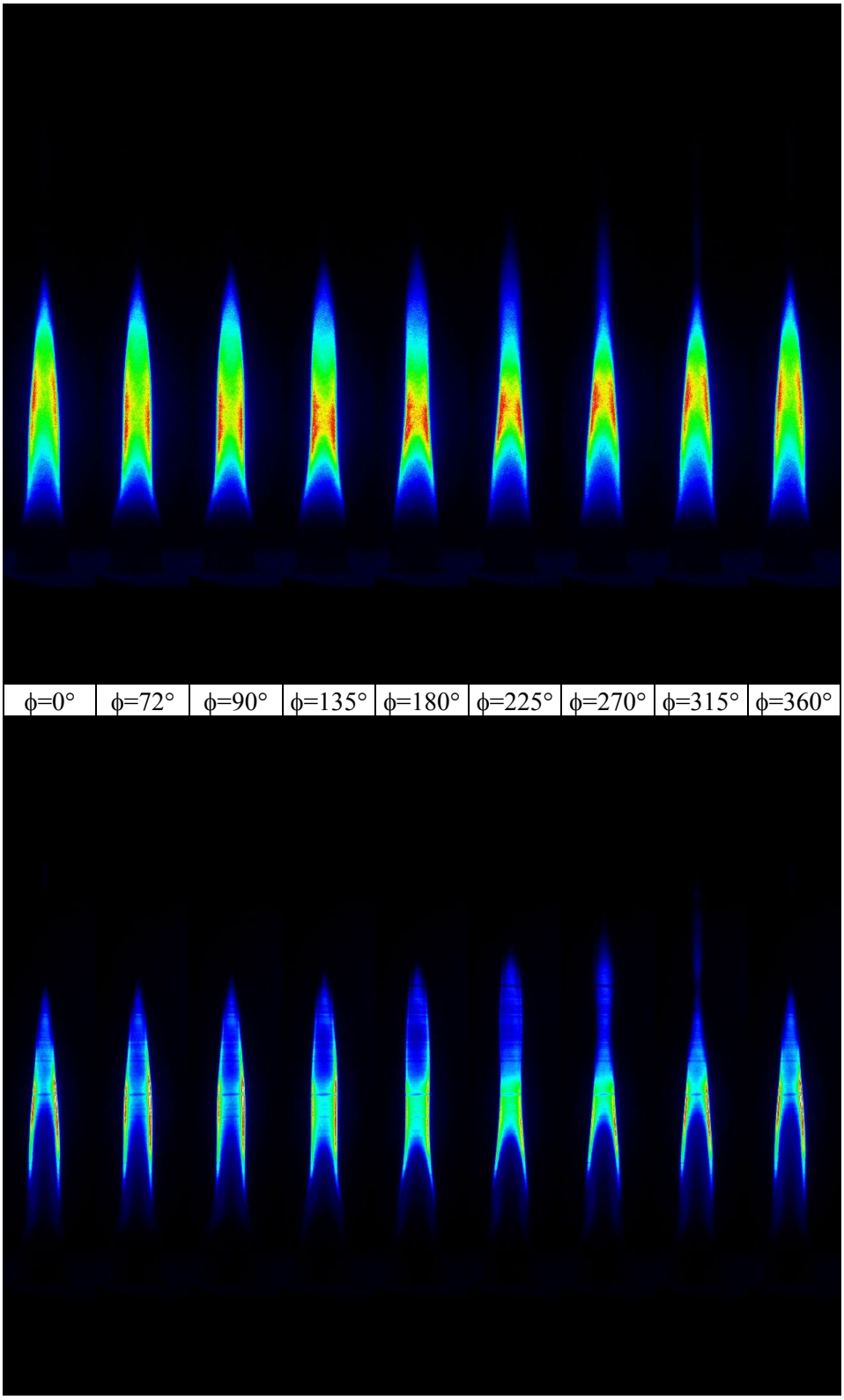

Figure 5.43 Phase-locked images of 75 mm pulsed flame (20 Hz)

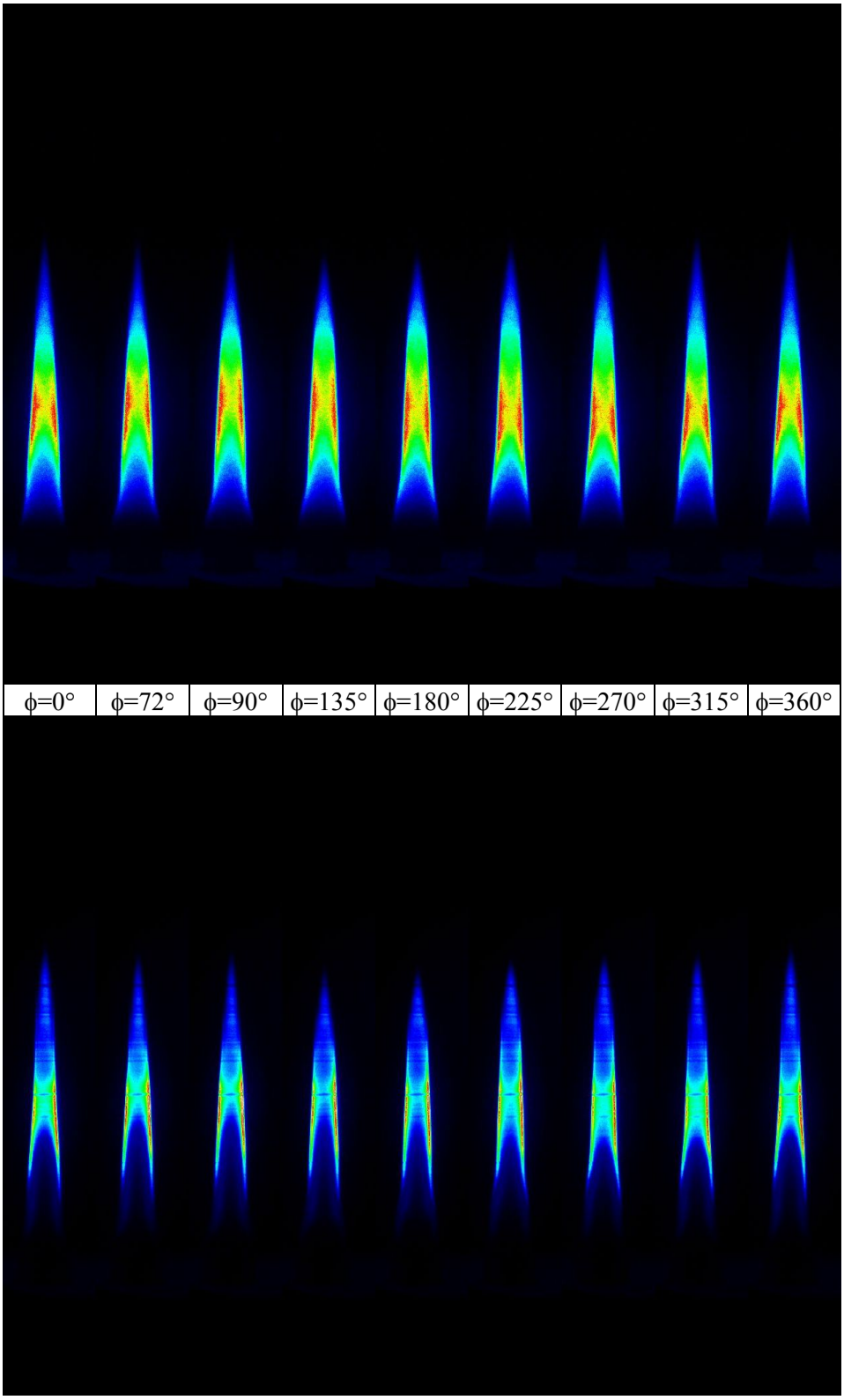

Figure 5.44 Phase-locked images of 75 mm pulsed flame (30 Hz)

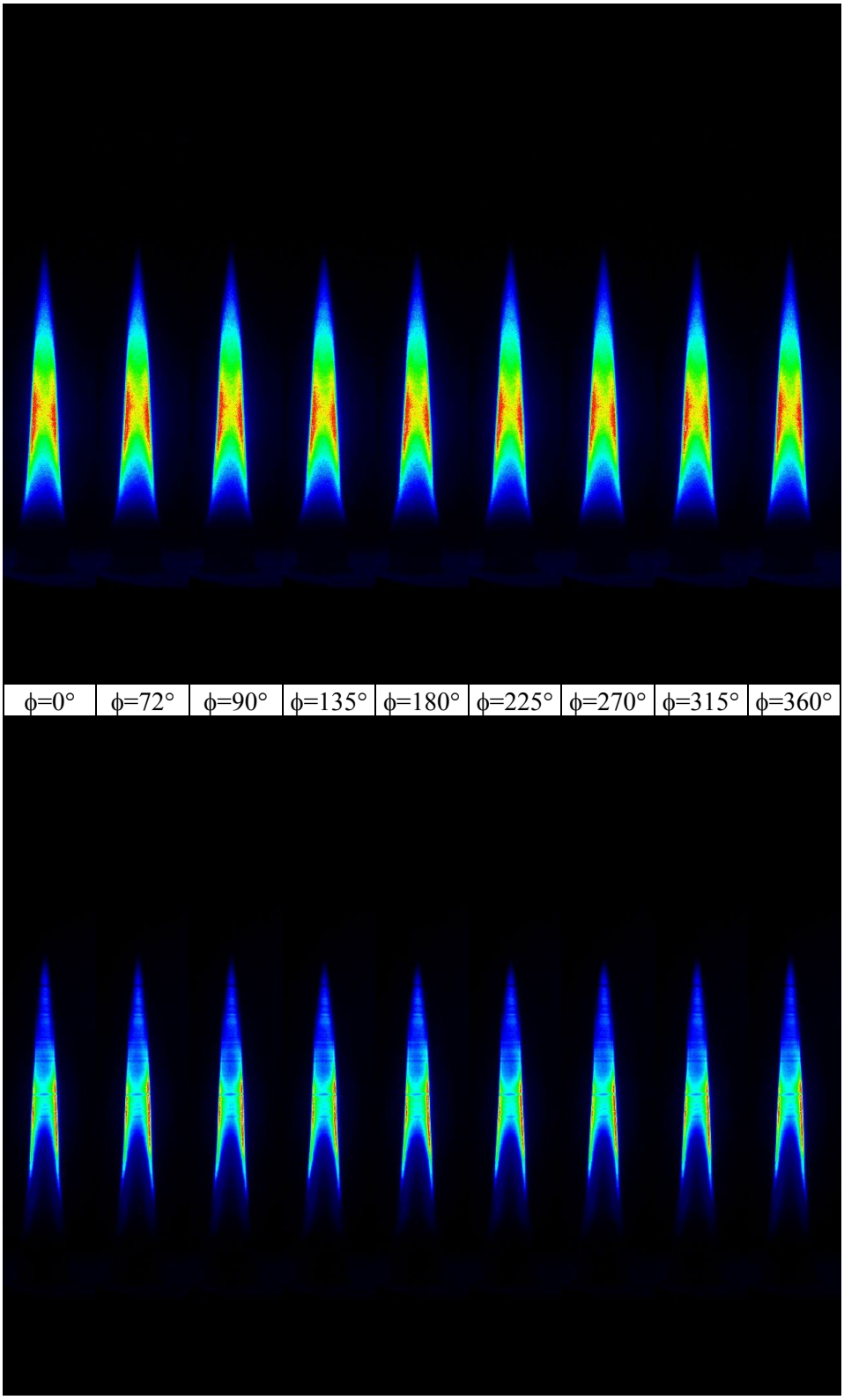

Figure 5.45 Phase-locked images of 75 mm pulsed flame (50 Hz)

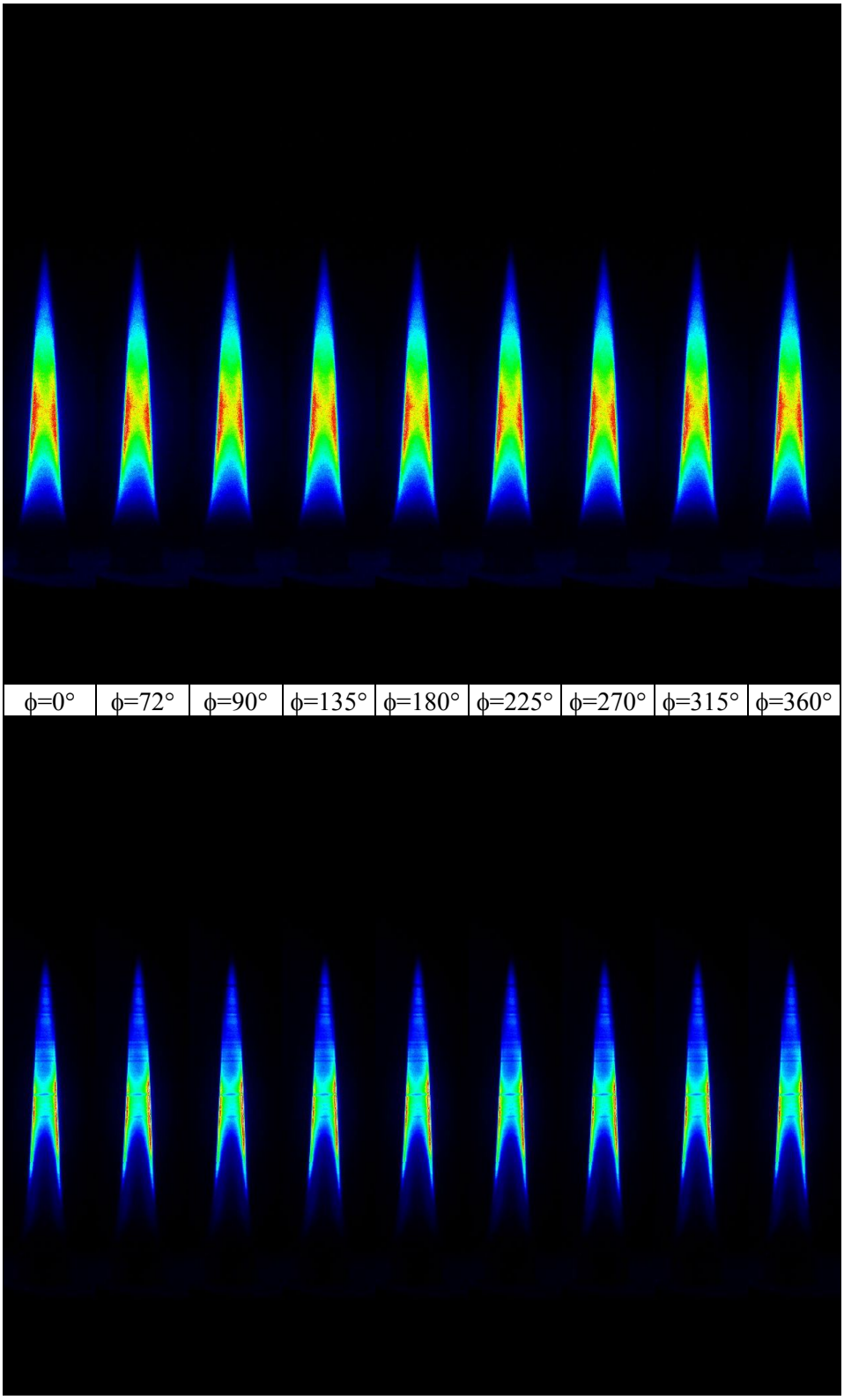

Figure 5.46 Phase-locked images of 75 mm pulsed flame (100 Hz)

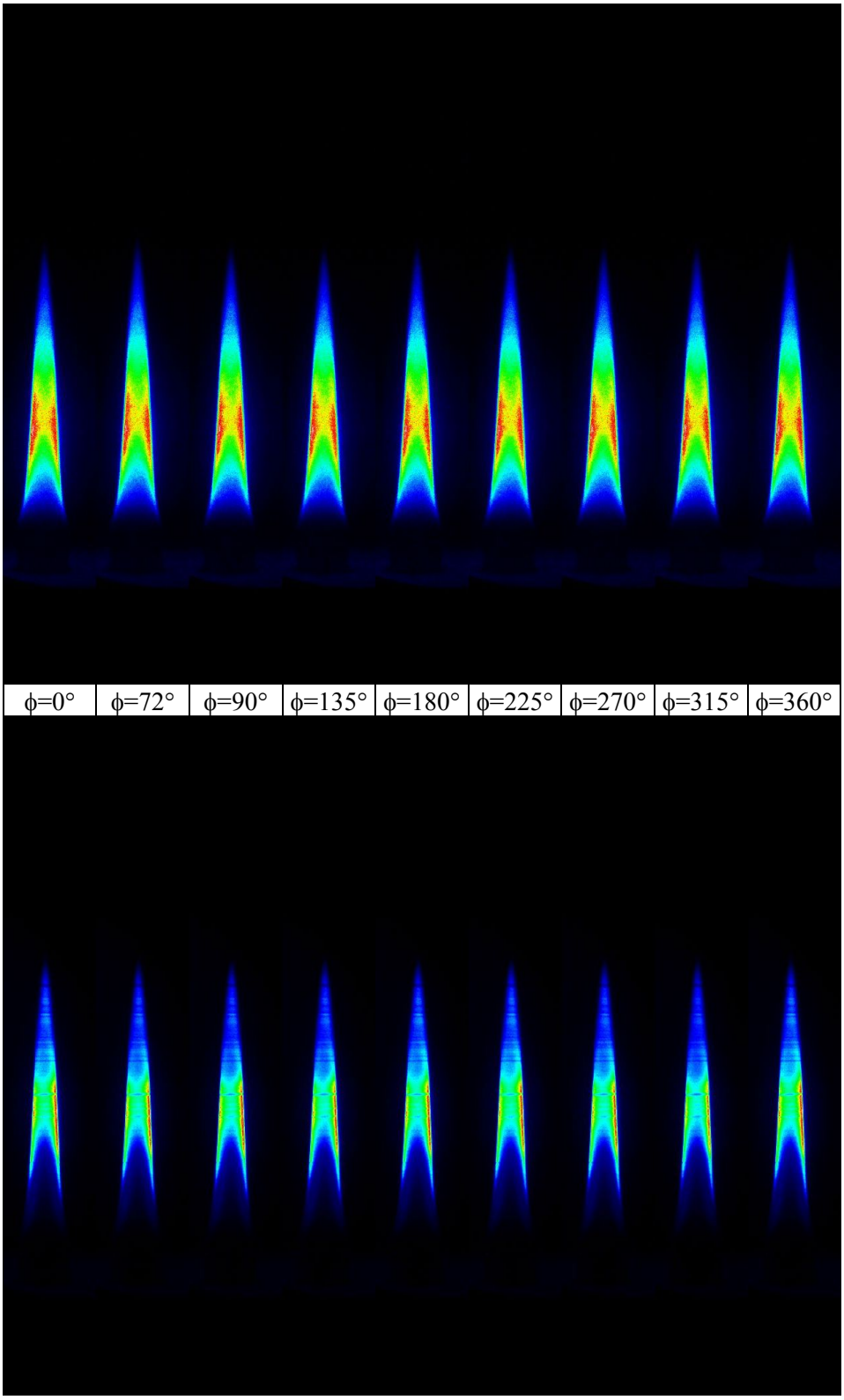

Figure 5.47 Phase-locked images of 75 mm pulsed flame (200 Hz)

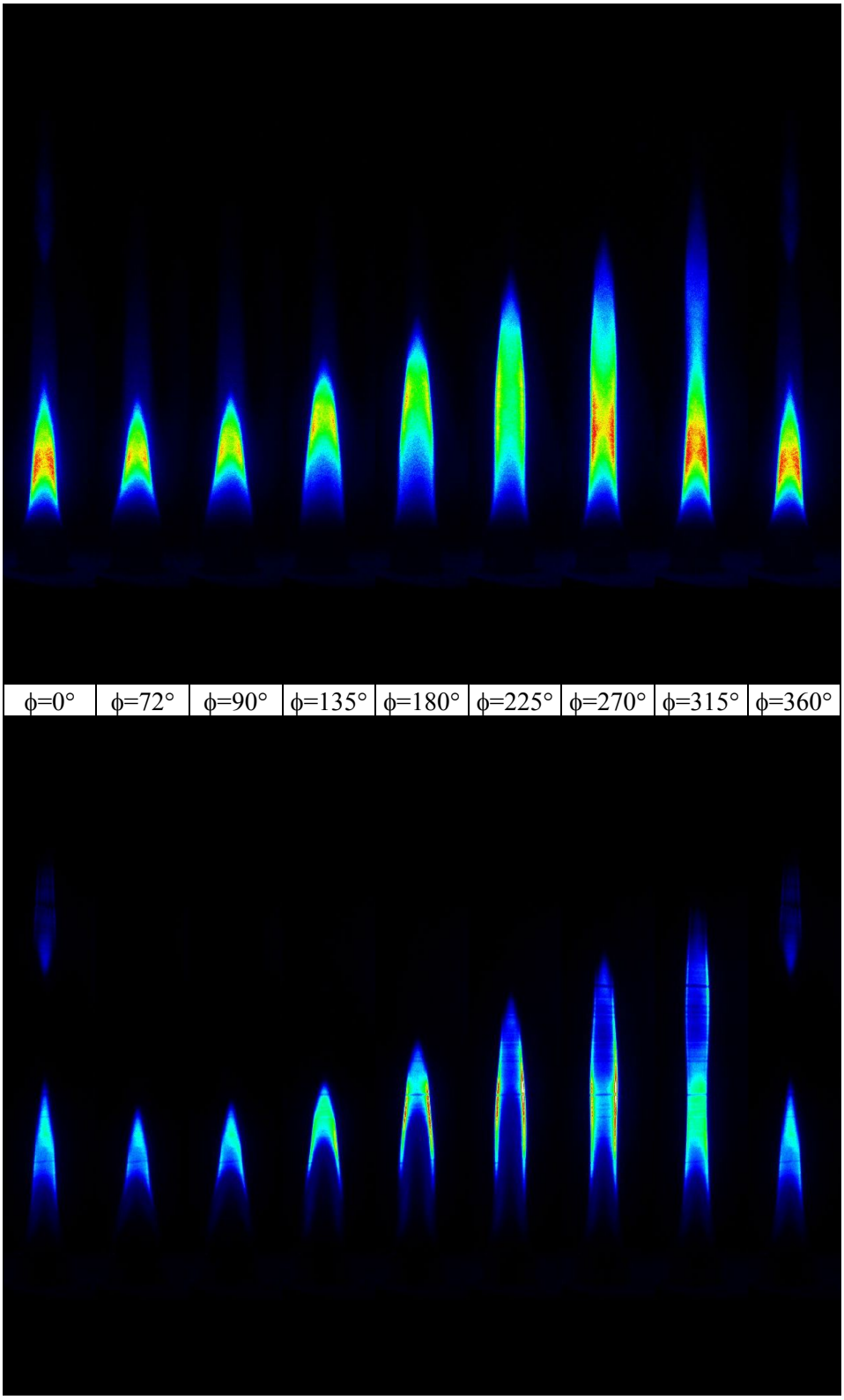

Figure 5.48 Phase-locked images of 55 mm pulsed flame (10 Hz)

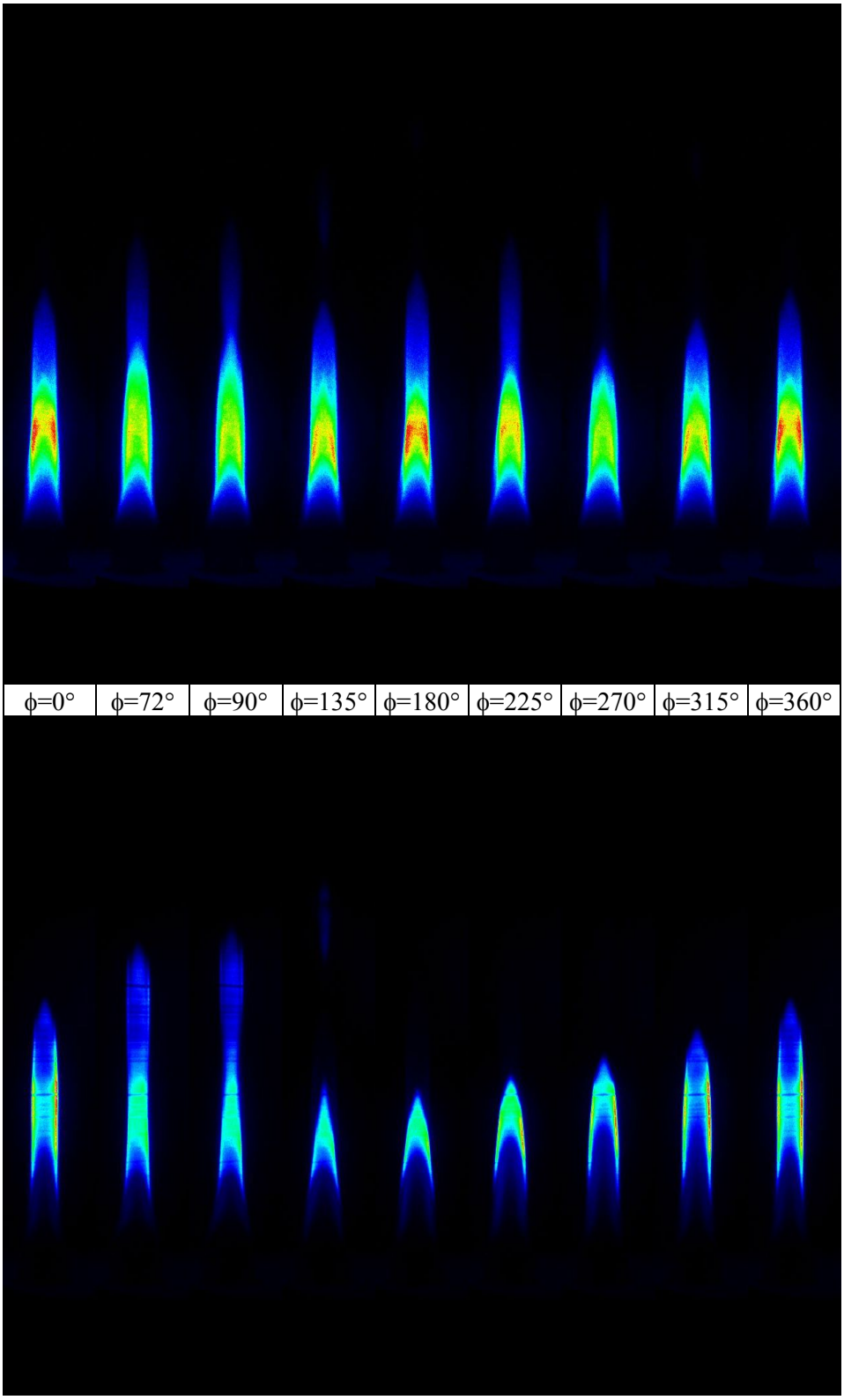

Figure 5.49 Phase-locked images of 55 mm pulsed flame (15Hz)

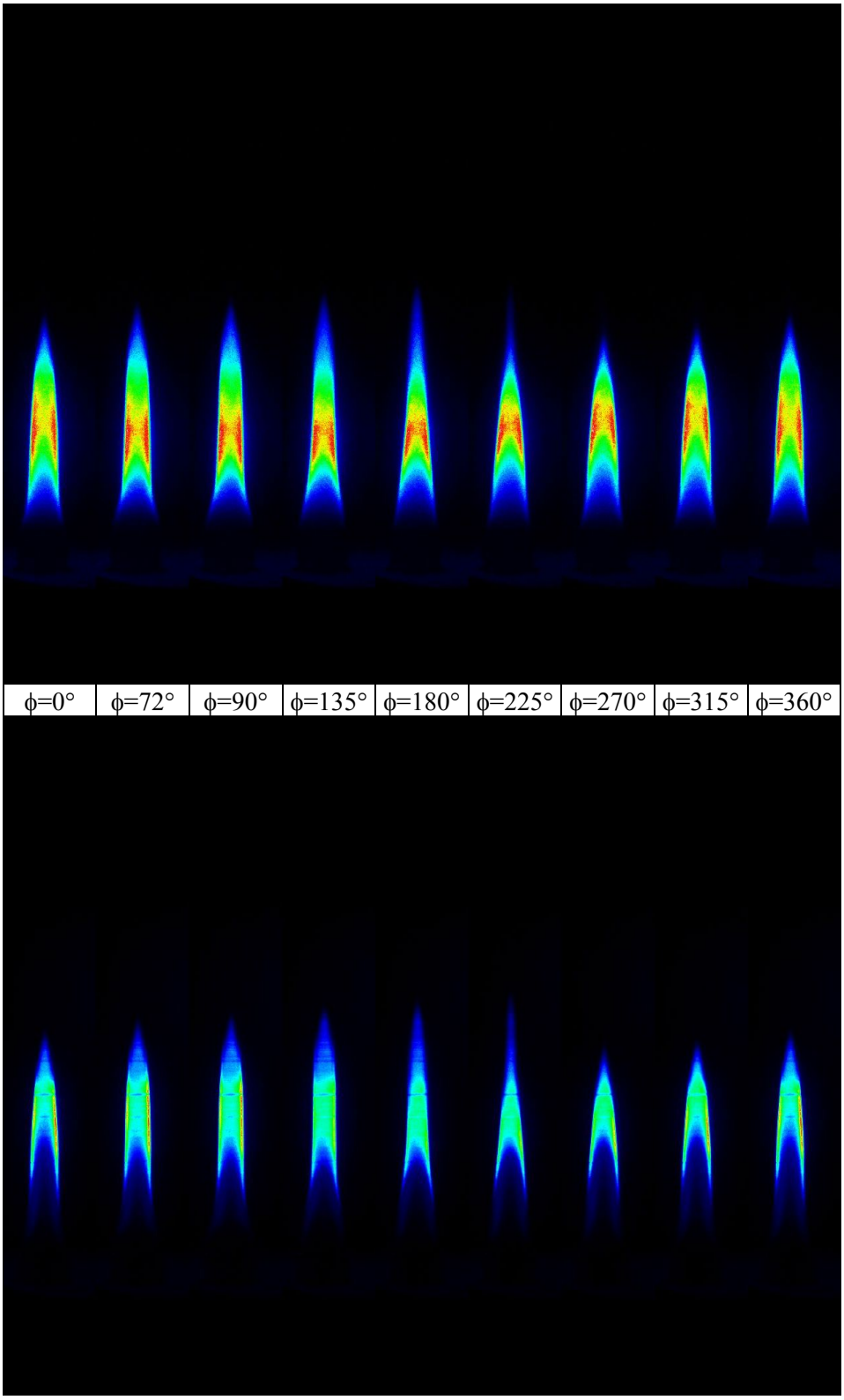

Figure 5.50 Phase-locked images of 55 mm pulsed flame (20 Hz)

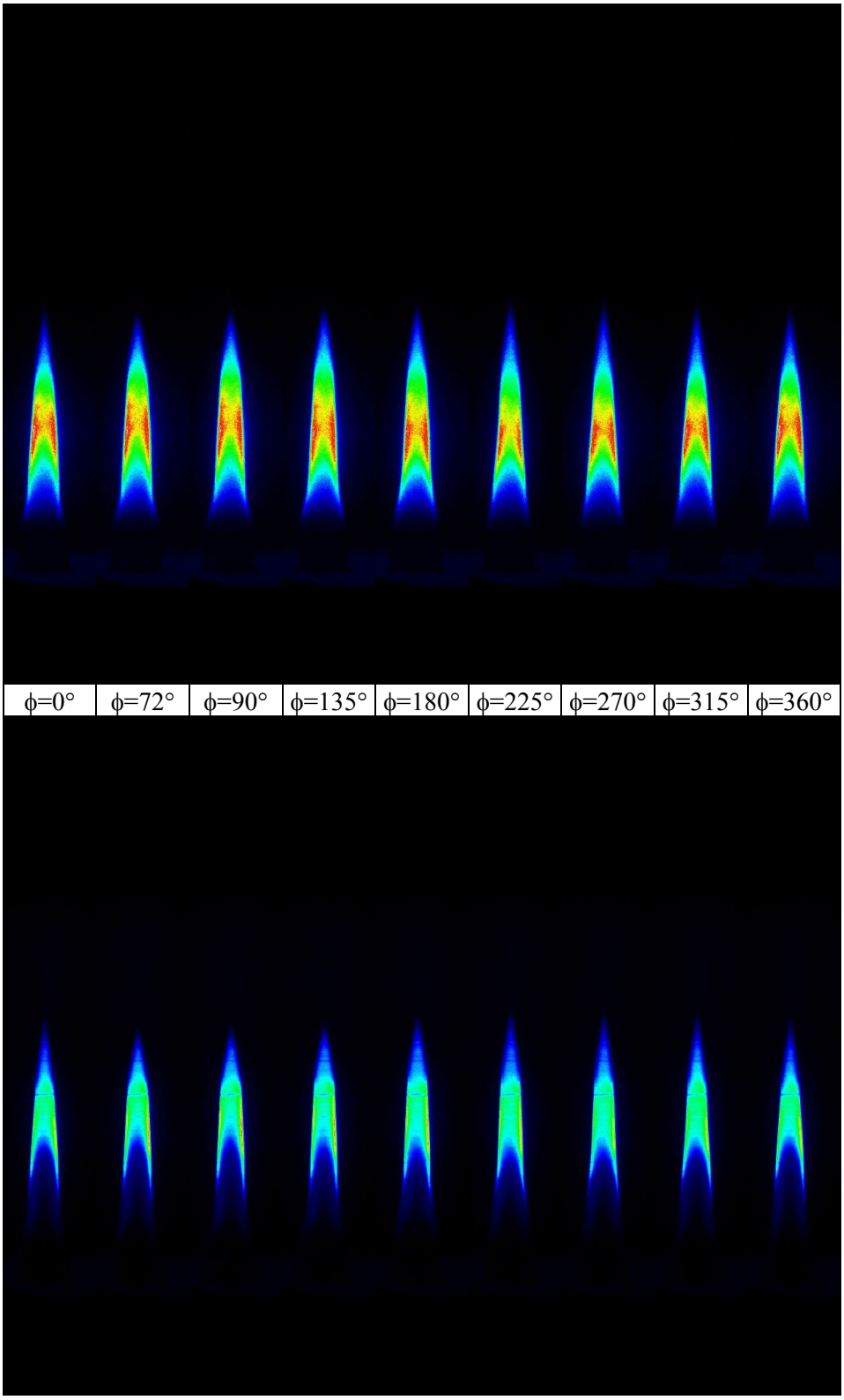

Figure 5.51 Phase-locked images of 55 mm pulsed flame (30 Hz)

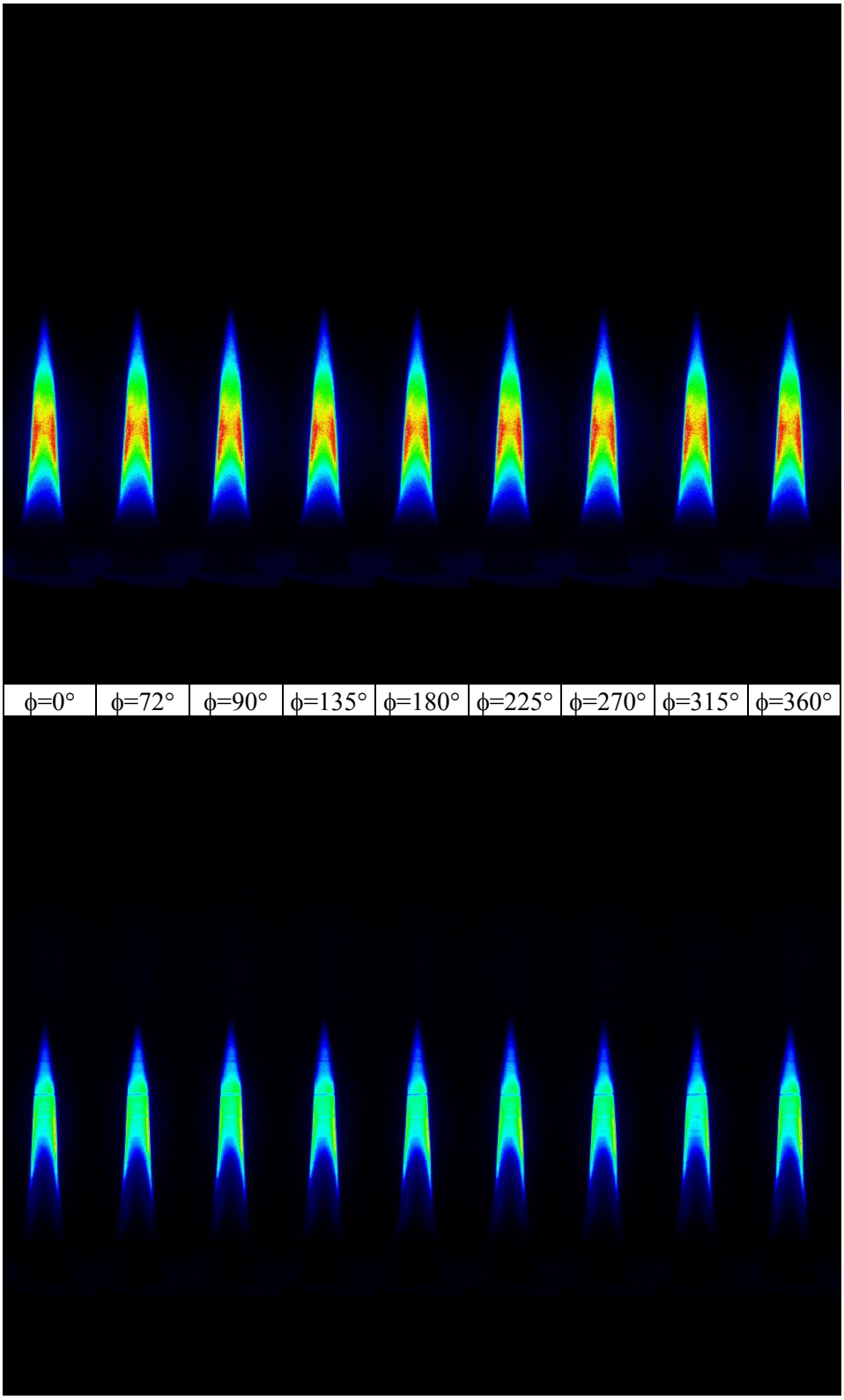

Figure 5.52 Phase-locked images of 55 mm pulsed flame (50 Hz)

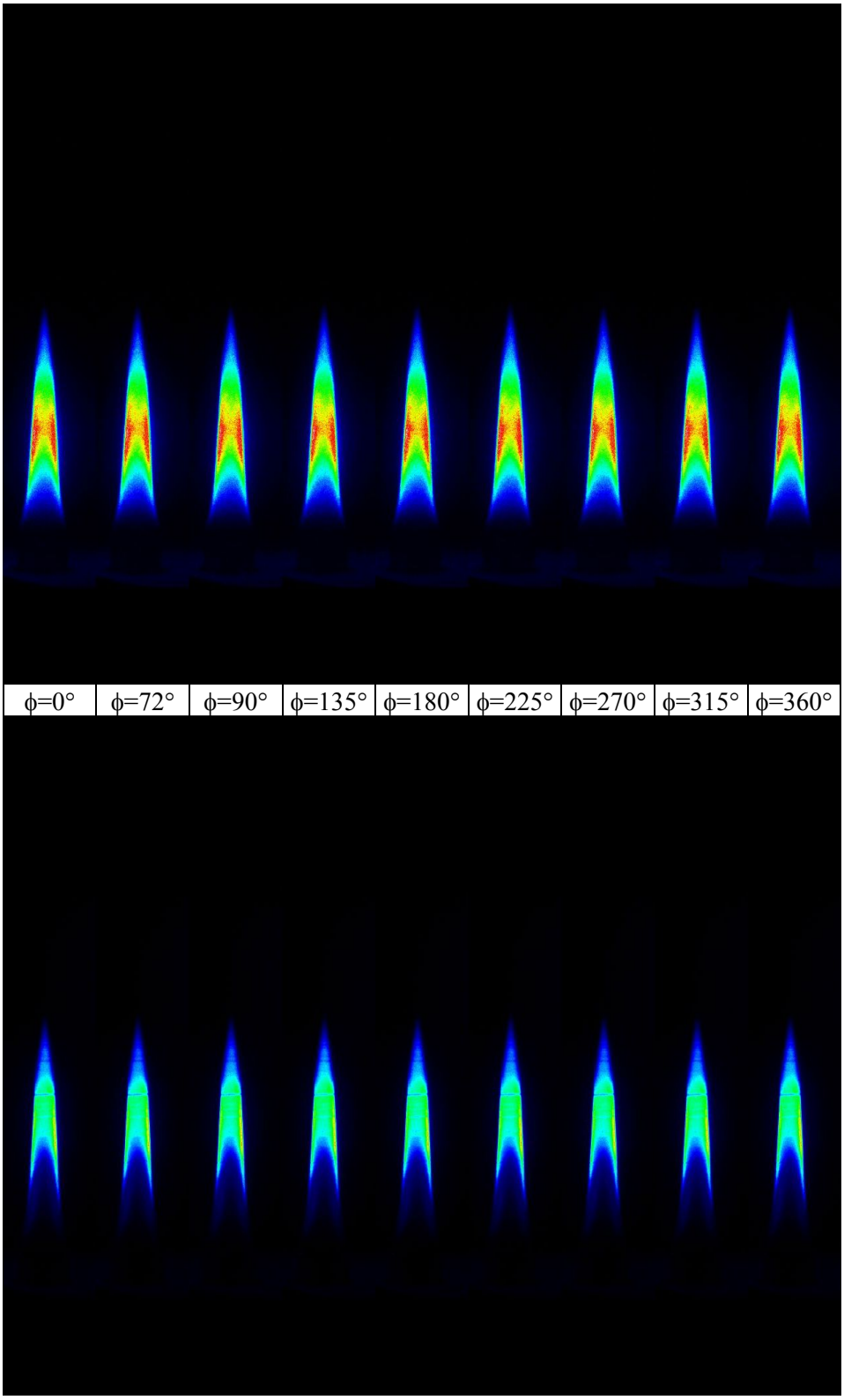

Figure 5.53 Phase-locked images of 55 mm pulsed flame (100 Hz)

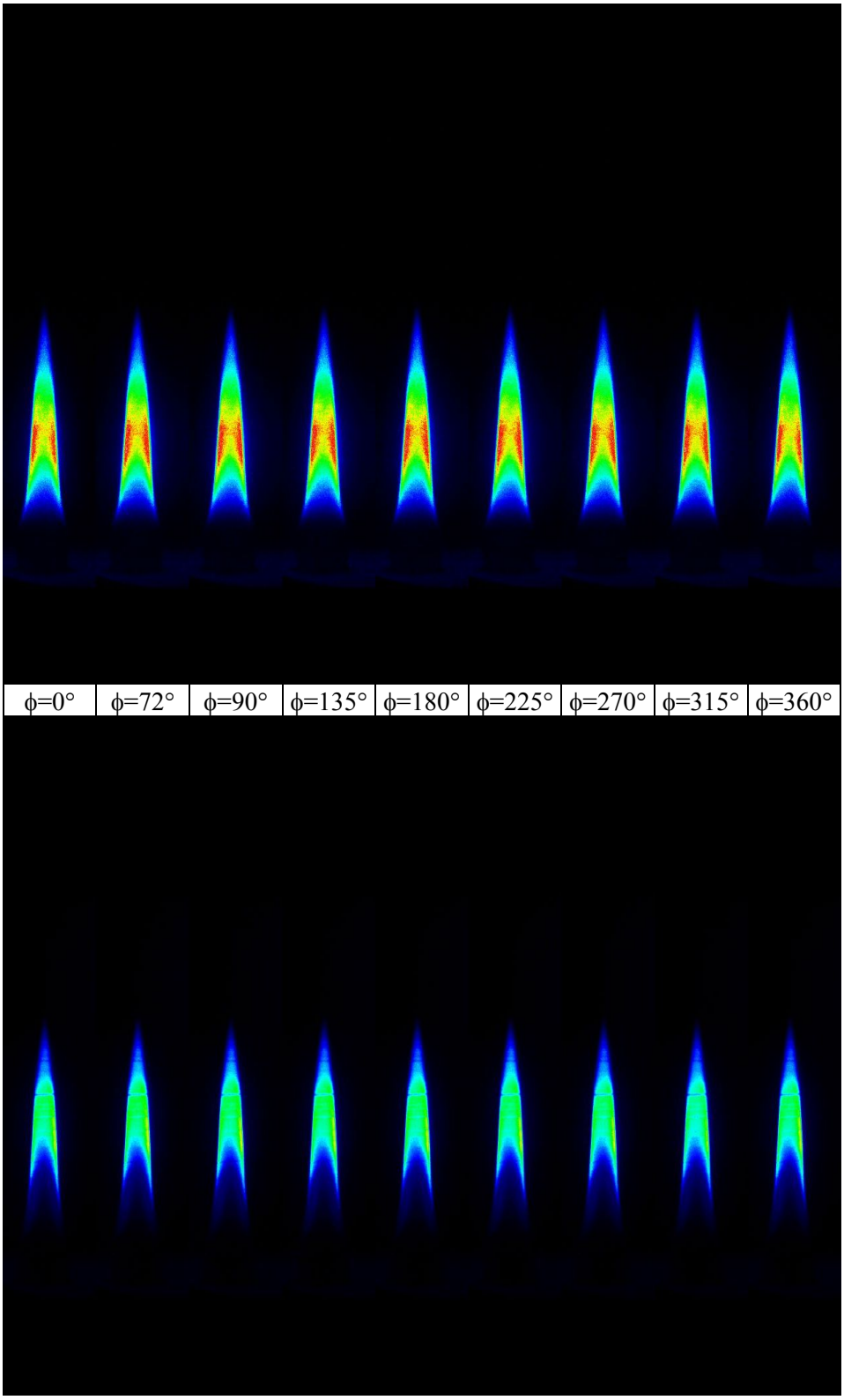

Figure 5.54 Phase-locked images of 55 mm pulsed flame (200 Hz)

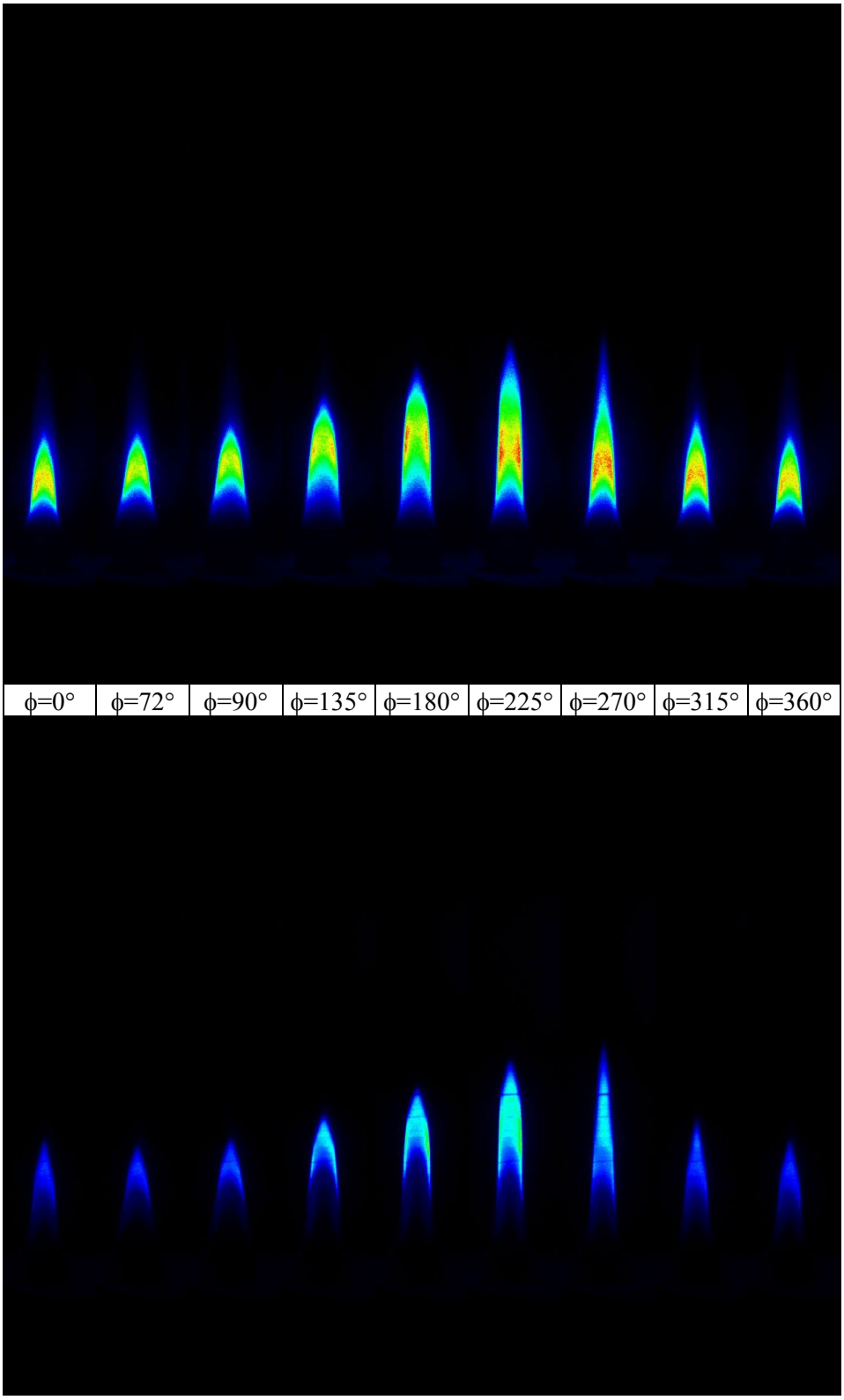

Figure 5.55 Phase-locked images of 35 mm pulsed flame (10 Hz)

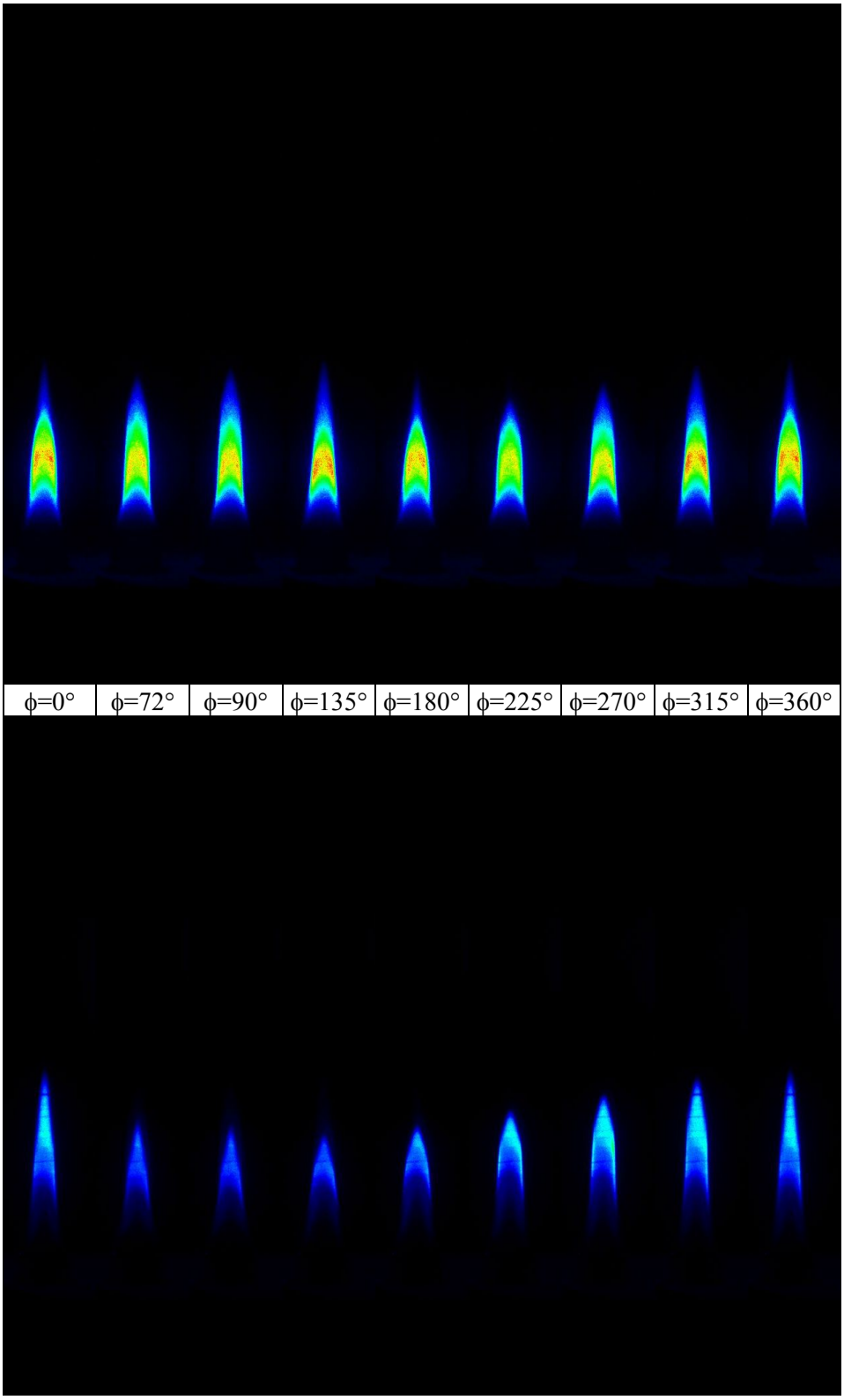

Figure 5.56 Phase-locked images of 35 mm pulsed flame (15Hz)

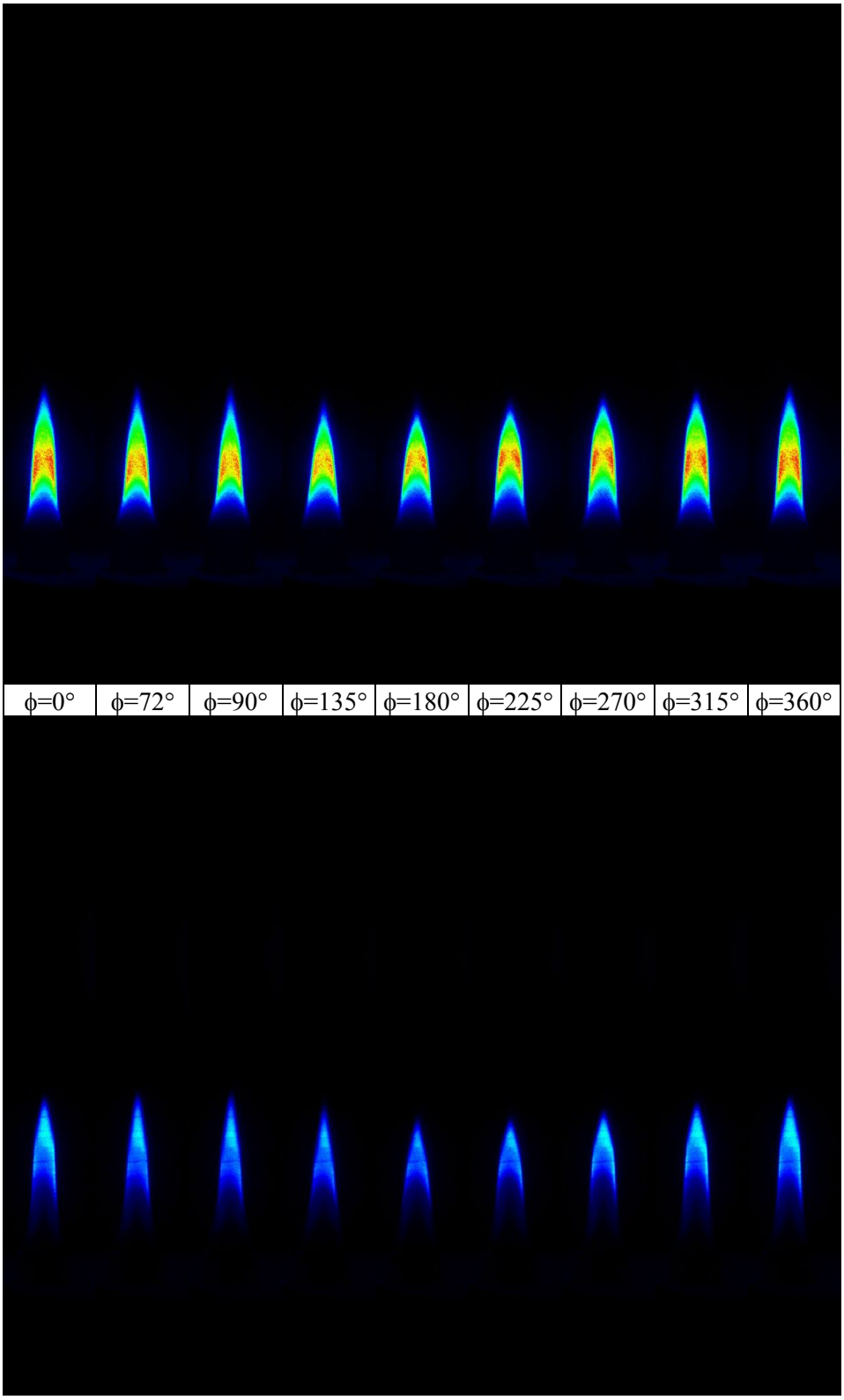

Figure 5.57 Phase-locked images of 35 mm pulsed flame (20 Hz)

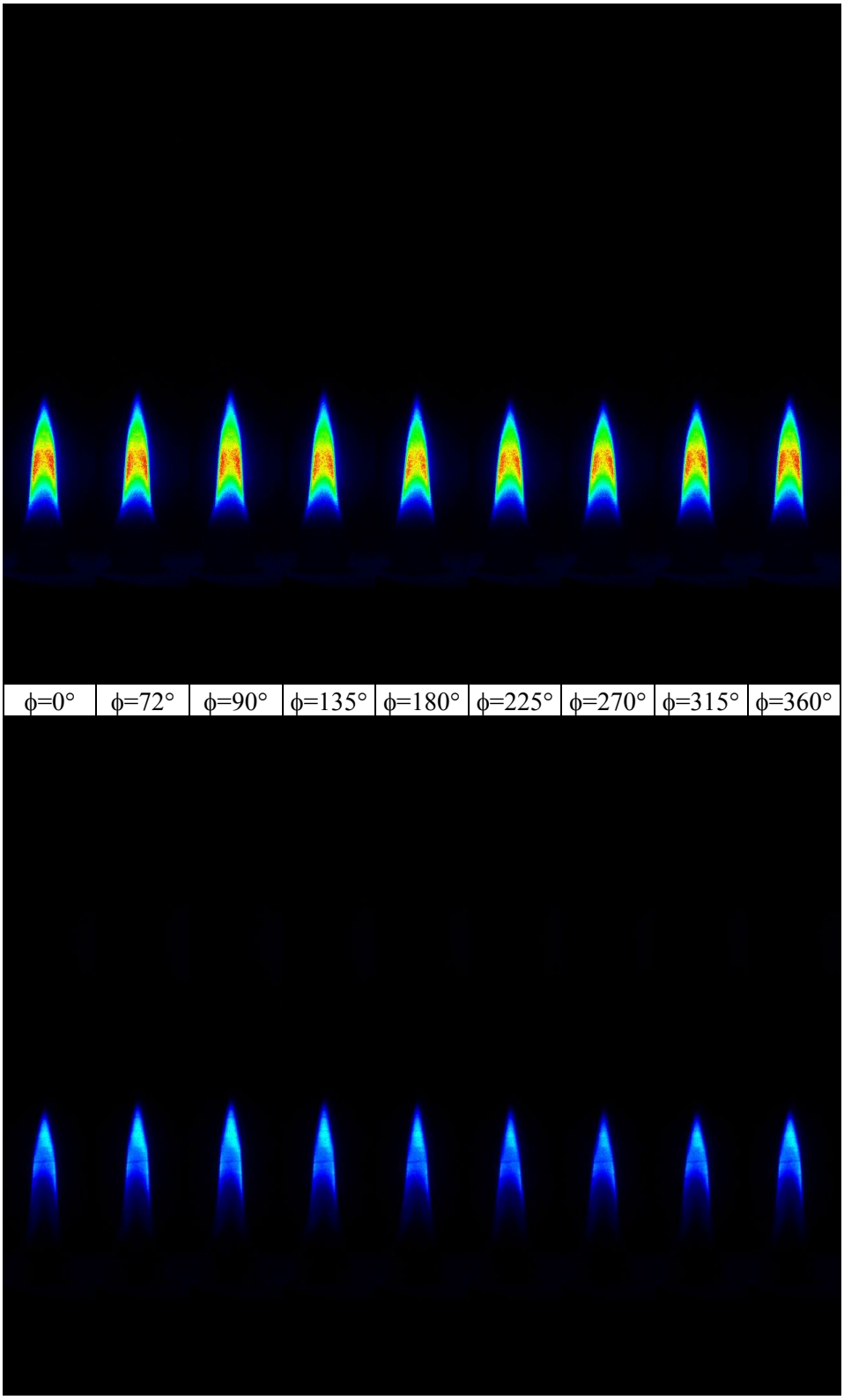

Figure 5.58 Phase-locked images of 35 mm pulsed flame (30 Hz)

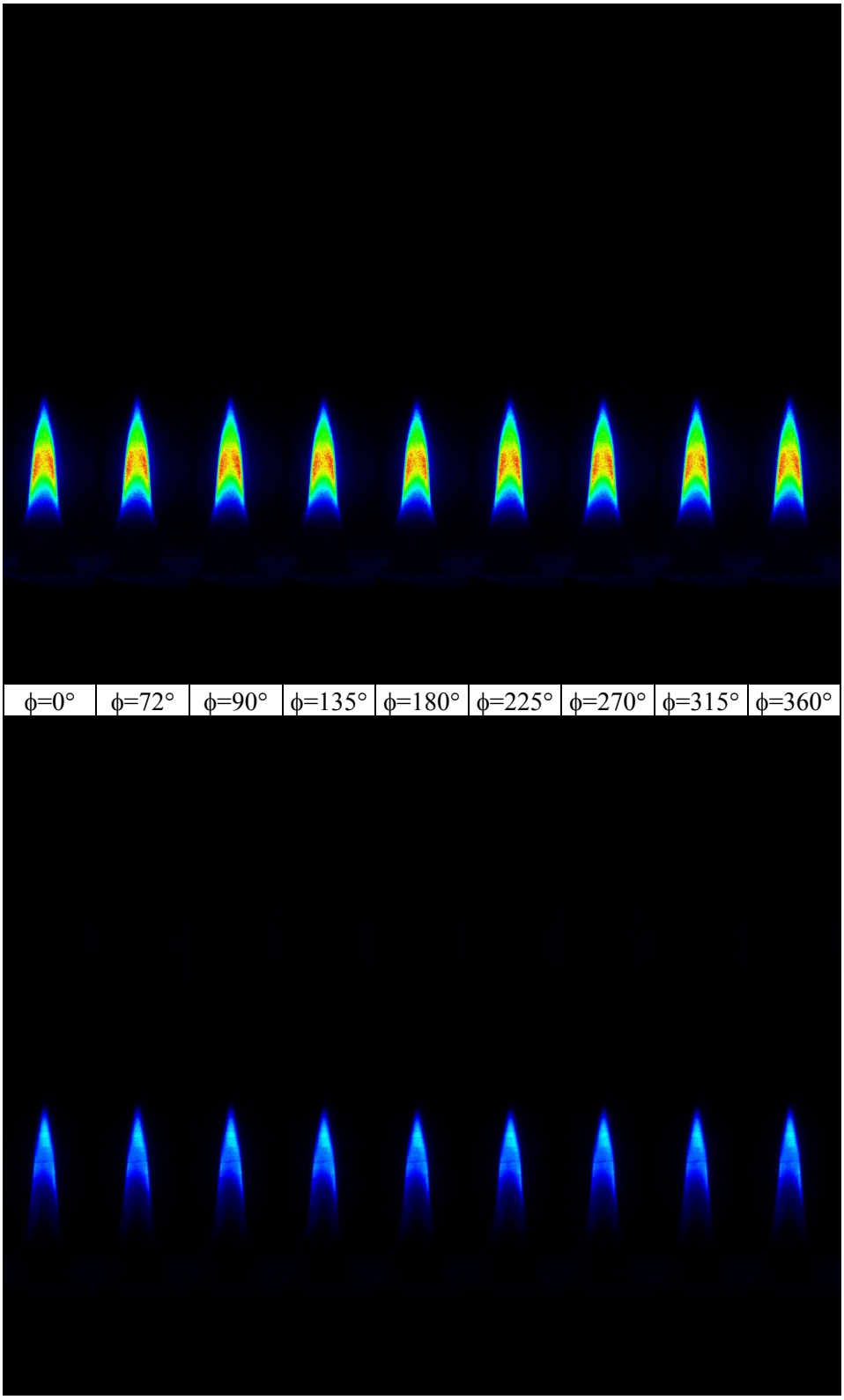

Figure 5.59 Phase-locked images of 35 mm pulsed flame (50 Hz)

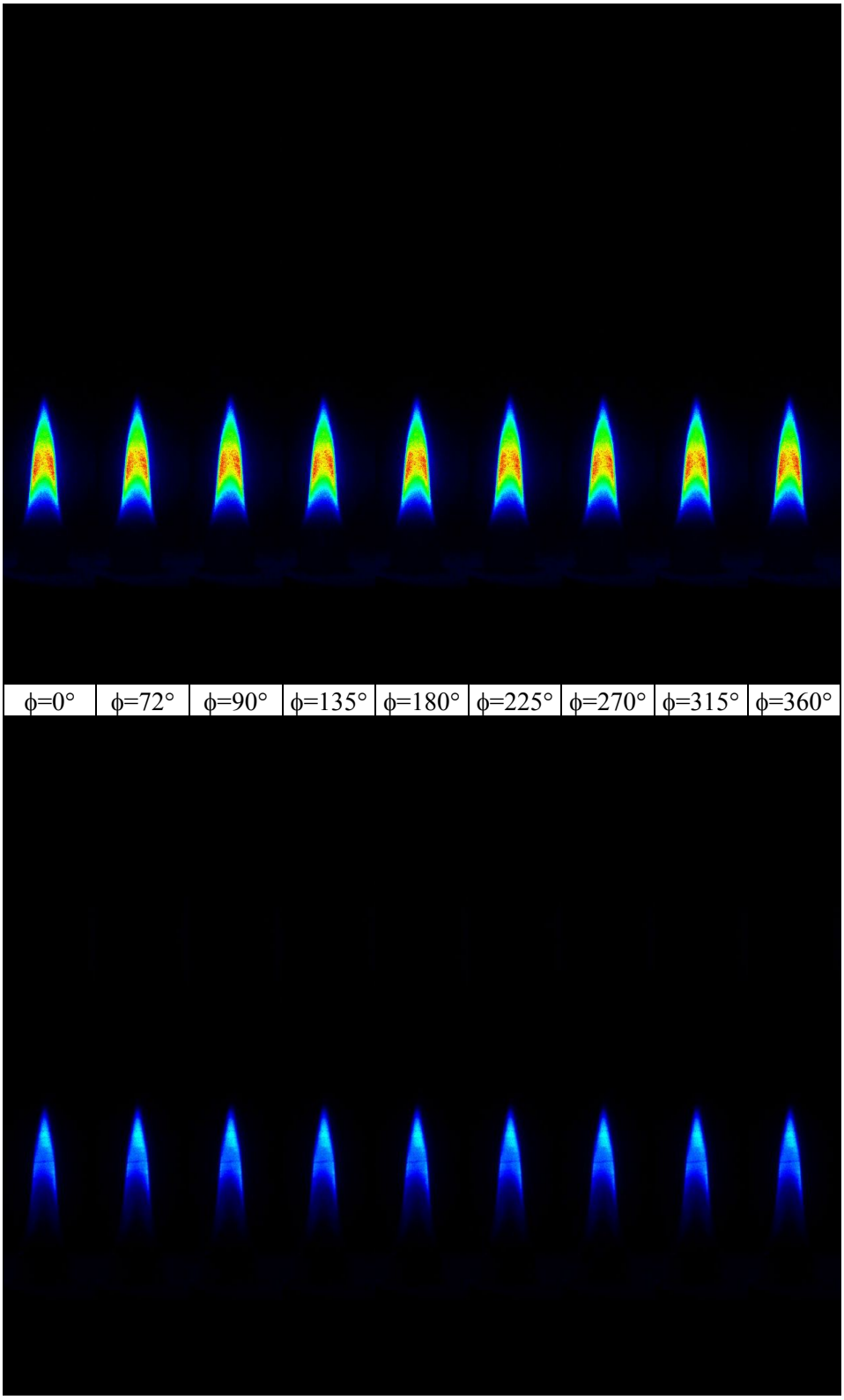

Figure 5.60 Phase-locked images of 35 mm pulsed flame (100 Hz)

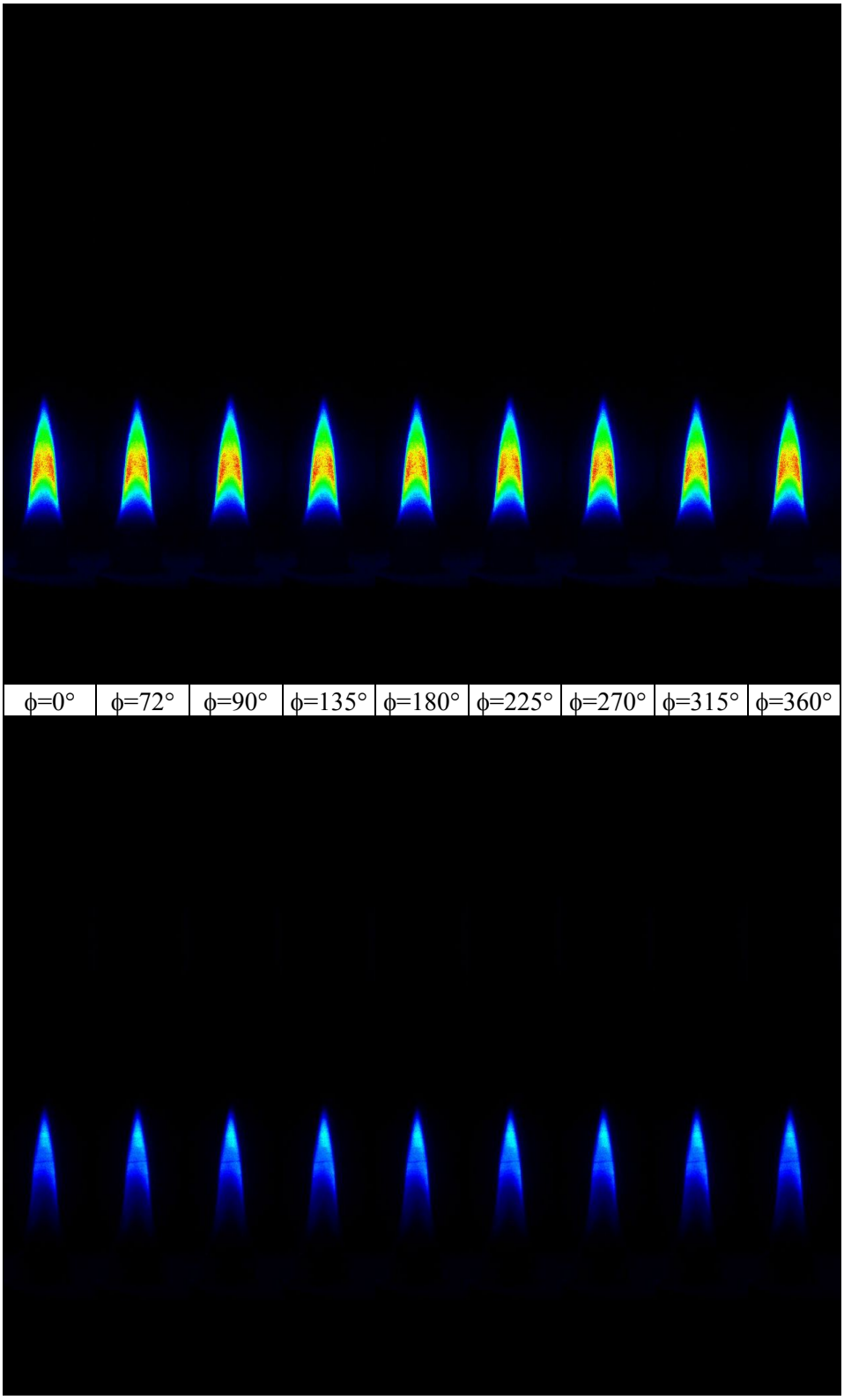

Figure 5.61 Phase-locked images of 35 mm pulsed flame (200 Hz)

CHAPTER VI

DISCUSSIONS AND CONCLUSIONS

6.1 Introduction

In the case of diffusion flames, two diffusing reactant streams (fuel molecules from the fuel supply and jet oxygen molecules from the surroundings) meet within a narrow flame sheet, which is positioned where the local concentrations of fuel and oxygen molecules are at a stoichiometric mixture (mixture fraction is 0.064 for an ethylene flame in air). The region between the flame sheet and conditions where the relative concentration of fuel molecules is twice the stoichiometric mixture is associated with the nucleation and growth of soot particles (fuel rich zone). Assuming that the outer boundary of the yellow luminous region roughly corresponds to the location of the flame sheet, the embedded image of the flame luminosity and the soot (LII) image (Figure 6.1) shows that soot tends to be both produced and consumed (oxidized) just inside the flame sheet. For buoyant diffusion flames, soot mainly nucleates near the flame sheet, at the outer boundary of the soot production region, and then moves radially inward for a time before approaching the flame sheet once again near the flame tip. This implies that fuel concentrations along a soot path line initially increase, then decrease. Furthermore, velocities along soot path lines progressively increase for buoyant flames. This implies that soot production times are proportionally larger than soot oxidation times in buoyant flames.

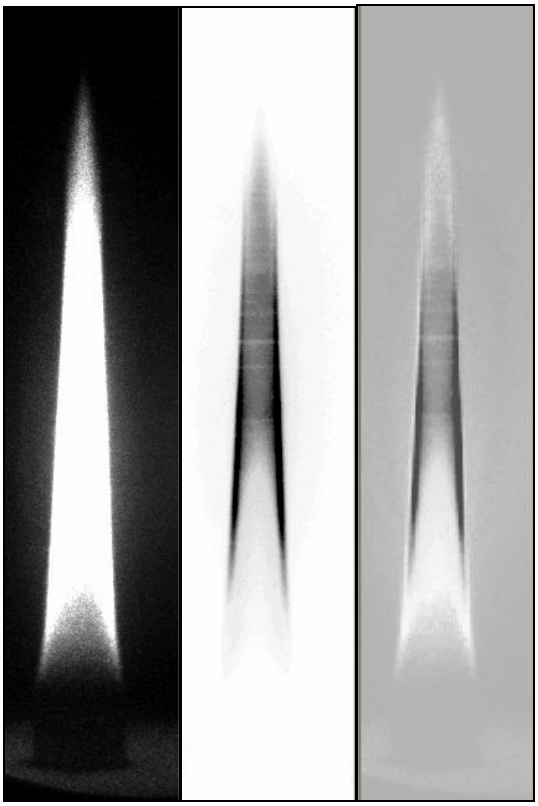

Figure 6.1 Flame emission (left), LII (middle), and the two images embedded in each other (right)

6.2 Steady Diffusion Flames

For the soot measurements, we first investigated a steady laminar flame to establish the baseline for comparisons. Soot for the steady laminar flame consists of primary particles of near spherical shape (Koylu 1996). The size of the primary particles and the degree of agglomeration (number of particles per aggregate) are strongly influenced by the position within the flame. Measurable amounts of soot are first observed in the annular region of the flame. The profiles of the soot volume fraction at different axial positions for the steady flame were shown in Fig. 5.6. The peak of the soot volume fraction in the annular region increases with increasing the axial distance from Z

= 10 to 40 mm and decreases with increasing axial distance for Z > 40 mm. The soot annulus at each height is defined as the radial location of maximum soot volume fraction. It is noted that the soot annulus is shifted toward the burner axis when we increase axial distance from Z = 10 to 70 mm. The maximum value of the peak soot volume fraction for the steady laminar flame (E1) is obtained at the axial distance Z = 40 mm. The maximum soot volume fraction (f_v) increased from about 1 ppm at 10 mm height until it reached a value of 14 ppm at 40 mm height. After this peak, f_v gradually decreased as the oxidation process dominated the soot field.

TEM photographs (Sapmaz 2000) of soot sampled at four heights, namely z = 25 mm, 30 mm, 35 mm, and 40 mm are given in Appendix H to discuss the soot types found in the steady flame. There are two types of soot with different physical and chemical structures present in the flame. The first type, called precursor particles, is translucent under the electron beam (see the smaller single particles in Fig. 6.1-a). The second type is the more familiar carbonaceous aggregates, which are highly opaque and consist of monodisperse spherical particles joined together (see Fig. 6.1-d). A further examination reveals that (Koylu et al. 1997) the translucent precursors, whose boundaries are difficult to identify, are of nonuniform sizes at z = 25 mm. As these soot precursor particles move to z = 30 mm at the flame centerline, they become more opaque, more spherical, and uniform in size. Similar microstructures can also be seen at a higher location, z = 35 mm. Interestingly, the precursor particles start aggregating before their transformation to mature soot (carbonization) is complete. As the mixture of both types of soot is transported higher in the flame, the type 1 particles are completely carbonized. This is evident from the presence of only type 2 aggregates at z = 40 mm.

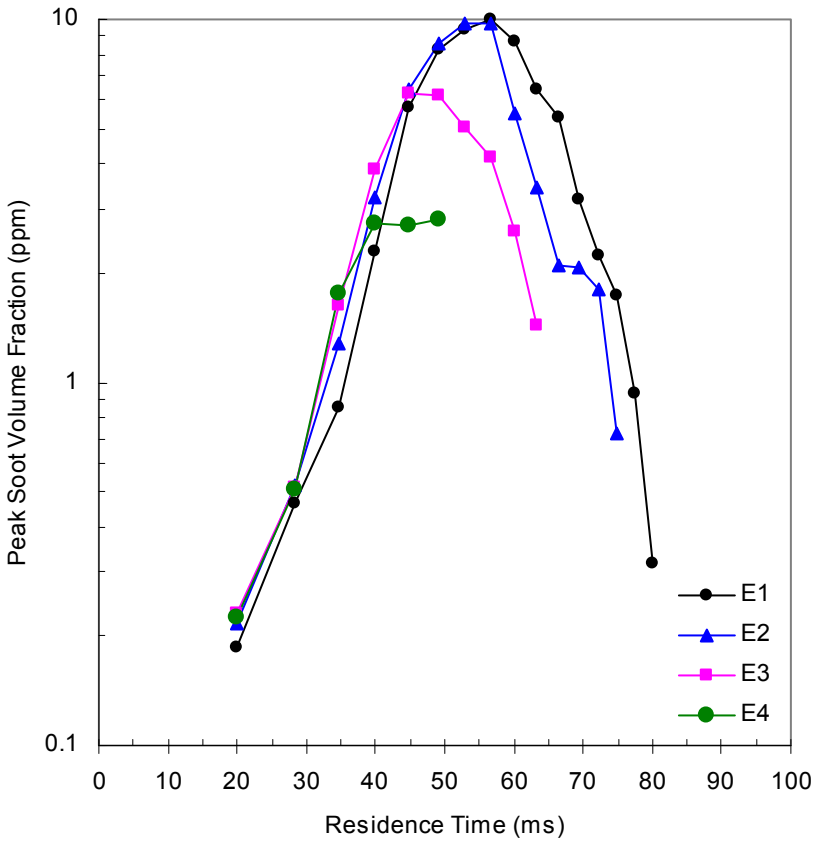

Figure 6.2 Comparison of soot volume fraction along the streak lines exhibiting the maximum soot volume fraction (annular region)

Each of the flames undergoes a similar evolution process, region of growth and region of oxidation (except E(4)), shown in Figure 6.2. Residence times are predicted by the simple expression, $t \cong \sqrt{2z/a}$, where z is the height above the burner (axial location), and a is gravitational acceleration (≈25 m/s^2) felt by the buoyant flames (Santoro 1987). As the fuel rate increases, the maximum soot volume fraction becomes higher and shifts to a slightly larger radial position. Along the center line (Figure 6.3), in contrast to the annular region, the maximum soot volume fraction values are nearly equal, with no

significant increase in soot volume fraction as the flow rate increases. From these observations, we can say that the annular region controls the soot formation and oxidation as the fuel rate is changed.

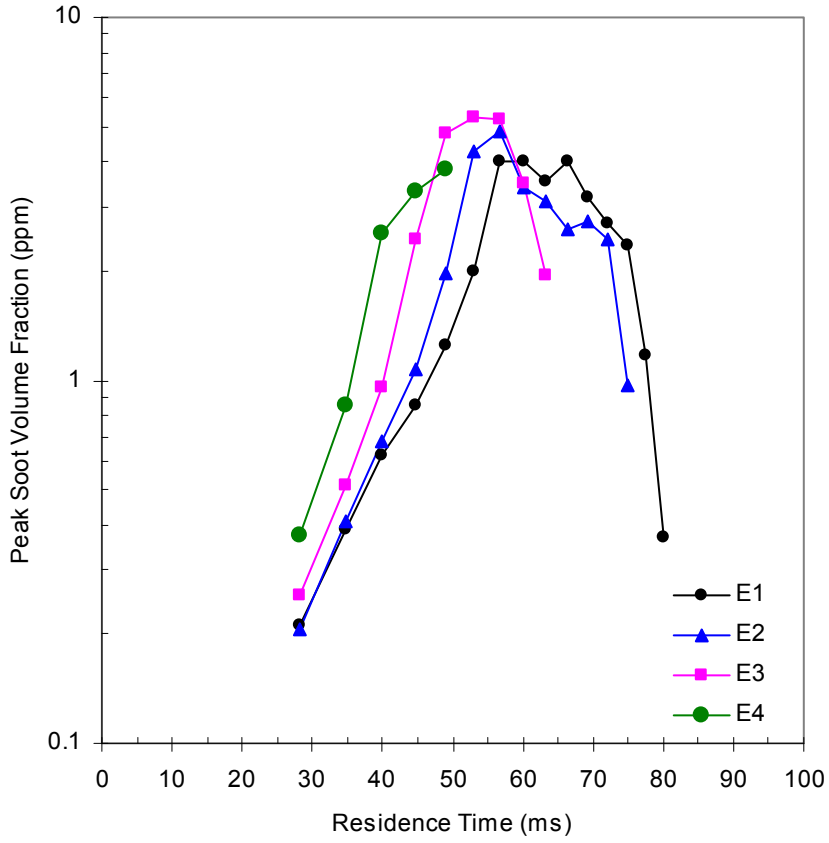

Figure 6.3 Comparison of soot volume fraction along the centerline of studied flames

A nondimensional axial coordinate ($\eta \approx 0.011$) was found to provide a good scaling in terms of location of the maximum soot volume fraction in steady flames (Roper 1977). Figure 6.4 shows the definition of this nondimensional parameter. The diffusion coefficient, D (=0.156 cm/s), and the air/fuel ratio, S (=14.28) were used to

calculate the axial coordinate. Axial distances (HAB) corresponding to maximum soot volume fraction values are 40 mm, 35 mm, 28 mm, and 20 mm for steady flames E1, E2, E3, and E4, respectively.

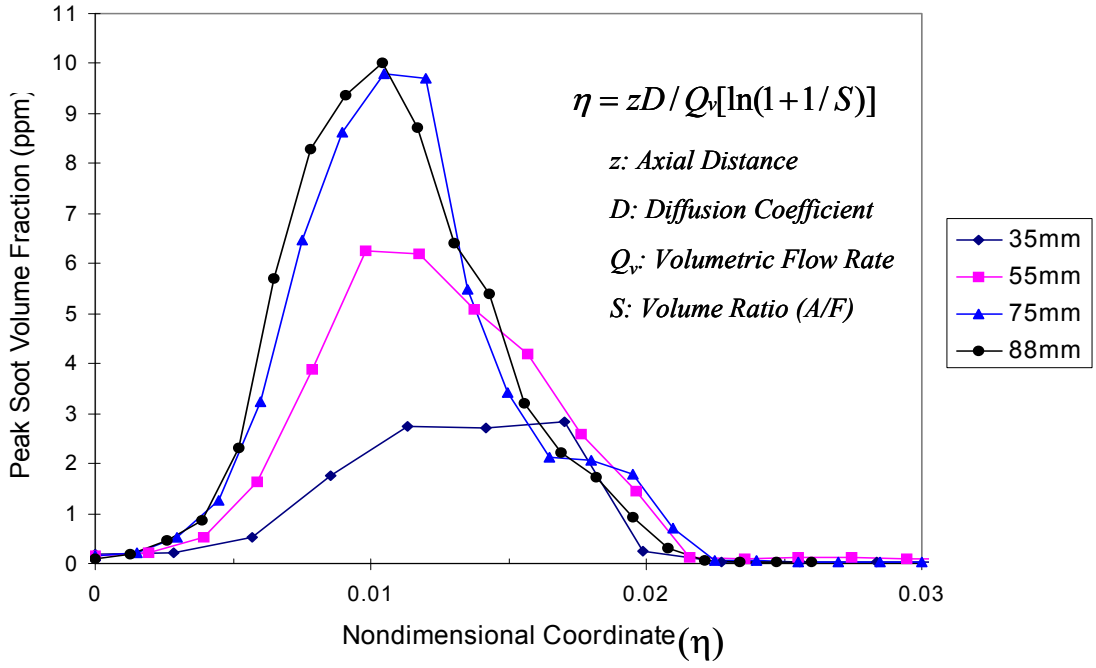

Figure 6.4 Peak soot volume fraction versus axial coordinate for steady flames

6.3 Pulsed Diffusion Flames

Images at the top of Fig. 5.34 show typical flame visible luminosity images of the pulsed E1 flame (f = 10 Hz). The laser beam was blocked for the visible luminosity images since these images are used only to show the shape and the height of the visible flames. The images show that the visible flame height and shape depend on the oscillation frequency of the flame and the phase (ϕ) over one pulsation period. The sequential images show the dynamics of the interactions between the generated vortices in the fuel and the flame (flame-vortex interactions). The large vertical structures

containing fuel pushes the flame surface in the axial and radial directions, showing the flame length elongation and the reduction region. Consequently, the flame surface is stretched causing local flame extinction. The average images (average of 10 instantaneous images) of soot volume fraction for the pulsed flames are shown at the bottom of Fig. 5.34. These are phase locked soot volume fraction (or LII) images obtained with a frequency of 10 Hz and a phase range between 0 and 360^o. The phase locked images for the pulsed flames reveal the entire motion process of the soot field during one pulsation period corresponding to time between 0 s ($\phi = 0$) and 0.1 s ($\phi=360^o$). The images show a strong growth of soot volume fraction as the soot field is convected to higher locations during the evolution of the second half of the flicker cycle ($\phi = 180 – 360^o$). During the first half of the flicker cycle ($\phi = 0 – 180^o$), the images show an opposite trend for the soot field. Figure 6.5 is the equivalent of Figure 5.6 so that the steady E(1) and the pulsed (10Hz) E(1) results can be compared in more detail. Comparison between radial profiles in Fig. 5.6 and Fig. 6.5 reveals the effect of pulsation in soot formation. The gap between the amount of soot produced in the annular region and the central region of the steady flame was diminished, and the peak soot volume fractions were observed in larger radial locations (further from flame center axis) when pulsation was introduced.

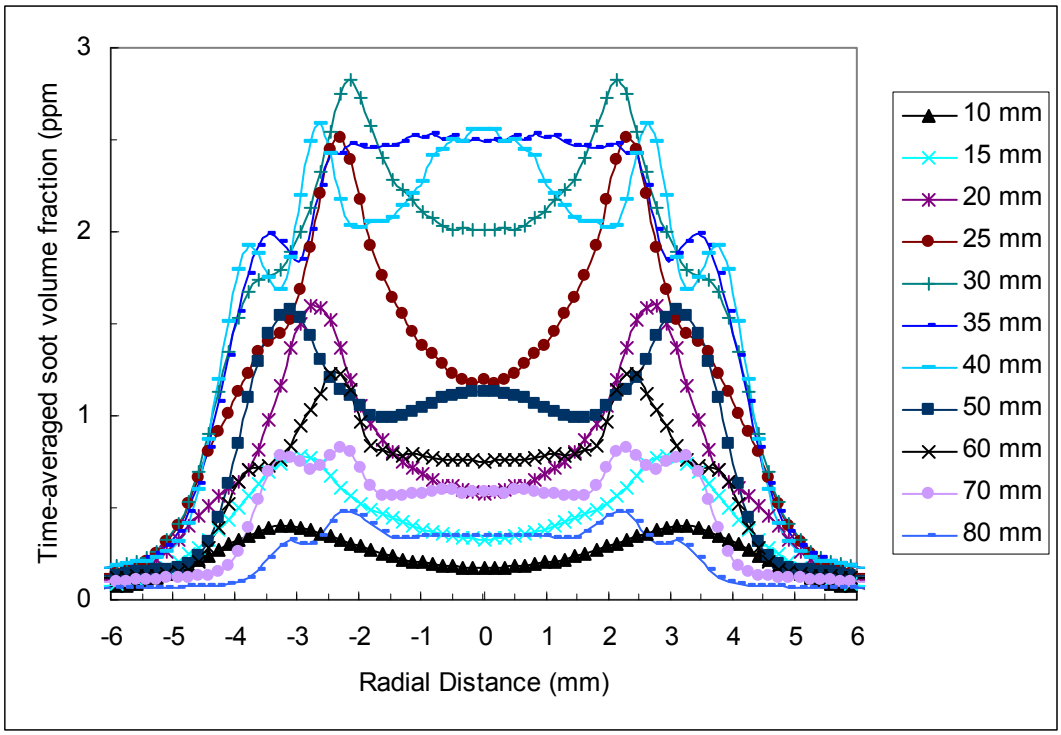

Figure 6.5 LII profiles for time-averaged pulsed E(1) flame at 10 Hz at various axial heights

To study the effect of the flame oscillation frequency on soot volume fraction, we needed to compare the overall soot volume fraction for the steady and pulsed flames. We spatially integrated the soot volume fraction values in the z direction between the burner tip and the visible flame height for the steady flame and for all of the phase-locked images for unsteady flames from the 2-D LII images. This was then followed by the time averaging for all of the phase-locked images (full cycle period) for unsteady flames. It is noted that the soot volume fraction images for different forcing frequencies are measured on the same scale (the same filter is used for different forcing frequencies). The result of time averaging and space integration in the axial direction is shown in Fig. 5.18. For the pulsed flame, the soot volume fraction increases by increasing the oscillation frequency

of the flame from 10 Hz to 200 Hz. The data presented in Table 5.4 show: (1) the total soot volume fraction in the flame for the steady flame is higher than the pulsed flames E(1) and E(2) and smaller than pulsed flames E(3) and E(4), and (2) the total soot volume fraction in the flame decreases by reducing the pulsing frequency (except E(4)).

The results obtained in this study are in good agreement with those obtained previously by Yang and Seitzman [16] using acoustical excitation of the flame. Yang and Seitzman reported in their study, that the total soot was decreased when the flame was acoustically forced at 320 Hz compared to the unforced flame. For the pulsing frequency of 10 Hz for E(1), the total soot volume fraction in the present study was nearly reduced by 28% of the luminous portion within the flame. Shaddix (1996) used acoustic excitation at 10 Hz (identical to the E(1) flame pulsed at 10 Hz) to have moderately and strongly flickering ethylene flames with the same mean flow rate of steady case. He concluded that the integrated soot volume fractions are essentially the same for all conditions (steady and flickering) when considering only the luminous portion within the flame. Regarding peak soot volume fractions, Shaddix (1996) observed up to a 54% increase compared to the steady case, whereas, we observed no change in the peak soot volume fraction. The disagreement between our results and Shaddix's results is possibly due to a fundamentally different approach used to control the fuel flow that can give rise to modification of the combustion and flow characteristics of flames, leading to different fuel/air mixing mechanisms compared to the case of acoustically excited flames. Shaddix suggested that for the flow rate and burner geometry, the ethylene flame was quite close to its maximum soot volume production (limitation of ethylene in its ability to convert fuel carbon to soot). Considering that a considerable amount of smoke from the flickering

ethylene flame was observed in the post flame region for pulsing frequencies less than 30 Hz, it might be possible that the limited soot produced did not have a long enough oxidation region or that repetitions of oversupply and a lack of the oxygen occurred at the breakup of the flame surface (clipped-off flamelet). This might be an explanation of why some part of the potential soot within the flame was lost and caused the reduction of the integrated in-flame soot volume fraction at the pulsing frequency of 10 Hz.

Primary particle diameters (d_p) were extracted from TIRE-LII experiments using the double-exponential fit method for different phases at 10 Hz (Fig. 6.6). Axial locations for radial profiles were selected at maximum soot volume fraction locations.

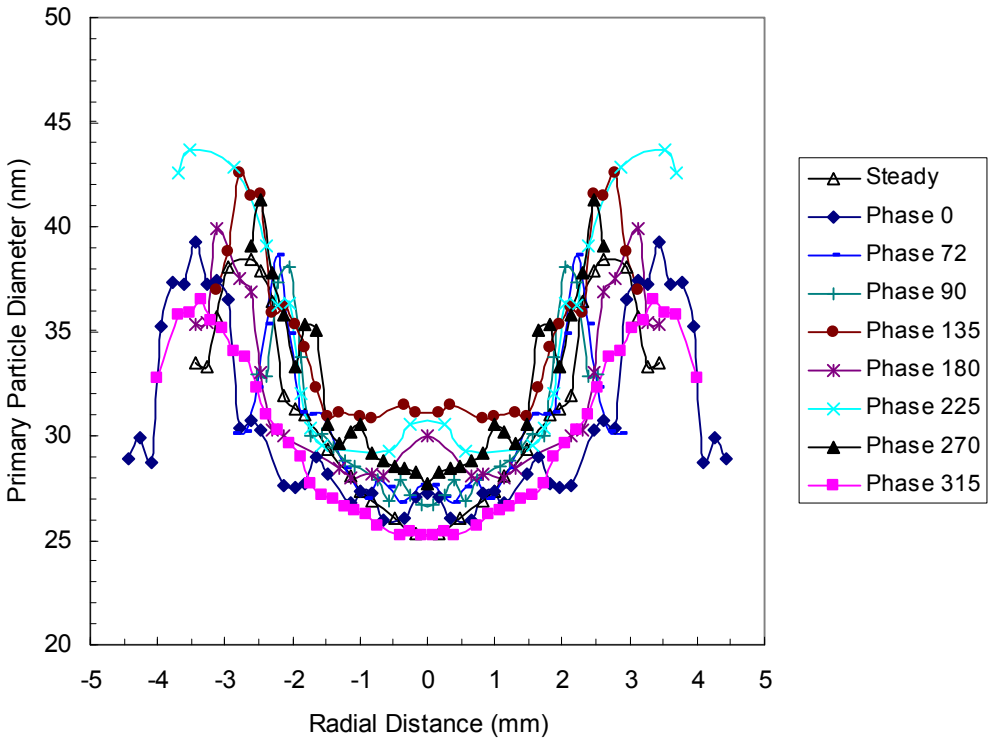

Figure 6.6 Primary particle diameter (d_p) radial profiles for different phases (Φ) for unsteady E(1) flame pulsed at 10 Hz

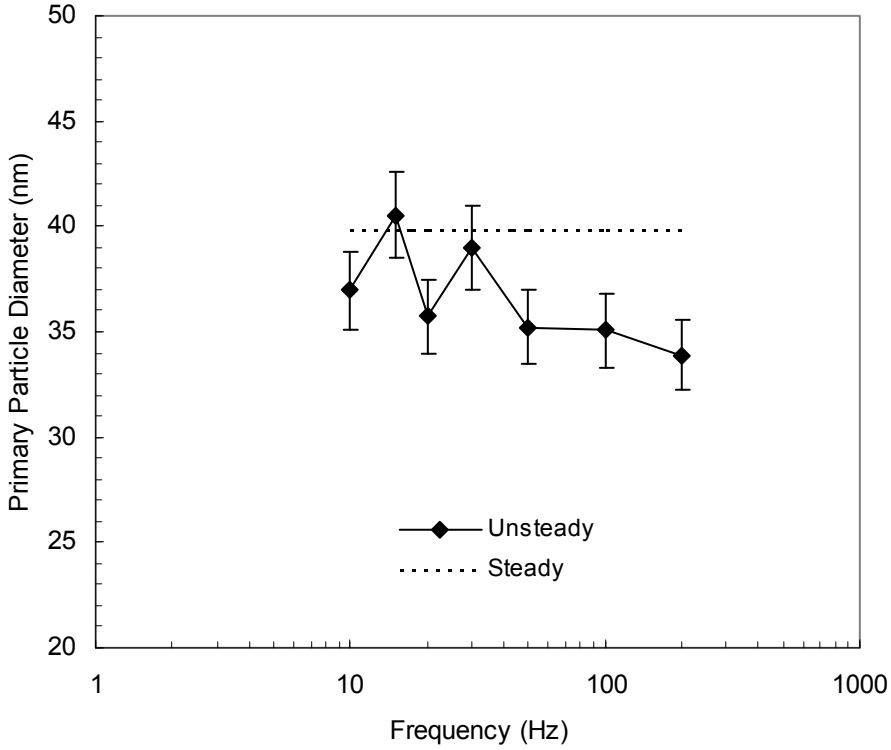

Figure 6.7 Primary particle diameter (d_p) at maximum soot volume fraction location for different pulsing frequencies for unsteady E(1) flames

The peak primary soot particle diameter (d_p) values were found to exist at the maximum soot volume fraction (f_v) locations. The peak values of d_p were between 36.5 nm and 43.7 nm for the 10 Hz E(1) flame whereas the peak d_p for the steady E(1) flame was 38.5 nm. To see the effect of pulsing frequency in the peak diameter, the maximum peak d_p values corresponding to the maximum $f_v(r,z)$ location out of all of the phases were plotted against the pulsing frequencies in Fig. 6.7. The d_p values changed between 40.5 nm and 34 nm while the peak f_v values changed between 10.5 ppm and 12 ppm. At maximum frequency (200 Hz), the soot particles were smaller in size by 15% compared to the steady case.

6.4 Other Issues

6.4.1 Experimental Uncertainty

There were uncertainties in the value of the soot refractive index (Figure 6.5) and its variation with flame temperature and the particle composition. The H/C ratio of soot could vary by a factor of five with height above the burner surface. The most commonly used soot refractive indices give *E(m)* values between 0.2 and 0.3 in the literature.

Experimental uncertainty on the results of the single LII images, average of 10 LII images, volume-integrated LII images and emission images are +/- 11.5%, 6.5%, 3.3%, and 0.3%, respectively with 95% confidence. The standard deviation of the laser energy per pulse measurements is +/- 4.5 %. Experimental uncertainty for post flame measurements is +/- 10%.

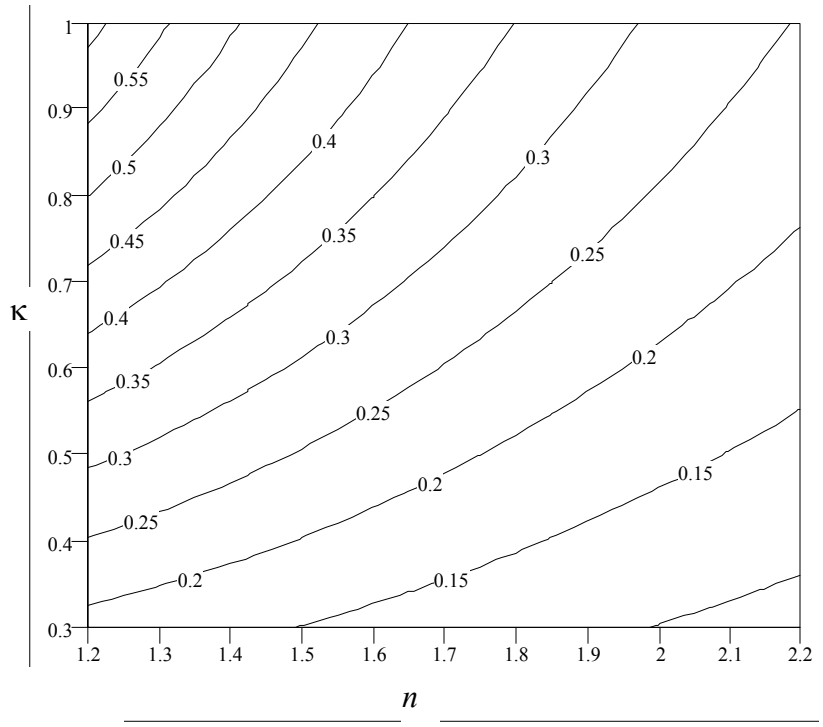

Figure 6.8 Sensitivity (contour plot) of E(m) function

6.4.2 Excitation Wavelength/Detection Wavelength

Since soot can be treated as a blackbody (Appendix F), it absorbs laser light in any wavelength (at 266 nm light, 532 nm light or 1064 nm light). In other words, soot will be heated to the incandescence temperature regardless of the excitation wavelength. UV excitation is preferred for Laser Induced Fluorescence (LIF) measurements because UV light electronically excites PAHs resulting in fluorescence along with incandescence (LII) (Vander Wal 1997). In comparing fundamental (1064 nm) and doubled (532 nm) Nd:YAG beams, there is a large reduction in C_2 interference for infrared excitation. C_2 interference changes linearly with laser fluence while the LII signal comes to a threshold value. It will affect the overall signal detected more than LII at detection near the emitting C_2 bands. In other words, the C_2 signal does not necessarily behave like the LII signal and it should be treated as a contamination of the LII signal. This suggests the IR excitation for LII purposes to avoid the C_2 interference. Vander Wal (1997) used the 266 nm excitation that yielded the LII and LIF signals together simultaneously along with the 1064 nm excitation that only yielded the LII signal with no interferences (in the same flame studied in this study) by using a 400 nm to 450 nm detection. He used these signals to find the onset of the fundamental material property change, which was at 33-34 mm HAB. Therefore, in his experiments, the LIF was contaminated with the LII. Visible excitation might yield molecular interferences for a particular excitation/detection scheme. If there is any interference, IR excitation can be employed to remove this issue or the detection spectral range can be adjusted with careful examination of the LII spectra to eliminate the interferences. Another method first suggested by Cignoli et al. (1994) is a delayed detection within 100 ns after the laser pulse to avoid the contributions from

molecular emissions as well as elastic scattering because of their short lifetime compared to the LII signal lifetime. Even though we were confident that there were no contributions after the LII spectra experiment, the non-delayed LII image was compared with a 50 ns and a 100 ns delayed detection LII image (600 nm detection filter). The delay time was kept under 100 ns due to the fact that delays longer than 100 ns would more significantly favor larger particles. The peak LII signals at each axial location was normalized with the peak signal in the overall flame (See Appendix E, Fig. E.1). Also, the LII signals at the centerline at each axial location (normalized by the maximum value) in the overall flame were presented (See Appendix E, Fig. E.2). The noise was due to the low laser fluence (a larger LII dependence on laser energy), a 5 image averaging, and no radial or axial binning. As can be seen from the figures, there was almost no change in the normalized values of delayed and non-delayed cases all across the flame (annular and central regions), as expected from LII spectra experiments.

6.4.3 Laser Defocusing Effect on the LII Signal

The laser defocusing effect on the LII signal is important for detection systems in which the sampling depth of field is greater than the laser sheet width (0.6 mm). The depth of field of a camera lens with a 50 mm focal length and a 1.4 lens f / stop focused at 400 mm is +/- 2 mm (398 mm near depth and 402 mm far depth). The laser sheet was a Gaussian laser sheet with 85% of its energy in a 0.3 mm half sheet thickness in the direction perpendicular to laser propagation (Section 4.4.6). In the axial direction, only 100 mm of laser sheet was used so that the laser sheet stayed within 80% of its intensity for the center half of its axial length of interest. The light sheet adjuster module was built as an adjustable Galilean telescope, preventing internal beam focusing. The laser sheet

was focused at the burner tip center. Around the focused distance (before and after laser sheet hit the burner tip), there was minimal beam defocusing effect (See Appendix D, Fig. D.1 and Fig. D.2). The radial profiles given in those figures are the normalized average representation of the radial profiles across all laser heights above the burner.

6.5 Correlation for Volume-integrated Time-averaged Soot Volume Fraction

The total soot production tendency of ethylene in the flame region was plotted in Fig. 6.9 in terms of the Strouhal number. The Strouhal number is a dimensionless number describing oscillating flow mechanisms. It is given as, $Str = f \cdot d/U$, where f is the oscillating frequency, d is the characteristic scale (internal diameter of fuel tube), and U is the average velocity of the gas fuel at the fuel tube exit. For the pulsation frequencies tested ($10\,Hz \le f \le 200\,Hz$) and the flames studied ($25 \le \mathrm{Re} \le 55$), the Strouhal number was found to range between 2.6 and 115. The results were plotted and shown in Fig. 6.10 for the maximum three flow rates (E(1), E(2), and E(3)) in terms of total soot formation by dividing by the Reynolds number (f_v/Re). In the efforts of expressing the results in terms of a correlation, it was decided to investigate two regions. The first region, referred to as Region I, is the region where f_v has a strong dependence on the Strouhal number (Str<8). The second region, referred to as Region II, is the region where f_v has a slight dependance on the Strouhal number ($\mathrm{Str} \ge 8$). For these two regions, two different correlations (linear fits with 95% confidence) were developed in the form:

$$f_v \,\mathrm{Re}^{-1} = a + b \cdot Str \tag{6.1}$$

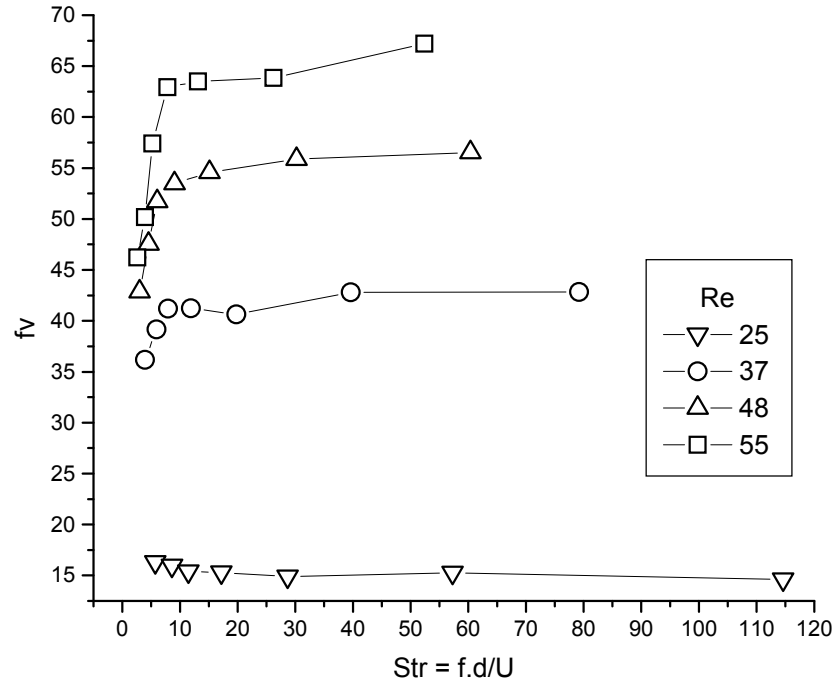

Figure 6.9 Total soot volume fraction versus the Strouhal Number

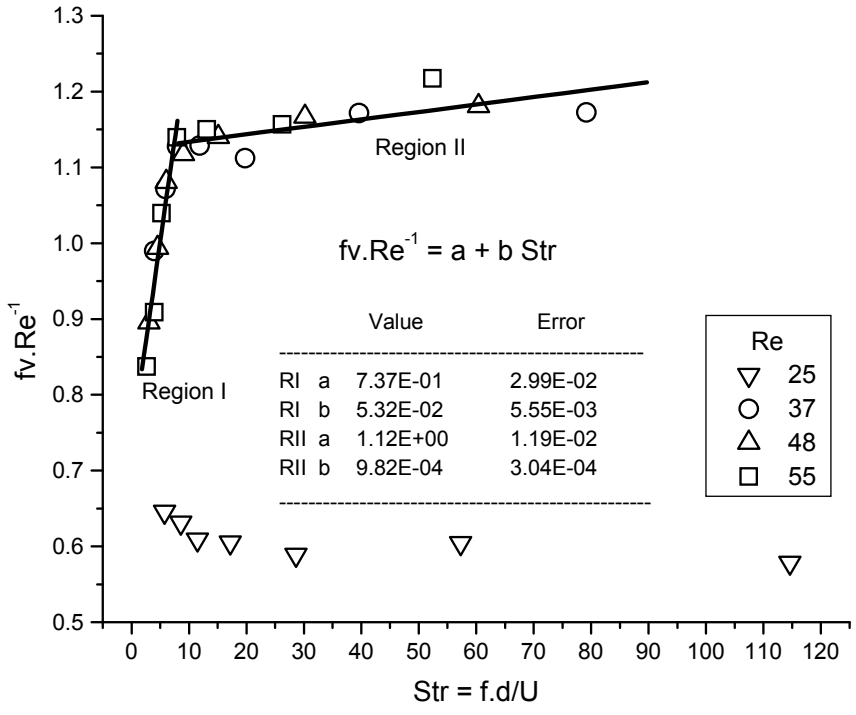

Figure 6.10 Correlation functions expressed in two regions for soot formation

The ratio of slopes for the two regions is 54, indicating the drastic change between them. In order to have a more physical and chemical explanation of soot formation, VHS valve characteristic parameters are calculated and presented in Appendix I. These parameters are namely, α_i (the injection duty cycle, α_i =0.2), Ri (the injection time, Ri=α_i/f), Ro (the off time, Ro=((1-α_i)/ α_i).Ri)), Vo (the volume of the injected gas in one period), Vt (the volume of the injected gas in one second), H (the height of an idealized puff cylinder with a base diameter equal to the fuel tube inner diameter, H=U.Ri), and P (pulse parameter, P=$(H/d)^{1/3}$, Hermanson et. al (2004)).

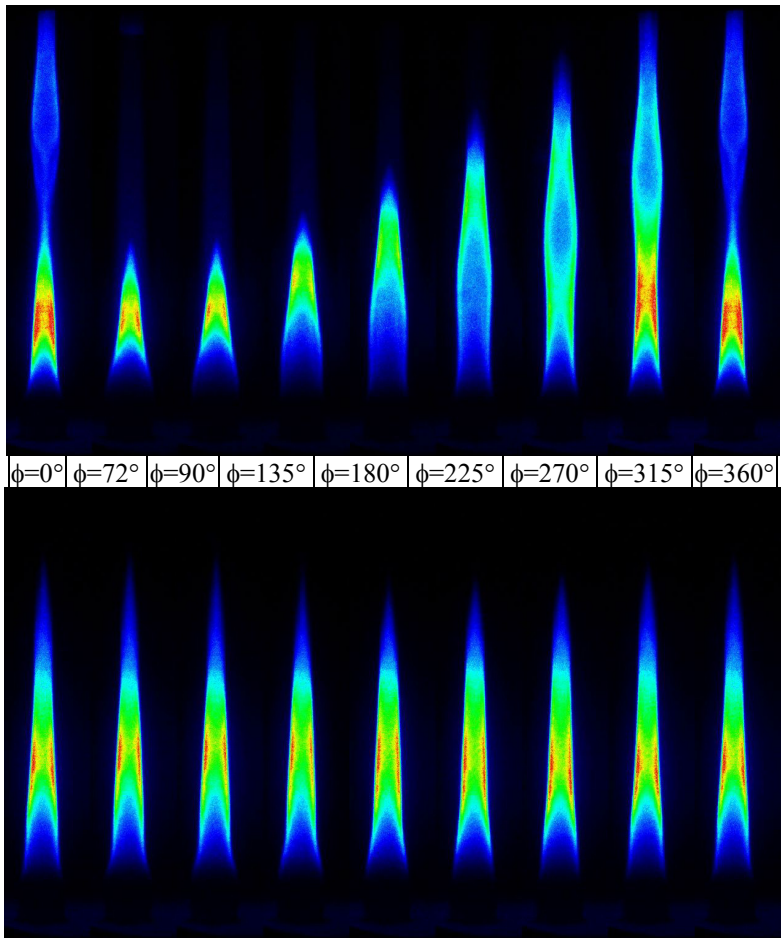

Figure 6.11 Bulk flickering flame, Type A (top), tip flickering flame, Type B (bottom)

For the steady laminar flames, the fuel and the air are supplied continuously resulting in a flame elongated in the direction opposite to the gravitational force (See Fig. 5.32). When the fuel flow is modulated by the VHS valve operation to create the unsteady or pulsed flames, the flame shapes, flame structure, and flame length are changed. This change is rather easy for the laminar flames due to the relatively low fuel exit velocities. Because the soot particles (unlike the gas molecules) are too large to diffuse, (therefore, they are convected at local gas velocities along the flow streamlines) and because the annular region (region close to the flame sheet, the outer boundary) controls the soot formation and the oxidation (See Sect. 6.2), the soot formation is greatly dependant on the unsteady fields introduced in this study. This dependence is very high when Str<8 (Region I (Fig. 6.10)). In this region, the laminar flame bulks up into a block of large flame by the flickering motion. The pulse parameter (P) is larger in this region as well as the height (H) of an idealized puff cylinder (1.4 mm $\leq$ H<4.2 mm). The visible flame heights were found to change between 47 mm and 106 mm for E(1) with 10 Hz pulsation (Fig. 6.11, top image), 63 mm and 104 mm for E(1) with 15 Hz pulsation, and 76 mm and 103 mm for E(1) with 20 Hz pulsation, corresponding to Str<8 conditions. On the other hand, when Str $\geq$ 8, only the flame tip oscillates. The pulse parameter (P) is smaller in this region as well as the height (H) of an idealized puff cylinder (0.2 mm<H $\leq$ 1.4 mm) The visible flame heights were found to change only in between 81 mm and 89 mm for E(1) with 30 Hz pulsation (Fig. 6.11, bottom image), corresponding to Str=8 condition. To distinguish between these two types of flickering, they are called as “Bulk” and “Tip” flickering. They were also called, Type A and Type B flickering by Sato et al. (2000). We observed the breakup of the flame surface for the bulk flickering

(Fig. 6.11, top image) and no breakup of the flame surface occurred for the tip flickering (Fig. 6.11, bottom image).

6.6 Summary

The experimental setup developed in this study was for two-dimensional imaging of soot particles in steady and unsteady (pulsed) laminar diffusion flames. A pulsed laser source, beam delivery and signal collection optics, and a detector were used as well as the timing electronics, synchronizing the laser, camera and data acquisition system. A pulsed laser source (the pulse duration of 5 ns) with a second harmonic module (532 nm) and a maximum frequency of 10 Hz was used. The dialectric mirrors were used to change the direction of the laser beam followed by a beam steering device that elevated the laser beam to the required height of the flame. The laser sheet adjuster module was used to obtain a laser sheet with a height of 150 mm and a thickness of 0.6 mm. The laser energy was 20 mJ per pulse, monitored during the experiment by a laser energy meter. The LII images were taken using an intensified two-dimensional CCD camera. The LII images were collected at 90 degrees using a 50 mm F.1.4 lens mounted on the camera. An interference filter with a 600 nm wavelength and 36 nm bandwidth was placed in front of the camera lens to collect the LII signals. This filter was used to detect only the LII signal and to eliminate the scattering signal at 532 nm. An axisymmetric, co-flowing, non-premixed ethylene laminar flame of 88 mm height at atmospheric pressure was generated. The burner was designed to duplicate the steady flame used in previous studies. This helped to make a comparison of the steady flame data obtained in this study using the LII and previous studies using a different diagnostic technique. The fuel nozzle

had an inner diameter of 11.1 mm and was surrounded by a 101 mm inner diameter ceramic honeycomb providing airflow around it. The burner was placed on the vertical and horizontal positioners on the optical table. The burner was adjusted using the positioners so that the laser sheet was passing through the centerline of the flame. A high-speed solenoid valve with a minimum spike time of 0.1 ms was selected according to the pressure and the flow rate of fuel. It was placed in the fuel line along with the solenoid circuit and the wave generator to pulse the flame. The wave generator provided the circuit with square waves at selected frequencies. For all of the frequencies tested in this study, the duty cycle of the valve was set to 20% (the valve opened for only 20% of the time period and closed for the remaining 80% of the time period). For the steady flame, a straight input signal was used instead of the square wave (keeping the valve open 100% of the time). The laser Q-Switch signal was used to trigger the laser fire, the wave generator and the camera controller. This enabled us to have the phase-locked LII images of the soot volume fraction. The WinView/32 software was used to acquire the LII images and control the controller and the PTG (Programming Timing Generator) of the ICCD camera. The gate width (duration) for each LII image was 100 ns.

The gas fuel used in this study was ethylene. Four different steady flames were generated with visible flame heights changing from 35 mm to 88 mm. The coflow air flow rates were kept constant at 1000 cm^3/s for all of the studied cases, namely, seven different frequencies (f = 10, 15, 20, 30, 50, 100, and 200 Hz) and eight different phases ($\phi = 0^o$, 72^o, 90^o, 135^o, 180^o, 225^o, 270^o, 315^o and 360^o=0°). Four fuel flow rates, eight phases, one steady and seven pulsing frequencies for each case were analyzed by capturing and processing 2508 images (44 images for steady and 2464 images for

unsteady). The resultant 456 images (8 images for steady and 448 images for unsteady) were given in Chapter 5 starting from Fig. 5.32 to Fig. 5.61.

6.7 Conclusions

Laser Induced Incandescence (LII) is used in a quantitative basis to measure the soot volume fraction in steady and flickering ethylene diffusion flames. The benefit of this study is to have better a understanding of soot formation and therefore, develop effective control strategies in producing changes in the flame structure, flame height, flame temperature and flame radiation. This can be achieved by introducing frequency dependant changes by oscillating the fuel concentrations while holding same mean fuel flow rate and Reynolds number dependant changes by altering the exit fuel flow rate for limiting the emission of soot. This study is significant because large range pulsing frequencies from 10 Hz to 200 Hz were introduced to create the unsteady flow fields in 28 flames (and corresponding 4 steady flames) by means of using a very-high-speed (VHS) solenoid valve. This is a fundamentally different approach to unsteady combustion for laminar flames in that this type of flow control enables us to have drastic modification of combustion and flow characteristics leading to enhanced fuel/air mixing mechanisms.

The major observations and conclusions of the present study are as follows:

- The Laser-Induced Incandescence (LII) technique has been developed to resolve 2-D soot volume fraction profiles with high temporal and spatial resolution. The feasibility of the implementation of the present data analysis was demonstrated in 32 different laminar ethylene/air flames (4 steady and 28 unsteady). The oscillation frequency of the pulsed flames was changed between 10 Hz and 200

- Although the LII technique along with other optical techniques did have many advantages, there were some problems associated with using these methods for obtaining data of soot parameters. When optical techniques were used very low in the flame, the measured signals might not be entirely due to solid particles but also could be due to the high molecular weight hydrocarbon molecules. Therefore, there was difficulty in distinguishing the optical means between soot precursors and mature soot particles, especially very low in the flame.
- The soot volume fractions for the steady flame obtained by LII showed good agreement with those obtained previously using the scattering/extinction technique. A nondimensional axial coordinate (η) provided a good scaling approach in terms of the location of the maximum soot volume fraction in steady flames.
- For the unsteady or pulsed flames, the phase locked soot images revealed the entire motion process of the soot field during one pulsation period. Local peak soot volume fraction in the flames increased up to a maximum 1.77 times for flickering flames.
- Analysis of time-averaged LII images revealed that the gap between soot formation in the annular region (higher f_v) and the central region (lower f_v) of the steady flame was diminished and peak soot volume fractions were observed in

larger radial locations (further from flame center axis) when pulsation was introduced.

- The total soot formation in the flame decreased by lowering the oscillation frequency by up to 1.4 times (except for the 35mm flame, where there was 1.2 times enhancement). *Soot suppression* is beneficial because continuum radiation from soot is the main heat load for combustion components and this controls their durability. Also, soot is a pollutant and can have carcinogenic effect. On the other hand, *soot enhancement* can be greatly utilized in the soot industry (tires, printing inks, coatings etc.) and furnaces as an intermediate (because it contributes a great deal to the heat transfer through radiation).
- A new correlation in the form of "$f_v \mathrm{Re}^{-1} = a + b \cdot Str$" was developed to express the total soot production tendency of the unsteady ethylene flames in the flame region for the pulsation frequencies tested ($10\,Hz \le f \le 200\,Hz$) and the fuel flow rates studied ($25 \le \mathrm{Re} \le 55$).
- Increasing the Reynolds number increased the volume-integrated soot volume fraction for steady and pulsed flames taking the flames to their limit to utilize the additional residence time for soot mass growth.
- The observed emission of smoke from pulsed flames with frequencies of less than 30 Hz showed the influence of the radiative cooling on soot oxidation and breakout in time-varying flames.
- The post flame soot aerosol measurements revealed that considerable concentrations of soot was detectable in flickering flames for pulsing frequencies

of less than 30 Hz (Str<8). The bulk flickering motion was probably the reason for this result in that the break out of flame surfaces caused repetitions of oversupply and the lack of oxygen occurred in the flame region, and overcooling because of excessive radiation probably made the soot particles too cool for rapid oxidation in the oxidation region (near the tip of the flame) causing them to appear as smoke at the post flame region.

- Three different TIRE-LII methods were tested to determine the primary soot particle diameter in a steady 88 mm ethylene flame (E1). TIRE-LII produced good agreement with the double-exponential fit method.
- The peak primary soot particle diameter (d_p) values were found to exist at the maximum soot volume fraction (f_v) locations. The pulsing at low frequencies (10 Hz and 15 Hz) resulted in the highest peak values of d_p. At maximum frequency (200 Hz), the soot particles were smaller in size by 15% compared to the steady case.

6.8 Future Recommendations

Some recommendations offered for future work are as follows.

1. Simultaneous detection of LII (with the ICCD camera) and TIRE-LII (with PMT) is recommended for more reliable, simultaneous soot concentrations and particle size measurements. Using a photo multiplier tube (PMT) is very useful for TIRE-LII experiments because of its fast response time and high sensitivity range.

2. Using an infrared laser source (the fundamental output 1064 nm of the Nd:YAG laser) for excitation of soot particles is recommended since it is less problematic as explained in Section 6.4.2.
3. Using high laser energy (>1 J/cm^2) for TIRE-LII experiments would be a better choice because of the fact that the double-exponential fit method would represent vaporization and heat conduction dominant regions better for all soot particles in the sample volume.
4. The velocity fields were not measured in steady and flickering flames. For that reason, the time histories of fluid parcels corresponding to flickering flames are unknown. Knowledge gained from the velocity field can be combined with this study (f_V (r,z)) to obtain the carbon conversion fraction (fraction of fuel converted to soot) using the expression, $\dot{m}_s(z) = \int_o^R 2\pi\rho_s \; f_v(r,z)\, u_z(r,z)\, r dr$.
5. Even though temperature measurements are challenging with thermocouple measurements due to the presence of soot in ethylene flames, these measurements could provide more reliable relative temperature changes in the presence of pulsation.
6. Other fuels, such as methane (less sooty than ethylene) and propane (more sooty than methane) can be investigated to extent this study.
7. Investigation of fully modulated flames by pulsation with a very low duty cycle (~1%) is another interesting area, recently being applied to turbulent jet flames by researchers. This could be applied to see the history of individual pulses and the effect of low duty cycles for laminar flames.

REFERENCES

Ai Y and Zhou H (2005) Simulation on simultaneous estimation of non-uniform temperature and soot volume fraction distributions in axisymmetric sooting flames. Journal of Quantitative Spectroscopy and Radiative Transfer 91:11-26

Allouis C, Beretta F and D'Alessio A (2003) Sizing soot and micronic carbonaceous particle in spray flames based on time resolved LII. Experimental Thermal and Fluid Science 27:455-463

Axelsson B, Collin R and Bengtsson PEE (2001) Laser-induced incandescence for soot particle size and volume fraction measurements using on-line extinction calibration. Applied Physics B: Lasers and Optics 72:367-372

Bengtsson PE and Alden M (1989) Application of a pulsed laser for soot measurements in premixed flames. Applied Physics B 48:155-164

Bohren CF and Huffman DR (1983) Absorption and scattering of light by small particles. New York: John Wiley & Sons

Brockmann M, Fischer M and Maller KM (1998) Exposure to carbon black: A cancer risk? International Archives of Occupational and Environmental Health 71:85-99

Burtscher H (2005) Physical characterization of particulate emissions from diesel engines: A review. Journal of Aerosol Science 36:896-932

Chatfield C (1978) Statistics for technology. Great Britain: Chapman and Hall

Chigier NA (1975) Pollution formation and destruction in flames. Progress in Energy and Combustion Science 1:3-15

Choi MY and Jensen KA (1998) Calibration and correction of laser-induced incandescence for soot volume fraction measurements. Combustion and Flame 112:485-491

Cignoli F, Benecchi S and Zizak G (1994) Time-delayed detection of laser-induced incandescence for the two-dimensional visualization of soot in flames. Applied Optics 33:5778-5782

Colbeck I, Atkinson B and Johar Y (1997) The morphology and optical properties of soot produced by different fuels. Journal of Aerosol Science 28:715-723

Dalzell WH and Sarofim AF (1969) Optical constants of soot and their application to heat-flux calculations. Journal of Heat Transfer 91:100-104

D'Anna A, Rolando A, Allouis C, Minutolo P and D'Alessio A (2005) Nano-organic carbon and soot particle measurements in a laminar ethylene diffusion flame. Proceedings of the Combustion Institute 30:1449-1456

Dasch CJ (1984) Continuous-wave probe laser investigation of laser vaporization of small soot particles in a flame. Applied Optics 23:2209

Dasch CJ (1992) One-dimensional tomography: A conversion of abel, onion-peeling, and filtered back projection methods. Applied Optics 31:1146-1152

Delhay J, Bouvier Y, Therssen E, Black JD and Desgroux P (2005) 2D imaging of laser wing effects and of soot sublimation in laser-induced incandescence measurements. Applied Physics B: Lasers and Optics 81:181-186

Demare D and Baillot F (2004) Acoustic enhancement of combustion in lifted nonpremixed jet flames. Combustion and Flame 139:312-328

Dobbins RA, Santoro RJ and Semerjian HG (1990) Analysis of light scattering from soot using optical cross sections for aggregates. 23rd Symposium (International) on Combustion, Orleans, France.

Dobbins RA, Fletcher RA and Chang H- (1998) The evolution of soot precursor particles in a diffusion flame. Combustion and Flame 115:285-298

Eckbreth AC (1996) Laser diagnostics for combustion temperature and species. The Netherlands: Gordon and Breach Publishers

El-Leathy AM, Xu F, Kim CH and Faeth GM (2003) Soot surface growth in laminar Hydrocarbon/Air diffusion flames. AIAA Journal 41:856-865

Ezekoye OA, Martin KM and Bisetti F (2005) Pulsed flow modulation of soot production in a laminar jet-diffusion flame. Proceedings of the Combustion Institute 30:1485-1492

Filippov A, Markus M, Roth P, Kauffeldt T and Muhlbauer H (1997) Comparative size analysis of ultrafine aerosol particles. Journal of Aerosol Science 28:S13-S14

Filippov AV, Markus MW and Roth P (1999) In-situ characterization of ultrafine particles by laser-induced incandescence: Sizing and particle structure determination. Journal of Aerosol Science 30:71-87

Fletcher TH, Ma J, Rigby JR, Brown AL and Webb BW (1997) Soot in coal combustion systems. Progress in Energy and Combustion Science 23:283-301

Gaydon AG and Wolfhard HG (1979) Solid carbon in flames. In: Flames:Their structure,radiation,and temperature. Great Britain: The Chaucer Press

Glassman I (1989) Soot formation in combustion processes. Twenty-Second Symposium (International) on Combustion, Seattle.

Glassman I (1977) Diffusion flames. In: Combustion. New York: Academic Press

Green RM and Witze PO (2000) Laser-induced incandescence and elastic-scattering measurements of particulate-matter volume fraction changes during passage through a dilution tunnel. Proceedings of the 10th International Symposium on Applications of Laser Techniques to Fluid Mechanics, Lisbon.

Hansen J and Nazarenko L (2004) Soot climate forcing via snow and ice albedos. Proceedings of the National Academy of Sciences 101:423-428

Hermanson JC, Johari H, Stocker DP and Hegdec UG (2004) Buoyancy effects in strongly pulsed turbulent diffusion flames. Combustion and Flame 139:61-76

Higgins KJ, Jung H, Kittelson D, Robets J and Zachariah M (2002) Size-selected nanoparticle chemistry: Kinetics of soot oxidation. Journal of Physical Chemistry Part A 106:96-103

Hult J, Omrane A, Nygren J, Kaminski CF, Axelsson B, Collin R, Bengtsson P and Alden M (2002) Quantitative three-dimensional imaging of soot volume fraction in turbulent non-premixed flames. Experiments in Fluids 33:265-269

Jacobson MZ (2001) Strong radiative heating due to the mixing state of black carbon in atmospheric aerosols. Nature 409:695-697

Jenkins TP, Bartholomew JL and DeBarber PA (2002) A laser-induced incandescence system for measuring soot flux in aircraft engine exhausts. AIAA Paper 3736. AIAA/ASME/SAE/ASEE Joint Propulsion Conference, Indianapolis.

Jessen PF and Gaydon AG (1967) Study of the absorption spectra of free radicals in flames. Combustion and Flame 11:11-16

Jenkins TP, Bartholomew JL, DeBarber PA, Yang P, Seitzman JM and Howard RP (2002) Laser induced incandescence for soot concentration measurements in turbine engine exhausts. AIAA Conference Paper 0828. 40th AIAA Aerospace Sciences Meeting and Exhibit, Reno, NV.

Jordan M and Zell ME- (2001) Possibilities for fluid-physics and combustion experiments on-board the international space station (ISS). Heat and Mass Transfer 37:533-542

Kamm S, Mohler O, Naumann K-, Saathoff H and Schurath U (1999) The heterogeneous reaction of ozone with soot aerosol. Atmospheric Environment 33:4651-4661

Kang KT, Hwang JY, Chung SH and Lee W (1997) Soot zone structure and sooting limit in diffusion flames: Comparison of counterflow and co-flow flames. Combustion and Flame 109:266-281

Kennedy IM, Yam C, Rapp DC and Santoro RJ (1996) Modeling and measurements of soot and species in a laminar diffusion flame. Combustion and Flame 107:368-382

Kent JH, Jander H and Wagner HG (1981) Soot formation in a laminar diffusion flame. 18th Symposium (International) on Combustion, Jeju, Korea.

Kim CH, El-Leathy AM, Xu F and Faeth GM (2004) Soot surface growth and oxidation in laminar diffusion flames at pressures of 0.1-1.0 atm. Combustion and Flame 136:191-207

Kim W, Sorensen CM, Fry D and Chakrabarti A (2005) Soot aggregates, superaggregates and gel-like networks in laminar diffusion flames. Journal of Aerosol Science In Press, Corrected Proof:

Kleeman M and Cass G (1998) Source contributions to the size and composition distribution of urban particulate air pollution. Atmospheric Environment 32:2803-2816

Köylü Ü Ö, McEnally CS, Rosner DE and Pfefferle LD (1997) Simultaneous measurements of soot volume fraction and particle size / microstructure in flames using a thermophoretic sampling technique. Combustion and Flame 110:494-507

Kruger V, Wahl C, Hadef R, Geigle KP, Stricker W and Aigner M (2005) Comparison of laser-induced incandescence method with scanning mobility particle sizer technique: The influence of probe sampling and laser heating on soot particle size distribution. Measurement Size and Technology 16:1477-1486

Lehre T, Bockhorn H, Jungfleisch B and Suntz R (2003) Development of a measuring technique for simultaneous in situ protection of nanoscaled particle size distributions and gas temperatures. Chemosphere 51:1055-1061

Lehre T, Suntz R and Bockhorn H (2005) Time-resolved two-color LII: Size distributions of nano-particles from gas-to-particle synthesis. Proceedings of the Combustion Institute 30:2585-2593

Linan A and Williams F (1993) Fundamental aspects of combustion. New York: Oxford University Press

Liu F, Smallwood GJ and Snelling DR (2005) Effects of primary particle diameter and aggregate size distribution on the temperature of soot particles heated by pulsed lasers. Journal of Quantitative Spectroscopy&Radiative Transfer 93:301-312

Manta V, Cignoli F, Iuliis S and Zizak G (2000) 2-D soot diagnostic with a two-color emission technique. 23th Event of Italian Section of the Combustion Institute, Napoli.

McCrain LL and Roberts WL (2005) Measurements of the soot volume field in laminar diffusion flames at elevated pressures. Combustion and Flame 140:60-69

Mccuen R (1985) Statistical methods for engineers. New Jersey: Prentice-Hall

McManus KR, Allen MG and Rawlins WT (1997) Quantitative detection and imaging of soot particles by laser induced incandescence. AIAA Conference Paper 97-0117. 35th AIAA Aerospace Sciences Meeting & Exhibit, Reno, NV.

Melsom JA (January 1998) Keeping the Rubber Industry in the Black http://www.astm.org/commit/custom1/D24.htm

Melton LA (1984) Soot diagnostics based on laser heating. Applied Optics 23:2201-2208

Mengüç P and McDonough J (1996) Understanding the chaotic nature of flames. Energeia 7:1-4

Menon S, Hansen JE, Nazarenko L and Luo Y (2002) Climate effects of black carbon aerosols in china and india. Science 297:2250-2253

Mewes B and Seitzman J (1997) Soot volume fraction and particle size measurements with laser-induced incandescence. Applied Optics 36:709-717

Michelsen HA (2003) Understanding and predicting the temporal response of laser-induced incandescence from carbonaceus particles. Journal of Chemical Physics 118:7012-7045

Mohammed RK, Tanoff MA, Smooke MD, Schaffer AM and Long MB (1998) Computational and experimental study of forced,time-varying,axisymmetric,laminar diffusion flames. 27th Symposium (International) on Combustion, Colorado.

Moreau C, Pauwels JF, Desgroux P and Therssen E (2003) Particle size and soot volume fraction measurements in atmospheric diffusion flame by laser-induced incandescence combined with cavity ring-down spectroscopy. Proceedings of the European Combustion Meeting, Orleans, France.

Murr LE and Soto KF (2005) A TEM study of soot, carbon nanotubes, and related fullerene nanopolyhedra in common fuel-gas combustion sources. Materials Characterization 55:50-65

Ni T, Pinson JA, Gupta S and Santoro RJ (1995) Two-dimensional imaging of soot volume fraction by the use of laser-induced incandescence. Applied Optics 34:7083-7091

Papadopoulos G, Bryant RA and Pitts WM (2002) Flow characterization of flickering methane/air diffusion flames using particle image velocimetry. Experiments in Fluids 33:472-481

Park J and Shin HD (1997) Experimental investigation of the developing process of an unsteady diffusion flame. Combustion and Flame 110:67-77

Peters N (1984) Laminar diffusion flamelet models in non-premixed turbulent combustion. Progress in Energy and Combustion Science 10:319-339

Pinder T and Atreya A (2003) Experimental and computational investigation of dynamic control strategies for nonpremixed flames. The Third Joint Meeting of the U.S. Sections of The Combustion Institute, Chicago.

Poinsot TJ, Trouve AC, Veynante DP, Candel SM and Esposito EJ (1987) Vortex-driven acoustically coupled combustion instabilities. Journal of Fluid Mechanics 177:265-292

Pueschel RF, Verma S, Howard SD, Ferry GV, Goodman J and Allen DA (1995) Soot aerosol in the atmosphere: Contributions by aircraft. Journal of Aerosol Science 26:S853-S854

Puri R, Richardson TF, Santoro RJ and Dobbins RA (1993) Aerosol dynamic processes of soot aggregates in a laminar ethene diffusion flame. Combustion and Flame 92:320-333

Qamar NH, Nathan GJ, Alwahabi ZT and King KD (2005) The effect of global mixing on soot volume fraction: Measurements in simple jet, precessing jet, and bluff body flames. Proceedings of the Combustion Institute 30:1493-1500

Qi H (2000) Soot particle properties in nonpremixed laminar flames using a thermophoretic sampling technique. Master Thesis. Florida International University, Miami, FL.

Qian J and Law CK (1997) On the spreading of unsteady cylindrical diffusion flames. Combustion and Flame 110:152-162

Quay B, Lee T,W., Ni T and Santoro RJ (1994) Spatially resolved measurements of soot volume fraction using laser-induced incandescence. Combustion and Flame 97:384-392

Saito M, Sato M and Nishimura A (1998) Soot suppression by acouistic oscillated combustion. Fuel 77:973-978

Santoro RJ, Semerjian HG and Dobbins RA (1983) Soot particle measurements in diffusion flames. Combustion and Flame 51:203-218

Santoro RJ, Yeh TT, Horwath JJ and Semerjian HG (1987) The transport and growth of soot particles in laminar diffusion flames. Combustion Science and Technology 53:89-115

Sapmaz HS (2000) Experimental study of soot by means of extinction and angular scattering measurements in laminar nonpremixed flames. Thesis. Florida International University, Miami, FL.

Sapmaz H, Lin CX, Ebadian MA and Ghenai C (2003) Soot particle measurements in steady and unsteady laminar diffusion flames using laser-induced incandescence. HT2003-47239. ASME Heat Transfer Conference, Las Vegas, Nevada.

Sato H, Amagai K and Arai M (2000) Diffusion flames and their flickering motions related with froude numbers under various gravity levels. Combustion and Flame 123:107-118

Schnaiter M, Horvath H, Mohler O, Naumann K-, Saathoff H and Schock OW (2003) UV-VIS-NIR spectral optical properties of soot and soot-containing aerosols. Journal of Aerosol Science 34:1421-1444

Schraml S, Heimgartner C, Fettes C and Leipertz A (2000) Investigation of in-cylinder soot formation and oxidation by means of two-dimensional laser-induced incandescence. 10th International Symposium on Applications of Laser Techniques to Fluid Mechanics, Portugal.

Schraml S, Dankers S, Bader K, Will S and Leipertz A (2000) Soot temperature measurements and implications for time-resolved laser-induced incandescence (TIRE-LII). Combustion and Flame 120:439-450

Shaddix CR, Harrington JE and Smyth KC (1994) Quantitative measurements of enhanced soot production in a flickering methane/air diffusion flame. Combustion and Flame 99:723-732

Shaddix CR and Smyth KC (1996) Laser-induced incandescence measurements of soot production in steady and flickering methane, propane, and ethylene diffusion flames. Combustion and Flame 107:418-452

Shaddix CR, Williams TC, Blevins LG and Schefer RW (2005) Flame structure of steady and pulsed sooting inverse jet diffusion flames. Proceedings of the Combustion Institute 30:1501-1508

Siegmann K and Siegmann HCE- (1997) The formation of carbon in combustion and how to quantify the impact on human health. Europhysics News 28:50-57

Siegmann K (2000) Soot formation in flames. Journal of Aerosol Science 31:217-218

Smooke MD, Mcenally CS, Pfefferle lD, Hall RJ and Colket MB (1999) Computational and experimental study of soot formation in a coflow,laminar diffusion flame. Combustion and Flame 117:117-139

Smyth KC, Harrington JE, Johnson EL and Pitts WM (1993) Greatly enhanced soot scattering in flickering CH4/Air diffusion flames. Combustion and Flame 95:229-239

Snelling DR, Smallwood GJ and Gulder OU (2000) Soot volume fraction characterization using the laser-induced incandescence detection method. 10th International Symposium on Applications of Laser Techniques to Fluid Mechanics, Portugal.

Snelling DR, Smallwood GR, Campbell IG, Medlock JE and Gulder OL (1997) Development and application of laser-induced incandescence as a diagnostic for soot particulate measurements. 90th Symposium of the Propulsion and Energetics Panel on Advanced Non-Intrusive Instrumentation for Propulsion Engines, Brussels, Belgium.

Snelling DR, Liu F, Smallwood GJ and Gulder OL (2004) Determination of the soot absorption function and thermal accommodation coefficient using low-fluence LII in a laminar coflow ethylene diffusion flame. Combustion and Flame 136:180-190

Starke R, Kock B and Roth PE- (2003) Nano-particle sizing by laser-induced-incandescence (LII) in a shock wave reactor. Shock Waves 12:351-360

Stipe CB, Higgins BS, Lucas D, Koshland CP and Sawyer RF (2005) Inverted co-flow diffusion flame for producing soot. Review of Scientific Instruments 76:1-5

Stipe CB, Choi JH, Lucas D, Koshland CP and Sawyer RFE- (2004) Nanoparticle production by UV irradiation of combustion generated soot particles. Journal of Nanoparticle Research 6:467-477

Straughan BP and Walker S (1976) Spectroscopy vol.3. London: Chapman and Hall Ltd.

Sunderland PB and Faeth GM (1996) Soot formation in hydrocarbon/air laminar jet diffusion flames. Combustion and Flame 105:132-146

Tian K, Liu F, Thomson KA, Snelling DR, Smallwood GJ and Wang D (2004) Distribution of the number of primary particles of soot aggregates in a nonpremixed laminar flame. Combustion and Flame 138:195-198

Urban D (April 2005) Microgravity Combustion Science http://exploration.grc.nasa.gov/combustion/

Vander Wal RL (1996) Laser-induced incandescence:Detection issues. NASA Report 198470.

Vander Wal RL (2000) Development and characterization of laser-induced incandescence towards nanoparticle (soot) detection. NASA Report 209309.

Vander Wal RL (1997) Brief communication: Investigation of soot precursor carbonization using laser-induced flourescence and laser-induced incandescence. Combustion and Flame 110:281-284

Vander Wal RLE- (1997) LIF-LII measurements in a turbulent gas-jet flame. Experiments in Fluids 23:281-287

Vander Wal RL, Jensen KA and Choi MY (1997) Simultaneous laser-induced emission of soot and polycyclic aromatic hydrocarbons within a gas-jet diffusion flame. Combustion and Flame 109:399-414

Vander Wal RL and Choi MY (1999) Pulsed laser heating of soot: Morphological changes. Carbon 37:231-239

Vander Wal RL, Ticich TM and Brock Stephens A (1999) Can soot primary particle size be determined using laser-induced incandescence? Combustion and Flame 116:291-296

Wagner HG (1981) Soot formation. In: Particulate carbon formation during combustion. New York: Plenum Press

Wainner R and Seitzman JM (1999) Soot diagnostics using laser-induced incandescence in flames and exhaust flows. AIAA Conference Paper 99-0640. 37th Aerospace Sciences Meeting and Exhibit, Reno, NV.

Wainner R and Seitzman JM (1999) Soot measurements in a simulated engine exhaust using laser-induced incandescence. AIAA Journal 37:738-743

Walker AP (2004) Controlling particulate emissions from diesel vehicles. Topics in Catalysis Vol. 28, Nos. 1–4, April 2004 28:1-4

Warnatz J, Maas U, and Dibble RW (2001) Combustion:Physical and chemical fundamentals, modeling and simulation, experiments, pollutant formation. Berlin: Springer

Will S, Schraml S, Bader K and Leipertz A (1998) Performance characteristics of soot primary particle size measurements by time-resolved laser-induced incandescence. Applied Optics 37:5647-5658

Will S, Schraml S and Leipertz A (1995) Two-dimensional soot-particle sizing by time-resolved laser-induced measurements. Optics Letters 20:2342-2344

Wilson R and Spengler JD (1996) Particles in our air: Concentrations and health effects. Massachusetts: Harvard University Press

Witze PO (2001) Qualitative laser-induced incandescence measurements of soot emissions during transient operation of a port fuel-injected engine. 3-18. The Fifth International Symposium on Diagnostics and Modeling of Combustion in Internal Combusiton Engines, Nagoya.

Wolff GT and Klimisch RL (1982) Particulate carbon. New york: Plenum Press

Xin Y and Gore JP (2005) Two-dimensional soot distributions in buoyant turbulent fires. Proceedings of the Combustion Institute 30:719-726

Xu F, Dai Z and Faeth GM (2002) Flame and soot boundaries of laminar jet diffusion flames. AIAA Journal 40:2439-2446

Yang P and Seitzman JM (2003) Soot concentration and velocity measurement in an acoustic burner. AIAA Conference Paper 03-1014. 41st AIAA Aerospace Sciences Meeting and Exhibit, Reno, NV.

Yang P, Seitzman JM and Wainner RT (2000) Particle vaporization velocimetry for soot-containing flows. AIAA Conference Paper 0645. 38th Aerospace Sciences Meeting and Exhibit, Reno, NV.

Young HD (1962) Statistical treatment of experimental data. New York: McGraw-Hill

Yu KH, Trouve A and Daily JW (1983) Low frequency pressure oscillations in a model ramjet combustor. Journal of Fluid Mechanics 232:47-72

Zhang J and Megaridis CM (1998) Soot microstructure in steady and flickering laminar methane/air diffusion flames. Combustion and Flame 112:473-484

Zhang J and Megaridis CM (1996) Soot suppression by ferrocene in laminar ethylene/air nonpremixed flames. Combustion and Flame 105:528-540

Zhao H and Ladommatos N (1998) Optical diagnostics for soot and temperature measurement in diesel engines. Progress in Energy and Combustion Science 24:221-255

APPENDICES

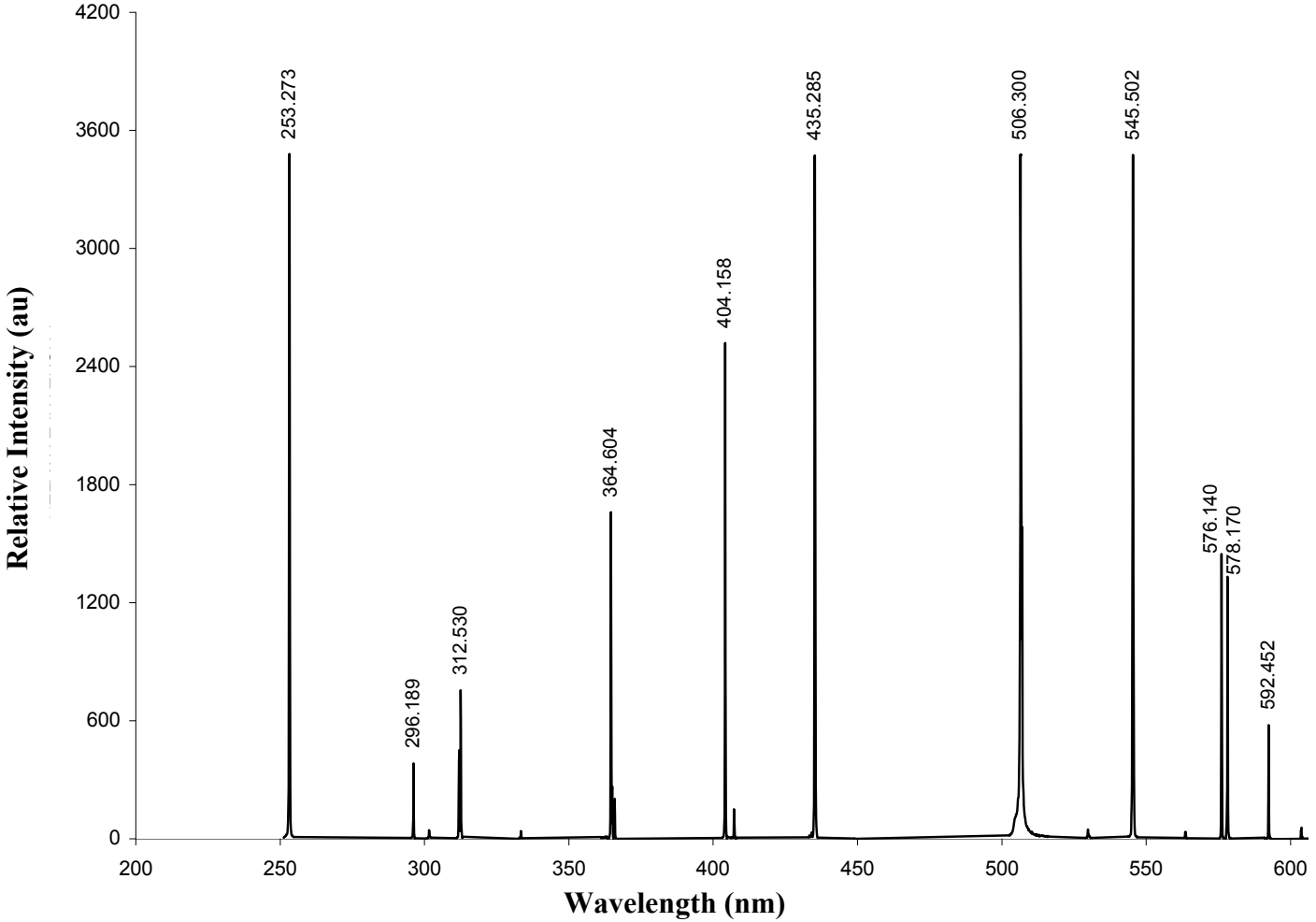

Appendix A.1 Calibration of the spectrometer with SpectruMM detector using mercury lamp

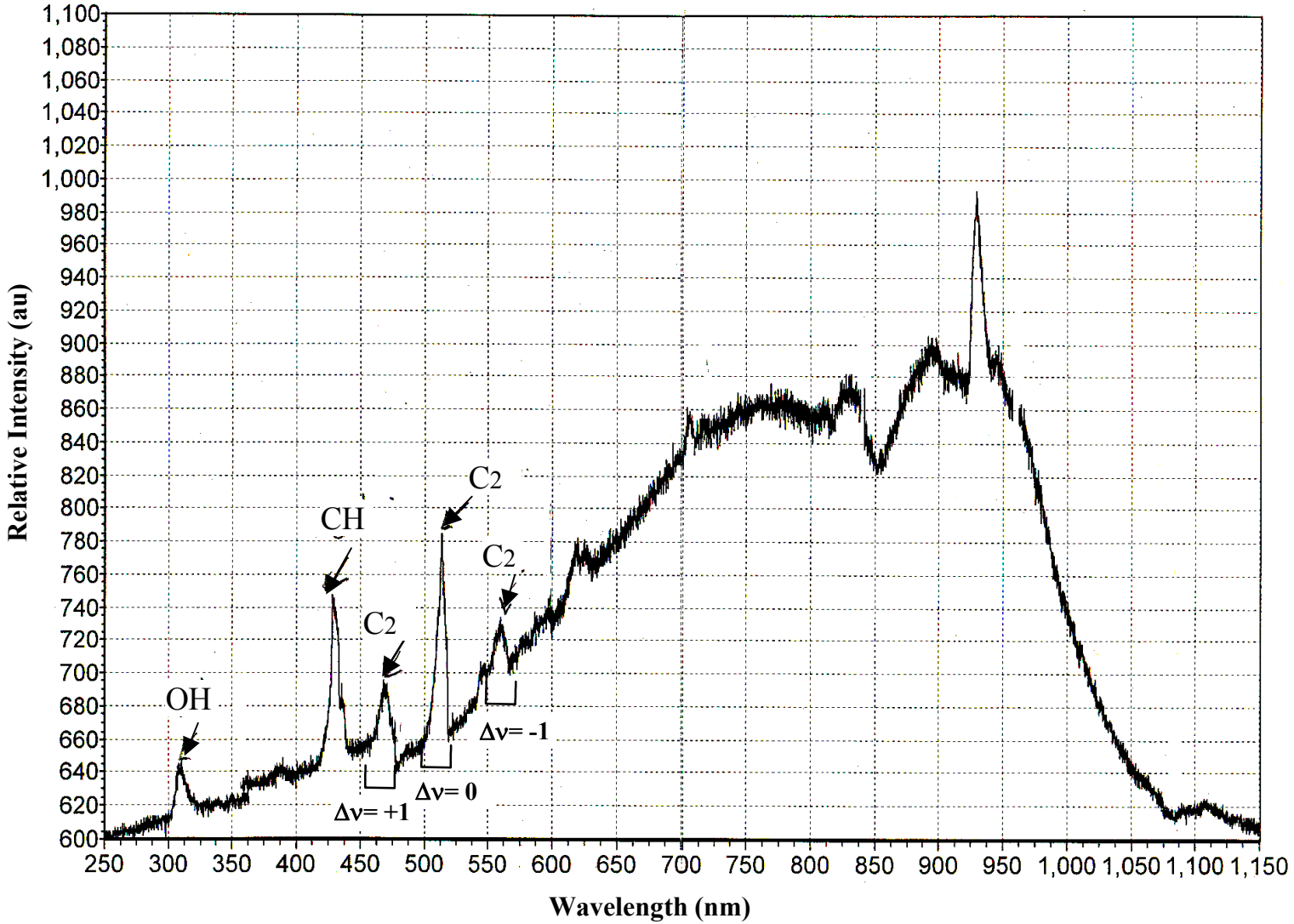

Appendix A.2 Spectrometer scan of ethylene flame for C_2 band emission

Appendix B WinView/32 Software Operating Parameters for LII Experiments

Setup: Hardware: Controller/Camera
    Controller Type: ST-133
    Controller version: 4
    Camera type: EEV 256x1024F CCD 30
    Shutter type: None
Setup: Hardware: Interface: High Speed PCI
Setup: Hardware: Cleans and Skips
    Number of cleans: 1
    Number of strips per clean: 256
    Vertical skips(number of blocks): 5
Setup: Detector Temperature: -20°C
Setup: Pulsers: PTG: Triggers
    Input Trigger Mode: External
    Threshold: 0.15 Volts
    Slope: Positive
    Coupling: DC
    Termination: High
Setup: Pulsers: PTG: Gating
    Mode: Repetitive or Sequential
    Gate Width: 100 ns
    Gate Delay: 52 ns
    Bracket Pulsing: Off
    Burst Mode: Off
Setup: Preferences: General
    Data File Type: WinX Data (spe) or TIFF File (tif)
Setup: Preferences: PTG Gate Mode Preferences
    Exposure Time: 0 ms
    Timing Mode: Internal Sync
    Shutter Control: Disabled Open
Acquisition: Experiment Setup: Main
    Intensifier Mode: Gate Mode
    Intensifier Gain: 256
    Exposure Time: 200 ms
    Gates per exposure: 2
    Accumulations: 1-10
    Number of Images: 1-100
    Use Region of Interest: Yes
Acquisition: Experiment Setup: Timing
    Timing Mode: PTG
    Shutter Control: Normal
    Safe Mode vs. Full Speed: Full Speed
Acquisition: Experiment Setup: ROI Setup
    (X1,Y1): (1,100) (X2,Y2): (1024,240)

Appendix C.1 Transmittance, Extinction Coefficient (K_{ext}) and Deconvolution Technique for steady flame E1 for HAB>40 mm

88-mm-high ethylene flame was investigated for their transmittance, which was obtained by dividing transmitted laser beam intensity by the incident laser beam intensity, i.e., I/I_0. The transmittance values as a function of radial position at several heights is shown in Figs. A.1. The radial step size was 0.381 mm. The radial distance (X = *r*) refers to the distance from centerline of the flame (X = 0) to the laser line, which corresponds to the path of the laser beam through the flame.

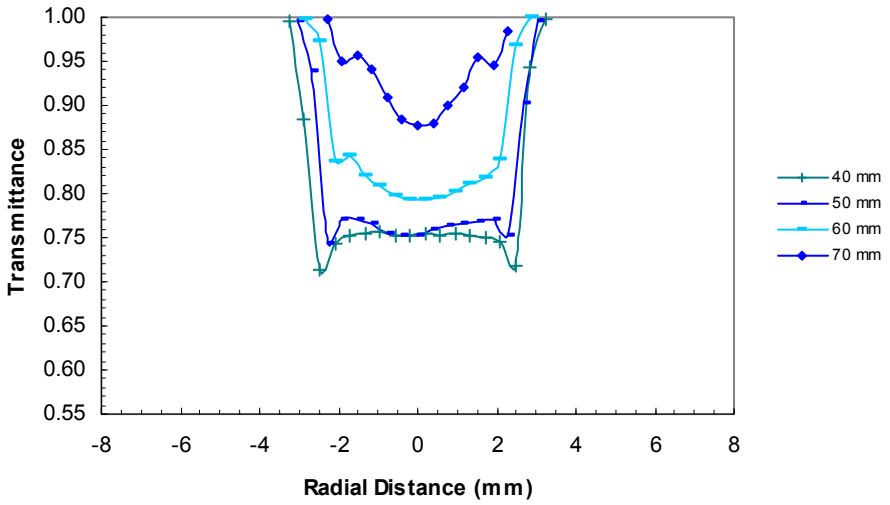

Figure C.1 Transmittance as a function of r for HAB>40 mm (E1)

The measured transmittance was the integrated value of the local extinction coefficient along the optical path through the flame. In order to calculate local extinction coefficients to be used later in the data analysis, these integrated measurements had to be converted to yield the local values. This was accomplished by applying one of the

possible inversion techniques, which namely, 3pt.-Abel (discrete Abel inversion using 3 point interpolation of projection data), 2pt.-Abel (discrete Abel inversion using 2 point interpolation of projection data), Onion-peel (deconvolution using inversion of an onion-peeling weighting of field data), Ram&LakFBP (deconvolution using cylindrical average of Ramachandran and Lakshminarayanan filtered back-projection method), Shepp&LoganFBP (deconvolution using cylindrical average of Shepp and Logan filtered back-projection method). 3pt.-Abel inversion technique was applied as the best solution to the transmittance data in the appropriate format, which is explained in detail by Sapmaz (2000). Symmetrical extinction coefficients, K_{ext} (mm^{-1}), were obtained and are given in Fig. A.2.

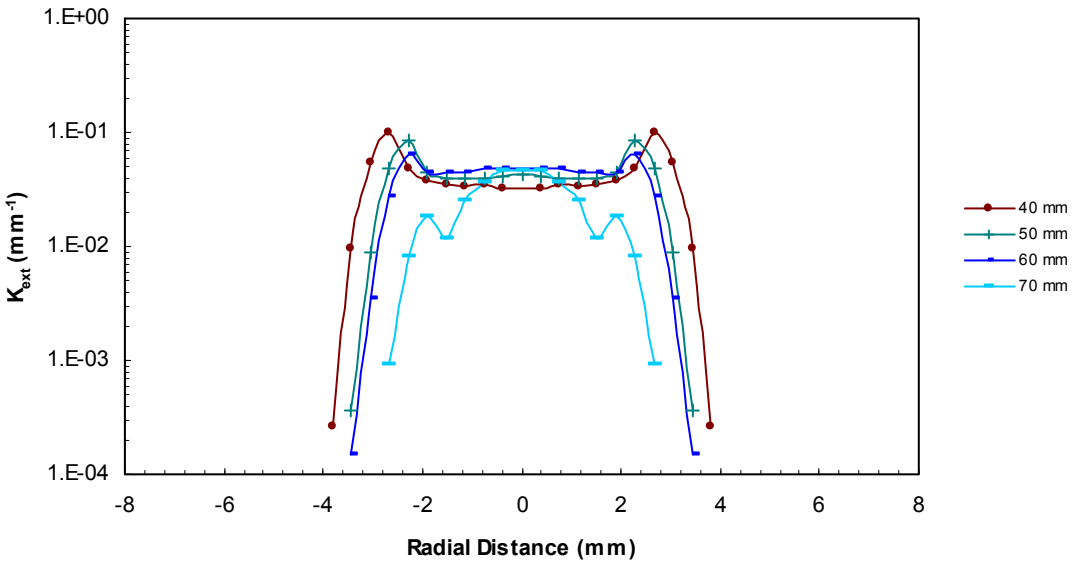

Figure C.2 Local extinction coefficients as a function of r for HAB>40 mm (E1)

Appendix C.2 Correction Table (90°)

HAB (mm) r (mm)	10	15	20	25	30	35	40	50	60	70
-5.715	1.0000									
-5.588	0.9994									
-5.461	0.9991									
-5.334	0.9989	1.0000	1.0000							
-5.207	0.9953	0.9996	0.9997							
-5.08	0.9935	0.9994	0.9995							
-4.953	0.9921	0.9992	0.9994	1.0000						
-4.826	0.9846	0.9938	0.9931	0.9998						
-4.699	0.9805	0.9912	0.9902	0.9997						
-4.572	0.9771	0.9891	0.9878	0.9997	1.0000					
-4.445	0.9717	0.9749	0.9682	0.9937	0.9994					
-4.318	0.9678	0.9675	0.9583	0.9910	0.9991					
-4.191	0.9643	0.9614	0.9502	0.9887	0.9989	1.0000	1.0000			
-4.064	0.9656	0.9516	0.9317	0.9641	0.9940	0.9997	0.9997			
-3.937	0.9646	0.9447	0.9201	0.9519	0.9917	0.9996	0.9995			
-3.81	0.9635	0.9385	0.9100	0.9420	0.9898	0.9995	0.9994	1.0000	1.0000	
-3.683	0.9666	0.9358	0.9018	0.9091	0.9598	0.9886	0.9893	0.9996	0.9998	
-3.556	0.9674	0.9319	0.8939	0.8904	0.9453	0.9834	0.9845	0.9994	0.9998	
-3.429	0.9678	0.9280	0.8864	0.8747	0.9336	0.9793	0.9806	0.9993	0.9997	
-3.302	0.9693	0.9348	0.8971	0.8611	0.8803	0.9309	0.9315	0.9901	0.9961	
-3.175	0.9699	0.9362	0.8988	0.8486	0.8520	0.9074	0.9077	0.9857	0.9944	
-3.048	0.9704	0.9367	0.8990	0.8370	0.8288	0.8885	0.8886	0.9822	0.9930	1.0000
-2.921	0.9714	0.9404	0.9041	0.8497	0.8327	0.8397	0.8338	0.9410	0.9686	0.9991
-2.794	0.9720	0.9420	0.9060	0.8506	0.8255	0.8108	0.8023	0.9208	0.9567	0.9987
-2.667	0.9725	0.9431	0.9071	0.8497	0.8173	0.7866	0.7761	0.9044	0.9471	0.9983
-2.54	0.9731	0.9445	0.9091	0.8613	0.8307	0.8024	0.7908	0.8592	0.9062	0.9912
-2.413	0.9735	0.9454	0.9102	0.8657	0.8328	0.8001	0.7873	0.8326	0.8839	0.9877
-2.286	0.9739	0.9461	0.9110	0.8686	0.8331	0.7956	0.7818	0.8103	0.8654	0.9848
-2.159	0.9741	0.9468	0.9123	0.8713	0.8363	0.8012	0.7821	0.8207	0.8642	0.9737
-2.032	0.9743	0.9473	0.9131	0.8732	0.8370	0.8009	0.7787	0.8168	0.8565	0.9673
-1.905	0.9745	0.9478	0.9137	0.8747	0.8370	0.7994	0.7746	0.8113	0.8484	0.9619
-1.778	0.9747	0.9485	0.9150	0.8764	0.8398	0.8005	0.7724	0.8082	0.8408	0.9620
-1.651	0.9749	0.9490	0.9157	0.8775	0.8406	0.7996	0.7689	0.8035	0.8333	0.9600
-1.524	0.9751	0.9494	0.9163	0.8784	0.8411	0.7982	0.7652	0.7985	0.8261	0.9578
-1.397	0.9752	0.9499	0.9172	0.8797	0.8423	0.7988	0.7624	0.7936	0.8187	0.9464
-1.27	0.9753	0.9502	0.9178	0.8805	0.8428	0.7981	0.7590	0.7886	0.8117	0.9398
-1.143	0.9754	0.9505	0.9183	0.8811	0.8430	0.7970	0.7555	0.7838	0.8052	0.9341
-1.016	0.9754	0.9508	0.9189	0.8825	0.8441	0.7970	0.7512	0.7786	0.7976	0.9221
-0.889	0.9754	0.9510	0.9193	0.8833	0.8445	0.7962	0.7473	0.7737	0.7910	0.9140
-0.762	0.9754	0.9511	0.9196	0.8839	0.8446	0.7952	0.7436	0.7690	0.7848	0.9070
-0.635	0.9754	0.9513	0.9196	0.8844	0.8452	0.7946	0.7409	0.7643	0.7786	0.8960
-0.508	0.9755	0.9514	0.9196	0.8848	0.8453	0.7937	0.7378	0.7598	0.7728	0.8879
-0.381	0.9755	0.9514	0.9196	0.8851	0.8453	0.7925	0.7346	0.7555	0.7673	0.8808
-0.254	0.9754	0.9514	0.9196	0.8853	0.8446	0.7899	0.7315	0.7504	0.7621	0.8741
-0.127	0.9754	0.9514	0.9196	0.8854	0.8440	0.7879	0.7284	0.7460	0.7571	0.8681
0	0.9753	0.9514	0.9195	0.8854	0.8434	0.7860	0.7254	0.7418	0.7524	0.8627

C.2 Correction Table (90°) (Continued)

0	0.9753	0.9514	0.9195	0.8854	0.8434	0.7860	0.7254	0.7418	0.7524	0.8627
0.127	0.9753	0.9514	0.9194	0.8854	0.8428	0.7842	0.7224	0.7378	0.7479	0.8579
0.254	0.9752	0.9513	0.9192	0.8852	0.8421	0.7824	0.7194	0.7341	0.7437	0.8536
0.381	0.9752	0.9513	0.9190	0.8850	0.8416	0.7813	0.7165	0.7309	0.7397	0.8499
0.508	0.9752	0.9512	0.9188	0.8847	0.8407	0.7795	0.7136	0.7276	0.7359	0.8469
0.635	0.9751	0.9510	0.9186	0.8842	0.8397	0.7777	0.7106	0.7244	0.7324	0.8446
0.762	0.9750	0.9509	0.9185	0.8837	0.8383	0.7754	0.7073	0.7214	0.7293	0.8450
0.889	0.9749	0.9507	0.9181	0.8830	0.8370	0.7733	0.7045	0.7184	0.7262	0.8437
1.016	0.9749	0.9504	0.9176	0.8822	0.8354	0.7710	0.7019	0.7156	0.7235	0.8432
1.143	0.9748	0.9502	0.9170	0.8808	0.8332	0.7679	0.6996	0.7130	0.7216	0.8463
1.27	0.9747	0.9498	0.9165	0.8798	0.8315	0.7654	0.6969	0.7103	0.7192	0.8461
1.397	0.9746	0.9495	0.9157	0.8787	0.8295	0.7625	0.6940	0.7076	0.7170	0.8466
1.524	0.9745	0.9490	0.9147	0.8771	0.8267	0.7585	0.6907	0.7049	0.7153	0.8514
1.651	0.9743	0.9485	0.9139	0.8757	0.8244	0.7555	0.6879	0.7022	0.7135	0.8507
1.778	0.9741	0.9479	0.9129	0.8740	0.8216	0.7521	0.6848	0.6992	0.7119	0.8500
1.905	0.9738	0.9471	0.9114	0.8718	0.8170	0.7469	0.6807	0.6949	0.7103	0.8473
2.032	0.9736	0.9465	0.9103	0.8697	0.8141	0.7433	0.6776	0.6918	0.7089	0.8481
2.159	0.9734	0.9458	0.9090	0.8671	0.8106	0.7386	0.6739	0.6874	0.7073	0.8498
2.286	0.9731	0.9449	0.9071	0.8637	0.8047	0.7284	0.6670	0.6711	0.7003	0.8555
2.413	0.9728	0.9440	0.9056	0.8600	0.8006	0.7247	0.6636	0.6746	0.7036	0.8562
2.54	0.9724	0.9428	0.9038	0.8548	0.7947	0.7190	0.6585	0.6810	0.7097	0.8575
2.667	0.9718	0.9412	0.9011	0.8425	0.7782	0.6973	0.6383	0.7013	0.7296	0.8618
2.794	0.9713	0.9397	0.8989	0.8390	0.7766	0.7020	0.6433	0.7052	0.7319	0.8619
2.921	0.9706	0.9377	0.8960	0.8339	0.7742	0.7101	0.6518	0.7118	0.7359	0.8621
3.048	0.9695	0.9336	0.8899	0.8171	0.7615	0.7339	0.6772	0.7338	0.7492	0.8627
3.175	0.9688	0.9319	0.8872	0.8183	0.7678	0.7391	0.6822	0.7347	0.7496	
3.302	0.9679	0.9292	0.8832	0.8202	0.7780	0.7478	0.6903	0.7363	0.7502	
3.429	0.9663	0.9212	0.8703	0.8228	0.8092	0.7758	0.7166	0.7414	0.7523	
3.556	0.9653	0.9212	0.8710	0.8273	0.8130	0.7771	0.7177	0.7415	0.7523	
3.683	0.9640	0.9212	0.8722	0.8342	0.8190	0.7792	0.7195	0.7416	0.7523	
3.81	0.9603	0.9201	0.8734	0.8536	0.8380	0.7857	0.7251	0.7418	0.7524	
3.937	0.9599	0.9216	0.8762	0.8571	0.8386	0.7858	0.7251			
4.064	0.9593	0.9239	0.8804	0.8625	0.8397	0.7858	0.7252			
4.191	0.9565	0.9288	0.8909	0.8789	0.8428	0.7860	0.7254			
4.318	0.9575	0.9311	0.8940	0.8798	0.8429					
4.445	0.9588	0.9346	0.8986	0.8811	0.8430					
4.572	0.9616	0.9446	0.9120	0.8852	0.8434					
4.699	0.9630	0.9455	0.9130	0.8853						
4.826	0.9649	0.9469	0.9145	0.8853						
4.953	0.9703	0.9509	0.9191	0.8854						
5.08	0.9709	0.9510	0.9191							
5.207	0.9718	0.9511	0.9192							
5.334	0.9746	0.9514	0.9195							
5.461	0.9747									
5.588	0.9749									
5.715	0.9753									

Appendix D Laser sheet focusing defocusing at the burner tip

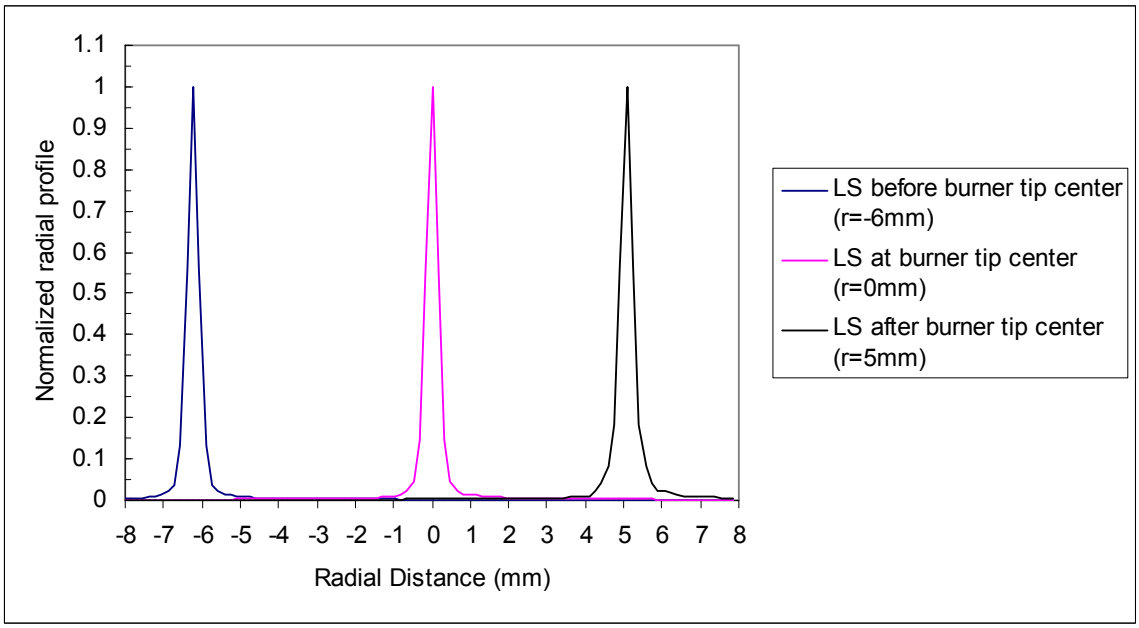

Figure D.1 Light sheet radial profiles before and after burner tip

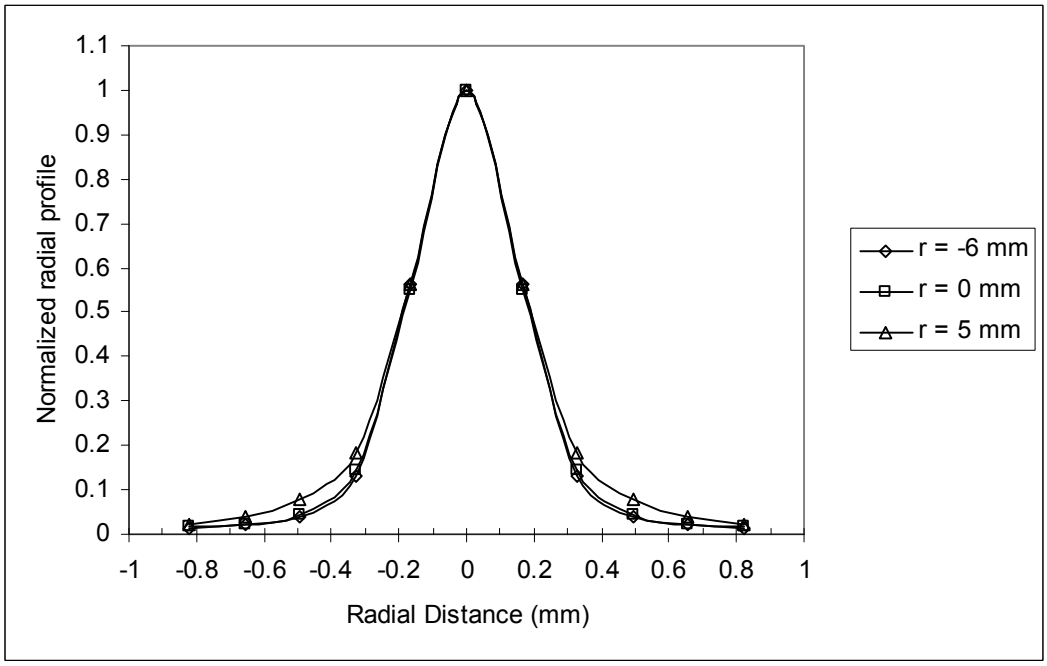

Figure D.2 Light sheet radial profiles before and after burner tip (superposed)

Appendix E Normalized delayed LII signal for 88 mm steady ethylene flame

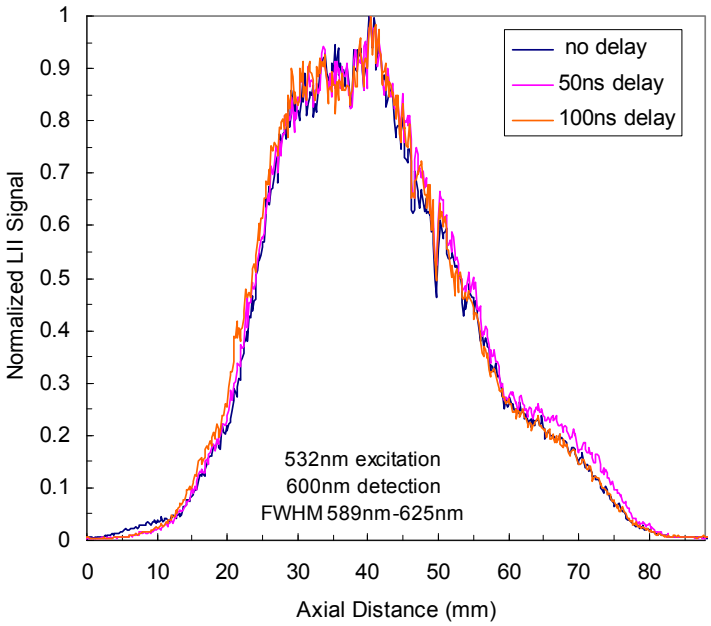

Figure E.1 Normalized LII peak signals with no delay and 50 ns and 100 ns delays (annular region)

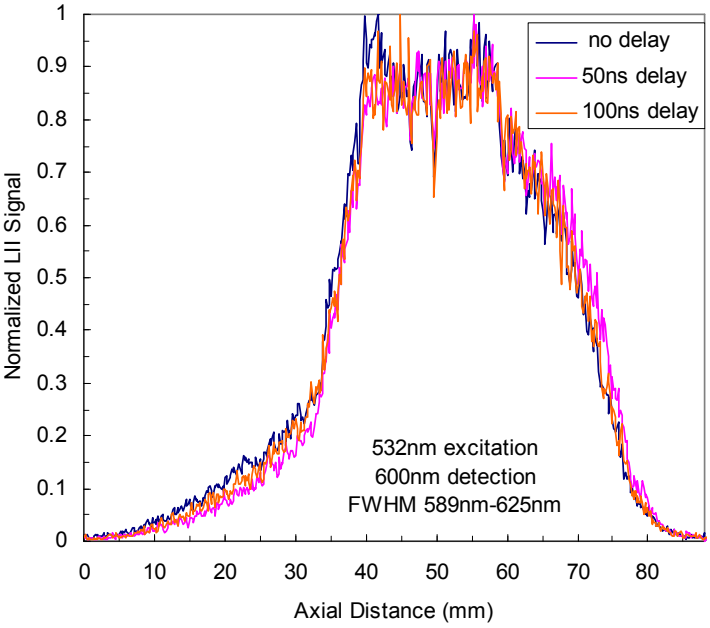

Figure E.2 Normalized LII signals at centerline with no delay and 50 ns and 100 ns delays

Appendix F Blackbody radiation curves for temperatures from 2000 K to 5000 K

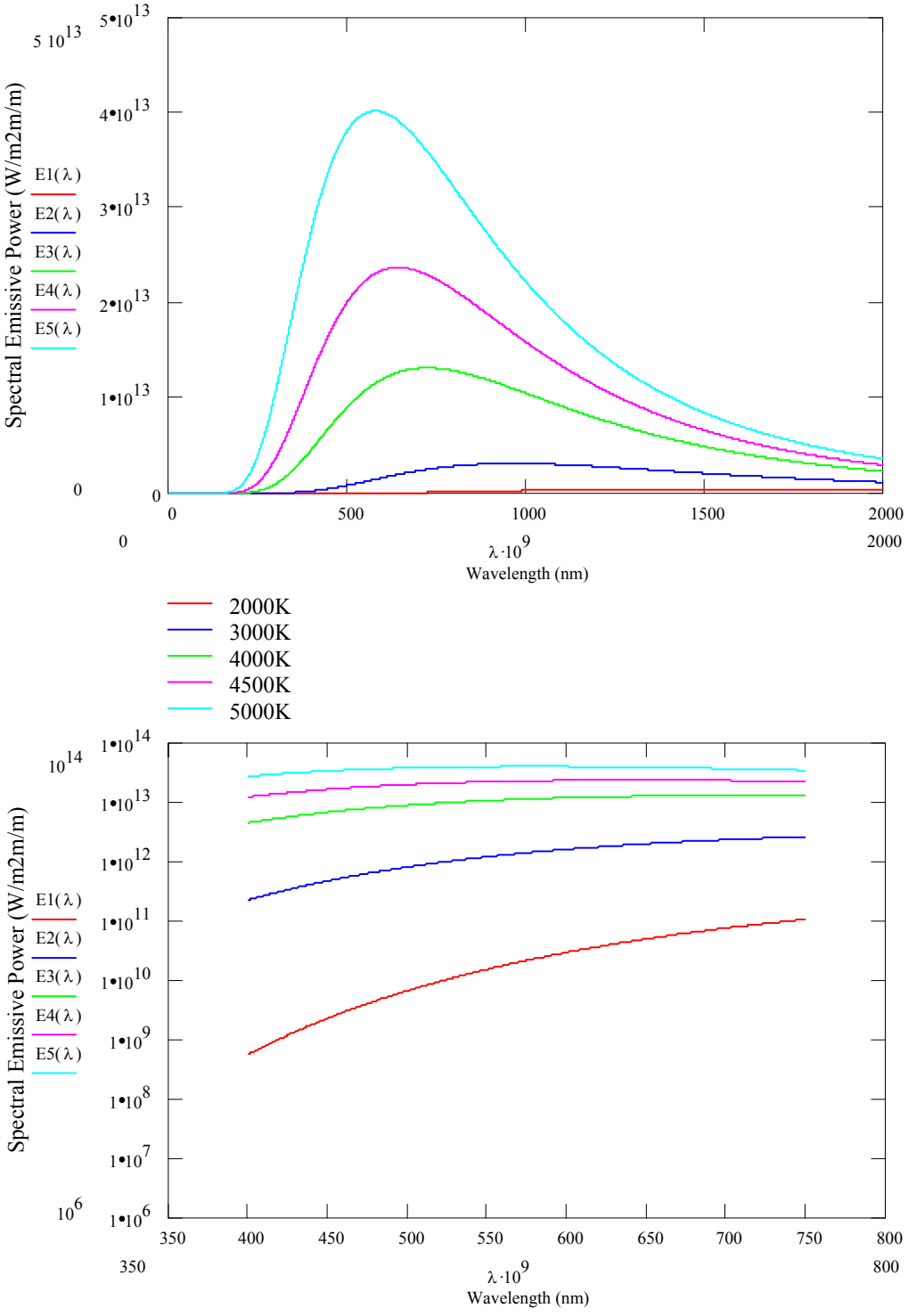

Figure F.1 Blackbody radiation curves: top image (normal), bottom image (log-log)

Appendix G Axial velocity & temperature values for 88 mm steady ethylene flame

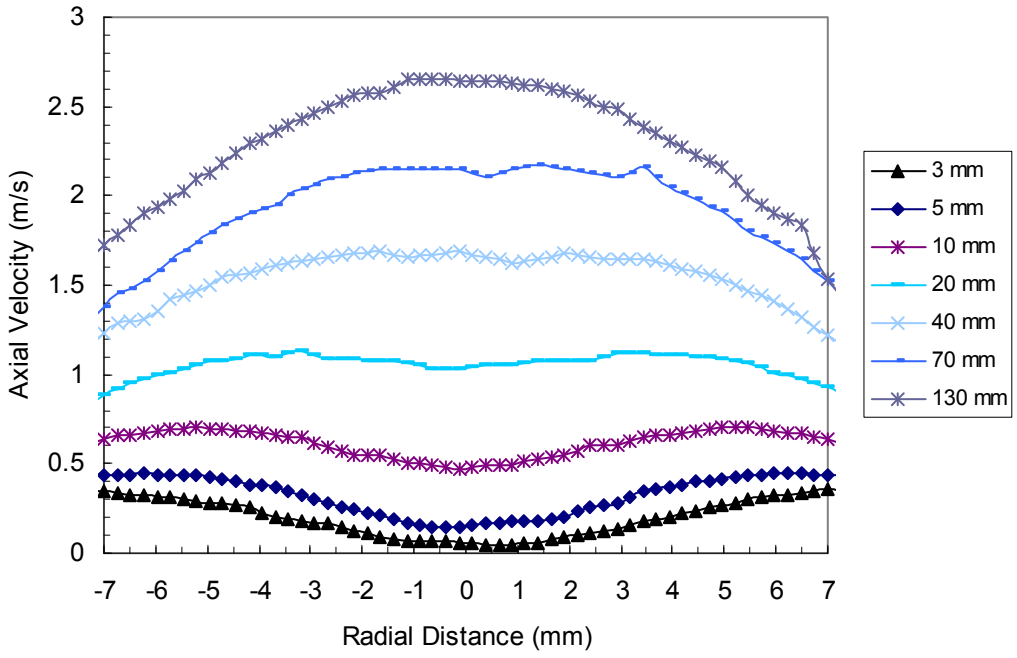

Figure G.1 Axial velocity for 88 mm steady ethylene flame (Santoro et al. 1987)

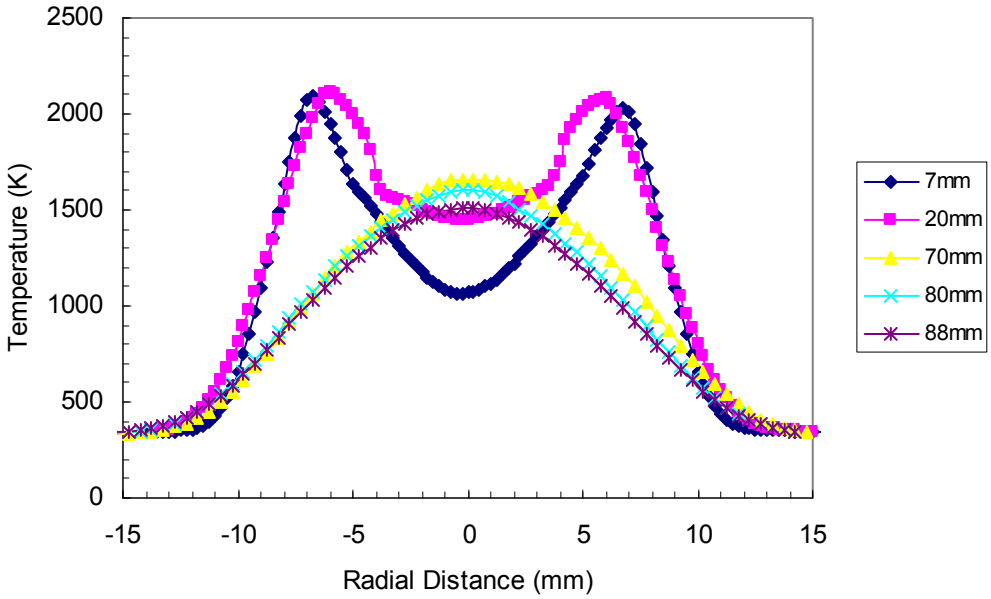

Figure G.2 Temperature values for 88 mm steady ethylene flame (Santoro et al. 1987)

Appendix H TEM photographs of soot sampled at centerline of steady diffusion flame (E1)

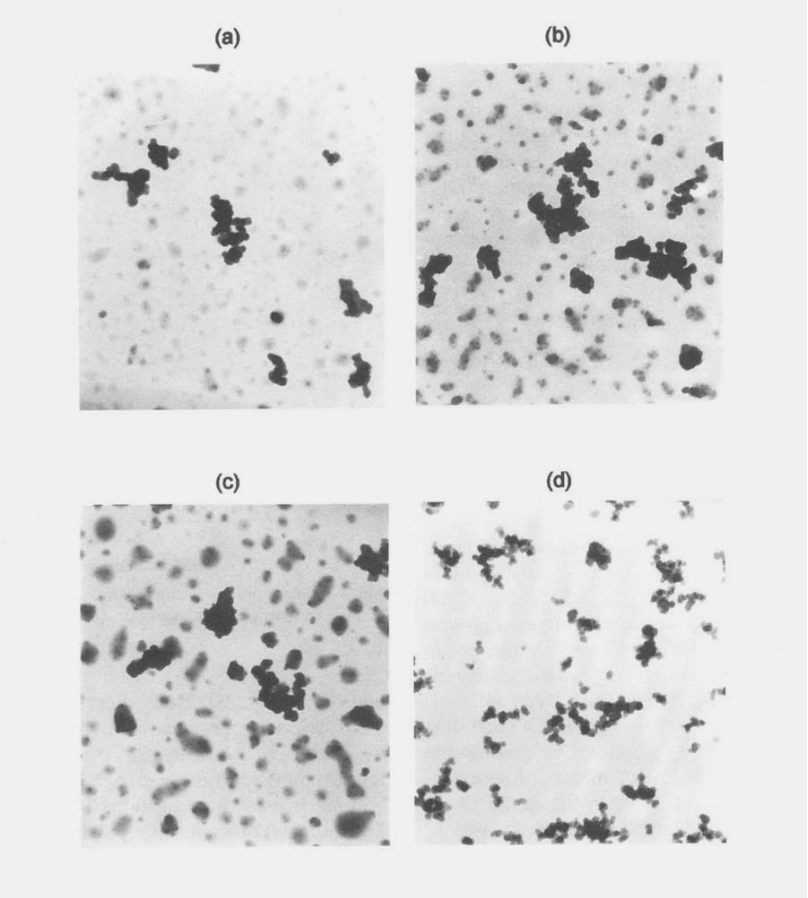

Figure H.1 TEM photographs of soot sampled along the centerline of the flame at several heights above the burner exit: (a) z = 25 mm, (b) 30 mm, (c) 35 mm, and (d) 40 mm (Sapmaz 2000)

Appendix I VHS valve characteristic parameters

E1		(ms)	(ms)	(cm^3)	(cm^3)	(mm)	
	f(Hz)	Ri	Ro	Vo	Vt	H	P
	10	20	80	0.406	4.064	4.2	0.723
	15	13.333	53.333	0.271	4.064	2.8	0.632
	20	10	40	0.203	4.064	2.1	0.574
	30	6.667	26.667	0.135	4.064	1.4	0.501
	50	4	16	0.081	4.064	0.84	0.423
	100	2	8	0.041	4.064	0.42	0.336
	200	1	4	0.02	4.064	0.21	0.266

E2		(ms)	(ms)	(cm^3)	(cm^3)	(mm)	
	f(Hz)	Ri	Ro	Vo	Vt	H	P
	10	20	80	0.352	3.522	3.64	0.69
	15	13.333	53.333	0.235	3.522	2.427	0.602
	20	10	40	0.176	3.522	1.82	0.547
	30	6.667	26.667	0.117	3.522	1.213	0.478
	50	4	16	0.07	3.522	0.728	0.403
	100	2	8	0.035	3.522	0.364	0.32
	200	1	4	0.018	3.522	0.182	0.254

E3		(ms)	(ms)	(cm^3)	(cm^3)	(mm)	
	f(Hz)	Ri	Ro	Vo	Vt	H	P
	10	20	80	0.269	2.69	2.78	0.63
	15	13.333	53.333	0.179	2.69	1.853	0.551
	20	10	40	0.135	2.69	1.39	0.5
	30	6.667	26.667	0.09	2.69	0.927	0.437
	50	4	16	0.054	2.69	0.556	0.369
	100	2	8	0.027	2.69	0.278	0.293
	200	1	4	0.013	2.69	0.139	0.232

E4		(ms)	(ms)	(cm^3)	(cm^3)	(mm)	
	f(Hz)	Ri	Ro	Vo	Vt	H	P
	10	20	80	0.186	1.858	1.92	0.557
	15	13.333	53.333	0.124	1.858	1.28	0.487
	20	10	40	0.093	1.858	0.96	0.442
	30	6.667	26.667	0.062	1.858	0.64	0.386
	50	4	16	0.037	1.858	0.384	0.326
	100	2	8	0.019	1.858	0.192	0.259
	200	1	4	9.29E-03	1.858	0.096	0.205

VITA

HAYRI SERHAT SAPMAZ

November 20, 1976	Born, Urfa, Turkey
1993-1998	B.S., Mechanical Engineering Middle East Technical University Ankara, Turkey
1998-2000	M.S., Mechanical Engineering Florida International University Miami, Florida
	Research Assistant Florida International University Miami, Florida
2000-2001	Research Scientist Hemispheric Center for Environmental Technology Miami, Florida
2001-2006	Graduate Research Assistant Applied Research Center Miami, Florida

PUBLICATIONS AND PRESENTATIONS

Sapmaz H., Lin C. X. and Ghenai C. (2006) Effect of Gas/Liquid Mass Ratio on the Penetration of Aerated Liquid Jet in Supersonic Cross Flow. 44th AIAA Aerospace Sciences Meeting and Exhibit, Reno, Nevada.

Sapmaz H., Alkan B., Lin C. X. and Ghenai C. (2005) Visualization of pulsed aerated liquid jet in supersonic cross flow. FEDSM2005-77192. ASME Fluids Engineering Division Summer Meeting and Exhibition, Houston, Texas.

Ghenai C., Sapmaz H. and Lin C. X. (2005) Characterization of aerated liquid jet in subsonic and supersonic cross flow. AIAA 2005-3580. 41st AIAA/ASME/SAE/ASEE Joint Propulsion Conference & Exhibit, Tucson, Arizona.

Ghenai C., Sapmaz H. and Lin C. X. (2005) Penetration of aerated liquid fuel jet in supersonic cross flow. IMECE2005-79736. ASME International Mechanical Engineering Congress and Exposition, Orlando, Florida.

Sapmaz H., Lin C. X. and Ghenai C. (2005) Soot measurements in pulsed diffusion flame using laser induced incandescence. IMECE2005-79737. ASME International Mechanical Engineering Congress and Exposition, Orlando, Florida.

Ghenai C., Sapmaz H. S., Lin C. X. and Ebadian M. A. (2003) 2-D modeling of co-pulverized Coal/Biomass combustion in furnace with static mixers. TED-AJ03-590. Proceedings of the 6th ASME-JSME Thermal Engineering Joint Conference, Hawaii.

Sapmaz H., Lin C. X., Ebadian M. A. and Ghenai C. (2003) Soot particle measurements in steady and unsteady laminar diffusion flames using laser-induced incandescence. HT2003-47239. ASME Heat Transfer Conference, Las Vegas, Nevada.

Koylu U. O. and Sapmaz H. S. (2001) Optical experiments in luminous flames and implications on soot refractive index. The Third International Symposium on Radiative Transfer, Antalya, Turkey.

Koylu U. O. and Sapmaz H. S. (2001) Soot particle sizing in flames using a two-angle scattering technique. The Second Joint Meeting of the US Sections of the Combustion Institute, Oakland, California.

Sapmaz H. S. (2000) Experimental study of soot by means of extinction and angular scattering measurements in laminar nonpremixed flames. Thesis. Florida International University, Miami, FL.

Ghenai C., Sapmaz H. S. and Lin C. X. Penetration height correlations for pure and aerated trasverse liquid jets in supersonic cross flow. Submitted to Experiments in Fluids Journal on August 29, 2005

Sapmaz H. S., Lin C. X. and Ghenai C. Measurements of soot volume fraction in pulsed hydrocarbon diffusion flame by laser induced incandescence. Submitted to Experiments in Fluids Journal on August 4, 2005

Ghenai C., Sapmaz H. S. and Lin C. X. Penetration of pulsed and aerated liquid jet in supersonic cross flow. Submitted to Journal of Propulsion and Power on July 19, 2005